INPUT-SHAPED MANUAL CONTROL OF HELICOPTERS WITH SUSPENDED LOADS

A Thesis
Presented to
The Academic Faculty

by

James Jackson Potter

In Partial Fulfillment
of the Requirements for the Degree
Doctor of Philosophy in the
George W. Woodruff School of Mechanical Engineering

Georgia Institute of Technology
December 2013

INPUT-SHAPED MANUAL CONTROL OF HELICOPTERS WITH SUSPENDED LOADS

Approved by:

Dr. William Singhose, Advisor
George W. Woodruff School of
Mechanical Engineering
Georgia Institute of Technology

Dr. Mark Costello
George W. Woodruff School of
Mechanical Engineering
Georgia Institute of Technology

Dr. Eric Johnson
Daniel Guggenheim School of
Aerospace Engineering
Georgia Institute of Technology

Dr. Amy Pritchett
Daniel Guggenheim School of
Aerospace Engineering
Georgia Institute of Technology

Dr. Wayne Whiteman
George W. Woodruff School of
Mechanical Engineering
Georgia Institute of Technology

Date Approved: 19 September 2013

ACKNOWLEDGEMENTS

This work would have been impossible to complete without the help of my advisors, colleagues, and friends. Firstly, I would like to thank my research advisor, Dr. Singhose, for providing challenging, interesting, and practical research questions. He has cultivated a balanced and active lab environment that I have greatly enjoyed being a part of, and his guidance has helped me become a better engineer.

Secondly, my committee's assistance was indispensable in completing this work. Dr. Costello shared valuable knowledge about helicopter dynamics and control. Dr. Pritchett was an amazing resource for manual control questions, and I always walked out of her office with far more insight than I brought in. Dr. Johnson's insightful feedback on my Ph.D. proposal spawned several of the ideas in this thesis. Lastly, I was extremely fortunate to have Dr. Whiteman as my teaching practicum mentor and as a much-needed – and high-scoring – subject in my final operator study.

Thank you to labmates Dr. Joshua Vaughan for providing perspective when I really needed it, and Dr. Khalid Sorensen for sharing a fun trajectory planning problem (and part of the solution). I have gotten to know C.J. Adams as a great student, officemate, collaborator, and teacher. Acknowledgements to my other engineering colleagues: Ali AlSaibie, Daichi Fujioka, Eileen Hernandez, Heather Humphries, Arto Kivila, Ehsan Maleki, Kelvin Peng, Brice Pridgen, and Sam Zarovy. I have also been lucky enough to join a group of close friends from the biology and chemistry graduate schools. Our time together could not have been better.

Above all, I want to thank my family for providing the best possible environment in which to live and to learn, my wife Rachel for being my favorite thing in the Universe, and the Universe for being.

TABLE OF CONTENTS

LIST OF TABLES

LIST OF FIGURES

SUMMARY

Helicopters are versatile vehicles that can serve a variety of roles. One role is that of a “flying crane” – a load is suspended from the helicopter by a cable, and the helicopter carries it to a target location. Unfortunately, the load naturally swings, which degrades control of the helicopter and makes it difficult for the pilot to put the load back on the ground. Control techniques designed to reduce this detrimental load swing have relied mainly on feedback of the load states, which is rarely available in modern full-scale helicopters.

This dissertation investigates the use of input shaping for reducing the load swing problem. Input shaping is a command-filtering technique which has improved the performance of many types of machines with unwanted flexibility, and does not require feedback. The investigation is conducted using two different, but complementary, approaches. One approach studies manual tracking tasks, where humans attempt to make a cursor follow a randomly moving target. The second approach studies horizontal repositioning maneuvers on two small-scale helicopter testbeds.

One of these testbeds is a novel design that constrains the helicopter and load to a vertical plane. A dynamic model is formed, and position control is achieved with a multi-loop feedback controller that mimics a human pilot. Several implementations of input shaping are tested, and their relative effectiveness is compared.

Both approaches are used to study how input shaping affects position control of a flexible element (the suspended load) and a driven base (the helicopter). Conventional input shapers that yield the best performance are identified, and new input shapers are created based on experimental results. A method for adjusting the vibration-limiting aggressiveness of any input shaper is also introduced.

CHAPTER I

INTRODUCTION

A helicopter can be used as a flying crane by hanging a load from cables attached to the helicopter body. The flying crane can carry water to put out forest fires, install transmission towers in remote locations, and deliver supplies to stranded ships and offshore oil rigs. Tasks such as these are often too expensive, too slow, or physically impossible to perform with other types of vehicles.

Unfortunately, the suspended load swings, which hinders load placement and can significantly degrade the *safety* of helicopter operations. This load swing, shown in Figure 1, applies external forces and moments to the helicopter.

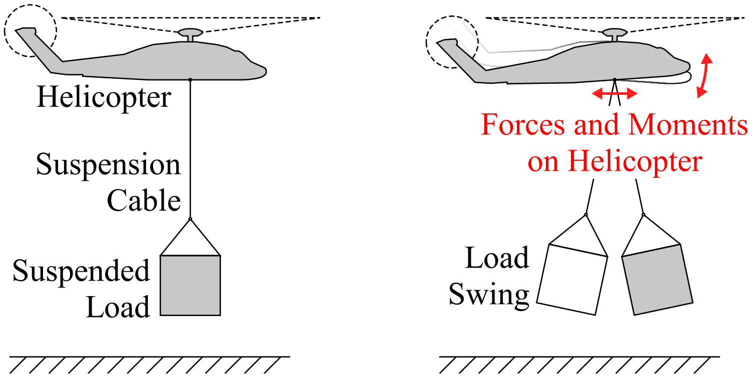

Figure 1: Helicopter with a swinging load

By trying to actively cancel the load swing, the helicopter pilot may actually amplify the problem if the control inputs are not in the correct phase relative to the swing [14, 98]. If pilots have difficulty getting the load under control, they are advised to “either lower it to the ground or jettison it promptly [98].” Helicopter accidents have been caused by loss of control due to excessive load swing, making this practice of abandoning the load necessary in extreme cases.

Reducing the amount of swing could increase both the safety and the *productivity* of suspended-load operations; once the load is positioned near its desired location, it cannot be lowered to the ground until the swing amplitude settles below an acceptable level. Keeping the swing at low amplitude could allow the pilot to deposit the load more quickly.

Figure 2 shows a high-level representation of a human-piloted helicopter with a suspended load. The pilot uses knowledge of the required task to generate a desired trajectory for the helicopter and uses the cockpit controls to make the helicopter follow this trajectory. The pilot's input generally goes through a flight control system designed to improve the helicopter's stability and performance.

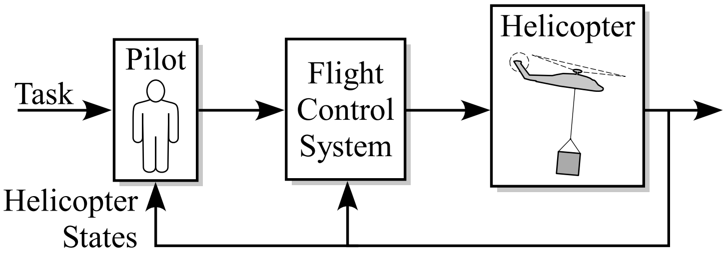

Figure 2: Helicopter controlled by human pilot and flight control system

Strategies for reducing detrimental load swing must modify one of the three blocks in Figure 2. Modifying the pilot block is equivalent to retraining the human operator. Proposed strategies to modify the helicopter have usually focused on adding some form of active load stabilization [86]. For example, previous studies have found that an actively controlled, moving suspension point could be an effective way to dampen the load swing [19, 20]. However, retrofitting existing heavy-lift helicopters with moving suspension points or other mechanisms would be costly compared to modifying the computerized flight control system.

A substantial research effort has focused on adding swing-reducing control strategies to the flight control system. Many proposed strategies rely on feedback of the suspended load states [11, 68, 36]. Such control algorithms have shown promise, but

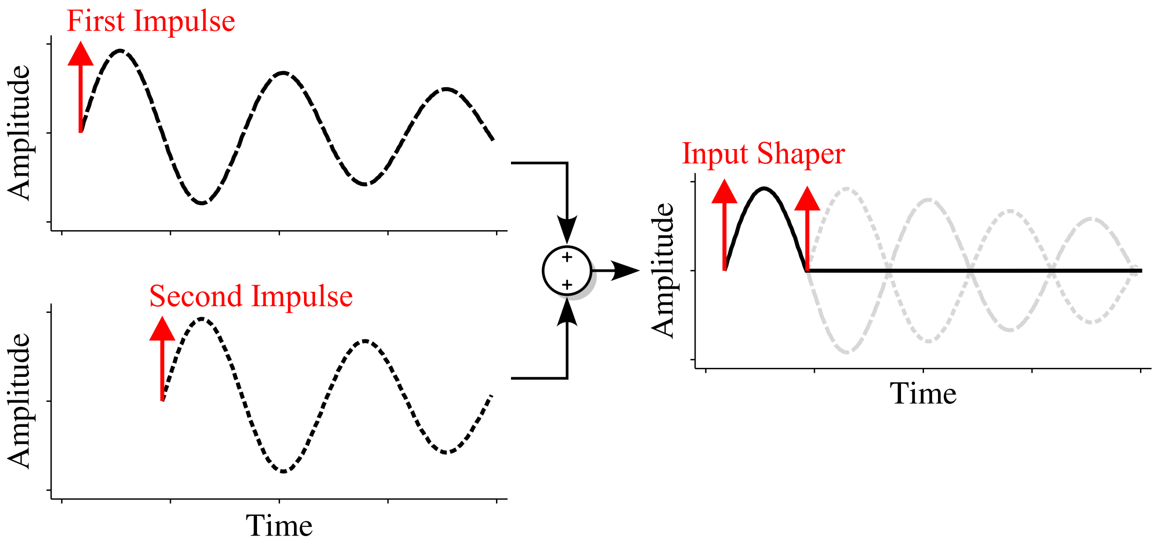

Figure 3: Two self-canceling impulses

they require real-time measurement of the suspension-cable angle, which is rarely available in current full-scale helicopters. This thesis will assume that the load states are unknown to the flight control system.

This thesis investigates the use of a command-filtering technique called *input shaping* that suppresses swing without requiring feedback of the suspended load states. The basic concept of input shaping is demonstrated in Figure 3. In the top of Figure 3, an impulse is applied to a flexible system, and induces a lightly damped response shown by the black line. A similar response (shown below the first response) results when a second impulse is applied a short time later. The right side of Figure 3 shows the response which results from both impulses. If the system is linear and time-invariant, the two responses combine, and the vibration is eliminated. The specially timed impulses can be convolved with an arbitrary function, and the resulting *input-shaped* function maintains the vibration-canceling properties of the original impulses. When used in this manner, the series of impulses is an *input shaper*, as shown in the right side Figure 3.

1.1 Research Goals & Methods

Suppressing vibration with input shaping has improved the performance of many machines. A few initial studies of its application to helicopters with suspended loads have been performed [11, 68]. However, much work remains to be done, especially for helicopters with a human pilot "in the loop."

The ultimate goal for this thesis project is to add input shaping to the flight control system of a full-scale helicopter with a human pilot. Before taking this major step, preliminary work must investigate: a) the performance of input shaping in small-scale experimental helicopter systems; b) how input shaping affects control of the load (flexible element) and the helicopter (driven base) with human operators participating in continuous-input control tasks; c) which input shapers provide the most benefit; and d) the best implementation of input shaping on a helicopter's flight control system.

To investigate input shaping's effect on human-controlled systems with flexibility (such as helicopters with suspended loads), this thesis will employ two approaches. One approach has been commonly used in the aerospace and helicopter-control communities to study human-in-the-loop control. Figure 4 shows a *manual tracking task*. A human operator views a display and uses an input device to try to make a cursor

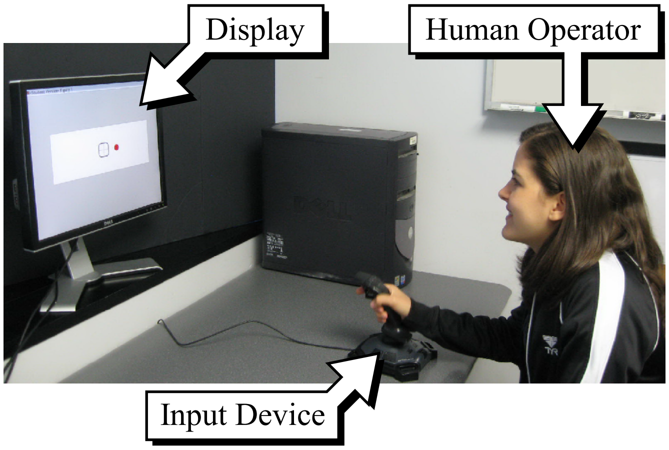

Figure 4: Single-axis manual tracking task

follow a randomly moving target. The cursor's dynamic response to the human's input is varied, and the resulting tracking performance and subjective difficulty are recorded, along with the human-machine system's control behavior.

In the second approach, the two small-scale helicopter testbeds shown in Figure 5 are used to investigate how input shaping affects the performance of horizontal repositioning tasks. Figure 5(a) shows a micro coaxial helicopter that is controlled with feedback from a motion-capture system. Figure 5(b) shows a larger model helicopter which is constrained to move in a vertical plane. A dynamic model of this helicopter is formed, and experimental data is used to estimate unknown parameter values. The helicopter is guided by a feedback controller that emulates the control of a human pilot. Horizontal repositioning maneuvers are simulated and experimentally validated. The effectiveness of several different implementations of input shaping is compared.

After investigating the effectiveness of conventional input shapers using the manual tracking and horizontal repositioning approaches, new input shapers are designed.

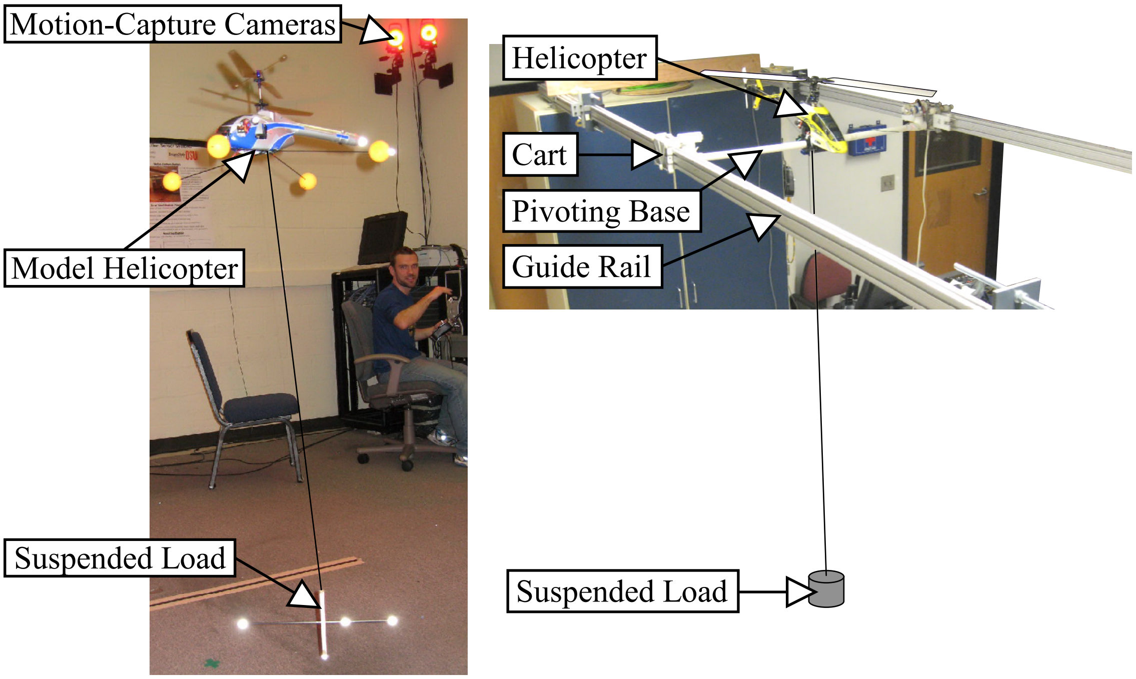

(a) Micro coaxial helicopter (b) 400-series helicopter

Figure 5: Small-scale helicopter testbeds

A technique that adjusts the vibration-limiting aggressiveness of any input shaper is proposed. This technique gives an operator flexibility in dealing with the tradeoff between suppressing vibration of the flexible element and maintaining good control over the driven base.

Input shapers are also designed using experimental results from manual tracking experiments. Experimental tracking performance with each conventional input shaper is compared to different characteristics of the input shaper (such as time of the final impulse, sum of impulse amplitudes squared, etc.) to find characteristics that correlate well with performance. A highly correlated characteristic is found, and is used to design input shapers that maximize tracking performance with a driven base while still limiting system vibration. The performance of new and conventional input shapers is compared using operator experiments and helicopter repositioning maneuvers.

1.2 Thesis Contributions

This thesis makes several significant contributions:

- A thorough study of conventional input shapers for manual control of systems with a lightly damped flexible mode (Chapters 3, 4, and 5)
- The finding that when humans control a low-frequency, lightly damped flexible element, the addition of input shaping allows the system to be well-characterized by the Crossover model (Chapters 3, 4, and 5).
- Novel input shapers designed to maximize human-controlled-system performance while controlling a driven base (Chapters 4 and 8).
- A method for continuously varying the vibration-limiting aggressiveness of any input shaper between unshaped and fully shaped (Chapter 4).

- A testbed and simulation model for studying the near-hover dynamics of a helicopter with a suspended load (Chapter 7).

- A study of the effectiveness of different implementations of input shaping for horizontal repositioning maneuvers (Chapter 7), including the result that conventional input shapers stabilize a system that uses load position as the outer-loop reference instead of helicopter position.

1.3 Dissertation Outline

Chapter 2 gives necessary background information about input shaping, manual control, and current methods for evaluating helicopters carrying suspended loads. Important knowledge gaps in the literature are identified.

Chapter 3 presents two manual tracking experiments with conventional input shapers. Chapter 4 shows how results from these experiments are used to design new input shapers. A third manual tracking experiment compares performance of the new input shapers with the conventional input shapers.

Chapter 5 describes manual tracking experiments that were performed with touch-screen input devices (Section 5.2), and with time delays in the input channel (Section 5.3). Results from these experiments are applicable to a large class of manual control applications for remotely operated vehicles.

Chapter 6 describes input-shaping experiments performed on a free-flying micro coaxial helicopter. Simple dynamic models of the helicopter are used to simulate horizontal repositioning maneuvers.

Chapter 7 presents a novel helicopter testbed that constrains the helicopter and load to move in a plane. A dynamic model of the helicopter and load is formed, and a human-inspired feedback controller enables position control of the helicopter. Horizontal repositioning maneuvers are performed with several implementations of input shaping.

Chapter 8 studies the performance of new and conventional input shapers as their form is varied along a continuum between unshaped and fully shaped. In addition, experiments search for optimal size of the negative impulse in a specified-negative-amplitude input shaper.

Chapter 9 summarizes the findings of this thesis, and proposes directions for future research.

CHAPTER II

BACKGROUND

This chapter gives background information about the main subject areas used throughout the thesis. Section 2.1 describes techniques for the design and analysis of conventional input shapers. Section 2.2 discusses the current practice for evaluating helicopter controllability and gives important conclusions of previous studies investigating the effects of a suspended load on control of the helicopter. Section 2.3 introduces the field of manual control and linear characterization of a human-controlled system. Knowledge gaps in the literature are identified at the end of each section.

2.1 Input Shaping

Input shaping is a command-filtering method that limits unwanted oscillation by strategically modifying a reference command [83, 88, 87, 77, 45, 46, 79, 100]. Figure 6 illustrates the input-shaping process. On the left side of Figure 6, a command is sent to a vibratory system, and causes residual oscillation. If the command is convolved

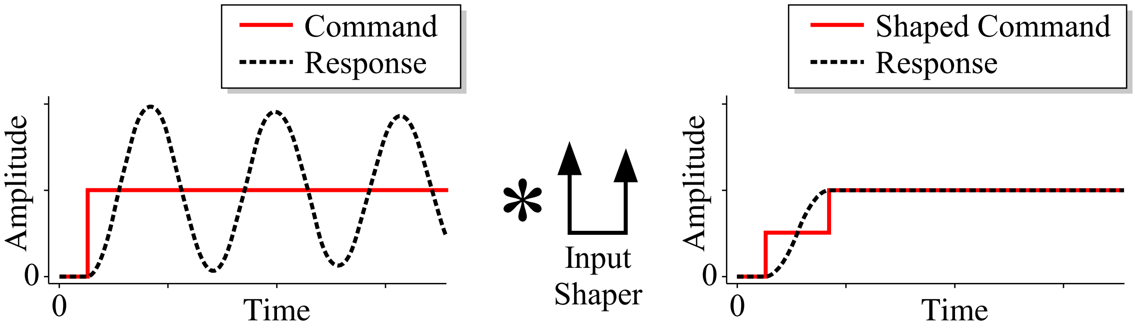

Figure 6: Input-shaping a reference command

with a specially designed series of impulses, called an input shaper, then the result is a shaped command that causes much less residual oscillation. This result is shown on the right side of Figure 6. A step command is shown in Figure 6 for simplicity, but any arbitrary command can be input-shaped in the same way, and will result in a similar reduction in vibration. Input shaping has proven effective on many kinds of machines with flexibility, including cranes [90, 12], robotic arms [26, 18, 51], coordinate measuring machines [42, 85], and satellites [106, 82, 5, 96].

Input shapers may have two or more impulses. The transfer function of a generic input shaper with n impulses is:

$$\mathbb{G}_{is}(s) = A_1 + A_2 e^{-t_2 s} + \cdots + A_n e^{-t_n s}, \tag{1}$$

where A_i are the impulse amplitudes, and t_i are the time locations of each impulse. Note that without loss of generality, the first impulse time is $t_1 \equiv 0$. An alternative way to represent input shapers is in matrix form. For example, the input shaper in (1) can be expressed as:

$$\begin{bmatrix} A_i \\ t_i \end{bmatrix} = \begin{bmatrix} A_1 & A_2 & \dots & A_n \\ 0 & t_2 & \dots & t_n \end{bmatrix}. \tag{2}$$

Figure 7 shows a block diagram of the operations required for applying an input shaper with n impulses. The reference command $u(t)$ is multiplied by a gain, and

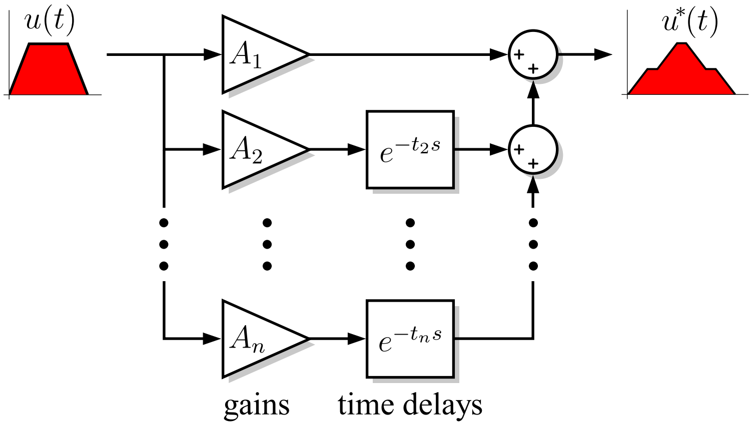

Figure 7: Input shaping mathematical operations

time-delayed for each impulse in the input shaper. The resulting amounts are summed to form the shaped command $u^*(t)$. This is among the simplest control methods in existence, and it can easily be implemented on any modern digital controller.

2.1.1 Input Shaper Design and Analysis Methods

The impulse amplitudes and time locations of an input shaper are designed using the estimated natural frequencies and damping ratios of the flexible modes to be suppressed. Different input shapers are designed using different combinations of performance requirements and mathematical constraints.

2.1.1.1 Constraint Equations

Input shapers are designed to suppress vibration. When a sequence of impulses is applied to an underdamped second-order system, the amplitude of residual vibration is given by:

$$V = \frac{\omega}{\sqrt{1-\zeta^2}} e^{-\zeta\omega t_n} \sqrt{\left(\sum_{i=1}^{n} A_i e^{\zeta\omega t_i} \cos\left(\omega t_i \sqrt{1-\zeta^2}\right)\right)^2 + \left(\sum_{i=1}^{n} A_i e^{\zeta\omega t_i} \sin\left(\omega t_i \sqrt{1-\zeta^2}\right)\right)^2} \quad (3)$$

where V is the vibration amplitude, ω is the natural frequency of the system, ζ is the damping ratio, and A_i and t_i are the amplitudes and time locations for impulse i.

Many of the basic input shapers (*Zero Vibration* input shapers) are formed by setting the vibration in (3) equal to 0. Note that the sine and cosine terms mean that there are an infinite number of impulse sequences that would satisfy this equation. More constraints are required to arrive at a single solution.

To force the impulse sequence to be as short in duration as possible, many input shapers minimize the time of the final impulse:

$$\min(t_n) \quad (4)$$

To ensure that the steady-state value of the reference command is preserved, the impulse amplitudes must sum to 1:

$$\sum_{i=1}^{n} A_i = 1 \tag{5}$$

In addition, amplitude constraints are often applied to the individual impulses to avoid solutions that contain infinitely large impulses:

$$A_{min} \leq A_i \leq A_{max}, \text{ for } i = 1 \text{ to } n. \tag{6}$$

For *positive input shapers*, all impulses are required to have positive amplitude:

$$A_i \geq 0, \text{ for } i = 1 \text{ to } n. \tag{7}$$

Shapers that do not enforce constraint (7) and contain one or more negative impulses are called *negative input shapers*.

A nonlinear optimization routine such as MATLAB's *fmincon()* function is used to design a sequence of impulses that satisfies all of the chosen constraints while minimizing a given quantity (usually chosen to be t_n, time of the final impulse). The resulting impulse sequence is an input shaper.

2.1.1.2 Vector Diagrams

Vector diagrams provide yet another way to represent an input shaper [80]. Figure 8 shows an arbitrary impulse sequence and its corresponding vector diagram. When converting between the two forms, all impulse amplitudes remain the same. The

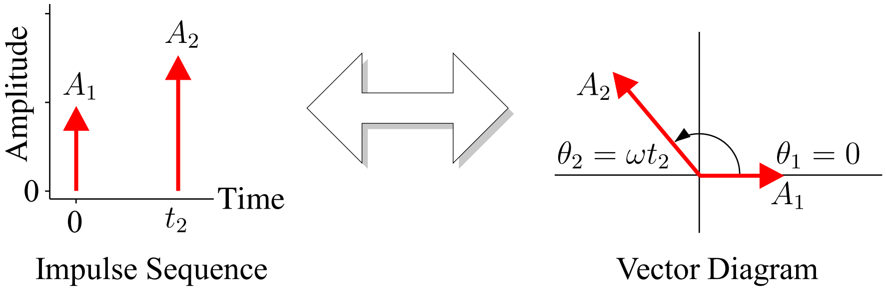

Figure 8: Vector diagram representation of an input shaper

main difference is that the time locations of the impulse sequence are converted to angles on a polar plot. For example, time t_2 becomes angle ωt_2, where ω is a chosen frequency. For input shaper analysis, this frequency is generally chosen to be the natural frequency of the oscillatory system, ω_n.

Figure 9 shows the vector, A_R, that results when the two impulses are added together. Vector diagrams are useful for input shaper design because the resultant vector indicates the amount of residual vibration that occurs when the impulses are applied to a flexible system with natural frequency ω. The amplitude $|A_R|$ is proportional to the amplitude of residual oscillation [76], and the angle $\angle A_R$ indicates the phase of oscillation relative to the response from an impulse at time $t = 0$ [80].

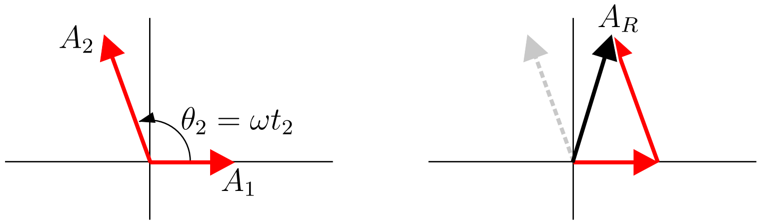

Figure 9: Resultant vibration vector

To create a sequence of impulses that produces no residual vibration when applied to a system with vibratory frequency ω, the designer can draw a vector diagram where the resultant vector is zero. An example of this is shown in Figure 10. The input shaper has impulse amplitudes $A_1 = 1$, $A_2 = -1$, and $A_3 = 1$. When the three vectors are added tip-to-tail, they return to the origin. Note that the second impulse

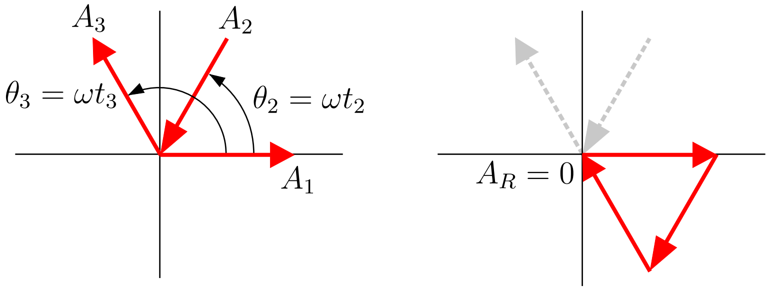

Figure 10: Impulse sequence with zero resultant vector

points toward the origin because it has a negative amplitude.

While the constraint equations are more useful for designing input shapers with computer-based optimization, the vector diagram method allows the engineer to design and analyze input shapers on the back of an envelope. It is an intuitive approach that relies on geometry instead of computation. It also provides insight into how the various input shapers achieve their low-vibration effects.

2.1.1.3 Sensitivity Curves

When the estimated values of natural frequency and damping ratio are inaccurate, the vibration-limiting ability of the input shaper is reduced. Sensitivity curves provide a way to study how much vibration a particular input shaper will allow when there are different amounts of error in the estimated frequency. Figure 11 shows one such sensitivity curve. The horizontal axis is the actual system frequency divided by the modeled frequency, and the vertical axis shows the residual vibration that results when the impulses are applied to the system. Note that when the frequency estimate is perfect ($\omega/\omega_m = 1$), no residual vibration is caused.

The width of the sensitivity curve at a given level of vibration is called *insensitivity*. For example, the width of the curve at 20% vibration is labeled in Figure 11. If this distance were wider, larger errors would be required to cause the same amount of

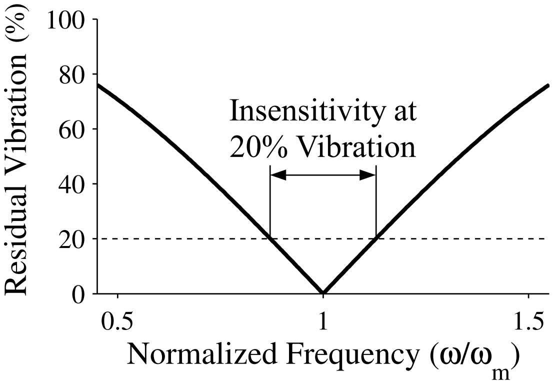

Figure 11: Sensitivity curve

vibration, and the input shaper would be more robust. Insensitivity quantifies how much effectiveness an input shaper has when frequency estimates are inaccurate.

2.1.2 Conventional Input Shapers

Now that input-shaper design and analysis have been introduced, this section will present some specific input shapers that are used in the thesis. These are certainly not the only input shaper types. For a more thorough coverage of input shapers and their characteristics, the author recommends [99, 101, 102].

2.1.2.1 Zero Vibration Input Shapers

By constraining the impulses to be all positive and the residual vibration to be zero when parameter estimates are perfect, a two-impulse *Zero Vibration* (ZV) shaper [87] is generated. The ZV shaper can be calculated in closed form:

$$\begin{bmatrix} A_i \\ t_i \end{bmatrix}_{ZV} = \begin{bmatrix} \frac{1}{1+K} & \frac{K}{1+K} \\ 0 & T_d \end{bmatrix}, \tag{8}$$

where T_d is the damped period of oscillation,

$$T_d = \frac{2\pi}{\omega_n \sqrt{1-\zeta^2}} \tag{9}$$

and

$$K = e^{\frac{-\zeta\pi}{\sqrt{1-\zeta^2}}}. \tag{10}$$

Allowing negative impulses and increasing the number of impulses to three, the *Specified-Negative-Amplitude* (SNA) input shaper [81] is formed:

$$\begin{bmatrix} A_i \\ t_i \end{bmatrix}_{SNA} = \begin{bmatrix} a & b & a \\ 0 & \frac{1}{\omega} cos^{-1}(\frac{-b}{2a}) & \frac{1}{\omega} cos^{-1}(\frac{b^2}{2a^2} - 1) \end{bmatrix}, \tag{11}$$

where $a = \frac{1-b}{2}$. The amplitudes depend on the chosen value of parameter b, which is the amplitude of the negative impulse.

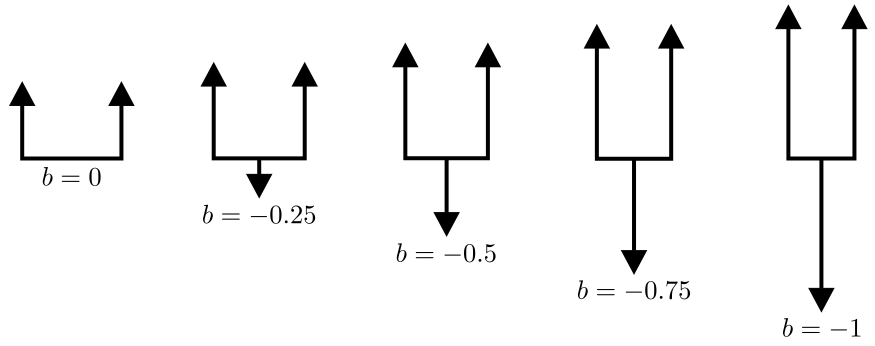

Figure 12: Specified-Negative-Amplitude (SNA) input shaper

Figure 12 shows SNA shapers for a range of b values between 0 and -1. With $b = 0$, the input shaper is equivalent to the ZV shaper. As the magnitude of b increases, the input shaper gets shorter in duration and produces a more aggressive command, but it also loses some robustness to modeling errors, increases actuator effort, and may excite unmodeled high modes more than the original command. When $b = -1$, the input shaper becomes a *Unity-Magnitude Zero Vibration* (UMZV) input shaper. This shaper has impulses of 1, -1, and 1, and can be applied to systems that only allow discrete on-off-type commands.

The sensitivity curves for some of the zero-vibration shapers are shown in Figure 13. The shapers are designed with zero damping, and the SNA shaper has a negative amplitude of 0.5. Note that while the ZV shaper has a maximum of 100% vibration, the SNA and UMZV input shapers have maxima of 200% and 300%. This means that they can cause more vibration than an unshaped command if the system has a vibratory mode at around 2.5× or 3× the modeled frequency.

This is a property of positive and negative input shapers in general – positive shapers never cause more vibration than the original command, while negative ones may excite vibration in unmodeled high modes.

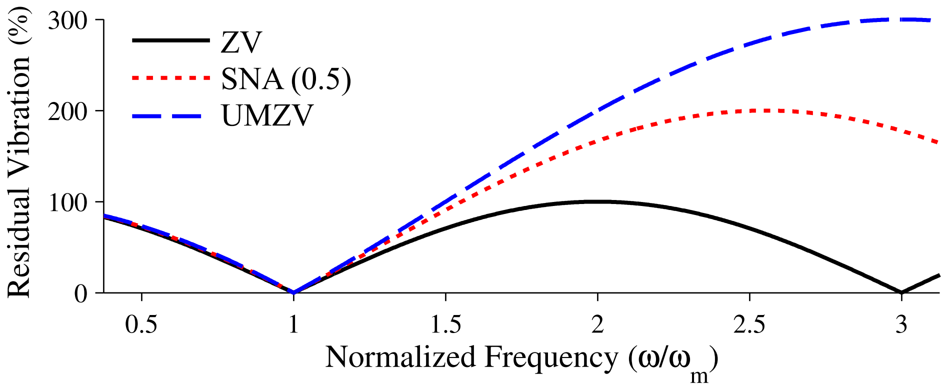

Figure 13: Sensitivity curves for zero-vibration input shapers

2.1.2.2 Robust Input Shapers

To maintain effectiveness in the presence of modeling errors, "robust" shapers have been developed [77, 80, 101, 84, 79]. These shapers are designed to have large insensitivity to modeling errors. Increased robustness generally comes at the cost of increased rise time.

One way to add robustness is to constrain not only the vibration at the modeled frequency to be zero, but also one or more derivatives of the vibration as a function of frequency. This can be seen from the sensitivity curve in Figure 14 that compares the ZV shaper to the *Zero Vibration and Derivative* (ZVD) shaper. The ZVD input shaper has zero slope at the design frequency. This is accomplished by setting the first derivative of (3) with respect to frequency equal to zero:

$$0 = \frac{dV}{d\omega} = \frac{d}{d\omega}\left(e^{-\zeta\omega t_n}\sqrt{\left(C[\omega,\zeta]\right)^2 + \left(S[\omega,\zeta]\right)^2}\right), \tag{12}$$

where

$$\begin{aligned} C[\omega,\zeta] &= \sum_{i=1}^{n} A_i e^{\zeta\omega t_i}\cos\left(\omega t_i\sqrt{1-\zeta^2}\right) &(13)\\ S[\omega,\zeta] &= \sum_{i=1}^{n} A_i e^{\zeta\omega t_i}\sin\left(\omega t_i\sqrt{1-\zeta^2}\right). &(14)\end{aligned}$$

Setting further derivatives of the vibration equation equal to zero produces even more robust shapers, called ZVDD, ZVDDD, and so on.

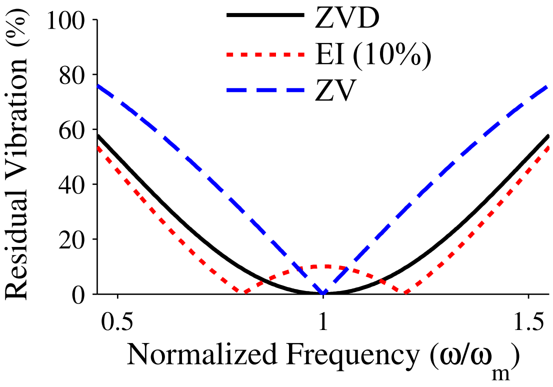

Figure 14: Sensitivity curves for conventional robust input shapers

Another way to increase robustness is to allow some residual vibration when the oscillatory frequency is guessed correctly. This is the approach used for the *Extra-Insensitive* (EI) input shaper. For the EI shaper in Figure 14, 10% residual vibration is allowed when the modeled frequency is perfectly accurate. The benefit is an increased zone of insensitivity for a given level of tolerable vibration.

Assuming zero damping, the ZVD and EI input shapers can be calculated as:

$$\begin{bmatrix} A_i \\ t_i \end{bmatrix}_{ZVD} = \begin{bmatrix} 0.25 & 0.5 & 0.25 \\ 0 & \frac{T_n}{2} & T_n \end{bmatrix}, \tag{15}$$

and

$$\begin{bmatrix} A_i \\ t_i \end{bmatrix}_{EI} = \begin{bmatrix} \frac{1+V_{tol}}{4} & \frac{1-V_{tol}}{2} & \frac{1+V_{tol}}{4} \\ 0 & \frac{T_n}{2} & T_n \end{bmatrix}, \tag{16}$$

where T_n is the natural period of oscillation, and V_{tol} is the tolerable vibration at the modeled frequency. Note that these input shapers are twice the duration of the ZV input shaper.

2.1.2.3 Specified-Insensitivity Input Shapers

Researchers have developed a powerful technique for tailoring an input shaper to a given system. Figure 15 shows a sensitivity curve where a set of points have been specified. The vibration values at these points are added to the constraints in the

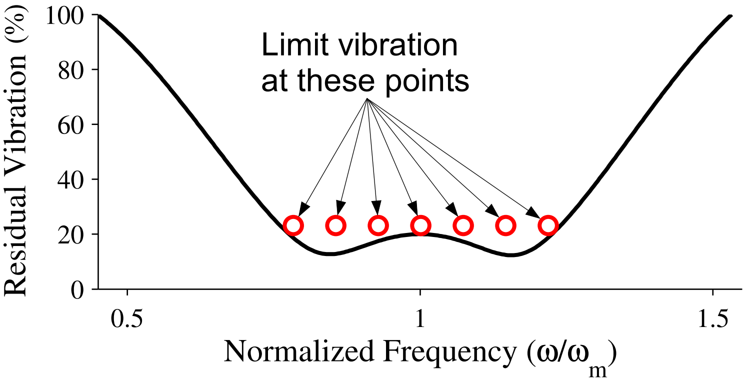

Figure 15: Specified-Insensitivity (SI) method

input shaper optimization function, and an input shaper which maintains vibration below these points is generated. The resulting *Specified-Insensitivity* (SI) input shaper is the shortest-duration input shaper that limits vibration below the points [78].

2.1.2.4 Reduced-Perceived-Lag Input Shapers

The time distribution of impulse amplitudes can have a major effect on how an input shaper behaves. Consider the unshaped and ZVD-shaped step commands in Figure 16. At any time $\hat{t}$, the input-shaped command consists of three summed components:

1. the current unshaped command, $u(\hat{t})$, multiplied by 0.25,
2. the unshaped command $\frac{T_n}{2}$ seconds ago, $u(\hat{t}-\frac{T_n}{2})$, multiplied by 0.5, and
3. the unshaped command T_n seconds ago, $u(\hat{t}-T_n)$, multiplied by 0.25.

These components are shown on the input-shaped command in Figure 16 as white, light grey, and dark grey areas, respectively. Note that the current unshaped command only contributes 25% of the current input-shaped command, while the unshaped command from $\frac{T_n}{2}$ seconds in the past contributes 50%. As a result, the current command can be "overpowered" by past commands.

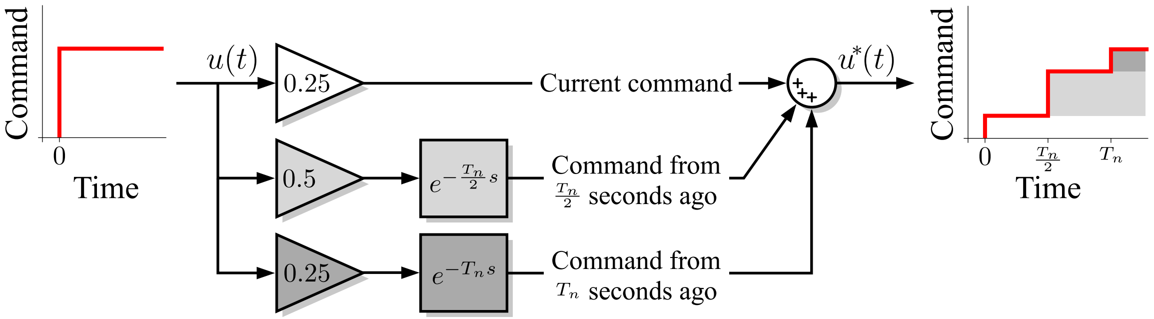

Figure 16: ZVD-input-shaped step command

If the impulse amplitudes in Figure 16 were [1, 0, 0] instead of [0.25, 0.5, 0.25], the input-shaped command would be equivalent to the unshaped command, and the current command at $\hat{t}$ would determine 100% of the input-shaped command. If the amplitudes were [0, 0, 1], then the input-shaped command would be completely determined by the unshaped command T_n seconds in the past, and the current command would have no immediate effect.

This comparison demonstrates that input shaper duration does not tell the whole story – making early impulses larger than later impulses weights the current command more heavily. The *Reduced-Perceived-Lag* (RPL) input shaper was developed with this principle in mind [26]. A typical RPL shaper is shown in Figure 17. The majority of the command is executed immediately by the large initial impulses, and then smaller impulses eliminate the remaining vibration later in time. This produces an

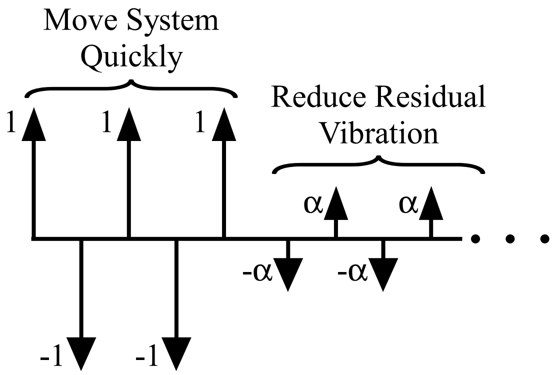

Figure 17: Reduced-Perceived-Lag (RPL) input shaper

input shaper which is highly responsive, thus reducing the perceived lag, even though it may not have the shortest duration as quantified by t_n.

It will be shown in Chapter 4 that in some circumstances, input shapers with large initial amplitudes like the RPL input shaper may be desirable for systems piloted by humans or human-like automatic controllers.

2.1.3 Research Gaps

Input shapers have traditionally been designed based on mathematical or dynamic constraints. No work has used human performance, either experimental or simulated, to drive input shaper design. This thesis will use several different approaches to design input shapers to maximize the performance of a human-controlled system.

2.2 Helicopters with Suspended Loads

A major goal of this thesis is to assess the effects of input shaping on the controllability of helicopters with suspended loads. In current practice, the controllability of an aircraft is described by a set of *handling qualities*.

2.2.1 Helicopter Handling Qualities

Helicopter handling qualities rate the suitability of a given helicopter and *flight control system* (FCS) for performing a designated role (utility, attack, etc.). In order to be approved for operation, a military helicopter must meet the handling qualities requirements given in ADS-33 [4] for the type of tasks it is intended to perform. Many civilian helicopters do not have this strict requirement, but meeting the guidelines is highly valued. Helicopters that require excessive pilot *compensation* to attain good performance are deemed to have poor handling qualities. Pilot compensation "... is the measure of additional pilot effort and attention required to maintain a given level of performance in the face of less favorable or deficient characteristics [16]."

Handling qualities are assessed with two main approaches: *predicted handling qualities* and *assigned handling qualities*. Predicted handling qualities are determined by extracting quantitative parameters, related to bandwidth and phase margin, from frequency-domain models of the combined helicopter and flight control system. Predicted handling qualities are based solely on the helicopter dynamics with no human pilot "in the loop." This thesis will not address predicted handling qualities; it will instead focus on assigned handling qualities.

2.2.1.1 Assigned Handling Qualities

Assigned handling qualities are determined by having human pilots use the helicopter to perform various maneuvers, called *Mission-Task-Elements* (MTEs). An example MTE is the Depart/Abort maneuver [4], illustrated in Figure 18. The helicopter begins in a stable hover, moves forward a prescribed distance of x_{travel}, and resumes hovering over a target position. The instructions give an approximate time that should be required to complete the maneuver, along with forward velocities and pitch angles that should be attained.

Pilots perform the Depart/Abort and other maneuvers with a required level of aggressiveness and precision, and they rate the helicopter's desirability on the Cooper-Harper handling qualities rating scale [16], shown in Figure 19. If the pilot can perform the maneuver well with low mental workload, then the helicopter is rated

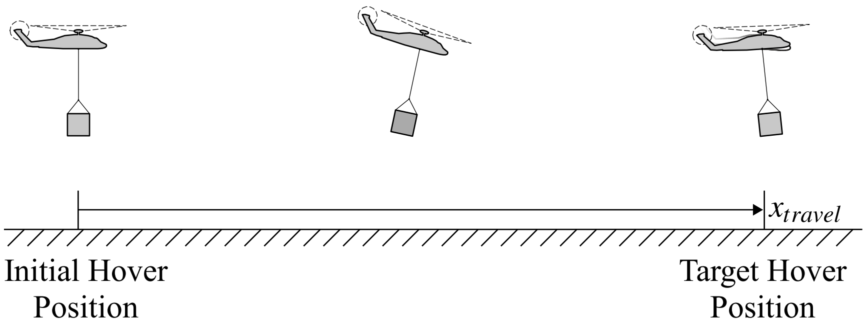

Figure 18: Depart/Abort maneuver

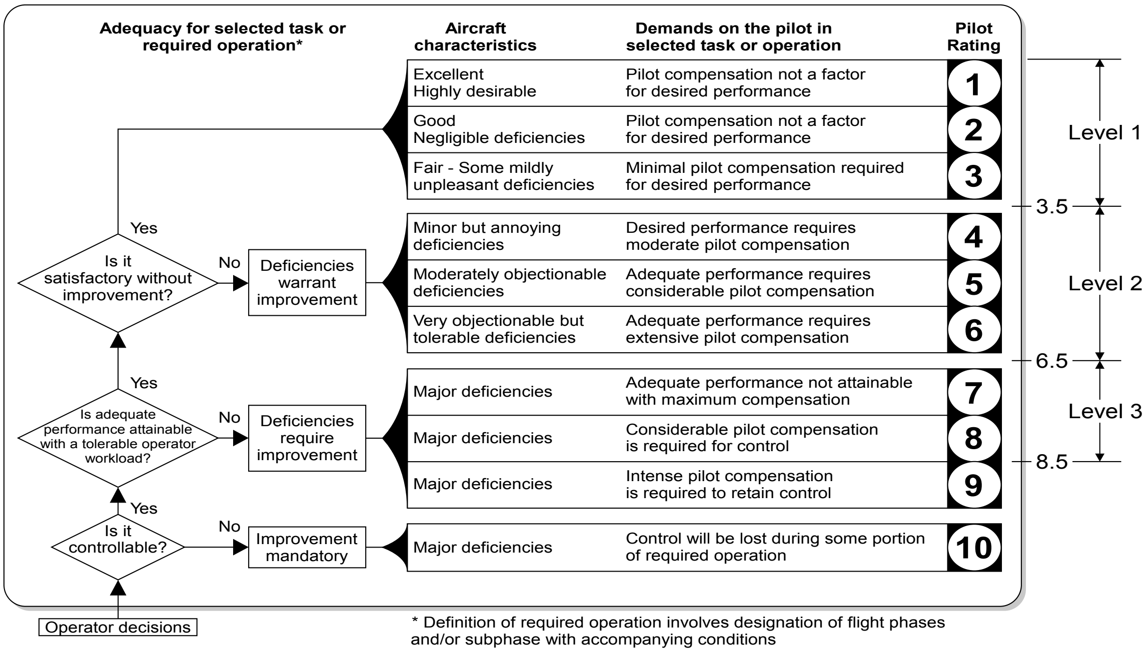

Aircraft characteristics	Demands on the pilot in selected task or operation	Pilot Rating
Excellent Highly desirable	Pilot compensation not a factor for desired performance	1
Good Negligible deficiencies	Pilot compensation not a factor for desired performance	2
Fair - Some mildly unpleasant deficiencies	Minimal pilot compensation required for desired performance	3
Minor but annoying deficiencies	Desired performance requires moderate pilot compensation	4
Moderately objectionable deficiencies	Adequate performance requires considerable pilot compensation	5
Very objectionable but tolerable deficiencies	Adequate performance requires extensive pilot compensation	6
Major deficiencies	Adequate performance not attainable with maximum compensation	7
Major deficiencies	Considerable pilot compensation is required for control	8
Major deficiencies	Intense pilot compensation is required to retain control	9
Major deficiencies	Control will be lost during some portion of required operation	10

* Definition of required operation involves designation of flight phases and/or subphase with accompanying conditions

Figure 19: Cooper-Harper rating scale

between 1 and 3, and is considered *Level 1.* If the pilot performed the maneuver adequately, but moderate to intense concentration was required, then the helicopter is rated between 4 and 6, and is *Level 2.* If the performance was not adequate, then the rating is 7 and below, with higher ratings indicating a higher workload required to keep the helicopter under control. Helicopters rated *Level 3* are unacceptable, and changes are required for the physical helicopter, the flight control system, or both.

Versions of this Cooper-Harper scale have been used in numerous studies requiring human operators to give numerical ratings of mental workload [23]. A modified Cooper-Harper scale will be used in several of the operator studies in this thesis.

2.2.2 Effects of a Suspended Load on Assigned Handling Qualities

It is well known that a suspended load can be detrimental to handling qualities, especially for low-speed (less than 45 knots) and near-hover (less than 15 knots) operations that require precise horizontal control [33, 65]. Several studies in 1990's and early 2000's identified two factors with strong effects on an externally loaded helicopter's handling qualities: suspension cable length, ℓ, and load mass ratio (LMR):

$$LMR = \frac{m}{M + m}, \tag{17}$$

where M is mass of the helicopter, and m is mass of the suspended load. The longer the suspension cable, and the heavier the load relative to the helicopter, the greater the negative effect on handling qualities. At low speeds, the suspension cable length and load mass ratio can be used to estimate the load swing frequency:

$$\omega_L = \sqrt{\frac{g}{\ell}\left(\frac{1}{1 - LMR}\right)} \tag{18}$$

where g is gravitational acceleration. For common values of load mass and cable length, the swinging mode is in the frequency range of manual control [65], and swing damping during low-speed flight ranges from around 0.1 to 0.3 [65]. Therefore, it is not surprising that human pilots tend to excite the lightly damped swinging mode.

Of the 5 Mission-Task-Elements required for externally loaded helicopters, 3 are especially impaired by the presence of a heavy suspended load [33]: Depart/Abort, Lateral Reposition, and Precision Hover maneuvers. Top-view schematic diagrams of these maneuvers are shown in Figure 20. As previously mentioned, the Depart/Abort maneuver starts with a low-speed longitudinal movement and ends with a steady hover over a target position. The Lateral Reposition maneuver is essentially the

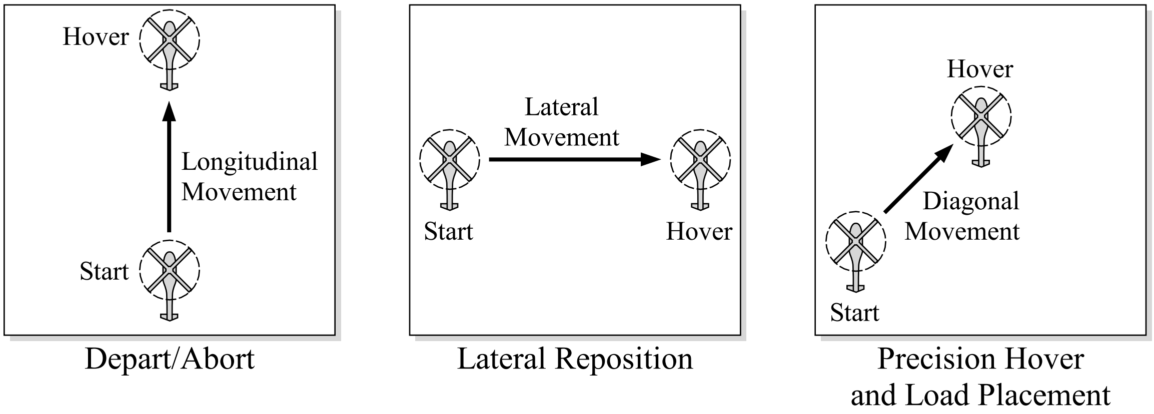

Figure 20: Horizontal repositioning maneuvers

same as Depart/Abort, except that the movement is lateral instead of longitudinal. The Precision Hover maneuver requires a slow diagonal movement before the hover.

These Mission-Task-Elements only consider positioning of the helicopter; they do not test how easy it would be to deposit the load [37]. One can imagine that when a heavy helicopter is carrying a relatively light load, such as a 46,000 pound Boeing Chinook helicopter carrying a 2,300 pound jeep, the load swing would have little effect on helicopter control, but the swing would still inhibit safe load placement. Therefore, Ivler proposed a new Mission-Task-Element called *Load Placement* to test the ability of a helicopter and control system to quickly translate, stabilize, and deposit a suspended load [36]. Load Placement is similar to the Precision Hover maneuver, but the suspended load must be steady enough to be safely deposited before the maneuver is complete.

These maneuvers all require a horizontal motion of a specific distance before hovering over a target position. Therefore, they will collectively be called *horizontal repositioning maneuvers*. This thesis will investigate simulated and experimental horizontal repositioning maneuvers with and without input shaping, and will quantify the difference using performance metrics such as peak load swing angle, load swing settling time, helicopter settling time, and amount of pilot control input.

2.2.3 Research Gaps

Little has been done to test horizontal repositioning tasks or other Mission-Task-Elements with input shaping. Two notable studies have used input shaping combined with cable angle feedback on experimental helicopter systems. Bisgaard *et al.* [11] showed good results with input-shaped lateral repositioning movements, but only showed a few example movements with basic input shapers. Ottander and Johnson [68] used input shaping to effectively suppress load swing while attempting to place cargo on a moving target. Both of these studies used unmanned helicopters. No studies have applied input shaping to either manned helicopters, or to helicopters with automatic flight controllers designed to mimic the control of human pilots.

2.3 Manual Control

Manual control theory studies the control behavior of humans using the tools and techniques of control theory. A common manual control experiment — the *manual tracking task* — will be used to study the control of flexible human-piloted systems in general, and helicopters with suspended loads in particular. Manual tracking tasks have frequently been used in aircraft piloting studies. The results of these studies informed many of the recommendations in ADS-33, so the helicopter-maneuver and manual-control approaches are related and complementary.

2.3.1 Manual Tracking Task

There are many situations where a human operator attempts to make the output of a system follow a desired state. For example, Figure 21 shows the task of recording an athlete with a tripod-mounted video camera. The goal of the camera operator is to keep the athlete centered in the camera frame. The actual camera direction is compared to its desired direction (pointed directly at the athlete), and corrective actions are made by applying force to the tripod handle. This activity is similar to eye tracking, where a human keeps a moving object in the center of his or her vision

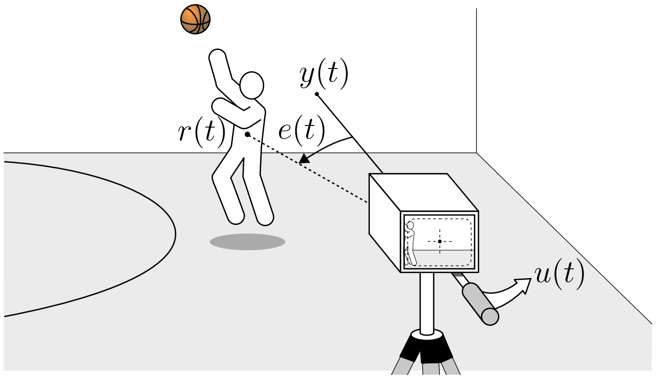

Figure 21: Video camera tracking task.

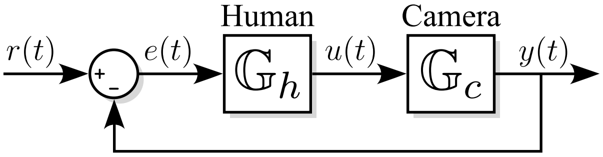

Figure 22: Block diagram of camera directional control.

[38]. In these activities, the human is an active part of a feedback control system.

Figure 22 gives a simplified block diagram of manual camera tracking. The camera operator is represented by the human block with transfer function $\mathbb{G}_h$, and the tripod's rotational dynamics is the camera block with transfer function $\mathbb{G}_c$. The athlete's direction relative to the tripod is the reference input, $r(t)$, the camera's actual direction is the camera output, $y(t)$, and the angle between the actual and desired directions is the error, $e(t)$. The operator's force on the handle is the command, $u(t)$. Other examples of manual control tasks include aiming a tank turret [95, 47], driving an automobile [28, 7], and piloting an aircraft [56].

Figure 23 shows a different type of tracking task. A crane is used to pick up a payload and move it to a target location. There are obstacles which must be avoided, and the crane operator plans a desired reference path, $r(t)$, around these obstacles and uses an input device to make the payload follow the path. Note that in this example, the reference path is generated by the human, not directly imposed by the environment. The human is both the path planner and the trajectory controller.

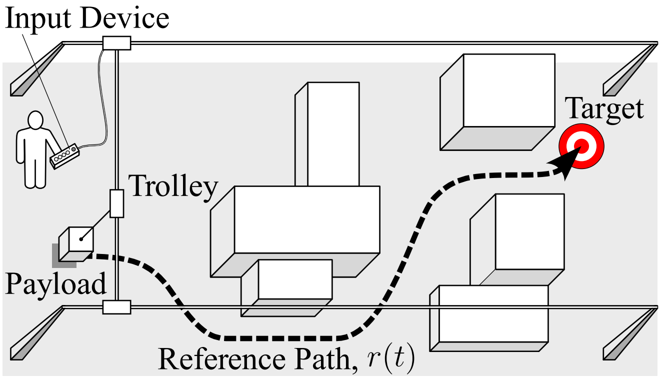

Figure 23: Overhead view of crane tracking task.

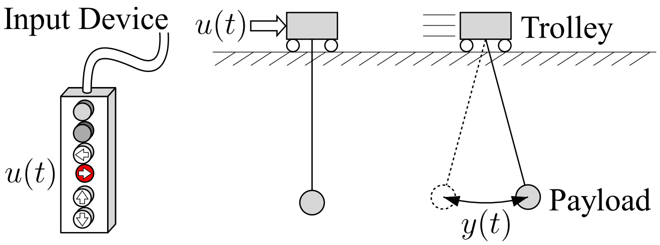

Figure 24: Flexibility in a manual tracking task

The difficulty of manual tracking is increased by time delays and flexibility in the system. Figure 24 shows a situation where the human operator's command, $u(t)$, drives a flexible system with an oscillatory output, $y(t)$. Previous studies have found that the operator's tracking ability degrades significantly when the controlled-element's dynamics include a relatively low-frequency flexible mode with a damping ratio below 0.35 [58]. Human operators tend to decrease their gain to avoid exciting the flexible mode, and the low gain results in degraded tracking performance [57]. Recall that the damping ratio of helicopter suspended load swing is between 0.1 and 0.3 in low-speed flight.

Previous studies have made extensive use of single-axis manual tracking tasks to investigate the control behavior of human-machine systems [57]. The basic setup is shown in Figure 25. A human operator views a display and uses an input device

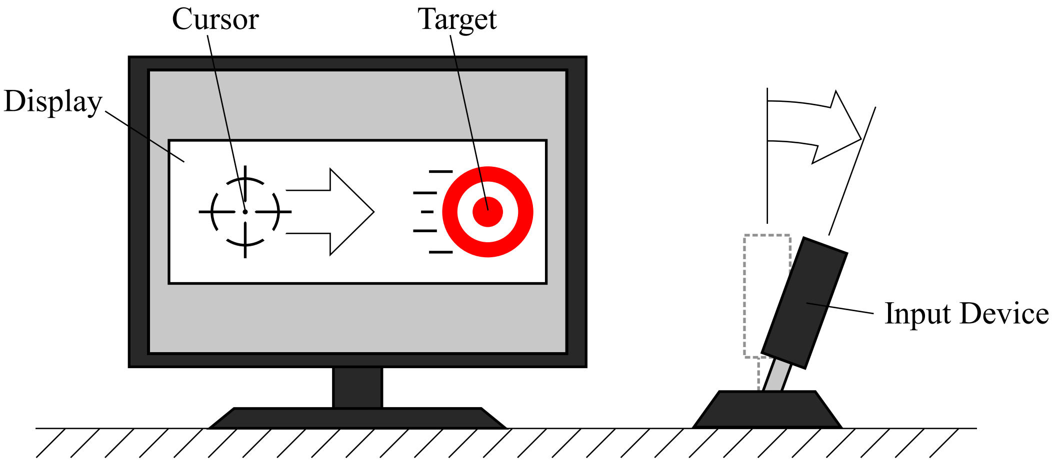

Figure 25: Elements of a single-axis manual tracking task

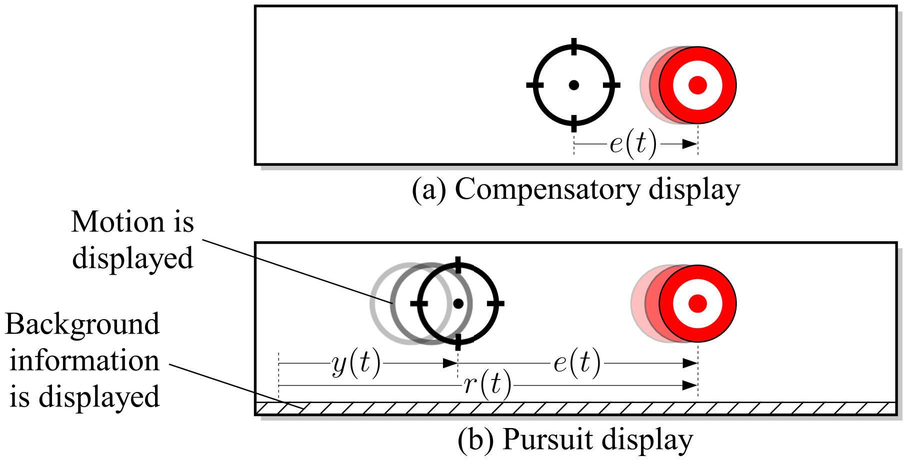

(a) Compensatory display

(b) Pursuit display

Figure 26: Two display types for a manual tracking task.

(usually a joystick or force stick) to generate commands. There are two objects on the screen: one is a *target* that represents the reference input, and the other is a *cursor* that represents the controlled-element output. The operator's goal is to make the cursor follow the target as closely as possible.

There are two main display types. Figure 26(a) is a *compensatory* display, where only the error between the target and the cursor is displayed. Figure 26(b) is a *pursuit* display, where information about the target and/or cursor positions is independently displayed in addition to the error. Pursuit displays give the operator more information about the system, which theoretically allows better tracking performance over compensatory displays [54, 71].

A diagram similar to Figure 26 will be shown to explain the displays used in each tracking experiment. Faint trailing copies of either the cursor or the target indicate that motion of the object is visible to the operator. Hatched lines inside the display rectangle mean that background information (a "ground" frame) is visible to the operator.

Tracking performance is usually quantified by root-mean-squared tracking error:

$$e_{rms} = \sqrt{\frac{1}{T}\int_0^T [e(t)]^2 dt}, \tag{19}$$

where T is the trial duration and $e(t)$ is the tracking error at time t. The tracking error has three main components: i) Error caused by the human's delay time, ii) error caused by deficiencies in the human's control processing, and iii) error caused by the human's not attempting to track parts of the signal that they know are beyond their capabilities [24].

Piloting a helicopter is a complicated multi-axis, multi-loop control task, so it might seem that studying one-dimensional control would be an oversimplification. However, it has been found that multi-axis tracking performance is highly related to one-axis tracking [94], and that information about the human controller derived from single-axis tracking tasks can be applied to multi-loop tasks [61].

2.3.2 Forcing Function Design

The target motion is prescribed by a *forcing function*. This function should be carefully designed so that the target motion meets several requirements:

- The target motion should be fairly representative of the real-world task being investigated.
- Tracking the target should be difficult enough to prevent boredom.
- Tracking the target should not be so difficult that the task is impossible.
- The target motion must appear random to the human operator.

The last requirement is to prevent the operator from predicting future behavior of the target. From past studies, it has been shown that the sum of 5 or more sine waves with arbitrary relative phase is unpredictable to human operators [55]. An example summed-sine forcing function is shown in Figure 27. The individual sine waves on the left of Figure 27 are combined to yield the more complicated function on the right. In equation form,

$$r(t) = \sum_{i=1}^{9} B_i sin(\omega_i t + \phi_i), \tag{20}$$

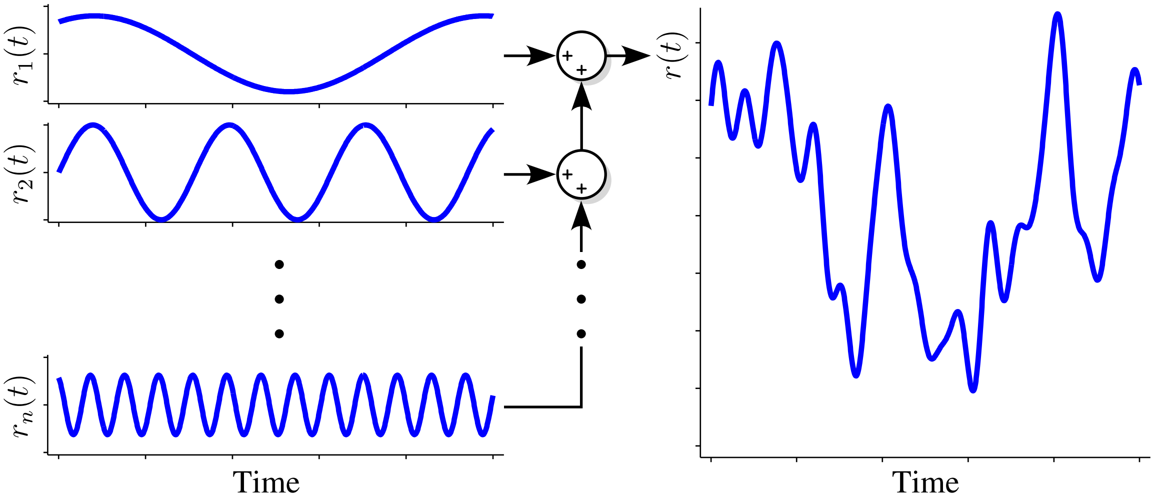

Figure 27: Sum-of-sines forcing function

where phase angles ϕ_i are randomly generated at the beginning of each trial. The amplitudes of each wave, B_i, must be chosen carefully. Each amplitude must be large enough to have a noticeable effect on $r(t)$, but cannot be so large that excessive power is added to the forcing function, making it infeasible to follow. In general, low-frequency sine waves are given large amplitudes, and waves with increasing frequency are given increasingly small amplitude [39]. The fastest sine wave often has an amplitude of about 1/10 the slowest sine wave.

The summed sine wave forcing function is widely used for manual tracking tasks. It is advantageous because it facilitates frequency-domain analysis, and it provides a convenient way to generate an unpredictable signal that tests control behavior over a wide range of frequencies simultaneously.

2.3.3 Precision Model of Human Controller

In a model of a human-machine system performing a tracking task, such as the one shown in Figure 28, we must ask how well the human's control behavior can be characterized by a linear transfer function? Humans are not inherently linear systems, but in many situations, especially under favorable conditions with easily controlled

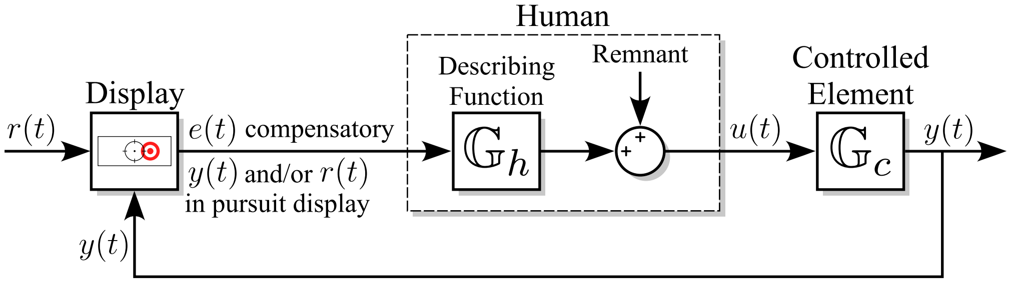

Figure 28: Manual control system with human remnant and describing function

elements, most of the human's control behavior can be characterized by a linear transfer function [31].

The operator is characterized as a *quasilinear system*, which has two components: the *describing function* ($\mathbb{G}_h$ in Figure 28) accounts for the part of the response that is linearly related to the input, and the *remnant* accounts for the remaining part of the response that cannot be attributed to the linear model. Most of the remnant appears to come from fluctuations in the system's effective time delay [54], nonsteady control behavior, and nonlinear anticipation or relay-like operations [60]. These effects are larger when tracking conditions are difficult [29]. The remnant has been found to have fairly constant power with no major peaks, and tends to be relatively small when tracking conditions are favorable [3].

One commonly used describing function for the human controller is the *precision model* [55], which approximates linear operator dynamics over a wide range of frequencies:

$$\mathbb{G}_h^{pm}(s) = \underbrace{K_h \frac{(T_z s + 1)}{(T_p s + 1)}}_{\text{equalization}} \underbrace{\frac{\omega_{nm}^2}{s^2 + 2\zeta_{nm}\omega_{nm}s + \omega_{nm}^2} e^{-\tau s}}_{\text{limitations}} \tag{21}$$

where K_h is the human's gain, T_z is the lead time constant, T_p is the lag time constant, τ is the effective time delay, and ω_{nm} and ζ_{nm} are the human's neuromuscular natural frequency and damping ratio, respectively. The model is divided into two parts. The human's *equalization* is constantly adjusted to improve tracking performance and to compensate for any dynamic deficiencies of the controlled element. The human also has inherent *limitations*. A second-order neuromuscular filter accounts for low-pass and oscillatory dynamics of the limb manipulating the input device. This is shown as the $2^n d$-order component in (21). The human also has a time delay due to signal transmission and processing delays. This time delay is shown on the right side of (21). The effective time delay and mental workload increase when the human is forced to generate significant phase lead [56].

In practice, the precision model is often reduced to the *simplified precision model* [55]. This model is valid for a narrower range of frequencies, and lag from the neuromuscular filter is incorporated into the effective time delay:

$$\mathbb{G}_h^{spm}(s) = K_h \frac{(T_z s + 1)}{(T_p s + 1)} e^{-\tau s} \tag{22}$$

2.3.4 Crossover Model of Human-Machine System

Early manual tracking studies had difficulty identifying a generic transfer function of the human operator alone, due to the human's highly adaptable control strategy. Researchers were much more successful when they considered the control behavior of the combined human-machine system. In particular, McRuer's *Crossover model* [56] provides a simple and reliable model of the human-machine system under a limited range of conditions. The Crossover model states that for a variety of controlled-element dynamics, the operator acts to make the open-loop human-machine system assume the form:

$$\mathbb{G}_h \mathbb{G}_c = \frac{K e^{-j\omega\tau}}{j\omega} \quad \text{near } \omega = K, \tag{23}$$

where K is the open-loop system gain, and τ is the effective time delay. Figure 29 shows a block diagram of the model. Note that the transfer function is written with the frequency operator $j\omega$ instead of the Laplace variable s. This is to emphasize that the model is only intended to apply in the frequency domain, and may not be accurate for non-sinusoidal inputs such as steps or ramps. Inputs should be continuous and must appear random to the human operator [56].

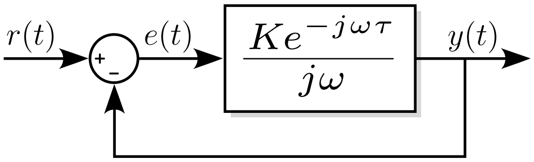

Figure 29: Crossover model of human-machine system

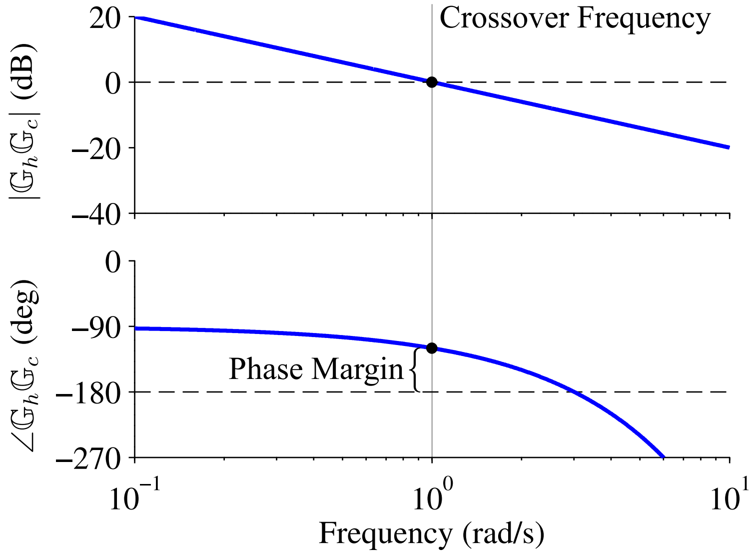

Figure 30: Bode diagram of the Crossover model

Figure 30 shows a Bode plot of the Crossover model transfer function. The frequency at which the amplitude $|\mathbb{G}_h\mathbb{G}_c|$ passes through 0 dB is called the *crossover frequency*, which is equivalent to gain K in (23). The *phase margin* is the difference (in degrees) between the phase $\angle\mathbb{G}_h\mathbb{G}_c$ and -180 at the crossover frequency. A larger phase margin indicates a more stable closed-loop system. Together, the phase margin and crossover frequency can be used as predictors of tracking performance [6].

The Crossover model is only meant to characterize tracking performance near the crossover frequency (this is the basis of its name). Fortunately, the control system's closed-loop response is generally dominated by its behavior near the crossover frequency [56]. This simple model has been used to predict pilot-involved oscillation [59] and to characterize handling qualities of aircraft, automobiles, and other human-controlled systems [27, 56]. Using the Crossover model as a basis, the human operator's transfer function near the crossover frequency can be approximated if the machine transfer function, $\mathbb{G}_c$, is known [54]:

$$\mathbb{G}_h = \frac{1}{\mathbb{G}_c}\frac{Ke^{-j\omega\tau}}{j\omega}. \tag{24}$$

This expression can be used to predict control demands on the human operator. It can give guidance to a system designer who wants to tune the dynamics of a machine to make it more easily controlled by the human. However, this useful equation is not valid if the human-machine system's behavior does not follow the Crossover model. Studies have found that the Crossover model breaks down if the controlled element has a relatively low-frequency ($\omega_n \leq 7.8\ rad/s$ [57]) oscillatory mode with a damping ratio below $\zeta = 0.35$ [58].

This thesis will deal with lightly damped oscillatory systems which are difficult for humans to control, and for which the Crossover model may not be readily applied. However, this thesis will show that the addition of input shaping allows the human-machine system to return to "normal" tracking behavior described by the Crossover model. In effect, input shaping can be used to greatly expand the applicability of the Crossover model.

McRuer and other researchers found that tracking performance and handling qualities ratings are best when tracking conditions allow a good fit to the Crossover model [53], and are much worse when the Crossover model is not a good fit [57, 58]. Therefore, it is expected that the improved resemblance to the Crossover model will be accompanied by quantitative and qualitative improvements in tracking performance.

2.3.5 Research Gaps

Many human operator studies have documented that input shaping improves the control of flexible machines [45, 46]. These studies usually used maze-like or point-to-point tasks and discrete (on/off) input devices. No studies have examined input shaping for tracking a randomly moving target using a continuous-input device. In the manual tracking literature, experiments have tested the control of lightly damped flexible elements, and have concluded that low frequency oscillation greatly degrades control and makes modeling the human-machine system very difficult. There is clearly a need to improve the modeling of such systems. Follow-up tests with input shaping added to the flexible controlled element have not been performed. Neither has input shaping applied to the control of a driven base (to simulate control of the helicopter) been studied.

CHAPTER III

MANUAL CONTROL OF FLEXIBLE SYSTEMS USING CONVENTIONAL INPUT SHAPERS

Previous manual tracking studies have concluded that systems with low-frequency, lightly damped flexibility are difficult for humans to control. This chapter demonstrates how input shaping can improve quantitative and qualitative measures of tracking performance by suppressing the system flexibility. Results from this chapter are used in Chapter 4 to design new input shapers.

3.1 Tracking Study # 1: Two-Frequency Experiment[1]

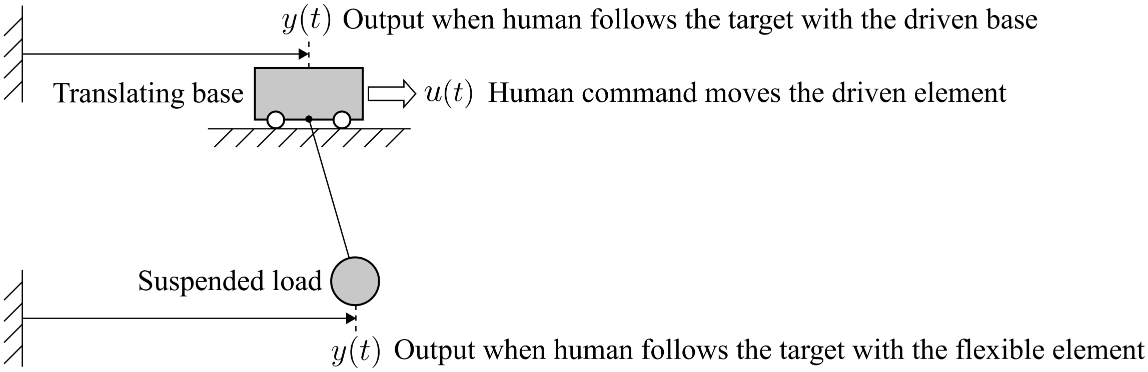

Figure 31: Oscillatory system under manual control

In this experiment, human operators controlled an oscillatory system like the load suspended from a translating base in Figure 31. The operators were asked to follow an unpredictably moving target with either the flexible element (suspended load) or

---

[1] Results from this experiment are published in [70].

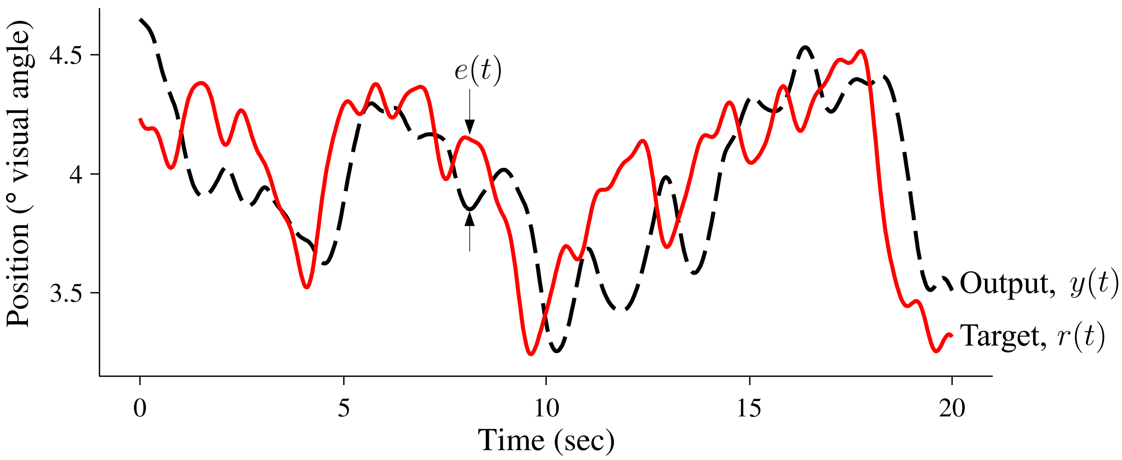

Figure 32: Target and cursor motion in manual tracking experiment

the driven element (translating base).

Figure 32 shows an example time history of the target position and the system output for a manual tracking trial. The system output, $y(t)$, represents the position of the controlled element (either the suspended load or the translating base) that is forced to follow the target. The difference between the target position and the output position is the error function, $e(t)$. Note that the output motion resembles the target motion, but it is shifted to the right by a fairly constant amount. This time shift is due to the human-machine system's unavoidable time delay. For information about display types, methods for generating the target motion, and common ways to characterize tracking performance of the human-machine system, see Section 2.3.

This experiment was an initial investigation of manual tracking with input shaping. Controlled elements with two different oscillatory frequencies were tested to verify that systems with low-frequency oscillation are more difficult for humans to control than systems with higher-frequency oscillation, and to determine how input shaping affects tracking performance in each frequency case.

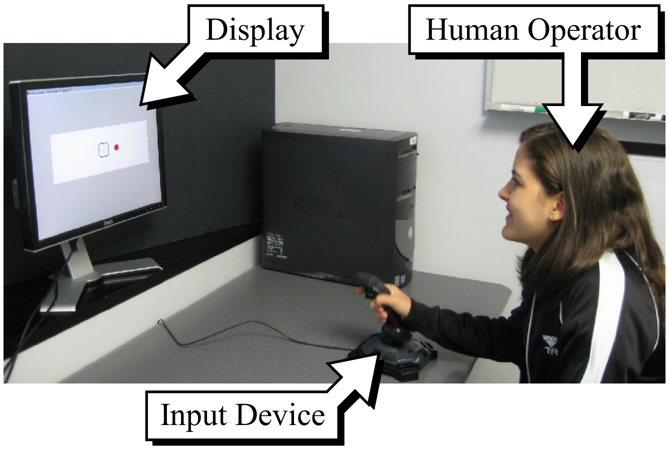

Figure 33: Experimental setup for Two-Frequency experiment

3.1.1 Participants & Procedure

Five subjects between 23 and 30 years of age participated in the study. All participants had experience driving cars, and at least some previous experience using a computer joystick. Subjects were not paid for their participation.

Each participant signed a consent form describing the risks and rewards involved in the experiment. Figure 33 shows a photo of the experimental setup. Subjects viewed a compensatory display which occupied around a 10° visual angle. They generated control inputs with a *Logitech Attack 3* spring-centered joystick. The joystick has a maximum angle of 20° from vertical. Around 0.5 Nm of torque is required to move the joystick from its neutral position, and a maximum torque of 1 Nm is required to hold the joystick at 20°.

The manual tracking experiment was implemented in MATLAB[2]. Each participant performed 5 trials, each trial lasting 120 seconds. The first 30 seconds of each trial allowed the subject to get accustomed to the controlled-element dynamics. Measurements from only the final 90 seconds were analyzed.

After each trial, the user was asked to rate the subjective difficulty of the control

---

[2] The MathWorks Inc., Natick, MA

Table 1: Controlled-element transfer functions for Two-Frequency experiment

Controlled Element	Transfer Function, $\mathbb{G}_c = \mathbb{Y}(s)/\mathbb{U}(s)$
Integrator	$\frac{K_c}{s}$
Integrator with High-Frequency Oscillatory Mode	$\frac{K_c}{s}\left(\frac{(5)^2}{s^2+2(0.1)(5)s+(5)^2}\right)$
Integrator with Low-Frequency Oscillatory Mode	$\frac{K_c}{s}\left(\frac{(1.25)^2}{s^2+2(0.1)(1.25)s+(1.25)^2}\right)$
ZV-Input-Shaped Integrator with High-Frequency Oscillatory Mode	$(0.578+0.422e^{-0.632s})\frac{K_c}{s}\left(\frac{(5)^2}{s^2+2(0.1)(5)s+(5)^2}\right)$
ZV-Input-Shaped Integrator with Low-Frequency Oscillatory Mode	$(0.578+0.422e^{-2.53s})\frac{K_c}{s}\left(\frac{(1.25)^2}{s^2+2(0.1)(1.25)s+(1.25)^2}\right)$

task by giving a numerical score between 1 (easiest) and 10 (hardest). The program saved all trial information and calculated RMS error and frequency-domain characteristics. The entire experiment lasted approximately 15 minutes for each subject.

The following five controlled elements were tested: a pure integrator, an integrator with an oscillatory mode of $\omega_n = 1.25$ rad/s, an integrator with an oscillatory mode of $\omega_n = 5$ rad/s, and ZV-input-shaped versions of the two oscillatory elements. All oscillatory modes had a damping ratio $\zeta = 0.1$. The transfer functions for these controlled elements are given in Table 1. The value of gain K_c was adjusted to allow the cursor's maximum velocity to match the maximum velocity of the reference input using reasonable joystick deflections. For this experiment, the gain was set to $K_c = 1.4737\ \frac{^\circ\text{ visual angle/sec}}{^\circ\text{ joystick deflection}}$.

These controlled-element dynamics were chosen to imitate real-world machines. Controlling the heading (direction) of a car is like a pure integrator. An integrator with an oscillatory mode of $\omega_n = 1.25$ rad/s is similar to an overhead crane with

Table 2: Forcing function for Two-Frequency experiment

Wave Number, i	Frequency, ω_i (rad/s)	Amplitude, B_i (° visual angle)
1	0.279	2.565
2	0.349	2.431
3	0.628	2.079
4	0.977	1.814
5	1.606	1.516
6	2.583	1.231
7	4.189	0.941
8	6.772	0.652
9	10.961	0.363

a 20-foot-long suspension cable. An integrator with an oscillatory mode of $\omega_n = 5$ rad/s is similar to a long-reach robotic arm [81]. The pure integrator is used both to allow comparison of the results to previous studies, and to serve as an example of an easily controlled element.

Subjects completed one trial with each controlled-element for a total of 5 trials. The trial order was randomized, and the subject was not told which element was used for each trial. Table 2 shows the frequency content of the forcing function that drove the target motion. The range of sine wave frequencies and amplitudes is similar to those from previous manual tracking experiments. Each sine wave in Table 2 completes a whole number of cycles in the 90 second trial time to improve the accuracy of frequency-domain calculations. Phase angles for each sine wave were randomly generated before each trial, so no two forcing functions were exactly alike.

Figure 34 shows a Bode plot of the oscillatory controlled element with and without input shaping. To generalize the analysis, the frequency axis has been normalized by the oscillatory mode's natural frequency, ω_n, and the amplitude curve has been normalized so that the system's open-loop gain is 1 (0 dB). The damping ratio is 0.1.

Note that at $\omega = \omega_n$, the unshaped amplitude curve has a large peak where

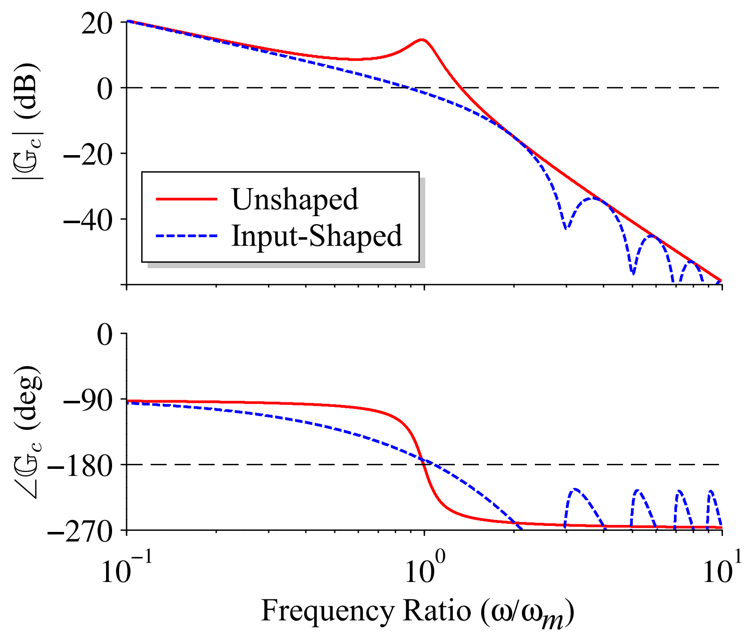

Figure 34: Bode diagram of an integrator with an oscillatory mode with frequency ω_n and damping ratio $\zeta = 0.1$

the phase curve passes through -180°. This unshaped system tends to be highly oscillatory, unless the human operator is able to improve the response by generating phase lead, reducing the open-loop gain, or both. In contrast, the input-shaped amplitude curve has no peak at the oscillatory frequency. The operator can use more aggressive inputs without fear of exciting the oscillatory mode.

3.1.2 Assumptions & Limitations

For this study, it was assumed that the operators gave full attention to the control task, and there were no major drug or fatigue-related factors that degraded performance. It was further assumed that their joystick command inputs did not exhibit significant nonlinearities such as saturation, rate-limiting, etc. These are reasonable assumptions based on recorded time histories of command inputs.

All participants were novice operators, meaning they did not have extensive experience with this kind of tracking task. This study seeks to compare the performance of an “average” human operator under different tracking conditions, and is less interested in the performance of highly specialized operators (such as professional crane operators, racecar drivers, and aircraft pilots), who might either adjust abnormally quickly to new conditions, or possibly be hindered by previous training due to negative transfer [105]. The goal is to determine what tracking situations are *inherently* easy or difficult for humans.

There is also value in testing the effectiveness of input shaping with novice operators – positive results indicate that there is no special training required to use input shaping. Performance improvements can be achieved immediately rather than after extensive training.

3.1.3 Results

3.1.3.1 Tracking Performance

Figure 35 shows the average tracking performance as quantified by root-mean-squared (RMS) error during the 90 second test period. For the high-frequency oscillatory system, performance was almost the same as with the simple integrator, and input shaping caused only a slight improvement in the average error. However, with the low-frequency system, the unshaped trials had very poor performance. The RMS error increased from approximately 0.8 to nearly 4.5 degrees visual angle. When input shaping was applied, the performance greatly improved, and the average error decreased from 4.43 to 1.28 degrees (a 71% reduction).

The low-frequency input-shaped error still appears to be higher than the simple integrator error, and shaped and unshaped high-frequency errors. This is mainly due to the time lag caused by the low-frequency input shaper. Because the oscillation is much slower for the low-frequency system, the spacing between impulses is larger, and thus the effective lag is larger. Note that although input shaping did not reduce the low-frequency oscillatory system tracking error completely back down to the level achieved with the simple integrator, it did transform the dynamics to a level that was

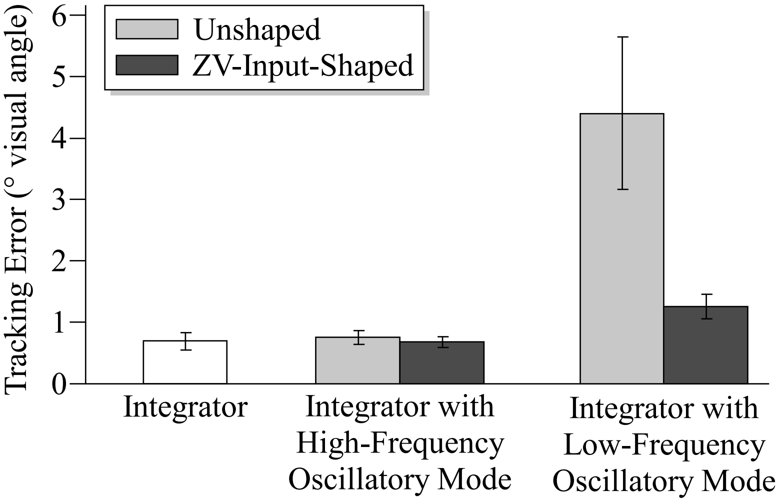

Figure 35: Tracking error for all controlled elements (mean ± SD)

fairly easy for the test subjects to track.

The shaped vs. unshaped and low vs. high frequency oscillatory systems were compared using two-way analysis of variance (ANOVA) and Tukey's honest significant difference (HSD) tests. There was no statistically significant difference between RMS error in the shaped and unshaped high-frequency systems and the input-shaped low-frequency system. RMS error in the unshaped low-frequency system was significantly higher than in the other three systems ($p < 0.05$).

3.1.3.2 Subjective Rating

Figure 36 shows the subjective ratings of task difficulty for each system. As expected, the integrator was the easiest system to control. The high-frequency oscillatory system was somewhat more difficult to control than the integrator, and input shaping was able to reduce the median difficulty. The unshaped low-frequency system was by far the most difficult to control.

Nonparametric statistical analyses were used because the subjective difficulty ratings are ordinal. Medians were compared instead of means, and Mann-Whitney U tests were used for post-hoc pairwise comparisons instead of Tukey's HSD test [25]. Note that by definition, the confidence interval cannot go below 1 or above 10 on the

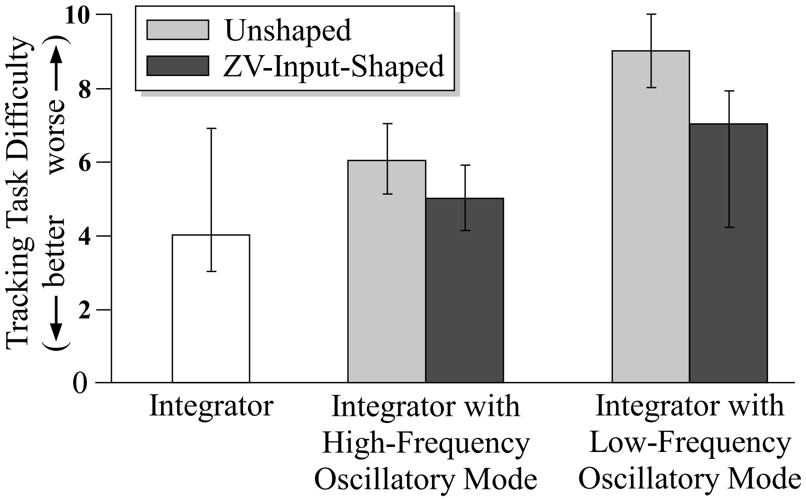

Figure 36: Difficulty ratings for all controlled elements (median with 95% CI)

scale. The same trend was observed: task difficulty in the unshaped low-frequency system is significantly greater than in the other three systems ($p < 0.02$) which were not significantly different from each other.

Based on results shown in Figure 35 and Figure 36, input shaping caused a statistically significant improvement in performance when used to suppress the low-frequency oscillation. Input shaping also appeared to be beneficial for the high-frequency element based on the average values, but the effect was not proven with statistical significance in this study. As anticipated, the higher-frequency oscillation was less detrimental to tracking performance than the low-frequency oscillation.

3.1.3.3 Control Behavior

Figure 37 shows Bode diagrams of the open-loop human-machine systems. Line segments are drawn between data points to make the curves easier to visualize, not to infer interpolation between points. Note that the integrator Bode plot in Figure 37(a) closely matches the form of the crossover model, shown previously in Figure 30.

For the unshaped high-frequency oscillation curves in Figure 37(b), there is a small peak in the amplitude curve near the resonant frequency. With the addition of input shaping, this resonant peak disappears, and the amplitude and phase curves both

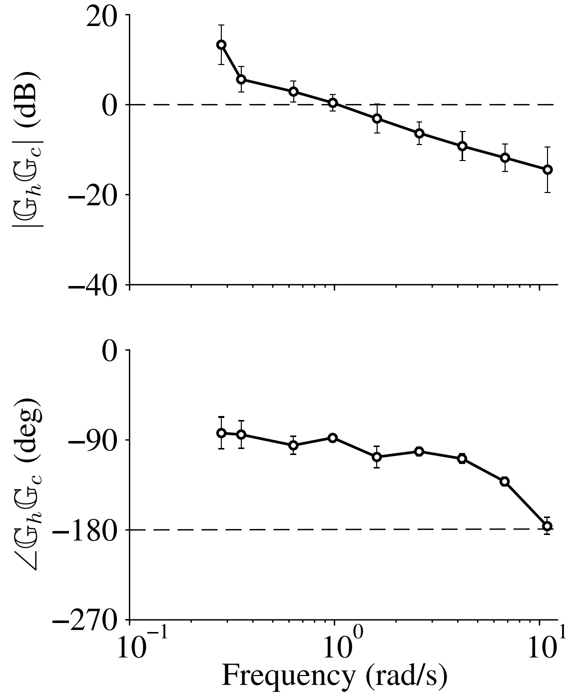

(a) Integrator

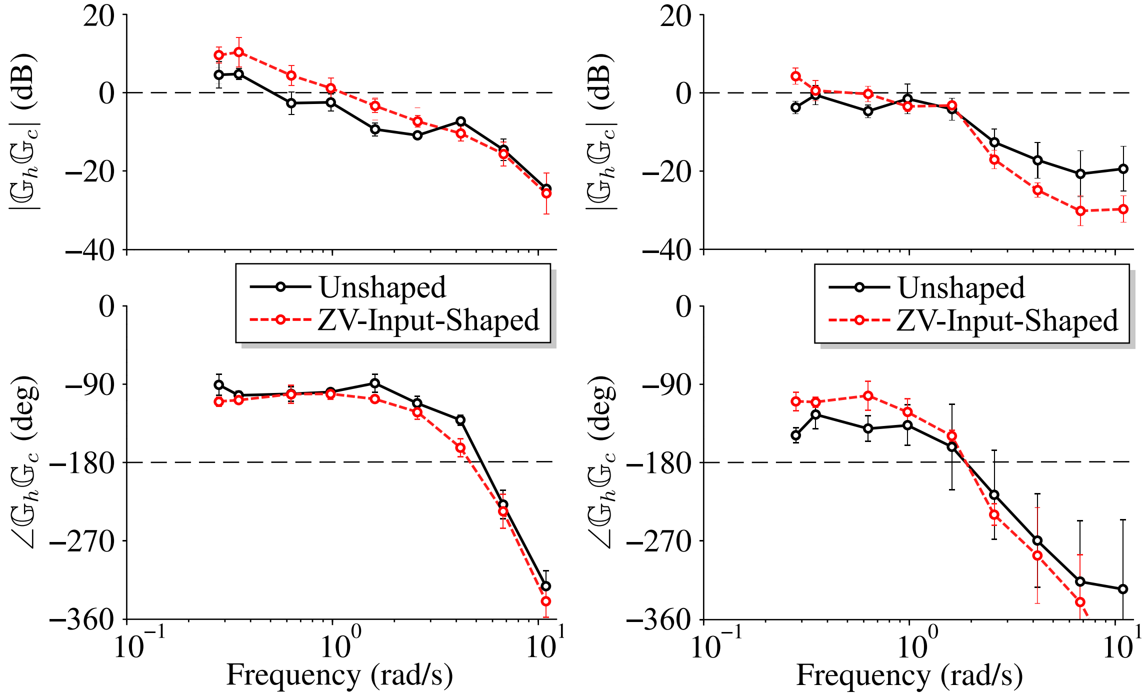

(b) High-frequency oscillatory mode (c) Low-frequency oscillatory mode

Figure 37: Frequency response of human-machine system (mean ± SD)

become smoother. The input-shaped curves are well-characterized by the crossover model. The data for the unshaped low-frequency oscillation in Figure 37(c) show large variability, especially at frequencies above the oscillatory mode's natural frequency. The amplitude curve never crosses above 0 dB. With the addition of input shaping, the amplitude and phase curves are shifted upward in a range of low frequencies. The phase characteristics are greatly improved. The input-shaped curves are somewhat more similar to the crossover model, although the similarity is not as strong as for the high-frequency input-shaped curves.

3.1.4 Discussion

If a controlled system has relatively low-frequency oscillations, then tracking tasks are very difficult. Furthermore, such oscillatory human-machine systems do not behave as predicted by McRuer's crossover model. The addition of input shaping suppressed vibration of the oscillatory mode, and it allowed the human operator to approach "normal" tracking behavior, as defined by the crossover model. Tracking performance greatly improved, and the operator's rating of task difficulty significantly decreased.

This experiment only used a ZV input shaper. The next section describes tests with a variety of different input shapers and documents which input shapers produce the greatest improvements.

3.2 Tracking Study # 2: Shaper-Correlation Experiment[3]

In the Two-Frequency experiment, input shaping was not applied to the translating base. While input shaping improves control of flexible elements, it may be detrimental to control of the driven base or vehicle. Input shaping delays part of the operator's command, and the modified command may create a less-intuitive vehicle response than the unshaped command. Time delays in aircraft control systems have been

---

[3] WooJung Choi assisted with data collection for this experiment.

associated with control problems such as pilot-induced oscillation [66].

The Two-Frequency experiment showed promising results using the simple ZV input shaper. This expanded experiment tests many different kinds of input shapers, and uses a more-complex controlled system with inertia and backdriving. That is, the load motion influences the base motion. The results of this experiment are used to design input shapers in the next chapter.

3.2.1 Participants & Procedure

A manual tracking experiment was administered to 11 human operators. Each participant signed a consent form describing the risks and rewards involved in the experiment. Operators did not receive monetary compensation. Figure 38 shows a photo of the experimental setup. Operators viewed a pursuit display that occupied around 10° visual angle, and they generated control inputs with a *Logitech Attack 3* spring-centered joystick, described in the previous experiment. The manual tracking experiment was implemented in MATLAB.

Two practice trials showed the operator how easy and how hard the control task could be. An extremely easy trial (unshaped driven base) was used to demonstrate an element that should be rated 1 or 2 on the difficulty scale shown in Table 3,

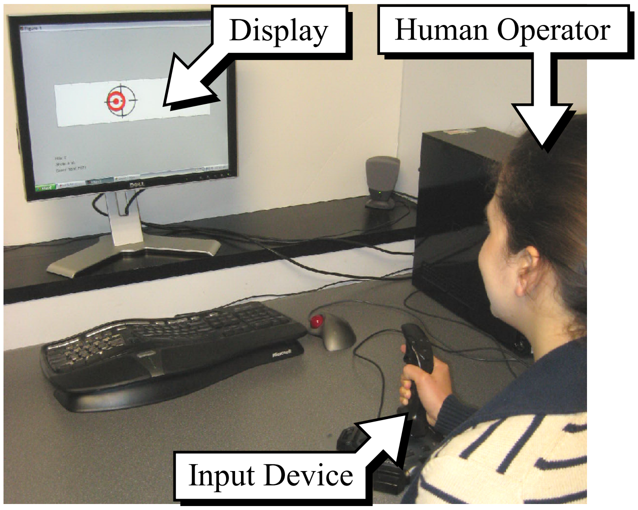

Figure 38: Experimental setup for Shaper-Correlation experiment

Table 3: Difficulty rating scale for Shaper-Correlation experiment

Rating	Description
1-3	Desired performance attainable with zero (1) to minimal (3) mental effort/compensation
4-6	Desired performance requires moderate (4) to intense (6) mental effort/compensation
7-9	Desired performance not met; Maintaining control requires mild (7) to intense (9) effort
10	Control cannot be maintained

and an extremely hard trial (unshaped flexible element) demonstrated an undesirable controlled system that should be rated very poorly. Operators were not informed which controlled elements were used as the "easy" and "hard" elements.

Operators then performed a set of 28 trials. To prevent fatigue, subjects were given a mandatory 2-minute break after every 5 trials. Each trial lasted 115 seconds. The first 15 seconds allowed the subject to get accustomed to the controlled-element dynamics, and only the final 100 seconds of the trial were analyzed. After each trial, the user was asked to consult the rating scale in Table 3, and rate the controlled-element dynamics from 1 (best) to 10 (worst). The scale is a simplified version of the Cooper-Harper scale discussed in Section 2.2. The experiment lasted around 1 hour and 20 minutes for each operator.

3.2.2 Tracking Trials

Operators controlled a translating base with a suspended load as shown in Figure 39. Control input $u(t)$ specifies a force applied to the base, the cart has position $x(t)$ and mass M, the load has position $y(t)$ and mass m, and is suspended from a cable of length ℓ. A translational damper with coefficient b_x is attached to the cart, and a damper with coefficient b_y is attached to the load.

Assuming small load-swing angles, this system can be characterized by the following state-space equation:

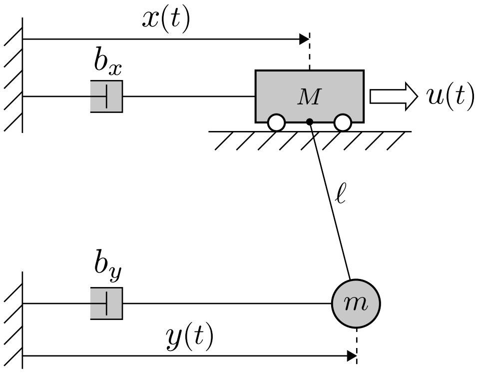

Figure 39: Translating base and suspended load

$$\frac{d}{dt}\begin{Bmatrix} x \\ \dot{x} \\ y \\ \dot{y} \end{Bmatrix} = \begin{bmatrix} 0 & 1 & 0 & 0 \\ -\frac{mg}{M\ell} & -\frac{b_x}{M} & \frac{mg}{M\ell} & 0 \\ 0 & 0 & 0 & 1 \\ \frac{g}{\ell} & 0 & -\frac{g}{\ell} & -\frac{b_y}{m} \end{bmatrix}\begin{Bmatrix} x \\ \dot{x} \\ y \\ \dot{y} \end{Bmatrix} + \begin{Bmatrix} 0 \\ \frac{1}{M} \\ 0 \\ 0 \end{Bmatrix} u, \tag{25}$$

where g is gravitational acceleration. The mass and damping parameter values were tuned such that the load swing had a frequency of 1.256 *rad/s* and a damping ratio of 0.1. The cart had a first-order velocity response with a time constant of 1 *sec* and a maximum velocity of 13.28 *deg/s*. Two load-mass ratios were tested: the *light* load was 1/1000 of the cart mass, so the load mass ratio was effectively 0; the *heavy* load was 1/3 of the total base+load mass, resulting in a load mass ratio of 0.33.

For each trial, the operator attempted to follow the target using either the base in Figure 40(a) or the load in Figure 40(b). The pursuit display presented background information (represented by the hatched ground lines) to the operators, allowing them to see the target and cursor motion independently.

Table 4 shows the frequency content of the reference input that drove the motion of the target. The range of sine wave frequencies is similar to those from previous manual-tracking experiments, except for sine wave 9. This very slow, large-amplitude wave only completed part of a cycle during the trial, which gave the target an overall baseline motion. From pilot studies, it was found that without this baseline motion,

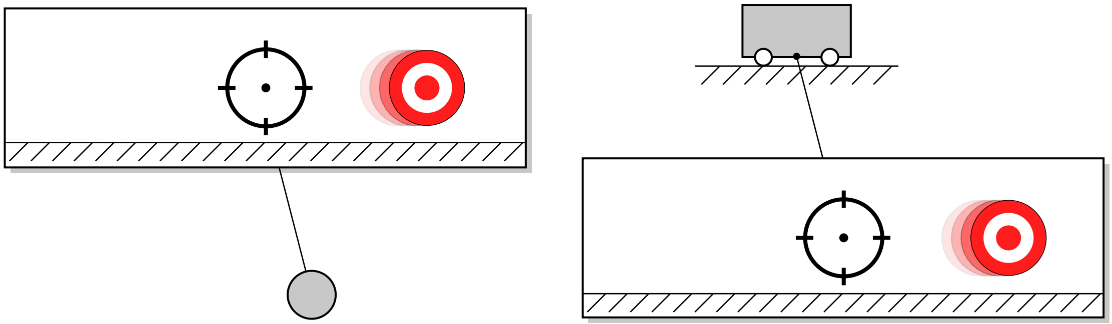

(a) Base control

(b) Load control

Figure 40: Displays for Shaper-Correlation experiment

Table 4: Forcing function for Shaper-Correlation experiment

Wave Number, i	**Frequency**, ω_i (rad/s)	**Amplitude**, B_i (° visual angle)
1	9.362	0.071
2	5.718	0.167
3	3.456	0.266
4	2.073	0.366
5	1.194	0.474
6	0.691	0.581
7	0.314	0.735
8	0.188	0.835
9	0.063	10.493

subjects would sometimes stop making control inputs to leave the cursor in one place, knowing that the target would eventually come back to it. This strategy was mostly used with the very difficult controlled elements. The addition of sine wave 9 eliminated this behavior because the target would drift away without returning.

To ensure that different randomly generated forcing functions had the same difficulty, only functions whose maximum excursions, maximum velocities, and maximum accelerations fell within certain bounds were used. Forcing functions were generated until a function that fit these criteria was found. It has been found that the difficulty of tracking a given forcing function heavily depends on the velocity and acceleration of the target motion [17]. The MATLAB program used to generate forcing functions with bounds on the target position and its derivatives is set out in Appendix B.1.

3.2.3 Input Shapers

The input shapers shown in Figure 41 were added between the command and the controlled element. For convenience, the figure displays shapers designed for zero damping instead of 0.1 damping as in the experiment. Impulse times are expressed in terms of the period of oscillation, T. Note that the unshaped case is equivalent to an input shaper with one impulse of amplitude 1 at time 0. The conventional ZV, SNA, UMZV, and ZVD input shapers were discussed in Section 2.1.

The "Test" input shapers were designed to test the hypothesis that input shapers with initial impulses larger than later impulses are more responsive, and allow better control over the driven base. The shapers are named Test3 and Test5 because they have 3 and 5 impulses, respectively. The Test input shapers were designed using vector diagrams, not with optimization routines.

Figure 42 shows vector diagrams of the Test3 and Test5 input shapers. To design the Test3 shaper in Figure 42(a), a large initial impulse of 0.75 was specified, and subsequent impulses were chosen to make the impulse amplitudes sum to 1 and the

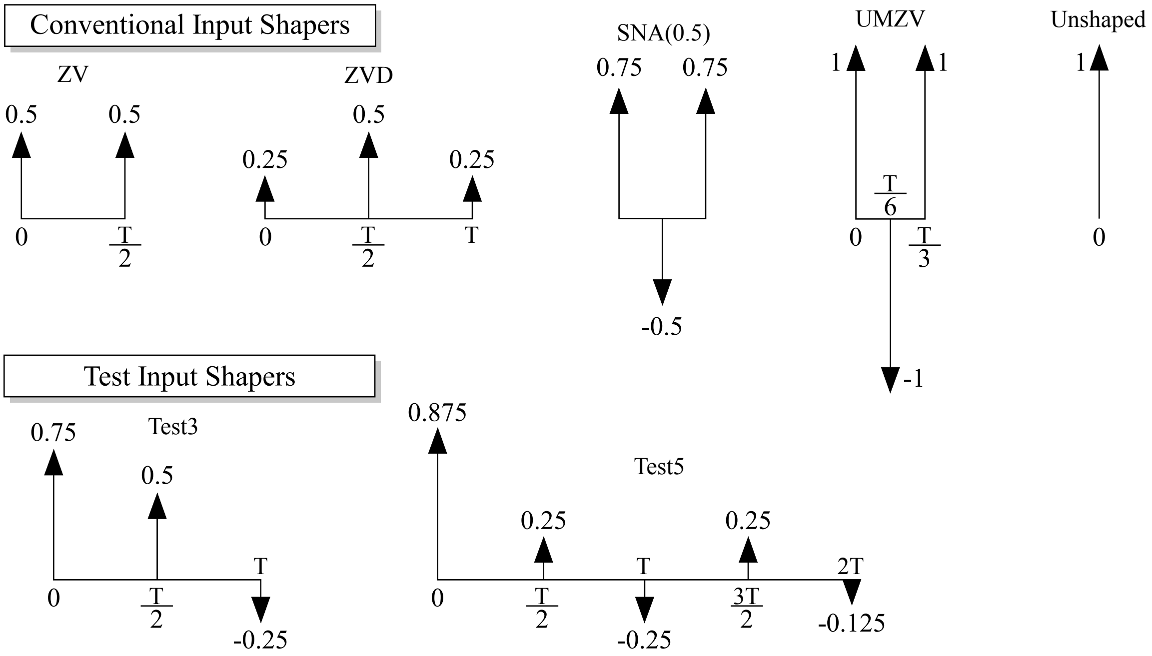

Figure 41: Input shapers used in Shaper-Correlation experiment

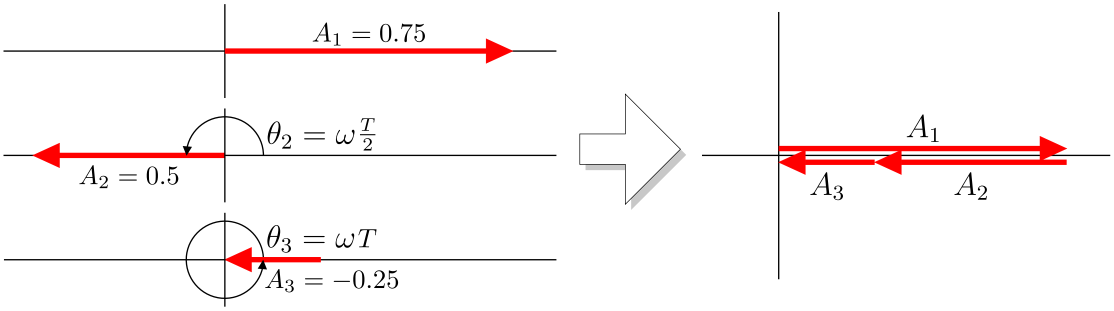

(a) Test3 input shaper

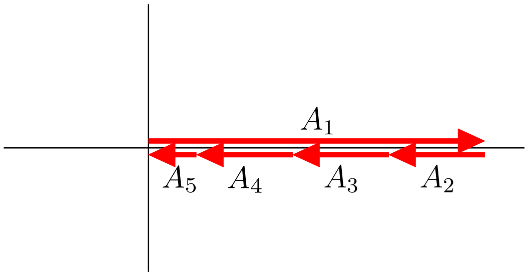

(b) Test5 input shaper

Figure 42: Vector diagrams of Test3 and Test5 input shapers

vector sum return to the origin. A path from the tip of the first impulse back to the origin was formed by using impulses at multiples of $\frac{T}{2}$. The amplitudes of the second and third impulses were chosen to decrease in magnitude so that the first impulse was the largest.

The same strategy was used to design the Test5 input shaper in Figure 42(b). Similar input shapers with other numbers of impulses (e.g., 4, 7, 8, and 9) can also be created.

3.2.4 Results

3.2.4.1 Tracking Performance

Figure 43 shows the root-mean-squared tracking error for controlling the driven base. Results for the light ($LMR = 0$) and heavy ($LMR = 0.33$) loads are compared. In Figure 43, the heavier load tended to degrade base control because load swing added a disturbance to the base motion. On average, tracking error was lowest with no

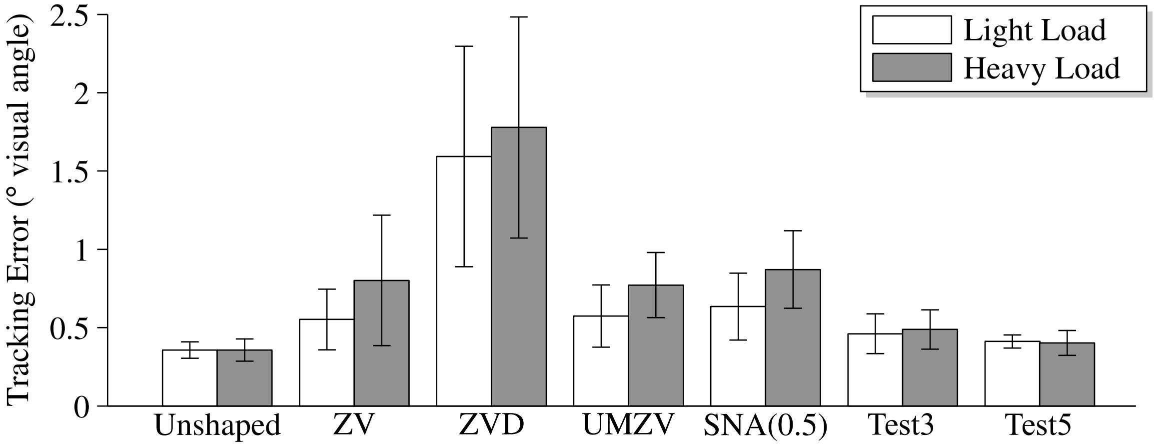

Figure 43: Tracking error for base control (mean ± SD)

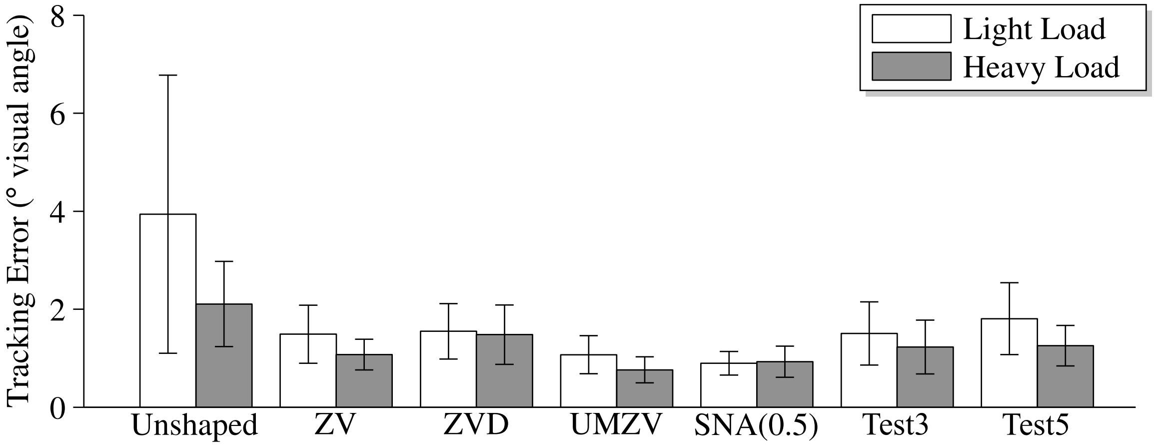

Figure 44: Tracking error for load control (mean ± SD)

input shaping, and with the Test3 and Test5 input shapers. The ZV, ZVD, and SNA input shapers yielded approximately the same performance. Performance was very poor with the ZVD input shaper.

Figure 44 shows tracking error for controlling the flexible load. The heavier load tended to improve load control, which is the opposite effect seen with base control. This is because when the subjects steered the load toward the target, the base (and therefore, the suspension point) was also pulled more strongly toward the target. Moving the suspension point over the suspended load tends to reduce the swing.

For controlling the load, tracking error was smallest with the SNA, UMZV, and ZV shapers, and largest with no input shaping. The ZVD and Test5 input shapers produced the worst performance, and the Test3 shaper was somewhat better.

3.2.4.2 Subjective Rating

Figure 45 shows the subjective rating results for controlling the driven base. Note that by definition, the confidence interval cannot go below 1 or above 10 on the scale. A heavy load tended to make controlling the base subjectively more difficult. The Test3 and Test5 input shapers were rated essentially the same as the unshaped case. The ZV, UMZV, and SNA shapers had similar ratings, and ZVD was rated the worst.

Subjective rating results for controlling the flexible load are given in Figure 46. The heavier load tended to decrease subjective difficulty. The unshaped trial with

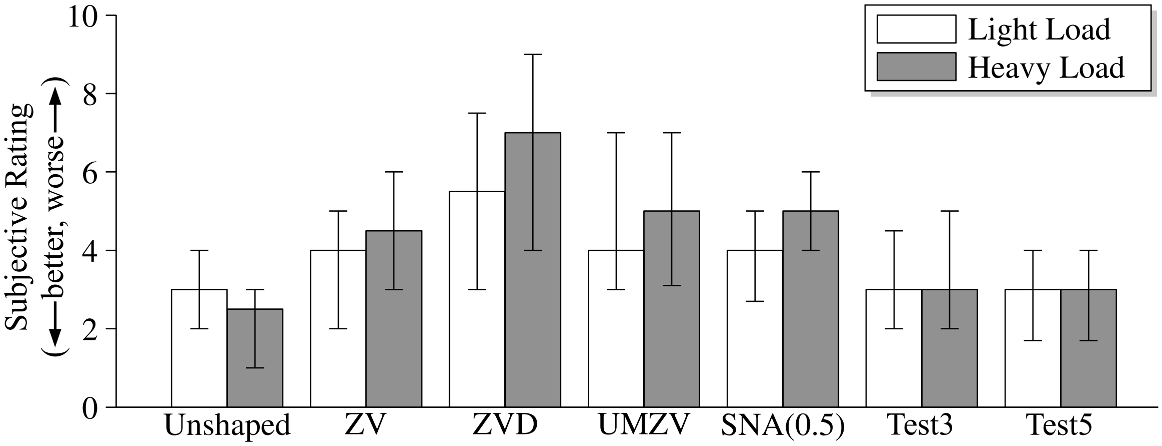

Figure 45: Rating for base control (median with 95% CI)

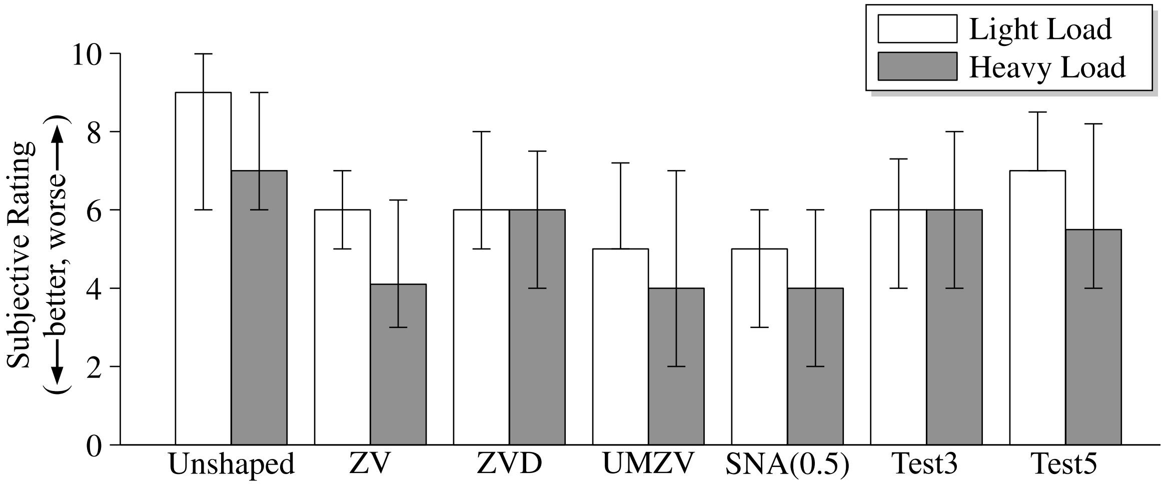

Figure 46: Rating for load control (median with 95% CI)

the light load was rated the worst. The UMZV and SNA input shapers were rated the best, followed by the ZV, Test3 and ZVD, and the Test5 shaper.

3.2.4.3 Control Behavior

A human-machine system's control behavior can be identified using both time-domain and frequency-domain techniques. It has been found that time-domain techniques can be superior to conventional Fourier-coefficients methods in terms of robustness to nonlinear and non-stationary control behavior and avoidance of interpolation errors [6]. MATLAB's *procest* function was used to form best estimates of the parameters of the Crossover model for each trial.

It was found that fitting a model to the whole trial at once produced relatively poor fits, mainly because humans tend to have time-varying inconsistencies in their control behavior [92]. Therefore, the trial was divided into sections. The final 90 seconds of each trial was broken into overlapping 15-second intervals spaced 5-seconds apart, as shown in Figure 47. For each interval, Crossover model parameters that produced a minimum-least-squares fit to the experimental data were found. The interval with the best fit to the Crossover model was selected, and the Crossover model parameters from this interval were chosen to represent the whole trial. Note that the chosen interval does *not* necessarily contain the best tracking performance, only the best fit

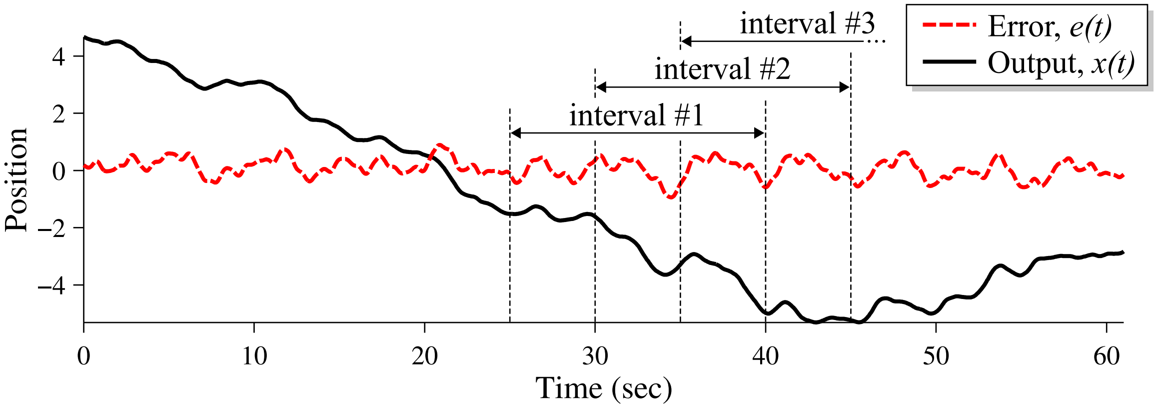

Figure 47: Intervals for Crossover model parameter fitting

to the Crossover model.

Three parameters were extracted from the Crossover model that produced the best-fitting interval: gain K, effective time delay τ, and phase margin ϕ_m. These parameters were discussed in Section 2.3.4. Goodness-of-fit to the Crossover model was quantified by *fit percentage*, which is calculated from the normalized-mean-squared error between the experimental and predicted output:

$$\%_{fit} = 100 \cdot \left(1 - \frac{\|x_s - x\|}{\|x - \bar{x}\|}\right), \tag{26}$$

where x is the experimental output, and x_s is the output of the estimated model simulation. A perfect model fit to the experimental data would have a fit percentage of $\%_{fit} = 100\%$, and the worst possible fit would have a percentage that approached $\%_{fit} = -\infty$. Figure 48 compares the simulated and experimental outputs for several

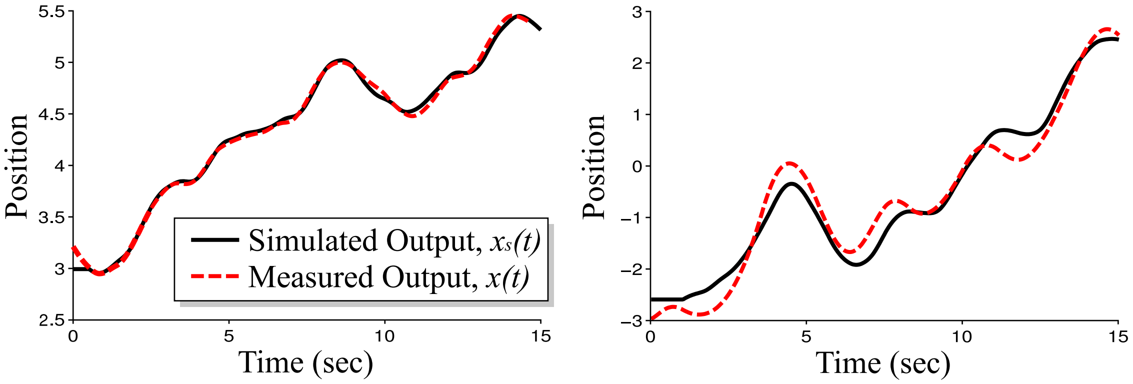

(a) Estimated model with 90% fit (b) Estimated model with 80% fit

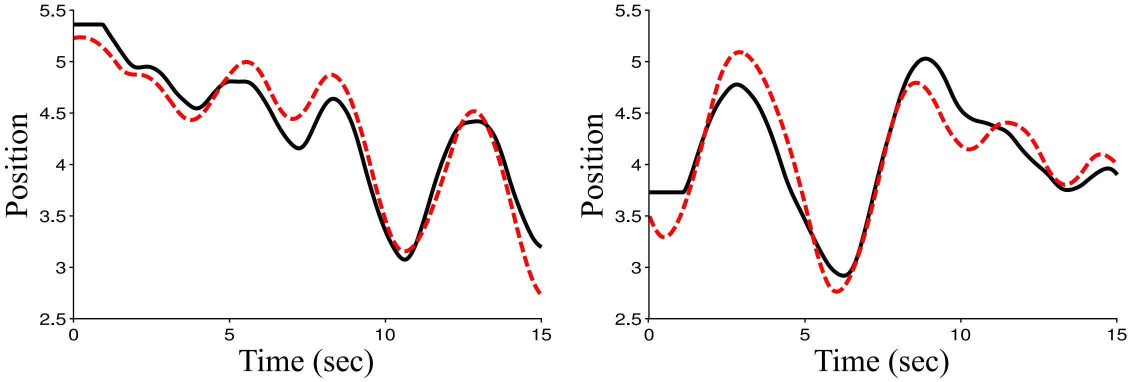

(c) Estimated model with 70% fit (d) Estimated model with 50% fit

Figure 48: Example 15-second intervals with different fit qualities

example fit percentages.

Table 5 shows the results of this analysis for controlling the driven base. For each input shaper, mean and standard deviation values of K, τ, ϕ_m, and $\%_{fit}$ are shown. Only results for the light load are given, as results for the heavy load were similar. As expected, unshaped base control showed the most desirable system characteristics of the highest gain, lowest effective time delay, highest phase margin, and highest fit percentage. The Test3 and Test5 shapers were nearly as good as the unshaped case. The ZVD shaper had the lowest gain, the smallest phase margin, and the largest delay. Recall that gain K is equivalent to the system's crossover frequency.

Table 6 shows Crossover model results for controlling the flexible load. The unshaped case had the lowest fit percentage. This important result means that all of

Table 5: Crossover model parameters for base control [mean (SD)]

	K (rad/s)	τ (sec)	ϕ_m (deg)	$\%_{fit}$
Unshaped	1.20 (0.42)	0.62 (0.26)	51.13 (11.66)	89.91 (4.09)
ZV	0.83 (0.29)	1.19 (0.50)	33.98 (30.13)	86.77 (4.83)
ZVD	0.54 (0.12)	2.30 (0.50)	18.76 (18.68)	80.00 (15.95)
UMZV	0.67 (0.29)	1.47 (0.24)	34.12 (26.98)	79.98 (7.68)
SNA(0.5)	0.68 (0.19)	1.44 (0.40)	32.67 (24.26)	84.29 (6.84)
Test3	0.84 (0.21)	0.97 (0.45)	44.75 (20.19)	86.82 (4.43)
Test5	1.05 (0.31)	0.83 (0.31)	40.83 (20.24)	87.94 (3.38)

Table 6: Crossover model parameters for load control [mean (SD)]

	K (rad/s)	τ (sec)	ϕ_m (deg)	$\%_{fit}$
Unshaped	0.86 (0.43)	1.31 (0.15)	27.69 (28.98)	69.64 (9.62)
ZV	0.77 (0.36)	1.39 (0.54)	7.69 (35.45)	71.81 (13.05)
ZVD	0.51 (0.30)	3.00 (1.79)	3.63 (34.36)	84.53 (7.31)
UMZV	0.77 (0.20)	1.36 (0.22)	30.12 (19.92)	76.34 (12.27)
SNA(0.5)	0.69 (0.19)	1.43 (0.24)	33.56 (17.06)	80.43 (12.31)
Test3	0.53 (0.36)	1.29 (0.46)	31.86 (46.20)	72.14 (11.17)
Test5	0.92 (0.40)	1.28 (0.17)	24.63 (24.90)	73.91 (8.78)

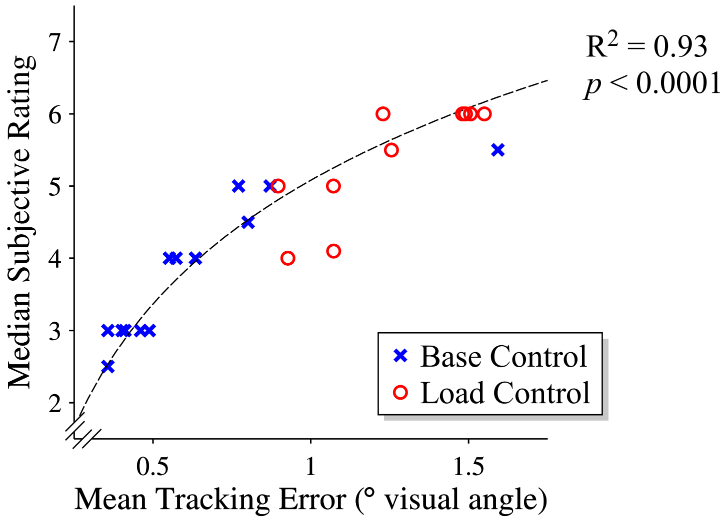

Figure 49: Performance vs. subjective rating for Shaper-Correlation experiment

the input shapers increased the applicability of the Crossover model – the human-machine system's control behavior was better captured by (23) when input shaping was applied.

The highest fit percentage was produced by the ZVD shaper, but the large delay and small phase margin indicate that the system did not perform well. This agrees with the RMS error results in Figure 43. The SNA input shaper produced the largest phase margin and a high fit percentage, and the UMZV input shaper also yielded good system performance.

3.2.4.4 Correlations

The operators' quantitative performance and qualitative ratings are compared in Figure 49. Each marker represents one combination of controlled element and input shaper. Trials where the operator controlled the driven base are in the lower left region of the plot, where tracking error is small and subjective rating is low. Trials where the flexible load is controlled are generally in the upper right region of the plot.

Mean tracking error and median subjective rating have a strong log-linear relationship with an R^2 value of 0.925 and an extremely high probability of a nonzero correlation (indicated by a p-value of < 0.0001). The dashed curve in Figure 49 is given by:

$$r_{sub} = 5.0791\ ln(e_{RMS}) + 2.4739, \tag{27}$$

where r_{sub} is subjective rating and e_{RMS} is root-mean-squared tracking error. This strong relationship confirms that operators based their ratings partly on tracking performance, as instructed by the simplified Cooper-Harper scale.

Another interesting relationship may exist between the quantitative and qualitative performance for a trial, and the control behavior (as quantified by the Crossover model) during that trial. As mentioned in Section 2.3.4, McRuer and other researchers found that tracking performance and rating are best when tracking conditions allow a good fit to the Crossover model [53], and are much worse when the Crossover model is not a good fit [57, 58]. It is hypothesized that the factors of tracking error and subjective rating should be highly correlated with the Crossover model fit percentage.

A more recent study found that tracking error was not well predicted by the crossover frequency (gain K), but was more related to the phase margin [6]. Therefore, a correlation between phase margin and root-mean-squared tracking error will also be investigated.

Figure 50 compares log-transformed mean tracking error to $\%_{fit}$ and ϕ_m. While not as strongly related as tracking error and subjective rating in Figure 49, the correlations are still significant. Crossover model fit has a relatively high R^2 value of 0.62, and the phase margin correlation in Figure 50(b) is somewhat weaker.

Figure 51 plots the median subjective rating against the same two parameters that were used in Figure 49. Because the tracking error and subjective rating are so closely related, it is unsurprising that the correlations are similar to the results shown in Figure 50. Subjective rating has a significant correlation with Crossover model fit and phase margin. The strength of the relationship is stronger with Crossover model fit than with phase margin.

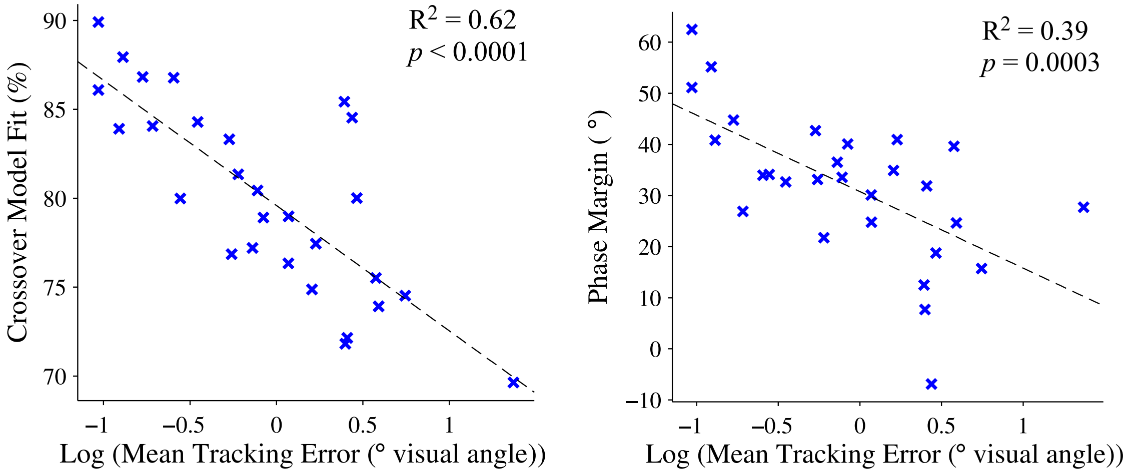

(a) Fit to Crossover model (b) Phase margin

Figure 50: Tracking error vs. Crossover model parameters

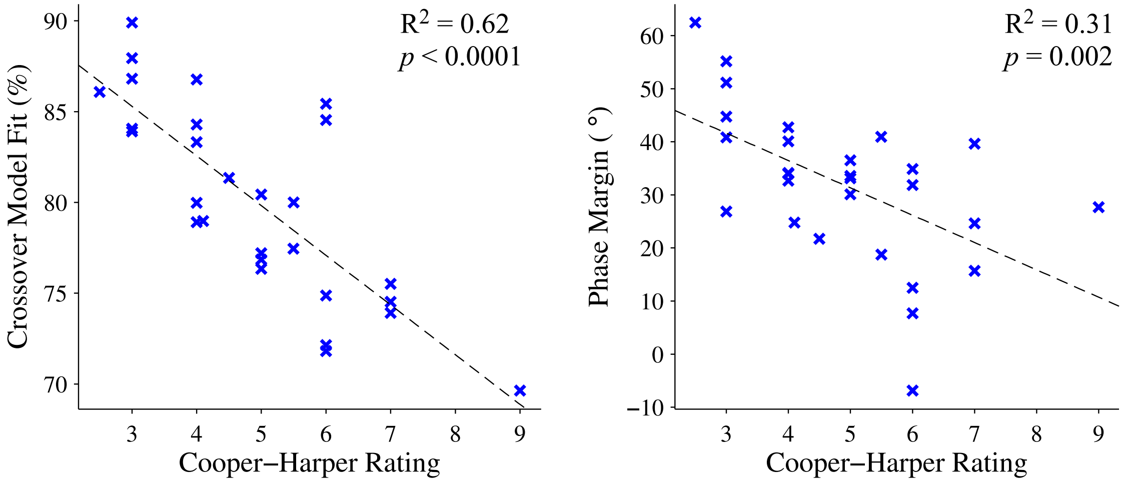

(a) Fit to Crossover model (b) Phase margin

Figure 51: Subjective rating vs. Crossover model parameters

3.2.4.5 Discussion

From the qualitative and quantitative results, it is evident that the new input shapers were effective at maintaining good tracking performance with the driven base. This gives some evidence that by heavily weighting the first impulse (the human operator's current command), the input shaper reacts more quickly and makes the system feel more responsive to the human operator.

Another notable result was the excellent tracking performance, subjective rating, and Crossover model characteristics of the SNA input shaper for controlling the flexible load. Compared to the unshaped case, the SNA shaper greatly increased the phase margin and improved the Crossover model fit. Figure 52 illustrates one possible reason that the SNA was better for load control and the Test3 and Test5 shapers were better for base control. Figure 52(a) shows the response of a driven base to a pulse command, and the response to the same command input-shaped by an SNA shaper. The flexible load response to this input-shaped command is shown by the dotted line. Figure 52(b) shows the same responses for the Test5 input shaper.

As seen in Figure 52(a), the SNA input shaper significantly modifies the base response at around $t = 2$ seconds. The input-shaped base briefly stops, and after it regains its velocity, the shaped response lags behind the unshaped response by approximately 1 second. The input-shaped load response is almost identical to the unshaped base response shifted in time. In other words, the SNA input shaper makes the flexible load respond like the driven base with a small delay. This response is much more intuitive than is the oscillatory response of an unshaped flexible load.

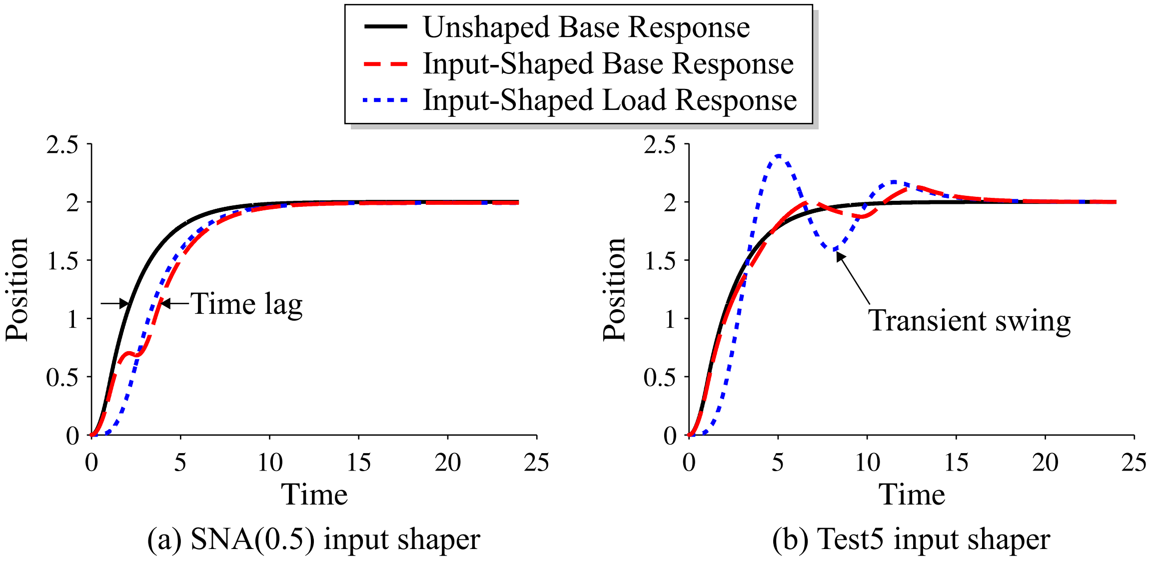

(a) SNA(0.5) input shaper

(b) Test5 input shaper

Figure 52: Base and load responses to input-shaped pulse command

In contrast, the Test5 input shaper in Figure 52(b) produces a fast base response which does not lag behind the unshaped response. The Test5 shaper causes small fluctuations in the input-shaped base response, but the dynamic behavior of the base is largely unchanged. However, the load has overshoot and large transient oscillation which is eliminated by later impulses. The Test5 input shaper does not create an intuitive load response like the SNA shaper.

Relationships were found between measures of quantitative tracking performance, qualitative rating of difficulty, and control behavior of the human-machine system. The relationships linking tracking performance to similarity of the human-machine system to the Crossover model were found in previous studies, and are confirmed in this study. The strong log-linear relationship between tracking performance and subjective rating was not mentioned in previous studies. It will be shown that this relationship holds for several other tracking experiments.

3.3 Conclusions

Controlling an oscillatory element with a “fast” natural frequency of 5 rad/s (which is above the active frequency region of manual control [65]) was much easier than controlling the slow natural frequency of 1.25 rad/s. Adding input shaping to this slower oscillatory system greatly improved tracking performance, subjective rating of difficulty, and resemblance of the open-loop human-machine system to McRuer’s Crossover model. Upon further study, it was found that all of the traditional input shapers enabled a better fit to the Crossover model when the operator was controlling the flexible element.

A significant correlation was found between Crossover model fit and tracking performance. This confirms a trend that has been noted in the literature – when the human-machine system’s control behavior is better described by the Crossover model, it performs better, and the human operator rates the system more favorably.

Traditional input shapers improved control of a flexible element and somewhat degraded control of the driven base. Two new input shapers were designed based on the intuitive concept that to maintain responsiveness, initial impulses should have larger amplitudes than later impulses. The new input shapers allowed better control of the driven element than conventional shapers while maintaining some improvement in control of the flexible load.

In the next chapter, a formal way of designing input shapers for improved control of the driven base will be proposed, along with a method to continuously adjust the vibration-limiting aggressiveness of any input shaper. This technique, called *partial input shaping*, may allow a pilot to adjust the “amount” of shaping using a dial in the cockpit.

CHAPTER IV

DESIGNING INPUT SHAPERS FOR MANUAL TRACKING

Using experimental data from manual tracking trials with conventional input shapers, new input shapers are designed. In this chapter, experimental performance with a given input shaper is compared to characteristics of the shaper, and a characteristic that is highly correlated with base-tracking performance is identified. Using this characteristic as a cost function in an optimization routine yields a new class of Reduced-Modification *(RM) input shapers. In addition, a method to adjust any input shaper between unshaped and fully input-shaped is introduced. The new input shapers are evaluated by using manual tracking experiments.*

4.1 Reduced-Modification Input Shapers

Now that tracking performance with conventional input shapers has been studied and quantified, a next step is to design novel shapers that can perform better than the conventional shapers. One approach is to find *characteristics* of input shapers that predict tracking performance, and then use those characteristics to drive an optimization routine that solves for new input shapers. Useful characteristics are identified by comparing the performance of each input shaper to the various characteristics of that shaper.

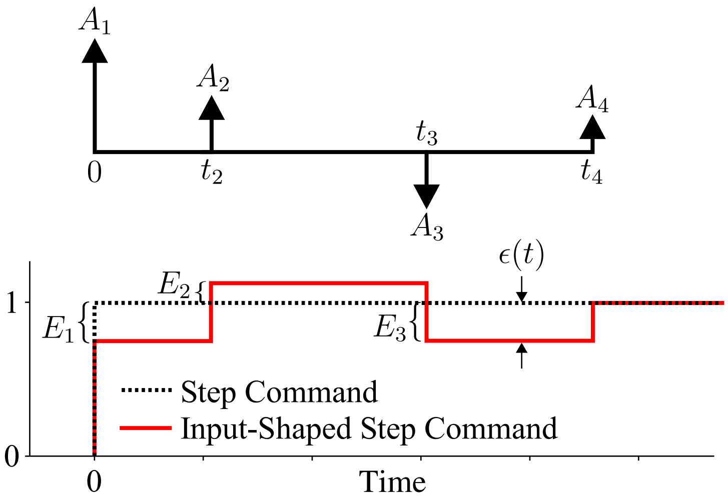

Figure 53: Impulse sequence and shaped step command

4.1.1 Input Shaper Characterization

The top of Figure 53 shows an arbitrary impulse sequence, and the bottom compares a step command to a command shaped by the impulse sequence. The labeled parameters in this figure will be used to calculate characteristics that describe the impulse sequence.

The impulse amplitudes and time locations are A_i and t_i. Two additional parameters are based on the difference between the shaped command and the original step command: the function $\epsilon(t)$ is the command difference at any time t, and E_i is the difference between the commands at the time each impulse is applied:

$$E_i = \epsilon(t_i). \tag{28}$$

Using these parameters, a set of characteristics can be computed for any given input shaper. Table 7 defines and describes the characteristics used in this thesis. Operations applied to the parameters include integration, summing, absolute value and squaring. Each characteristic yields a performance measure that describes a quality of the input shaper.

Table 7: Input shaper characteristics

Characteristic	Description
t_n	Time location of final impulse
$\frac{\sum A_i t_i}{\sum A_i}$	Centroid of impulses (allowing negative amplitudes)
$\frac{\sum \lvert A_i \rvert t_i}{\sum \lvert A_i \rvert}$	Centroid of impulse magnitudes
$\sum \lvert A_i \rvert$	Sum of impulse magnitudes
$\sum A_i t_i$	Sum of impulse amplitudes × time locations
$\sum \lvert A_i \rvert t_i$	Sum of impulse magnitudes × time locations
$\sum A_i^2$	Sum of squared impulse amplitudes
$\sum A_i^2 t_i$	Sum of squared impulse amplitudes × time locations
$\sum A_i t_i^2$	Sum of impulse amplitudes × squared time locations
$\sum \lvert A_i \rvert t_i^2$	Sum of impulse magnitudes × squared time locations
$\sum A_i^2 t_i^2$	Sum of squared impulse amplitudes × squared time locations
$\max(\lvert \epsilon \rvert)$	Maximum command difference magnitude
$\int \epsilon dt$	integrated command difference
$\int \lvert \epsilon \rvert dt$	integrated command difference magnitude
$\int \epsilon t dt$	integrated command difference × time
$\int \lvert \epsilon \rvert t dt$	integrated command difference magnitude × time
$\int \epsilon^2 dt$	integrated squared command difference
$\int \epsilon^2 t dt$	integrated squared command difference × time
$\int \epsilon t^2 dt$	integrated command difference × time squared
$\int \lvert \epsilon \rvert t^2 dt$	integrated command difference magnitude × time squared
$\int \epsilon^2 t^2 dt$	integrated squared command difference × time squared
$\max(\lvert E_i \rvert)$	Maximum impulse difference
$\sum E_i$	Sum of impulse differences
$\sum \lvert E_i \rvert$	Sum of impulse difference magnitudes
$\sum E_i t_i$	Sum of impulse differences × time locations
$\sum \lvert E_i \rvert t_i$	Sum of impulse difference magnitudes × time locations
$\sum E_i^2$	Sum of squared impulse differences
$\sum E_i^2 t_i$	Sum of squared impulse differences × time locations
$\sum E_i t_i^2$	Sum of impulse differences × squared time locations
$\sum \lvert E_i \rvert t_i^2$	Sum of impulse difference magnitudes × squared time locations
$\sum E_i^2 t_i^2$	Sum of squared impulse differences × squared time locations

4.1.2 Characteristics that Predict Tracking Performance

The Shaper-Correlation experiment in Section 3.2 tested manual tracking performance using a variety of input shapers. In each tracking trial, the operator's command was shaped by an impulse sequence. Recall that the "unshaped" case is essentially shaped by an impulse with magnitude 1 at time $t = 0$.

Table 8: Input shaper characteristics vs. tracking performance [R^2 (p)]

	Base Control		Load Control	
	Mean Error	Median Rating	Mean Error	Median Rating
t_n	0.0036 (0.8375)	0.0048 (0.8147)	0.0387 (0.5001)	0.0009 (0.9198)
$\frac{\sum A_i t_i}{\sum A_i}$	0.8929 (0)	0.8378 (0)	0.1107 (0.2451)	0.1154 (0.2347)
$\frac{\sum \|A_i\| t_i}{\sum \|A_i\|}$	0.3817 (0.0185)	0.2486 (0.0696)	0.188 (0.1214)	0.0577 (0.4079)
$\sum \|A_i\|$	0.0134 (0.6937)	0.0151 (0.6754)	0.2423 (0.0738)	0.3124 (0.0377)
$\sum A_i t_i$	0.8929 (0)	0.8378 (0)	0.1107 (0.2451)	0.1154 (0.2347)
$\sum \|A_i\| t_i$	0.1109 (0.2447)	0.1679 (0.1457)	0.4898 (0.0053)	0.3365 (0.0297)
$\sum A_i^2$	0.0903 (0.2964)	0.0067 (0.7806)	0.0467 (0.458)	0.0975 (0.2772)
$\sum A_i^2 t_i$	0.0224 (0.6092)	0.1365 (0.1935)	0.2593 (0.0629)	0.3433 (0.0277)
$\sum A_i t_i^2$	0.9002 (0)	0.8221 (0)	0.0401 (0.4927)	0.052 (0.4332)
$\sum \|A_i\| t_i^2$	0.0094 (0.7419)	0.0002 (0.9634)	0.0514 (0.4358)	0.0001 (0.9762)
$\sum A_i^2 t_i^2$	0.0908 (0.295)	0.2301 (0.0826)	0.3637 (0.0224)	0.3855 (0.0178)
$\max(\|\epsilon\|)$	0.2677 (0.0581)	0.4982 (0.0048)	0.3958 (0.0159)	0.4989 (0.0047)
$\int \epsilon dt$	0.8929 (0)	0.8378 (0)	0.1107 (0.2451)	0.1154 (0.2347)
$\int \|\epsilon\| dt$	0.8027 (0)	0.6416 (0.0006)	0.1651 (0.1494)	0.0965 (0.2796)
$\int \epsilon t dt$	0.9002 (0)	0.8221 (0)	0.0401 (0.4927)	0.052 (0.4332)
$\int \|\epsilon\| t dt$	0.4215 (0.012)	0.2241 (0.0873)	0.0735 (0.3483)	0.005 (0.8105)
$\int \epsilon^2 dt$	0.8462 (0)	0.8631 (0)	0.1616 (0.1541)	0.1734 (0.1385)
$\int \epsilon^2 t dt$	0.8742 (0)	0.8447 (0)	0.1642 (0.1506)	0.1541 (0.165)
$\int \epsilon t^2 dt$	0.8552 (0)	0.7593 (0)	0.0062 (0.7893)	0.0167 (0.6595)
$\int \|\epsilon\| t^2 dt$	0.0379 (0.5048)	0.0007 (0.931)	0.0077 (0.7649)	0.0177 (0.6507)
$\int \epsilon^2 t^2 dt$	0.8903 (0)	0.6964 (0.0002)	0.1009 (0.2684)	0.0518 (0.434)
$\max(\|E_i\|)$	0.2677 (0.0581)	0.4982 (0.0048)	0.3958 (0.0159)	0.4989 (0.0047)
$\sum E_i$	0.2789 (0.0522)	0.5049 (0.0044)	0.292 (0.0461)	0.4021 (0.0149)
$\sum \|E_i\|$	0.2493 (0.0691)	0.4548 (0.0082)	0.3786 (0.0192)	0.4489 (0.0087)
$\sum E_i t_i$	0.4303 (0.0108)	0.6199 (0.0008)	0.1582 (0.1591)	0.2496 (0.0689)
$\sum \|E_i\| t_i$	0.3041 (0.0409)	0.4077 (0.014)	0.3228 (0.034)	0.2764 (0.0535)
$\sum E_i^2$	0.1056 (0.257)	0.2668 (0.0586)	0.2189 (0.0915)	0.3047 (0.0407)
$\sum E_i^2 t_i$	0.6162 (0.0009)	0.6614 (0.0004)	0.0306 (0.5496)	0.077 (0.3369)
$\sum E_i t_i^2$	0.0874 (0.3047)	0.2292 (0.0833)	0.1923 (0.1168)	0.2639 (0.0603)
$\sum \|E_i\| t_i^2$	0.1078 (0.2518)	0.0511 (0.437)	0.0484 (0.45)	0.0013 (0.9019)
$\sum E_i^2 t_i^2$	0.3106 (0.0384)	0.4376 (0.01)	0.1667 (0.1472)	0.1943 (0.1147)

This section seeks to identify input shaper characteristics that are strongly correlated with tracking performance by plotting them against the tracking error and subjective rating corresponding to the input shaper. Table 8 shows the linear correlation between each characteristic and aggregate measures of tracking performance from the Shaper-Correlation experiment.

One noticeable feature of Table 8 is the lack of high R^2 values in the load control columns, indicating that no characteristics were highly correlated with tracking performance using the flexible load.

For controlling the driven base, there were several characteristics that were strongly correlated with performance: $\int \epsilon^2 t^2 dt$, $\int \epsilon^2 t dt$, $\int \epsilon^2 dt$, $\frac{\sum A_i t_i}{\sum A_i}$, $\sum A_i t_i$, $\sum A_i t_i^2$, $\int \epsilon dt$, and $\int \epsilon t dt$ all had significant correlations ($p <, 0.0001$) and R^2 values around 0.9. Therefore, if an input shaper can be designed to decrease these measures, then control of the base will be improved.

The characteristics $\frac{\sum A_i t_i}{\sum A_i}$, $\sum A_i t_i$, $\sum A_i t_i^2$, $\int \epsilon dt$, and $\int \epsilon t dt$ are not useful as cost functions for optimization because they allow impulse amplitudes to remain negative by not squaring or taking an absolute value, and many different combinations of positive and negative amplitudes can sum to zero. The optimizer cannot find a unique solution that minimizes a cost function formed from one of these characteristics.

The integrals $\int \epsilon^2 t^2 dt$ and $\int \epsilon^2 t dt$ are viable cost functions, but the input shapers they produce are very similar to ZV shapers. The $\int \epsilon^2 dt$ characteristic, highlighted in Table 8, was by far the most interesting characteristic for input shaper design. Minimizing this characteristic results in input shapers similar to the Test3 and Test5 input shapers in the Shaper-Correlation experiment. Scatter plots of the $\int \epsilon^2 dt$ characteristic against tracking error and subjective rating are shown in Figures 54(a) and 54(b), respectively. Both correlations have a significant ($p < 0.0001$) probability of a nonzero correlation, and R^2 values around 0.85.

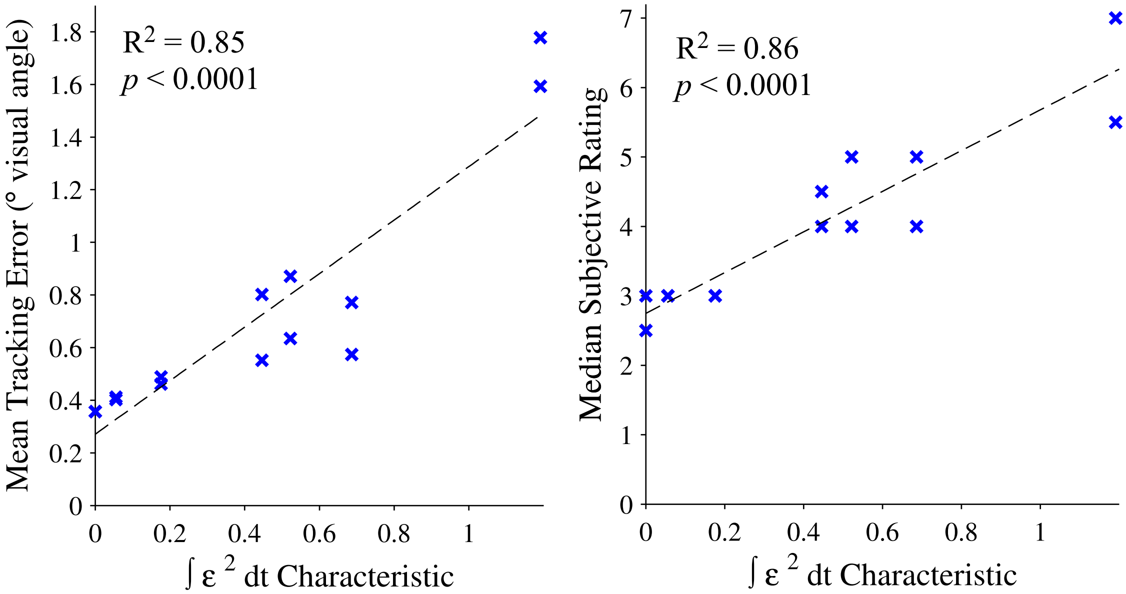

(a) Correlation with mean tracking error (b) Corellation with median rating

Figure 54: Tracking performance vs. $\int \epsilon^2 dt$ input shaper characteristic

The following are 3-, 4-, and 5-impulse input shapers that limit the residual vibration to 0 at the modeled frequency and minimize $\int \epsilon^2 t dt$:

$$\begin{bmatrix} A_i \\ t_i \end{bmatrix}_{RM_3} = \begin{bmatrix} 0.766 & 0.507 & -0.273 \\ 0 & 0.523\,T & 0.957\,T \end{bmatrix} \tag{29}$$

$$\begin{bmatrix} A_i \\ t_i \end{bmatrix}_{RM_4} = \begin{bmatrix} 0.839 & 0.323 & -0.344 & 0.182 \\ 0 & 0.510\,T & 1.015\,T & 1.452\,T \end{bmatrix} \tag{30}$$

$$\begin{bmatrix} A_i \\ t_i \end{bmatrix}_{RM_5} = \begin{bmatrix} 0.878 & 0.245 & -0.246 & 0.258 & -0.137 \\ 0 & 0.523\,T & 1.006\,T & 1.513\,T & 1.950\,T \end{bmatrix}, \tag{31}$$

where T is the natural period of oscillation. These input shapers will be called *Reduced-Modification* (RM) shapers because minimizing $\int \epsilon^2 dt$ keeps the input-shaped command as close to the unshaped command as possible, while still achieving zero vibration. In a practical sense, it attempts to reduce modification of the operator's original command.

The new cost function can be combined with zero-derivative constraints on the sensitivity curve to produce robust versions of the 4- and 5- impulse shapers:

$$\begin{bmatrix} A_i \\ t_i \end{bmatrix}_{RM_4D} = \begin{bmatrix} 0.460 & 0.700 & 0.055 & -0.215 \\ 0 & 0.593\,T & 0.825\,T & 1.512\,T \end{bmatrix} \tag{32}$$

$$\begin{bmatrix} A_i \\ t_i \end{bmatrix}_{RM_5D} = \begin{bmatrix} 0.572 & 0.667 & -0.238 & -0.162 & 0.161 \\ 0 & 0.510\,T & 0.947\,T & 1.465\,T & 2.000\,T \end{bmatrix}. \tag{33}$$

The duration of these input shapers depends mainly on the number of impulses. The 4-impulse shapers (30) and (32) have approximately the same duration, as do the 5-impulse shapers (31) and (33). The main differences between the regular and robust (with the zero derivative constraint) versions of the input shapers is that the robust shapers suppress more vibration when modeling errors are present, and the regular shapers have much larger amplitudes for the first impulse, making them more responsive. Figure 55 shows sensitivity curves for input shapers (29) through (33), and a ZV input shaper for comparison. The regular RM input shapers have less robustness then the ZV shaper, and the RM input shapers with the zero-derivative constraint have more robustness.

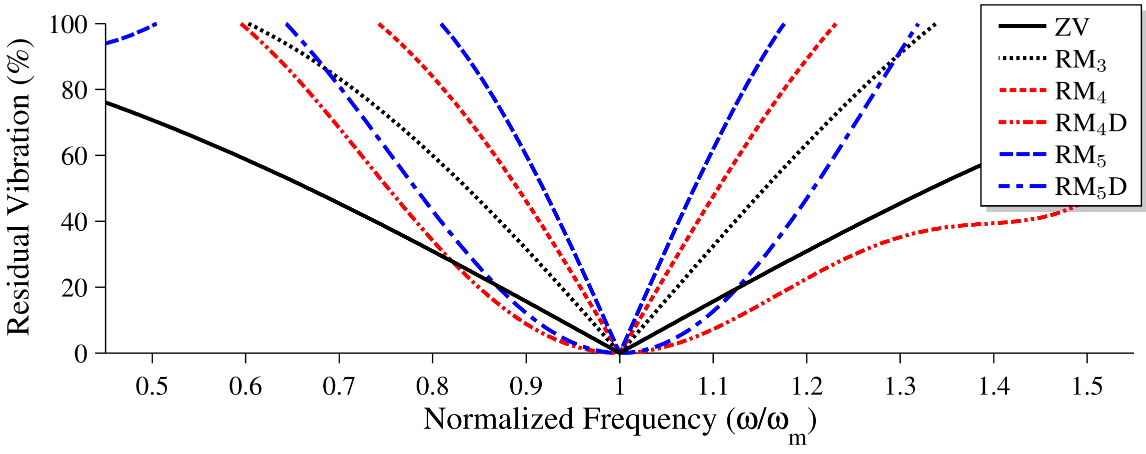

Figure 55: Sensitivity curves for RM shapers

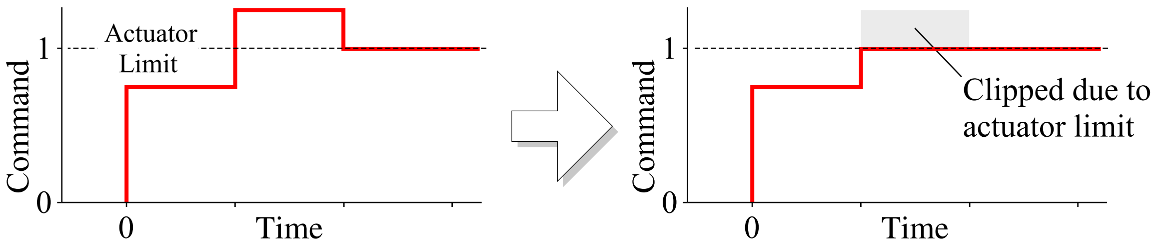

Figure 56: RM$_3$-shaped step command that approaches the actuator limit

4.1.3 Actuator Saturation

The new RM input shapers are only useful on systems where control inputs do not approach the actuator limits. This is because each RM shaper has a period of time where its impulse amplitudes sum to greater than 1. If the system is being driven to its command limits, the excess command will be clipped, or *saturated*. This concept is illustrated in Figure 56. The input-shaped command exceeds the actuator limit represented by the dashed line, and the resulting command is clipped. The input shaper's effectiveness will be greatly decreased unless additional techniques are used to mitigate this effect [89].

4.2 Partial Input Shaping

The previous section presented a new class of input shapers with large initial impulses and smaller subsequent impulses. This section shows a technique that can be used to adjust the initial impulse size of any input shaper. The resulting impulse sequence produces commands that do not suppress all vibration, but are more like the unshaped command and should aid control of the driven base. Recall that in the Shaper-Correlation experiment, it was found that input shaping made controlling the flexible load easier, and controlling the driven base somewhat harder. This is shown conceptually in Figure 57. Note that there is a large unexplored region between these two extremes.

Hypothetically, if impulse sequences that behaved somewhere between an input

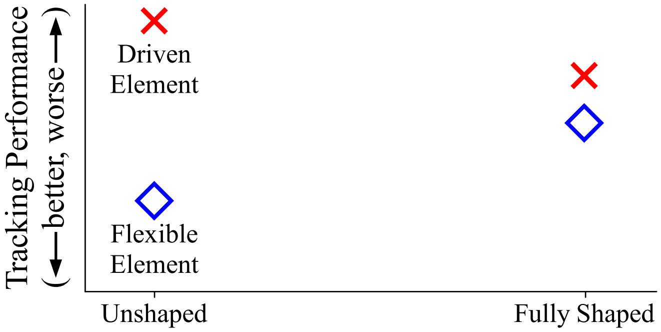

Figure 57: Manual tracking with and without input shaping

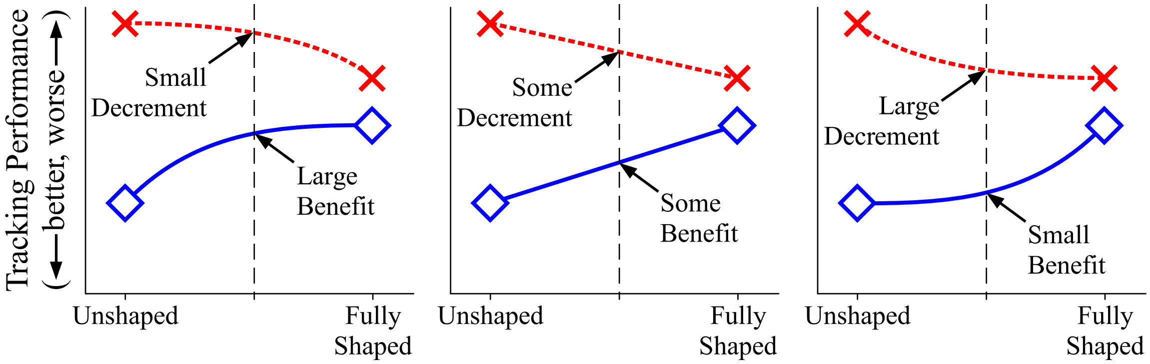

(a) Beneficial (b) Neutral (c) Detrimental

Figure 58: Hypothetical curves between unshaped and input-shaped performance

shaper and no input shaper could be created, then the tracking performance would likely (but not necessarily) be between the performance at the two endpoints. Figure 58 shows a few possibilities for what the intermediate curves could resemble. If base-tracking performance degraded more gradually than load-tracking performance improved, as in Figure 58(a), then an intermediate impulse sequence (represented by the dashed line) could be extremely beneficial to the system's overall performance. The intermediate impulse sequence would be less useful if the curves were fairly linear like in Figure 58(b), or if base-tracking performance degraded more quickly than load-tracking performance improved, as in Figure 58(c).

The exact shapes of the curves in Figure 58 are unknown, and the shapes probably depend on the specific task and input shaper. This discussion was merely to make the point that an intermediate impulse sequence *could* be useful. One method for creating such an impulse sequence is as follows.

Consider an input shaper with n impulses. As required of any input shaper, the impulse amplitudes must sum to 1:

$$\sum[A_1\ A_2\ \cdots\ A_n] = 1. \tag{34}$$

The first impulse amplitude is increased by a chosen amount α, and all other impulses are unchanged:

$$\begin{bmatrix} A_i \\ t_i \end{bmatrix} = \begin{bmatrix} (A_1+\alpha) & A_2 & \dots & A_n \\ 0 & t_2 & \dots & t_n \end{bmatrix}. \tag{35}$$

The sum of amplitudes for the resulting impulse sequence is:

$$\begin{aligned} &\sum[(A_1+\alpha)\ A_2\ \cdots\ A_n] \\ &= \sum([A_1\ A_2\ \cdots\ A_n] + [\alpha\ 0\ \cdots\ 0]) \\ &= \sum[A_1\ A_2\ \cdots\ A_n] + \sum[\alpha\ 0\ \cdots\ 0] \\ &= 1+\alpha. \end{aligned} \tag{36}$$

The new input shaper must be scaled by this factor to maintain an impulse sum of 1. In matrix form, the resulting input shaper becomes:

$$\begin{bmatrix} A_i \\ t_i \end{bmatrix} = \begin{bmatrix} \frac{A_1+\alpha}{1+\alpha} & \frac{A_2}{1+\alpha} & \dots & \frac{A_n}{1+\alpha} \\ 0 & t_2 & \dots & t_n \end{bmatrix}. \tag{37}$$

For simplicity, the current demonstration assumes that the impulse times remain constant. As the value of α approaches ∞, the input shaper in (37) approaches a form that is equivalent to no input shaper:

$$\begin{bmatrix} A_i \\ t_i \end{bmatrix} = \begin{bmatrix} 1 & 0 & \dots & 0 \\ 0 & t_2 & \dots & t_n \end{bmatrix}. \tag{38}$$

This relationship makes no assumptions about the number of impulses or the amplitudes and time locations of the impulses (except that $t_1 = 0$). Therefore, the technique can be applied to any input shaper.

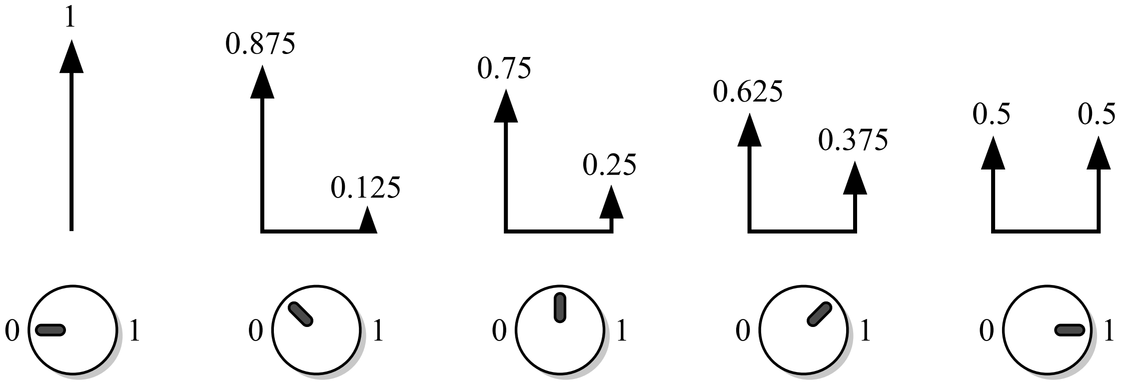

Figure 59: Adjusting the "strength" of a ZV input shaper

As α is increased, the shaped command becomes more similar to the unshaped command, and the input shaper loses some of its vibration-limiting effectiveness – residual vibration is allowed even at the modeled frequency. This technique will be referred to as *partial input shaping* because only part of the vibration is suppressed. This technique allows the "amount" of input shaping to be continuously varied. Human operators could use a simple input device (such as a dial in a helicopter cockpit) to adjust an input shaper between 0 (no input shaping) and 1 (full input shaping). This concept is illustrated in Figure 59. When the dial is turned to 0, input shaping is turned off. As the dial is turned toward 1, the second impulse of the input shaper increases in size and cancels more of the vibration caused by the first impulse. A normal ZV shaper results when the dial is turned to 1.

One way to choose the first-impulse weighting α in (37) is to pick a value that allows some amount of vibration, $V_{partial}$, at the modeled frequency. Figure 60 shows the sensitivity curve for a ZV shaper with several values of $V_{partial}$. An α value of 0.33 produces a partial ZV shaper that allows 25% vibration, and an α value of 1 produces a shaper that allows 50% vibration. For other input shapers, the α values that result in these levels of vibration will be different, in general.

Thus, there are two related values that can be used to specify a partial input shaper: first-impulse weighting, α, and allowed vibration, $V_{partial}$. The symbol $V_{partial}$

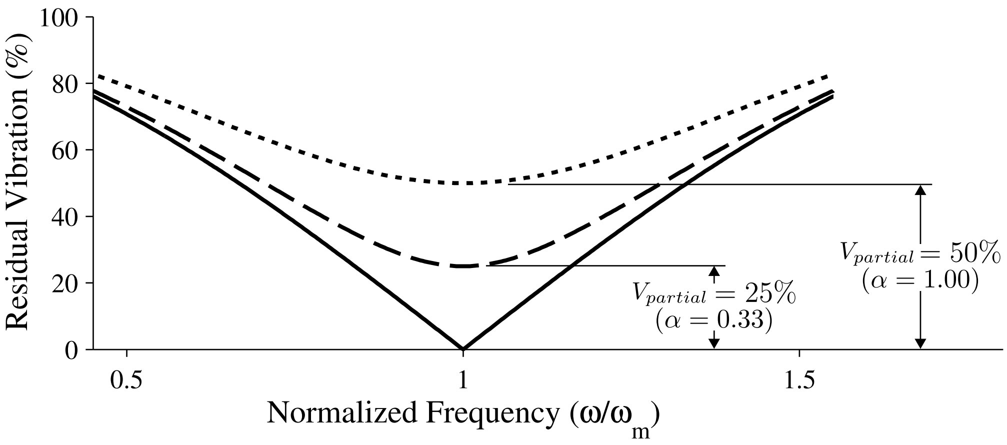

Figure 60: Sensitivity curve for partial ZV input shapers

is used to distinguish the vibration allowed for partial input shaping from V_{tol}, the tolerable vibration allowed for Extra-Insensitive input shapers. Specifying $V_{partial}$ is useful because it gives an intuitive measure of how much vibration is allowed, regardless of the type of input shaper. The $V_{partial}$ method becomes less reliable with some input shapers when damping is significant because the sensitivity curve shapes become less regular.

An alternative method is to simply specify the value of the first-impulse weight α. The input shaper is unchanged when α is zero, and approaches an unshaped impulse sequence when α gets large relative to 1. A value of $\alpha = 10$ produces a practically unshaped command for normal input shapers.

4.3 Tracking Study # 3: Shaper-Validation Experiment[1]

This section presents a follow-up study to test the effectiveness of the new input shapers compared to conventional ones. There were several differences between this experiment and the previous two experiments:

1. Input shapers were designed with and without 10% error in the estimated natural frequency to test how tracking performance with each input shaper would be affected by modeling error.

2. Two display types were tested for load control – one display fixed the viewpoint to the load, and the other fixed the viewpoint to the base. Controlling the load with a base-fixed display corresponds to a helicopter pilot looking down at the load from the helicopter cockpit.

3. Operators were given a specific mechanical system to envision controlling.

4. The experiment was designed to resemble a video game – it had a storyline, background music, and a more detailed graphical design than previous experiments. This was an effective way to keep the volunteer operators' attention over the 1.25-hour-long experiment.

5. Between 2 and 4 operators were tested simultaneously to improve the consistency of instructions and testing conditions.

6. Each operator only controlled one type of element for the entire experiment: either the driven base or the flexible load.

Results compare tracking performance, Cooper-Harper rating, and Crossover model parameters for 12 different input-shaping conditions with and without modeling error.

---

[1] Dr. Charles Ume provided the lab space and computers used for this experiment.

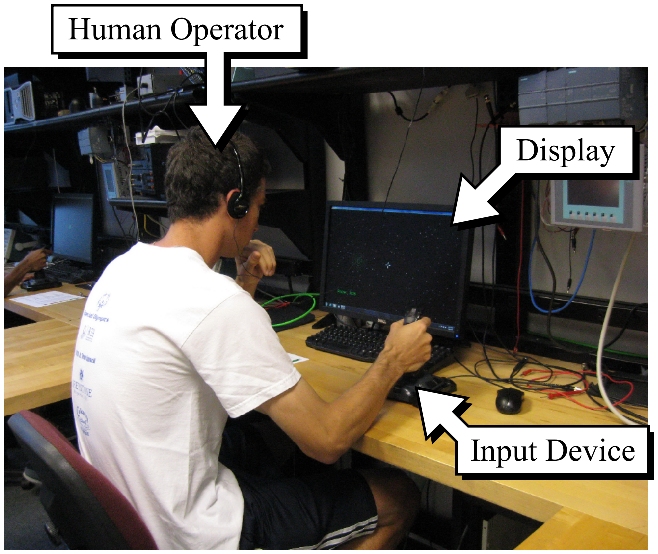

Figure 61: Experimental setup for Shaper-Validation experiment

4.3.1 Participants & Procedure

The tracking experiment was administered to a total of 39 novice participants: 13 participants (10 male and 3 female) controlled the driven base, 13 participants (10 male and 3 female) controlled the load with a load-fixed display, and 13 participants (10 male and 3 female) controlled the load with a base-fixed display. A room with multiple computers was used to test between 2 and 4 operators at the same time. The verbal instructions and testing conditions were exactly the same for operators testing at the same time, which should reduce experimental variability resulting from those factors.

Each participant signed a consent form describing the risks and rewards involved in the experiment. Figure 61 shows a photo of the experimental setup. Subjects viewed a pursuit display which occupied around 10° visual angle, and they generated control inputs with a *Logitech Attack 3* spring-centered joystick, described in the Two-Frequency experiment of Section 3.1.

An introduction explained that the operator would be controlling futuristic laser

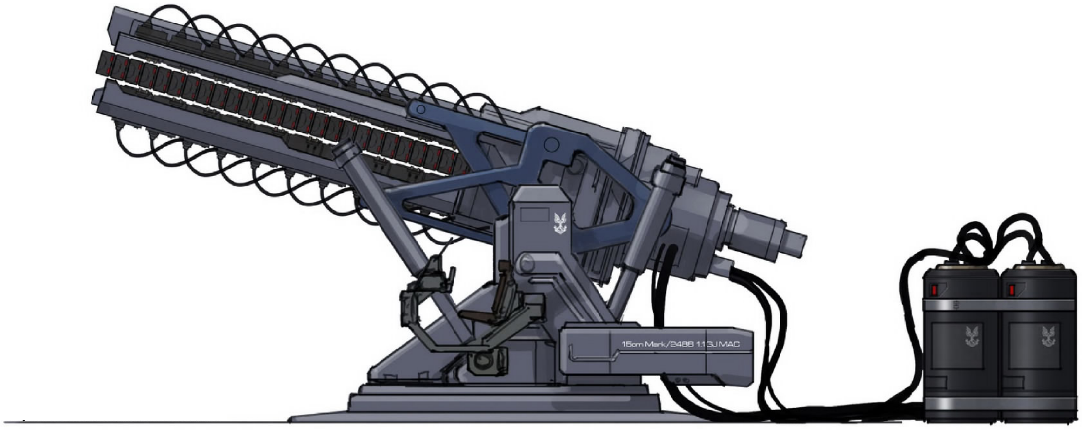

Figure 62: Laser cannon shown to operators in Shaper-Validation experiment

cannons like the one shown in Figure 62[2]. Operators used their joystick to swivel the cannon left and right, with the goal of shooting an object coming toward the Earth. Many cannons would be tested, and "unfortunately," some cannons had dynamic problems such as time delays and flexibility between the base and cannon motion, and were less suitable for the task of shooting the object. The operator's job was to determine which cannons would be best to choose for shooting the object and saving the Earth.

This framework was used to explain the correct interpretation of the Cooper-Harper rating scale, shown in Figure 63. Cannons should be rated highly (1 to 3) if operators could use it to perform the shooting task well without much mental effort, moderately (4 to 6) if adequate performance required moderate to intense concentration, and poorly (7 or more) if adequate performance was not attainable even with full concentration. Ratings of 8, 9, and 10 indicate increasing amounts of concentration required for maintaining basic control over the cannon.

Two practice trials showed the operator how easy and how hard the control task

---

[2] "Mac Cannon" by Isaac Hannaford. Accessed online, Jan. 2013, <www.isaachannaford.com>

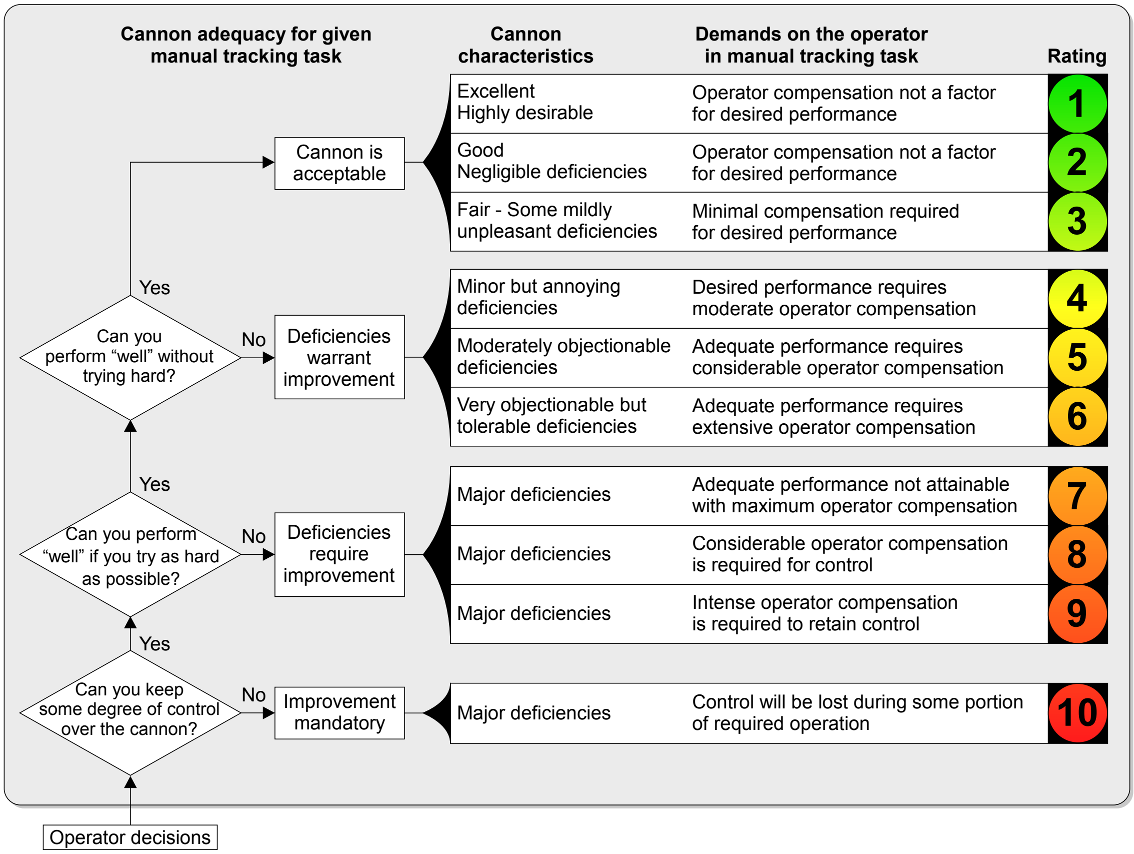

Figure 63: Modified Cooper-Harper rating scale for Shaper-Validation experiment

could be. An extremely easy trial (unshaped driven element) was used to demonstrate an element that should be rated 1 or 2 on the Cooper-Harper scale, and an extremely hard trial (unshaped flexible element) demonstrated an undesirable element that should be rated around 8 or 9. Operators were not informed which controlled elements were used as the "easy" and "hard" elements.

A set of 24 trials was performed. To reduce fatigue, subjects were given a mandatory 1-minute break after every 5 trials. Each trial lasted 115 seconds. The first 15-second period allowed the subject to get accustomed to the controlled-element dynamics, and only the final 100 seconds of the trial were analyzed. After each trial, the user was asked to assign a rating from the Cooper-Harper scale.

4.3.2 Tracking Trials

Operators controlled the translating base with the suspended load shown previously in the Shaper-Correlation experiment (Figure 39 and dynamic Equation (25)). The load swing had a natural frequency of 1.256 rad/s and a damping ratio of 0.1. The cart had a first-order velocity response to joystick input with a time constant of 1 sec and a maximum velocity of 13.28 deg/s. All trials used a load-mass ratio of 0.33.

The three displays used in this experiment are shown in Figure 64. The base control in Figure 64(a) and load control with load-fixed display in Figure 64(b) keep the cursor centered on the screen, and show background information (represented by motion of the hatch lines) along with the target position.

The load control with base-fixed display in Figure 64(c) has a viewpoint fixed to the base position, and the cursor oscillates about the center of the screen. This is meant to mimic the view of a helicopter pilot (or a crane operator sitting in the

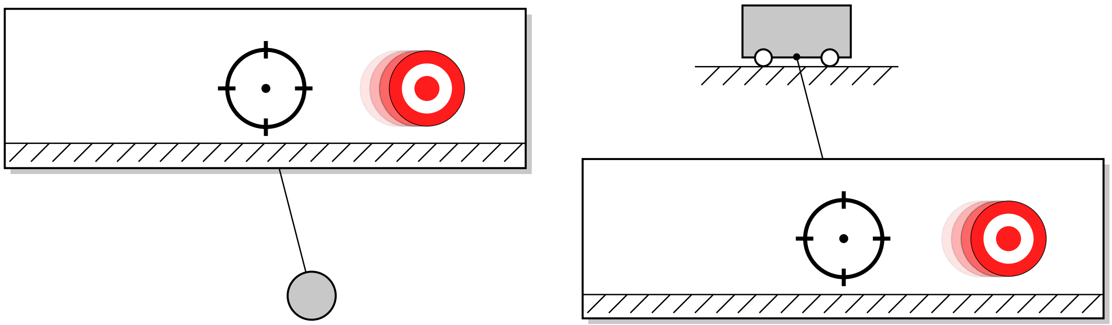

(a) Base control

(b) Load control; load-fixed display

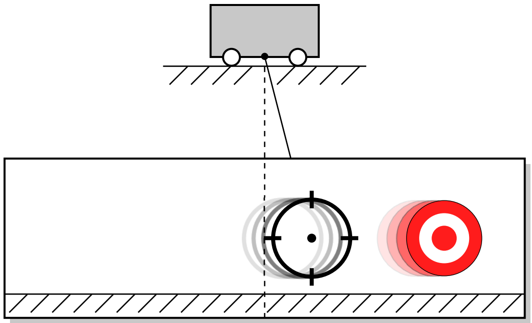

(c) Load control; base-fixed display

Figure 64: Displays for Shaper-Validation experiment

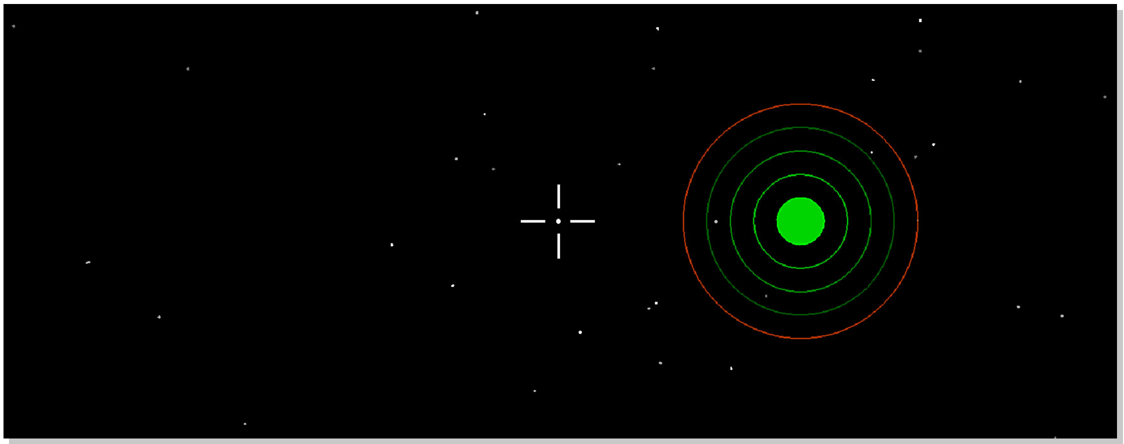

Figure 65: Visual appearance of Shaper-Validation experimental trial

crane's trolley) looking downward at the load.

The diagrams in Figure 64 show the information presented to the operator, but not how this information is presented graphically. Figure 65 shows the graphical appearance of the tracking task. The target moved unpredictably left and right, and background information was provided by the stars. Recall that the operators were aiming cannons to shoot an object in the sky.

The forcing function used in the Shaper-Correlation experiment (Table 4) was used for this experiment. Once again, only functions with maximum excursions, maximum velocities, and maximum accelerations falling within certain bounds were used.

4.3.3 Input Shapers

A total of 12 input shapers were tested. Each shaper was designed either for the correct swinging frequency and damping ratio, or with 10% modeling error in the estimated swing frequency. Specifically, the load swing frequency was held constant at 1.256 rad/s, but the input shaper was designed for a frequency of 1.396 rad/s. The residual vibration effects of this modeling error can be analyzed with the sensitivity curves in Figure 66.

Figure 66(a) shows sensitivity curves for the zero-vibration input shapers used in the experiment. When the shapers are designed for the incorrect frequency, they allow

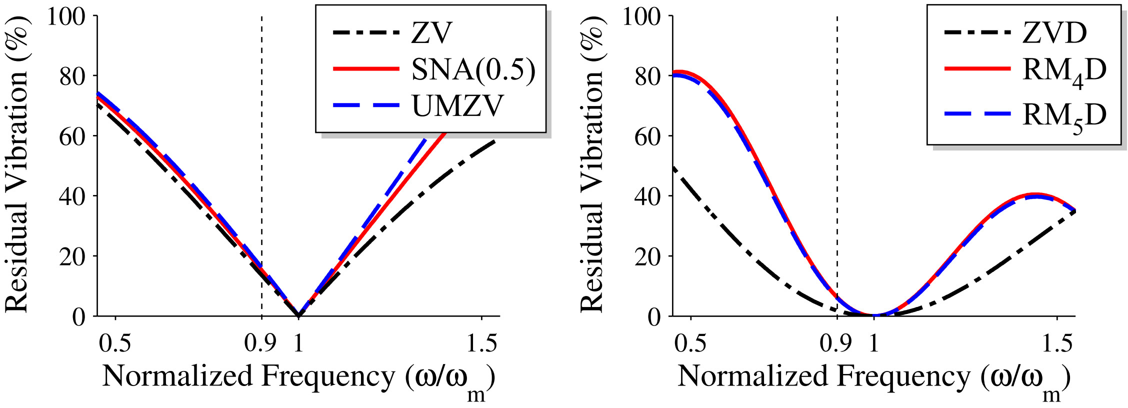

(a) Zero-vibration input shapers

(b) Robust input shapers

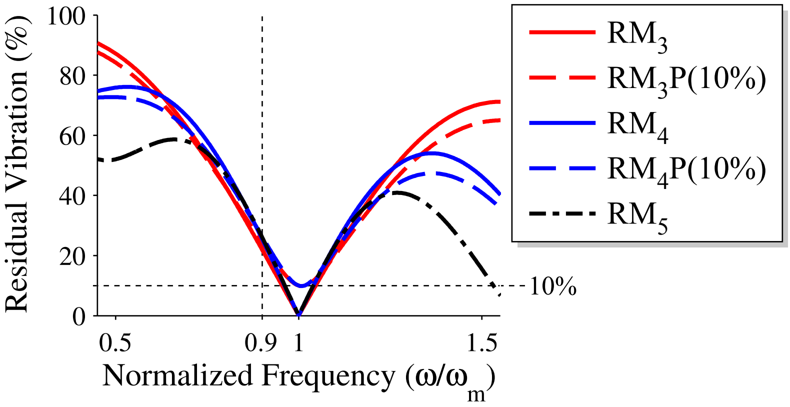

(c) Reduced-modification input shapers

Figure 66: Sensitivity curves for input shapers in Shaper-Validation experiment

around 13.5% residual vibration compared to an unshaped command. The robust input shapers in Figure 66(b) only allow between 1.8% (ZVD) and 6.1% ($\mathrm{RM}_4\mathrm{D}$) vibration. The reduced-modification shapers in Figure 66(c) are the least robust, and allow between 21.9% (RM_3) and 26.1% (RM_5) vibration. These shapers are designed to facilitate control of the driven base, but they do not have ideal properties for controlling the flexible load. Tracking performance may decline when error is added to the modeled frequency.

Figure 66(c) shows both the full and partial input shapers. Note that even though there is a 10% difference in residual vibration at the modeled frequency, the difference away from the modeled frequency is small.

4.3.4 Results

4.3.4.1 Tracking Performance

Figure 67 shows the RMS tracking error results for controlling the driven base. The error bars show one standard deviation above and below the mean. Two immediately noticeable results are that the robust input shapers (RM_4D, RM_5D, and ZVD) performed poorly, and the non-robust RM input shapers performed better than conventional input shapers. As expected, the unshaped case showed the smallest tracking error. The addition of modeling error in ω_m slightly increased the mean tracking error for most input shapers.

Results for load control with a load-fixed display are given in Figure 68. The worst cases were the unshaped and RM_5 input shaper with modeling error. The 3 and 4-impulse RM input shapers had lower tracking error than the unshaped case, but not as low as the conventional input shapers. For most input shapers, adding modeling error increased the standard deviation and slightly increased the mean error.

Figure 69 shows results for controlling the flexible load with a base-fixed display. Most of the trends are similar to results from the load-fixed display. The RM input shapers performed better than the unshaped case, and not as well as the ZV, SNA,

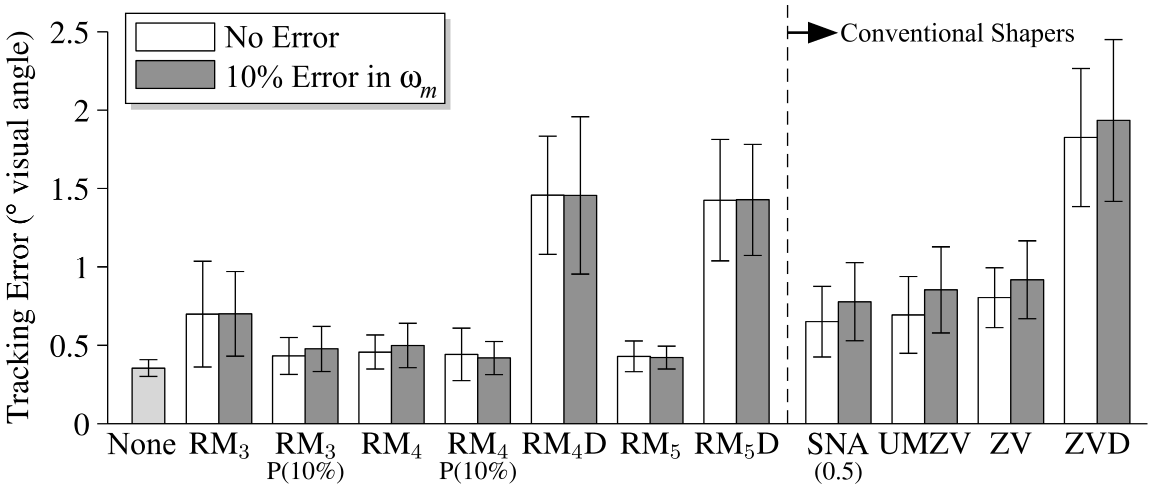

Figure 67: Tracking error for base control (mean ± SD)

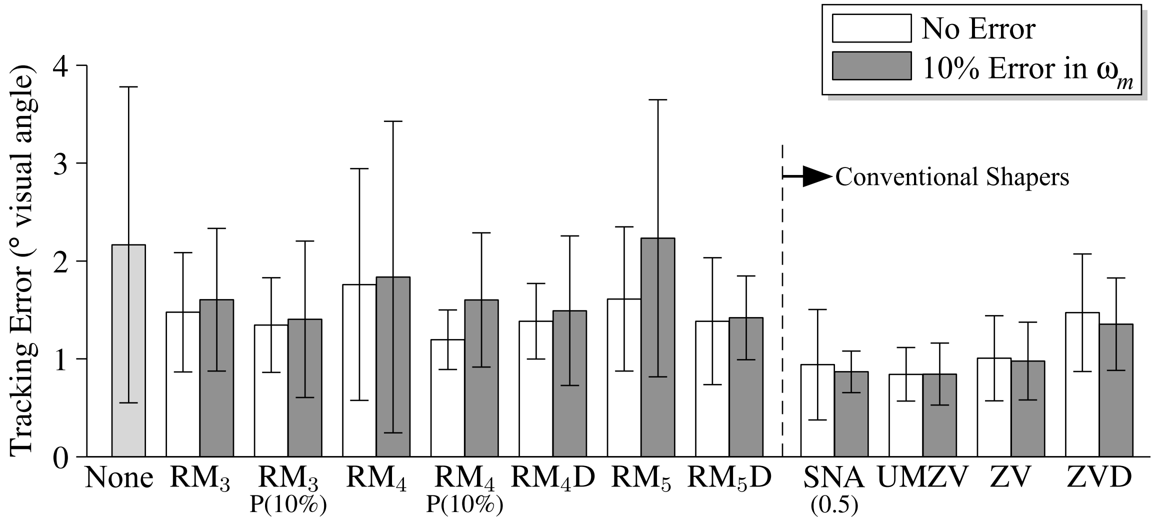

Figure 68: Tracking error for load control with load-fixed display (mean ± SD)

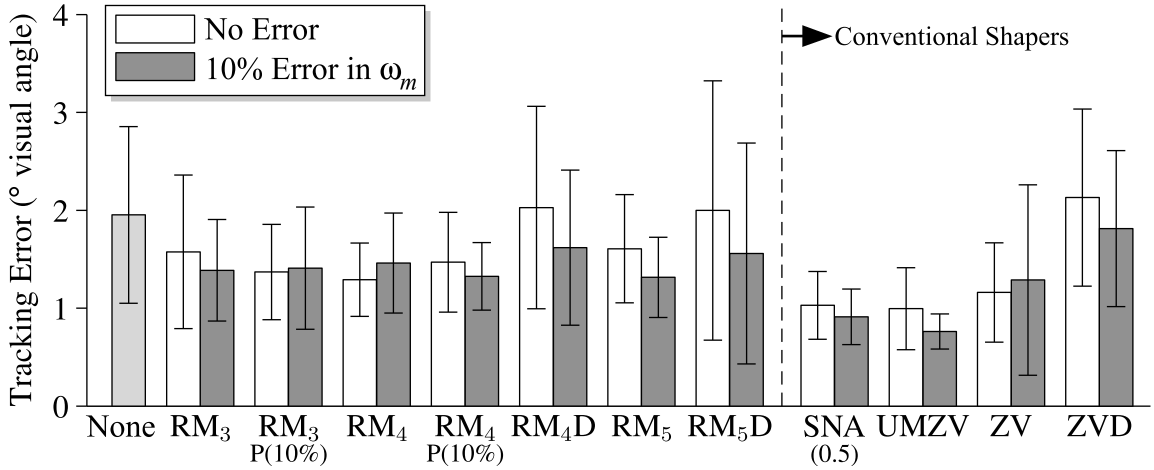

Figure 69: Tracking error for load control with base-fixed display (mean ± SD)

and UMZV shapers. It appears that time lag might have been more detrimental with this type of display than with the load-fixed display: the long-duration robust input shapers performed worse than did the oscillatory unshaped and RM_5 cases. This is in contrast to the load-fixed display, where the robust input shapers outperformed the RM_4 and RM_5 input shapers.

A surprising result is the improved performance of a few of the input shapers with modeling error compared to the perfectly designed input shapers. The input shapers with modeling error were shorter in duration because the estimated natural frequency was faster than the real frequency. The improvement in tracking performance with modeling error indicates that when operators controlled the load using the base-fixed display, the benefit of a slightly shorter input shaper partly offsets the extra vibration due to the modeling error. This was not the case for the other two displays, where modeling error tended to degrade performance.

4.3.4.2 Subjective Rating

Figure 70 shows the Cooper-Harper ratings for controlling the driven base. The unshaped case was rated the most desirable, and the three robust input shapers were the least desirable. The non-robust RM input shapers were rated as good or better than the conventional shapers. The SNA input shaper was the best conventional shaper, and it was approximately as good as the 3-impulse RM shaper.

Figure 71 shows the ratings for load control with a load-fixed display. The best-rated input shapers were the ZV, SNA, and UMZV shapers. The robust RM shapers were somewhat better than the ZVD shaper. As usual, the unshaped case had the worst rating, followed closely by the RM_5 input shaper. The median rating did not show consistent increasing or decreasing rating trends when error was added to the modeled ω_n.

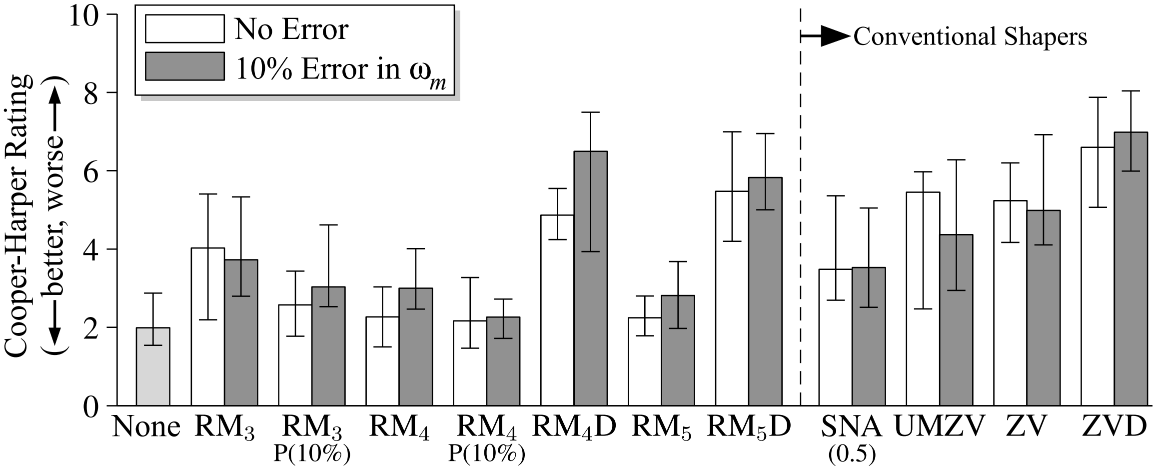

Figure 70: Rating for base control (median with 95% CI)

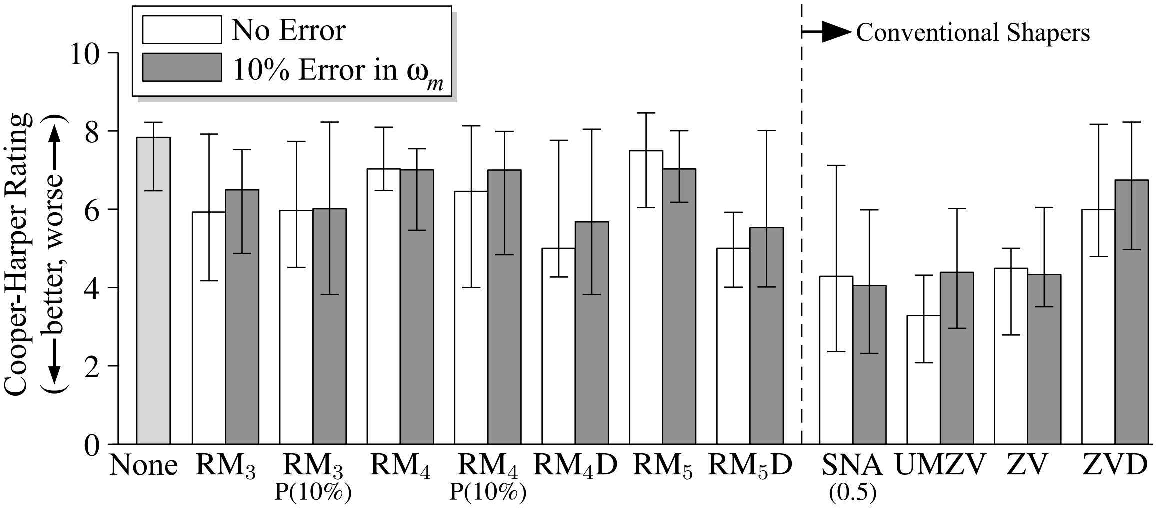

Figure 71: Rating for load control with load-fixed display (median with 95% CI)

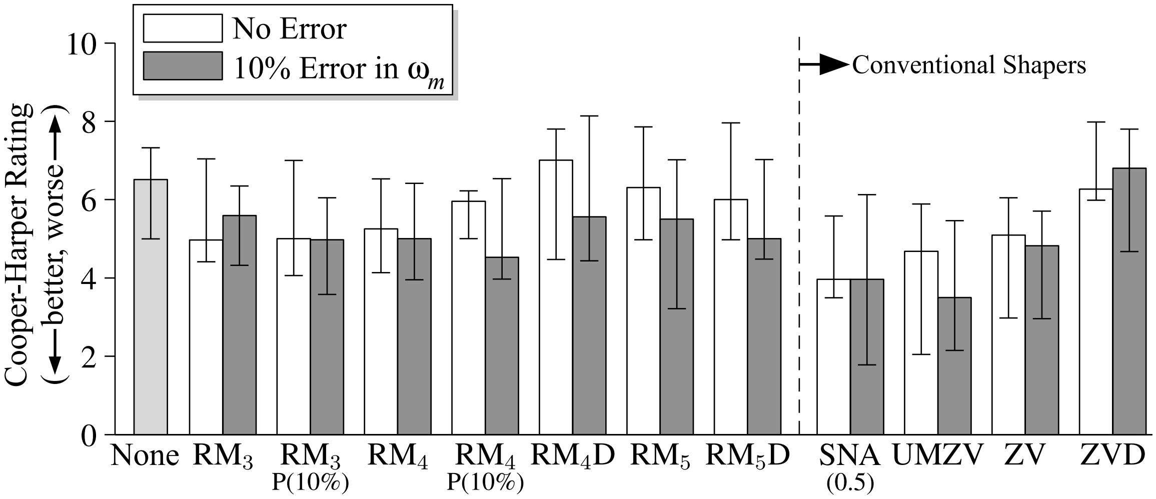

Figure 72: Rating for load control with base-fixed display (median with 95% CI)

Figure 72 gives rating results for load control with a base-fixed display. The robust input shapers were rated similarly to the unshaped case. The SNA and UMZV input shapers were rated the best, followed by the ZV and non-robust RM shapers. There was not a consistent trend with modeling error – a few input shaping cases with modeling error were rated better than the perfectly designed shapers, and a few were rated more poorly with the error.

4.3.4.3 Control Behavior

For each input shaper, mean and standard deviation values of K, τ, ϕ_m, and $\%_{fit}$ were calculated. Only results for the perfectly designed input shapers are given because trends for the input shapers with modeling error were similar.

Table 9 shows Crossover model parameters for base control. The unshaped case had the lowest effective delay, highest phase margin, and highest fit percentage with the lowest standard deviation. The next best systems were produced by the $\text{RM}_4\text{P}(10\%)$, and RM_4, and RM_5 input shapers. The ZVD shaper had the lowest fit percentage and crossover frequency (gain K). The partial input shapers showed higher average fit percentages and lower effective time delays than their fully shaped versions (RM_3 and RM_4).

Table 10 shows the Crossover model results for load control with the load-fixed display. All input shapers except for RM_5 (which is designed to be similar to no input shaping) increased the fit percent from the unshaped case. Once again, the Crossover model was more applicable to the input-shaped systems. The ZVD shaper had the largest fit percentage, but a large effective delay and low phase margin, indicating poor system performance. This is verified by the rating and tracking error results.

Table 9: Crossover model parameters for base control [mean (SD)]

	K (rad/s)	τ (sec)	ϕ_m (deg)	$\%_{fit}$
Unshaped	0.96 (0.37)	0.56 (0.38)	60.15 (20.03)	85.30 (3.41)
RM_3	0.90 (0.18)	1.15 (0.43)	32.14 (23.21)	78.15 (6.18)
$\text{RM}_3\text{P}(10\%)$	0.87 (0.50)	0.73 (0.59)	19.58 (57.94)	81.79 (6.67)
RM_4	1.04 (0.38)	0.74 (0.30)	49.87 (15.00)	79.90 (6.61)
$\text{RM}_4\text{P}(10\%)$	1.01 (0.37)	0.69 (0.35)	50.42 (24.92)	82.02 (5.91)
RM_4D	0.81 (0.20)	1.61 (0.16)	15.23 (19.88)	78.69 (5.93)
RM_5	0.85 (0.34)	0.70 (0.49)	39.27 (45.30)	81.60 (6.53)
RM_5D	0.94 (0.16)	1.55 (0.12)	5.90 (17.41)	77.33 (4.98)
SNA(0.5)	0.79 (0.17)	1.56 (0.34)	19.79 (20.07)	78.75 (7.10)
UMZV	0.74 (0.28)	1.52 (0.48)	5.80 (33.48)	78.03 (6.12)
ZV	0.84 (0.16)	1.63 (0.24)	11.91 (17.51)	80.68 (5.85)
ZVD	0.65 (0.14)	1.60 (0.24)	29.53 (16.38)	69.82 (13.49)

Table 10: Parameters for load control with load-fixed display [mean (SD)]

	K (rad/s)	τ (sec)	ϕ_m (deg)	$\%_{fit}$
Unshaped	0.82 (0.46)	1.24 (0.42)	15.53 (39.03)	71.52 (14.29)
RM_3	0.58 (0.38)	1.43 (0.72)	23.33 (55.03)	72.11 (14.03)
$RM_3P(10\%)$	0.63 (0.37)	1.31 (0.51)	27.30 (39.31)	75.87 (10.85)
RM_4	0.77 (0.42)	1.19 (0.44)	20.24 (41.93)	73.87 (17.72)
$RM_4P(10\%)$	0.55 (0.44)	1.19 (0.56)	19.54 (54.45)	76.79 (12.11)
RM_4D	0.56 (0.37)	1.49 (0.80)	6.82 (49.44)	79.14 (7.58)
RM_5	0.78 (0.37)	1.51 (0.75)	28.83 (26.18)	71.19 (11.42)
RM_5D	0.70 (0.33)	1.41 (0.49)	15.06 (39.75)	77.57 (9.00)
SNA(0.5)	0.65 (0.26)	1.78 (0.99)	34.95 (22.71)	80.90 (11.97)
UMZV	0.82 (0.41)	1.47 (0.48)	24.14 (38.44)	84.24 (7.24)
ZV	0.65 (0.24)	2.01 (1.20)	23.76 (23.99)	85.17 (9.71)
ZVD	0.63 (0.23)	2.32 (1.07)	12.83 (25.54)	86.26 (7.62)

Table 11: Parameters for load control with base-fixed display [mean (SD)]

	K (rad/s)	τ (sec)	ϕ_m (deg)	$\%_{fit}$
Unshaped	0.98 (0.40)	1.49 (1.25)	26.99 (23.70)	74.56 (8.37)
RM_3	0.75 (0.28)	1.39 (0.21)	31.93 (19.01)	76.66 (11.38)
$RM_3P(10\%)$	0.94 (0.29)	1.36 (0.22)	16.10 (28.14)	77.37 (9.11)
RM_4	0.78 (0.23)	1.36 (0.27)	28.42 (23.51)	76.26 (7.75)
$RM_4P(10\%)$	0.88 (0.49)	1.18 (0.41)	11.73 (41.84)	72.72 (6.79)
RM_4D	0.82 (0.22)	1.57 (0.15)	16.84 (17.64)	77.86 (7.89)
RM_5	0.86 (0.38)	1.12 (0.36)	16.30 (35.88)	75.17 (7.05)
RM_5D	0.92 (0.31)	1.56 (0.40)	8.82 (26.14)	81.84 (6.40)
SNA(0.5)	0.70 (0.26)	1.26 (0.20)	38.62 (22.58)	77.22 (10.13)
UMZV	0.73 (0.30)	1.16 (0.23)	40.28 (24.57)	82.21 (7.18)
ZV	0.68 (0.33)	1.75 (0.80)	15.2 (42.13)	80.27 (6.92)
ZVD	0.57 (0.19)	1.89 (0.52)	29.25 (20.33)	79.11 (10.03)

High fit percentages and high phase margins were produced by the SNA and UMZV input shapers.

Table 11 shows results for load control with a base-fixed display. All input shapers except for $RM_4P(10\%)$ produced better fits to the crossover model than did the unshaped case. Robust input shapers had the largest effective delays. The UMZV shaper produced the largest phase margin and highest fit percentage. Desirable system characteristics were also produced by the SNA, RM_3, and RM_4 input shapers.

4.3.4.4 Load Oscillation when Controlling the Driven Base

When operators controlled the base, their only goal was to follow the target as closely as possible, and the flexible load may have been oscillating excessively. This would correspond to a tanker truck's liquid sloshing or a helicopter's suspended load swinging with large amplitude while the driver or pilot focused on controlling the vehicle. One desirable effect of input shaping would be to keep the system vibration at a low amplitude even if the human operator's concentration was elsewhere.

Figure 73 shows the root-mean-squared load deflection during the base-control trials. It is clear that the UMZV and SNA input shapers were effective at minimizing the load deflection. The ZVD and ZV shapers were less effective, but they still produced mean deflections that were lower than deflection in the unshaped trial.

An unexpected result was that a few of the RM-input-shaped trials (especially the RM$_3$, RM$_4$D, and RM$_5$D trials) had more load swing than the unshaped trial. The poor performance of the RM shapers seems to be related to the amount of operator control input during the trial. Figure 74 compares the control input during each of the RM-shaper trials to the corresponding load deflections from Figure 73. The trials with more control input had more load swing. The correlation is significant

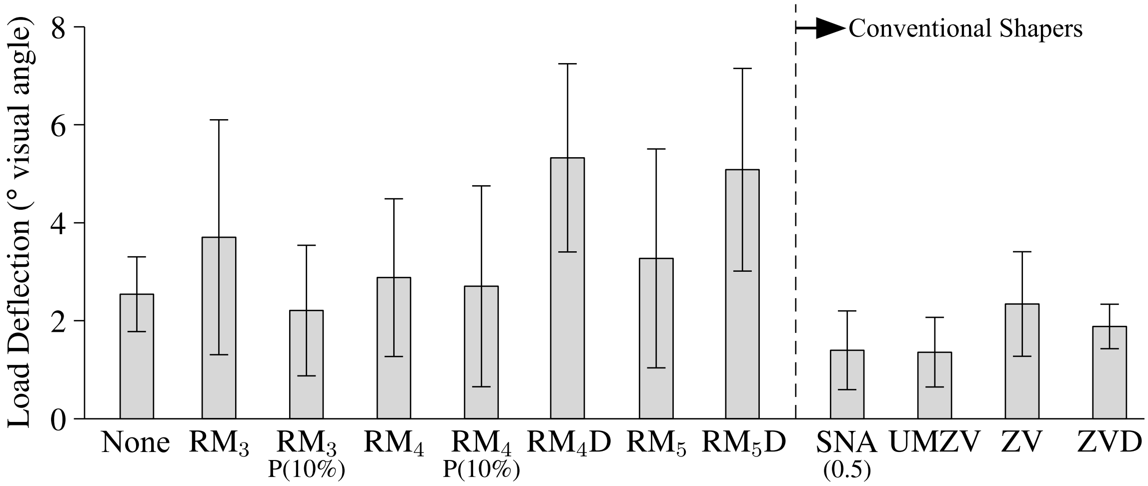

Figure 73: Load swing during base-control trials (mean ± SD)

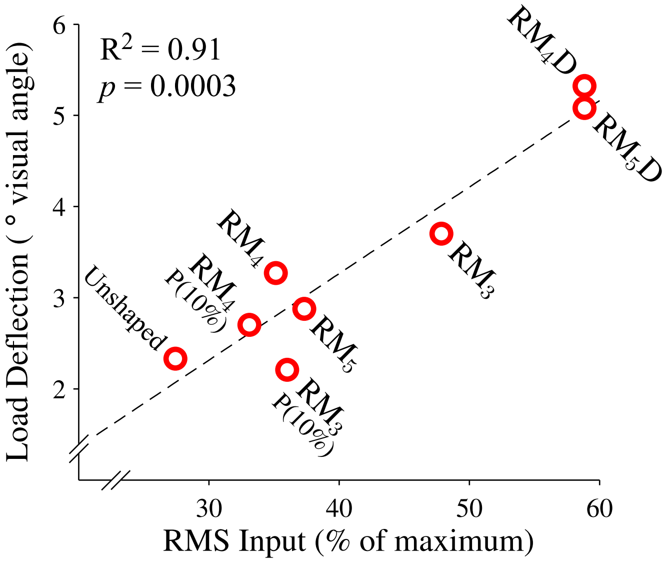

Figure 74: Load swing vs. control input during base-control trials

($p = 0.0003$), and the R^2 value is 0.91.

As shown in Figure 74, operators used less input for the unshaped trial than for any of the RM-shaped trials. The RM shapers made the base somewhat harder to control, so operators had to use more corrective input, and the base did not stay as close to the target position in general (see tracking error results in Figure 67). The base's movements about the target were larger, which excited more payload swing. The RM input shapers allow transient oscillation, and this oscillation did not get cancelled out fast enough relative to the time scale of the tracking task.

4.3.5 Correlations

The operators' aggregate tracking error and subjective ratings are compared in Figure 75. Just like in the Shaper-Correlation experiment, there is a strong log-linear correlation with an R^2 value of 0.829, and an extremely high probability of a nonzero correlation (indicated by a p-value of < 0.0001). The curve's equation is:

$$r_{CH} = 4.6244\ ln(e_{RMS}) + 3.0679, \tag{39}$$

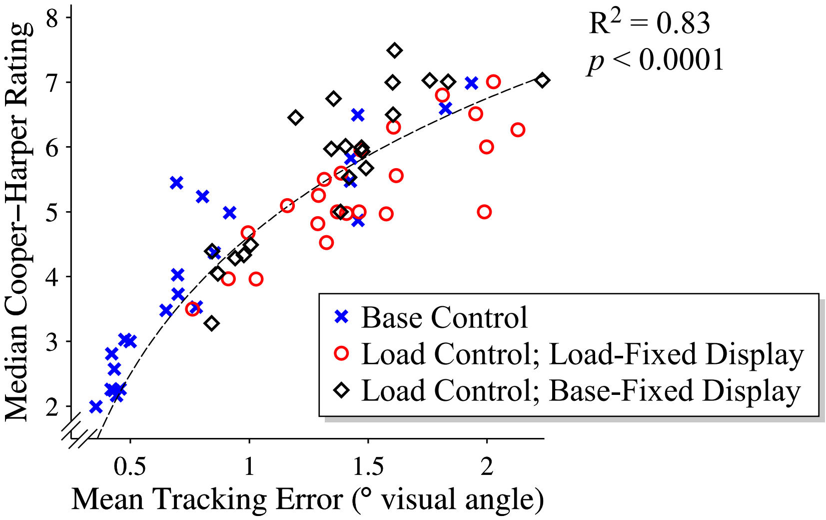

Figure 75: Performance vs. subjective rating for Shaper-Validation experiment

where r_{CH} is Cooper-Harper rating and e_{RMS} is root-mean-squared tracking error. Confirming this relationship between quantitative and qualitative results is a way to ensure that operators were basing their ratings partly on tracking performance. The other major component of the Cooper-Harper rating should be the mental effort required to achieve the trial performance.

Crossover model fit and phase margin are compared to log-transformed tracking error in Figure 76, and to Cooper-Harper rating in Figure 77. These plots do not include data from the load control with base-fixed display trials.

The Crossover model parameters were better correlated with tracking error than with Cooper-Harper rating. The strongest relationship was between tracking error and fit percentage, with an R^2 value of 0.45. This is shown in Figure 76(a). The weakest relationship was between Cooper-Harper rating and phase margin in Figure 77(b). The p value was 0.04, and the R^2 value was under 0.1.

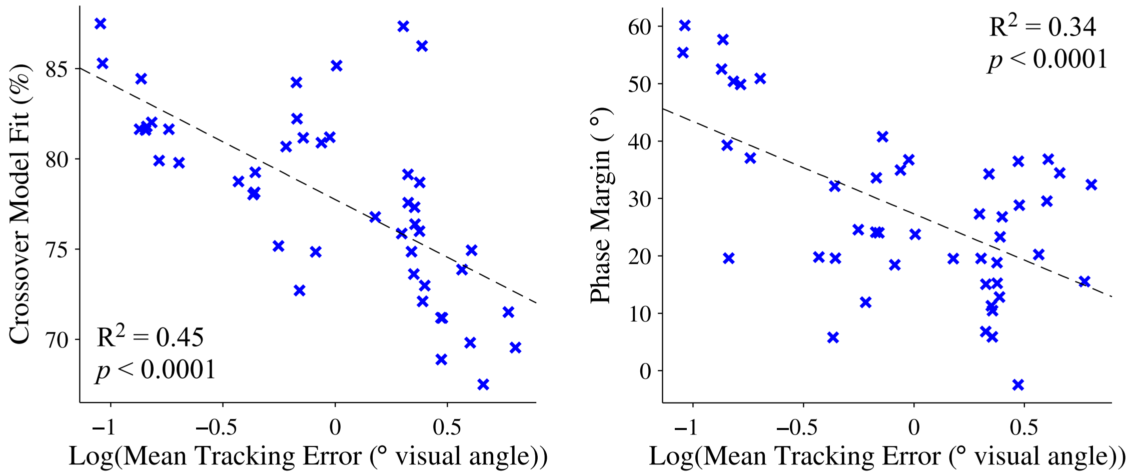

(a) Fit to Crossover model (b) Phase margin

Figure 76: Tracking error vs. Crossover model parameters

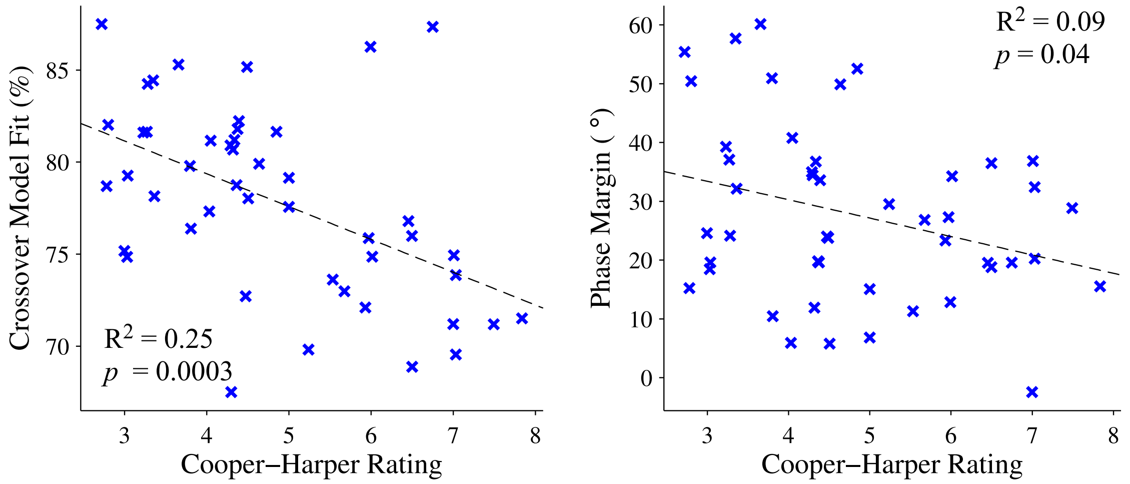

(a) Fit to Crossover model (b) Phase margin

Figure 77: Subjective rating vs. Crossover model parameters

4.3.6 Discussion

Robust input shapers performed poorly relative to non-robust shapers, even when there was 10% modeling error in the estimated swing frequency. This indicates that for these manual tracking tasks, long time delays in the input shaper were more detrimental to performance than allowing some vibration.

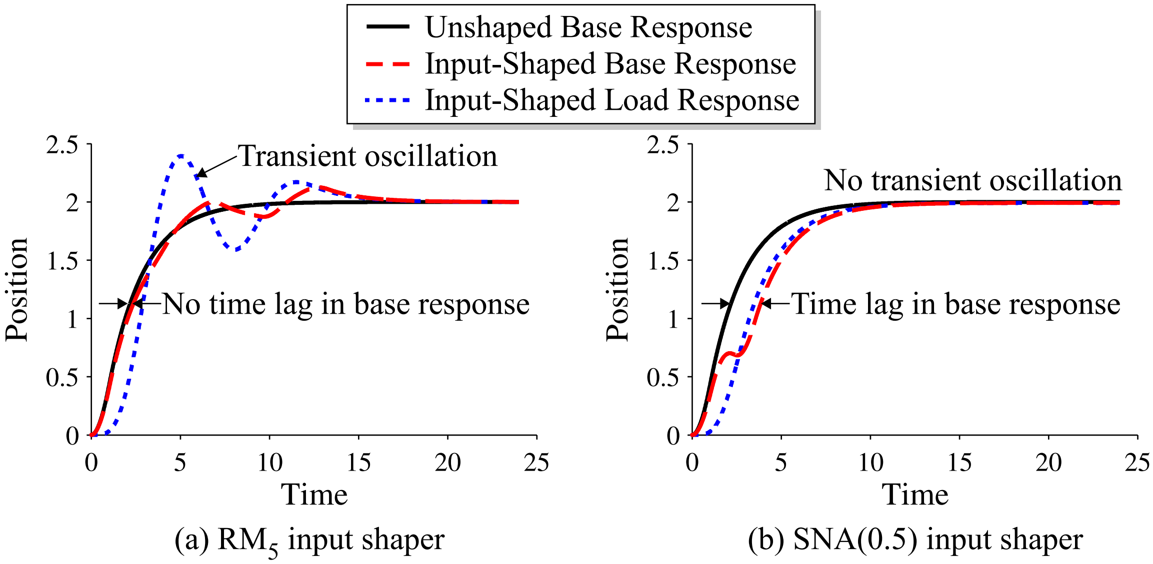

(a) RM_5 input shaper (b) SNA(0.5) input shaper

Figure 78: Base and load responses to input-shaped pulse command

In general, the RM shapers were better than conventional input shapers for controlling the driven base, and the non-robust conventional shapers were better for controlling the flexible load. This same result was found in the Shaper-Correlation experiment. A likely explanation is illustrated in Figure 78. The RM-shaped response in Figure 78(a) allows transient load oscillation but does not lag behind the unshaped response, while the SNA-shaped response in Figure 78(b) lags behind the unshaped response but suppresses all load oscillation.

The SNA and UMZV shapers reduced swing of the suspended load while operators controlled the driven base. RM input shapers were not effective at reducing load swing, and a few of the RM shapers actually increased the swing. It should be noted that the manual tracking tasks considered here are categorically different from discrete point-to-point tasks, where there is enough time for transient swing to be eliminated after a movement is complete. In these tracking tasks, commands change rapidly, and at least some transient swing is present for the whole trial. The ideal input shaper may differ depending on the kind of trial being performed. Input shapers that are best for manual tracking may not be the best for point-to-point tasks, and vice-versa.

4.4 Conclusions

Quantitative results from the Shaper-Correlation experiment were plotted against characteristics of the input shapers used, and a characteristic ($\int \epsilon^2 dt$) that correlated strongly with performance was identified. Input shapers designed by minimizing this characteristic are called *Reduced Modification* (RM) input shapers because their shaped command is as similar to the unshaped command as possible, in a least-squared-error sense. These input shapers cannot be used on systems that are driven near their control or actuator limits because they require a command of up to 125% of the original, unshaped command. If the unshaped command already requires 100% of the system's capabilities, the extra 25% of the input-shaped command will be clipped, and the input shaper will lose its effectiveness.

A second input shaping innovation was presented: a method for increasing the first impulse magnitude of an input shaper, which gives the current command more weight. Any input shaper can be adjusted between fully input shaped (the original input shaper) and unshaped (an impulse with magnitude 1 at time $t = 0$). This technique is called *partial input shaping* because only part of the residual vibration is eliminated by the modified input shaper. The resulting input-shaped command is more like an unshaped command, which experiments found to be ideal for controlling the driven base. Partial input shaping gives an operator more flexibility in dealing with the tradeoff between vibration suppression and control of the driven base.

An operator study investigated the effectiveness of these new input shapers. The tested robust input shapers performed relatively poorly, even when there was error in the modeled frequency. The RM shapers were best for controlling the driven base, and the SNA and UMZV shapers were best for controlling the flexible load, and greatly reduced load swing when operators controlled the driven base. Input shaping improved tracking performance, reduced subjective difficulty, and increased applicability of the Crossover model when operators controlled the flexible load.

CHAPTER V

TOUCHSCREENS AND TIME DELAYS: SPECIAL TOPICS FOR REMOTELY OPERATED MACHINES

Remotely operated machines are an important and growing class of human-controlled system. These systems may experience communication delays, and may be controlled using nontraditional input devices. Two manual tracking experiments are used to investigate these two factors. The first tracking experiment in Section 5.2 compares manual control with novel touchscreen input devices and a traditional spring-center joystick. The second experiment in Section 5.3 studies manual control of a flexible system with and without input shaping, with different amounts of time delay in the input channel.

5.1 Motivation

After the introduction of the iPhone in 2007, followed by the iPad in 2010, small touchscreen devices have become ubiquitous. These portable devices pack a large array of sensors into a small package. A growing number of applications (or "apps") allow the touchscreen devices to be used for a wide range of functions. A promising application is to use touchscreen devices as input devices for machine control.

Touchscreen interfaces have several advantages over traditional, hard-wired mechanical input devices: the functionality and layout of controls on the screen can be changed instantly without physical reconstruction costs; if one touchscreen input device is disabled, the control program can be quickly loaded onto another unit,

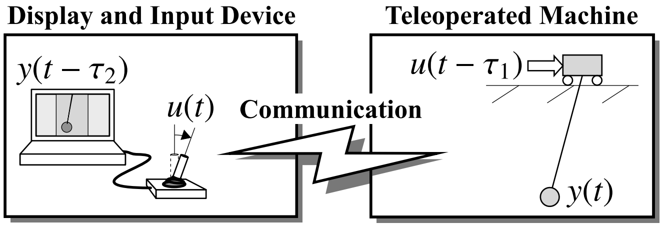

Figure 79: Time delay in a manual tracking task.

avoiding downtime of the controlled machine; the device's light weight and wireless signal transmission allow the operator to freely move around the workspace. Little research has studied the use of touchscreen input devices for controlling mechanical systems such as cranes and unmanned aerial vehicles.

Figure 79 depicts a teleoperated machine. The machine transmits video to the human operator, who uses an input device to send commands to the machine. There is a time delay, τ_1, between the time the command is issued and when it is executed. There may also be a delay, τ_2, between the video transmission and reception. This chapter will examine only delays in the command channel. Previous research has found that, as the time delay increases, tracking error and other performance measures degrade [2, 30]. Some examples of manually controlled systems which may contain both flexibility and time delays include remotely operated cranes, robotic arms, and unmanned aerial vehicles carrying suspended loads [52]. A list of investigations into the effects of time delay on manual tracking is given in [73]. It is unknown how time delays impact the effectiveness of input shaping for controlling a flexible system.

5.2 Tracking Study # 4: Touchscreen Experiment[1]

It is likely that touchscreens will become more popular as input devices for human-controlled machines. However, little work has examined the performance of touchscreen input devices relative to traditional devices.

---

[1] This section is based on work by Arto Kivila.

This section describes a manual tracking experiment that compares the quantitative and qualitative performance of several touchscreen-based interfaces to the performance of a traditional joystick. This experiment focuses only on input devices, and does not involve input shaping or controlled-element flexibility.

5.2.1 Participants & Procedure

Figure 80 shows the experimental setup. Operators viewed a computer display and performed a series of manual tracking tasks with either a joystick or a touchscreen interface. Each trial lasted 115 seconds. The first 15-second period allowed the operator to become familiar with the controlled-element dynamics. Only measurements from the final 100 seconds of the trial were analyzed.

The controlled-element transfer function between the operator's input caused a velocity response with a first order lag:

$$\frac{X(s)}{u(s)} = \frac{K}{s(s+1)}, \tag{40}$$

where the value of gain K was adjusted to allow the cursor's maximum velocity to match the maximum velocity of the reference input The display (base-fixed pursuit) is shown in Figure 81. Note that this experiment does not involve flexibility or input

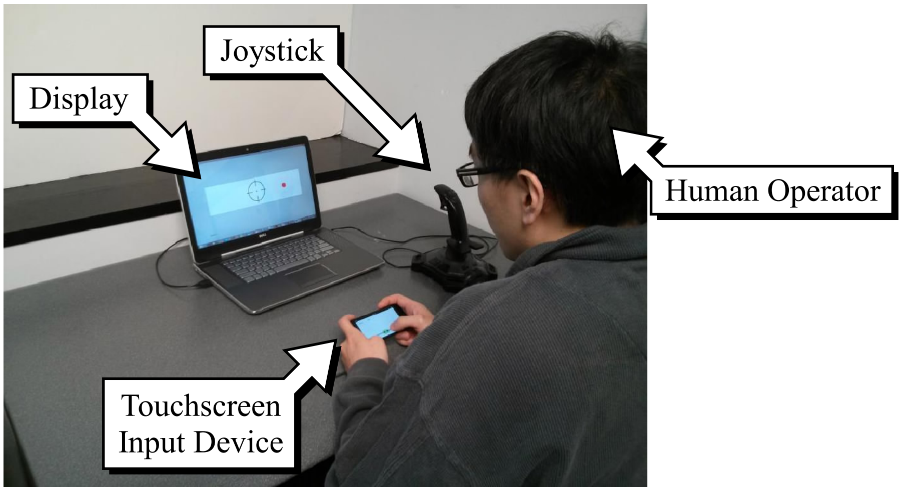

Figure 80: Experimental setup for Touchscreen experiment

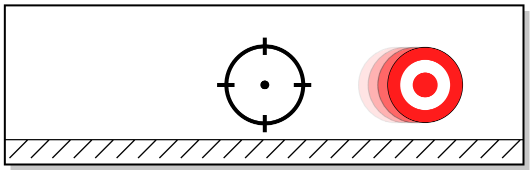

Figure 81: Display for Touchscreen experiment

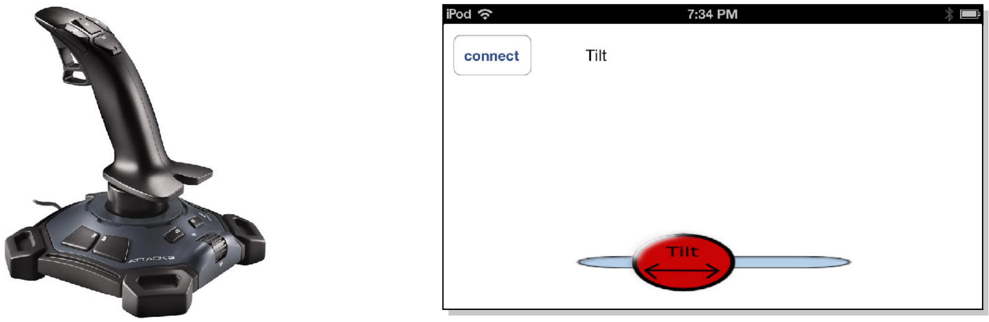

(a) Spring-centered joystick (b) Tilt touchscreen interface

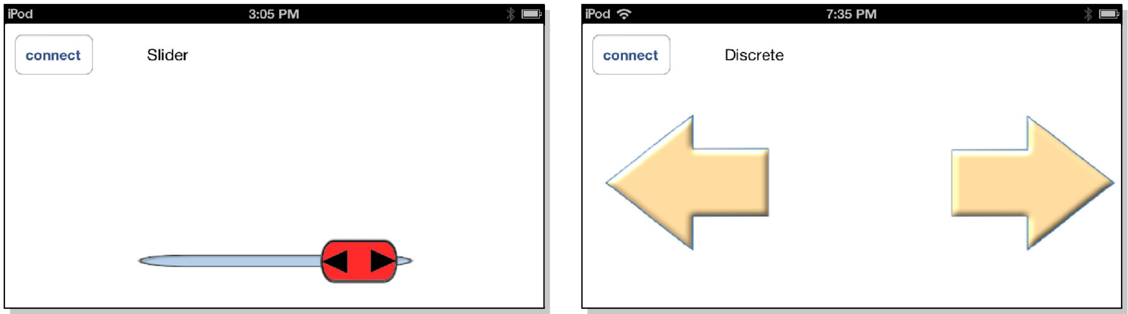

(c) Slider touchscreen interface (d) Buttons touchscreen interface

Figure 82: Command interfaces for Touchscreen experiment

shaping. Only differences between command interfaces are investigated.

The joystick and touchscreen interfaces can be see in Figure 82. The physical joystick shown in Figure 82(a) was a *Logitech Attack 3* described in the Two-Frequency experiment of Section 3.1. The three touchscreen interfaces were displayed on a 2^{nd}-generation iPod Touch with a 3" × 2" screen. The Tilt controller in Figure 82(b) uses the touchscreen device's physical tilt angle to determine a command. The maximum and minimum commands are reached when the device is tilted to ±50°.

The slider interface shown in Figure 82(c) works much like the joystick. The operator drags a finger left and right on the screen, and the finger position (relative to the center “zero” position) determines the command. The device plays a loud beeping sound and resets itself to the zero position when the operator releases the button.

The Discrete Buttons controller in Figure 82(d) sends the maximum positive or negative command when a button is pressed and a zero command when no button is pressed. The large buttons allowed the user to hold the touchscreen device in both hands, while using the left and right thumbs to give left and right commands without looking at the screen. The maximum command amplitudes for the joystick and touchscreen interfaces were all equal.

Table 12 shows the frequency content of the forcing function that drove the motion of the target. This is the same forcing function used for the Shaper-Correlation experiment in Chapter 3.

Operators performed one practice trial with each interface. They then performed two blocks of 4 trials (one with each interface) in random order. Before each trial, the display showed the name of the interface that would be used. After each trial, the operator answered a series of qualitative questions. Fourteen novice operators (4 female and 10 male) between the ages of 21 to 29 years participated. The experiment lasted a total of 30 minutes, and subjects were not paid for their participation.

Table 12: Forcing function for Touchscreen experiment

Wave Number, i	**Frequency**, ω_i (rad/s)	**Amplitude**, B_i (deg visual angle)
1	9.362	0.071
2	5.718	0.167
3	3.456	0.266
4	2.073	0.366
5	1.194	0.474
6	0.691	0.581
7	0.314	0.735
8	0.188	0.835
9	0.063	10.493

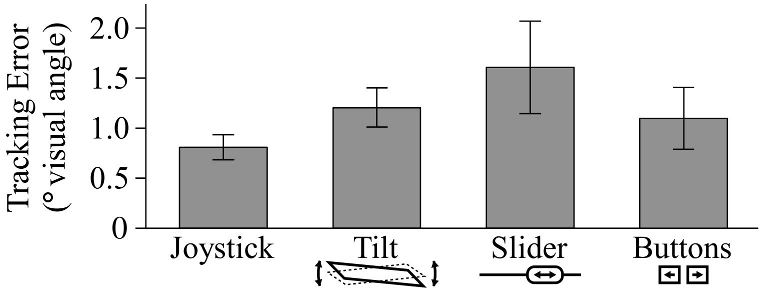

Figure 83: Tracking error for Touchscreen experiment (mean ± SD)

5.2.2 Results

5.2.2.1 Tracking Performance

Figure 83 shows the root-mean-squared tracking error results. The joystick performed the best, followed by the Discrete Buttons controller, the Tilt controller, and the Slider controller. The standard deviation was also largest for the Slider controller.

Two tests were used to determine statistical significance between the RMS tracking errors: a one-way analysis of variance (ANOVA) and Tukey's honestly significant difference test (HSD). It was found that only the difference between the Tilt controller and the Buttons controller is not statistically significant ($p = .058$). The other comparisons were far below the required p value at 95% confidence level.

5.2.2.2 Subjective Rating

Operators were asked to rate their preference for each interface compared to the joystick, and the results are given in Figure 84. Operators preferred the Tilt and Buttons interfaces over the Slider. The joystick was, on average, preferred to any of the touchscreen devices. However, compared to the far superior tracking performance of the joystick, it is surprising that operators rated the Tilt and Buttons interfaces nearly the same as the joystick.

Figure 85 shows results for the question "How confident were you in the command you were issuing?" The joystick gave operators the most confidence because it gives several forms of feedback. The spring-return force increases as the joystick is moved

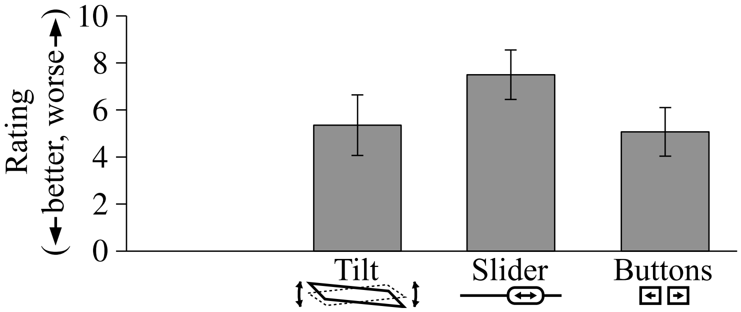

Figure 84: Rating for "How did the interface compare to the joystick?" 1 = much better; 5 = about the same; 10 = much worse (mean ± SD)

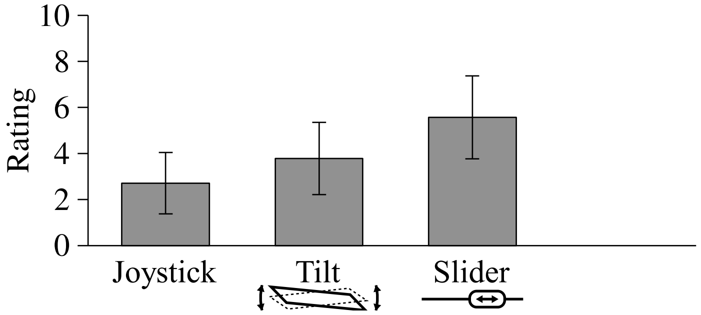

Figure 85: Rating for "How confident were you in the command you were issuing?" 1 = very sure; 10 = very unsure (mean ± SD)

away from zero position, and larger hand motions are probably easier to see, and to sense with proprioception. The Tilt interface gave operators the second-most confidence. This interface used gross motion of the device to send commands, so again, hand motion could be used to help determine the command that was issued. The Slider interface gave the least confidence. It did not use physical motion of the device to generate commands – the command value was only represented by graphics on the screen. Operators were not asked to rate their confidence about the commands issued with the Buttons interface.

5.2.2.3 Control Behavior

Figure 86 shows example error and command histories issued by each of the command interfaces. The joystick and Buttons controllers use different types of input (continuous vs. discrete), but keep the error to a similar low level. The Slider was the worst

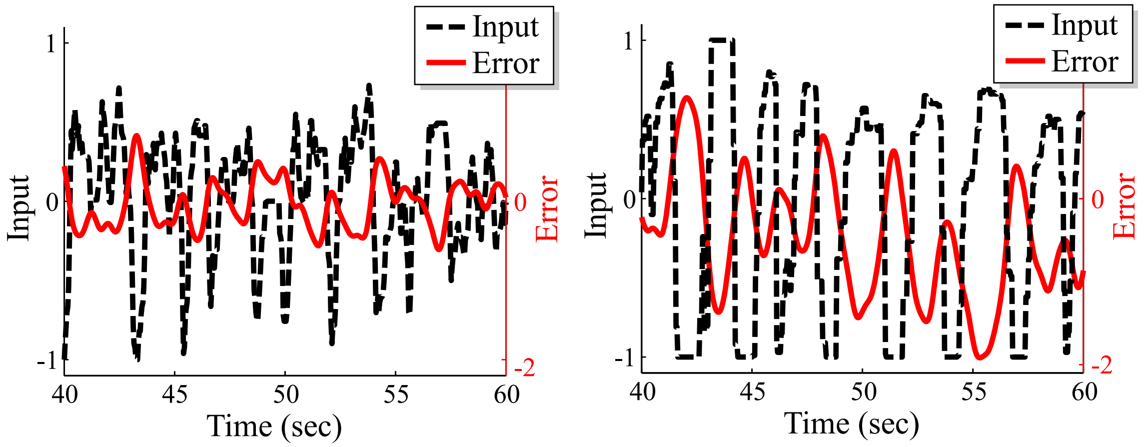

(a) Joystick input

(b) Tilt input

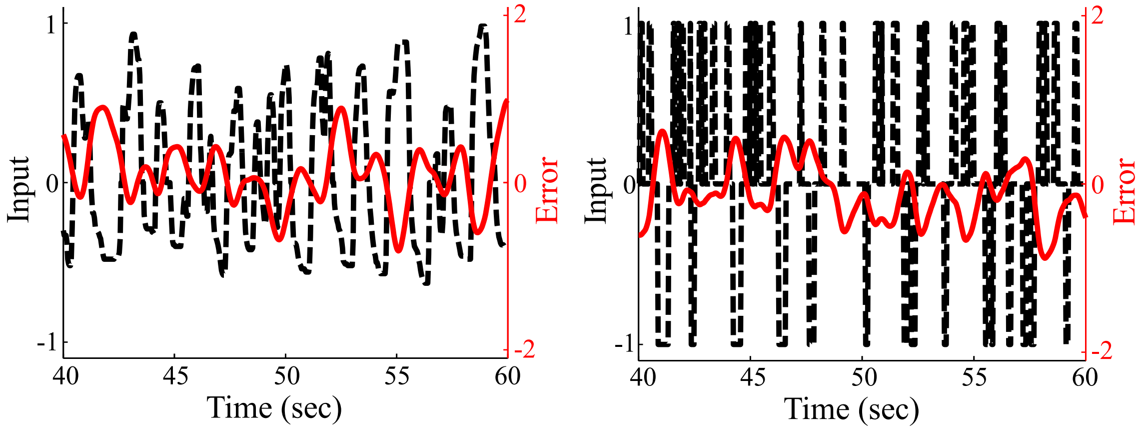

(c) Slider input

(d) Buttons Input

Figure 86: Example commands in response to tracking error

for minimizing tracking error, but that is not obvious from this small sample.

Table 13 shows Crossover model parameters for the different command interfaces. The joystick resulted in a system with the highest gain (crossover frequency), phase margin and $\%_{fit}$, and the lowest effective delay. The Slider had the lowest gain, ϕ_m and $\%_{fit}$, and highest effective delay. Of the touchscreen interfaces, the Buttons controller produced the system with the most desirable Crossover model parameters. The Buttons controller produced a system with a high gain, low time delay, and large phase margin and fit percentage. These trends in the Crossover model parameters agree with the quantitative tracking results shown previously in Figure 83.

Figure 87 compares log-transformed mean tracking error to Crossover model fit,

Table 13: Crossover model parameters for Touchscreen experiment

	K (rad/s)	τ (sec)	ϕ_m (deg)	$\%_{fit}$
Joystick	1.37 (0.53)	0.48 (0.18)	54.82 (12.11)	86.13 (5.70)
Tilt	1.03 (0.47)	0.72 (0.28)	38.32 (32.58)	80.64 (16.71)
Slider	0.84 (0.49)	0.78 (0.39)	29.81 (45.34)	75.91 (8.13)
Buttons	1.16 (0.58)	0.61 (0.40)	47.22 (32.85)	82.92 (5.05)

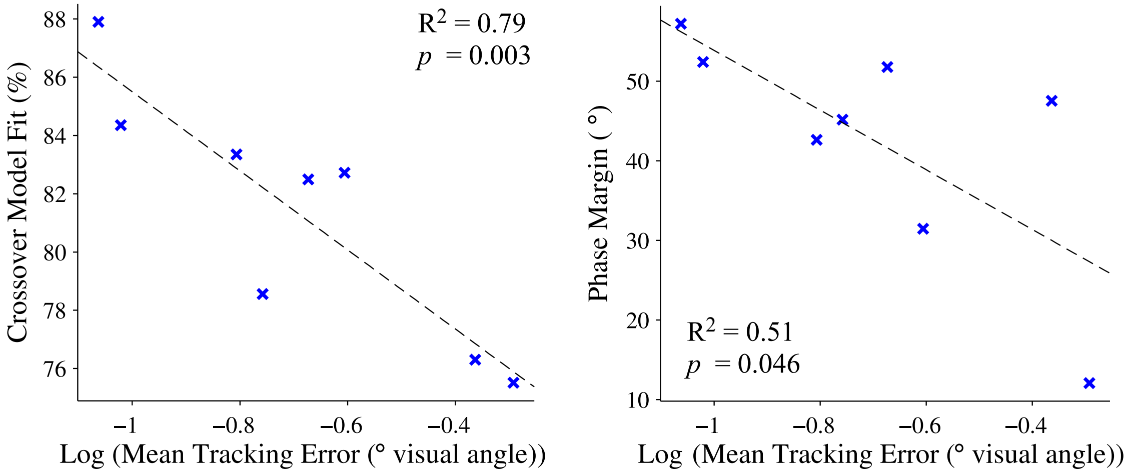

(a) Fit to Crossover model

(b) Phase margin

Figure 87: Tracking error vs. Crossover model parameters

$\%_{fit}$, and phase margin, ϕ_m. As shown in Figure 87(a), the Crossover model fit was strongly correlated with tracking error. There was a significant ($p = 0.003$) probability of a nonzero correlation, and a high R^2 value of 0.79.

Phase margin in Figure 87(b) was not as strongly correlated with tracking error. The probability of a nonzero correlation was barely significant ($p = 0.046$), and the R^2 value was 0.51.

5.2.3 Discussion

The joystick was a better command interface than the touchscreen interfaces, according to the performance metrics in this experiment. The joystick's physical motion and force feedback may have helped the operators accurately determine commands sent to the controlled element. The joystick is also a familiar type of input device. As humans gain more experience with touchscreen devices, their preferences may change.

The Slider interface performed the most poorly. It provided auditory feedback when the slider was released, but did not provide force feedback like the joystick, or position feedback like the joystick and Tilt controller. Operators had difficulty estimating the command sent to the controlled element. The Tilt interface was better than the Slider interface, possibly because the command corresponded to a large visible motion instead of graphics on the screen. The Buttons controller was better than other touchscreen interfaces because operators generally did not have to look at the interface once their hands were set. In addition, discrete, on-off input has been found to be beneficial for manual tracking, especially with difficult controlled elements. It has been documented that human operators sometimes use discrete-type input even with continuous-input devices [107, 29]. Reasons for this will be discussed in the next section.

Crossover model parameters showed a strong correspondence with the quantitative tracking results. The systems that one would predict to perform well based on the parameter values did perform well, and vice-versa.

5.3 Tracking Study # 5: Time-Delay Experiment

Now that several potential command interfaces for teleoperated machines have been compared, an operator experiment will be used to investigate a common phenomenon in teleoperated systems: transport delay. This experiment studies how time delays impact the effectiveness of input shaping for improving control of a flexible system.

5.3.1 Participants & Procedure

The experimental setup is shown in Figure 88. Participants viewed a pursuit display that occupied approximately 10° visual angle, and they generated control inputs with a Logitech Attack 3 spring-centered joystick.

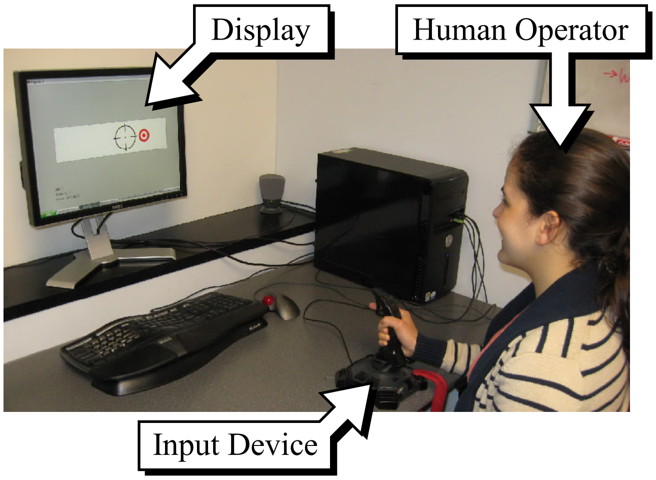

Figure 88: Experimental setup for Time-Delay experiment

Table 14 shows the transfer functions of the three controlled elements in this experiment: an integrator, an integrator with a flexible mode, and a ZV-input-shaped integrator with a flexible mode. Each transfer function includes a variable time delay, τ. The value of gain K was adjusted to allow the cursor's maximum velocity to match the maximum velocity of the reference input using reasonable joystick deflections. For this experiment, the gain was set to $K = 0.3396 \, \frac{{}^\circ \text{ visual angle/sec}}{{}^\circ \text{ joystick deflection}}$.

The integrator transfer function is equivalent to controlling the base in Figure 89(a) with a velocity command. The flexible transfer functions are equivalent to controlling the load in Figure 89(b) by moving the base. Note that the target and

Table 14: Controlled-element transfer functions for Time-Delay experiment

Controlled Element	Transfer Function, $\mathbb{G}_c = \frac{\mathbb{Y}(s)}{\mathbb{U}(s)}$
Integrator	$\frac{K_c}{s} e^{-\tau s}$
Integrator with Oscillatory Mode	$\frac{K_c}{s} \left(\frac{\omega_n^2}{s^2 + 2\zeta\omega_n s + \omega_n^2} \right) e^{-\tau s}$
ZV-Input-Shaped Integrator with Oscillatory Mode	$(A_1 + A_2 e^{-t_2 s}) \frac{K_c}{s} \left(\frac{\omega_n^2}{s^2 + 2\zeta\omega_n s + \omega_n^2} \right) e^{-\tau s}$

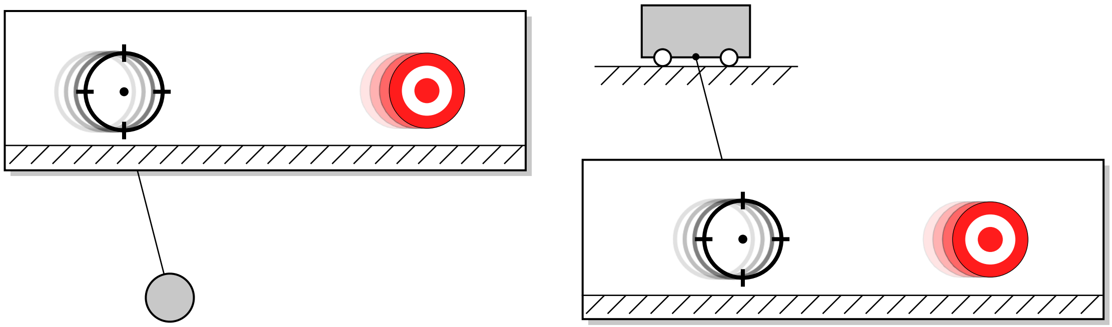

(a) Base control (b) Load control

Figure 89: Displays and controlled states for Time-Delay experiment

cursor motions are shown independently, and the cursor does not stay centered in the screen. This will be called a ground-fixed pursuit display.

The flexible mode had a natural frequency of $\omega_n = 1.579\ rad/s$ and a damping ratio of $\zeta = 0.1$. This frequency was slow enough to cause tracking difficulty, but not so slow that extremely long trial durations would be required to allow multiple oscillations. It is also a frequency that could be encountered in real-world tracking tasks: a crane with a 4-meter payload-suspension cable length would oscillate with approximately this frequency. The ZV input shaper for this natural frequency and damping ratio is:

$$\mathbb{G}_{zv}(s) = 0.5783 + 0.4217e^{-2.00s}. \tag{41}$$

Table 15 gives the frequency content of the reference input that drove the motion of the target. The range of sine wave frequencies is similar to those from previous manual tracking experiments, except for sine wave 9. This extremely slow wave was included to give the target an overall baseline motion. From pilot studies, it was found that without this baseline motion, participants would sometimes stop making control inputs to leave the cursor in one place, knowing that the target would eventually come back to it. The addition of sine wave 9 eliminated this behavior.

Before the real tracking trials, participants completed several practice trials to become accustomed to the tracking task and different controlled-element dynamics.

Table 15: Forcing function for Time-Delay experiment

Wave Number, i	Frequency, ω_i (rad/s)	Amplitude, B_i (° visual angle)
1	9.362	0.120
2	5.718	0.256
3	3.456	0.395
4	2.074	0.536
5	1.194	0.688
6	0.691	0.839
7	0.314	1.057
8	0.189	1.198
9	0.031	16.920

Two of the practice trials showed the participant how easy and hard the control task could be. An extremely easy trial (integrator with no time delay) was used to demonstrate a controlled element that should be rated 1 or 2 on the Cooper-Harper scale, and an extremely hard trial (flexible system with a long time delay) demonstrated an undesirable controlled element that should be rated very poorly.

Participants then performed a series of trials with each of the controlled elements in Table 14 using time delay values of 0, 0.2, 0.4, 0.6, 0.8, and 1.0 second. The trial order was randomized, and the participant was not told which element would be used for each trial. Each trial lasted 115 seconds. The first 15-second period allowed the participant to become familiar with the cursor dynamics. Only measurements from the final 100 seconds of the trial were analyzed. After each trial, the user was asked to consult the Cooper-Harper rating scale shown in Figure 90, and rate the controlled element on a scale of 1 (best) to 10 (worst).

Eighteen volunteer human operators (17 males and one female, between 20 and 31 years of age) were recruited from the student body of the Georgia Institute of Technology. All participants had experience driving cars, and at least some previous experience using a computer joystick. Each participant signed a consent form

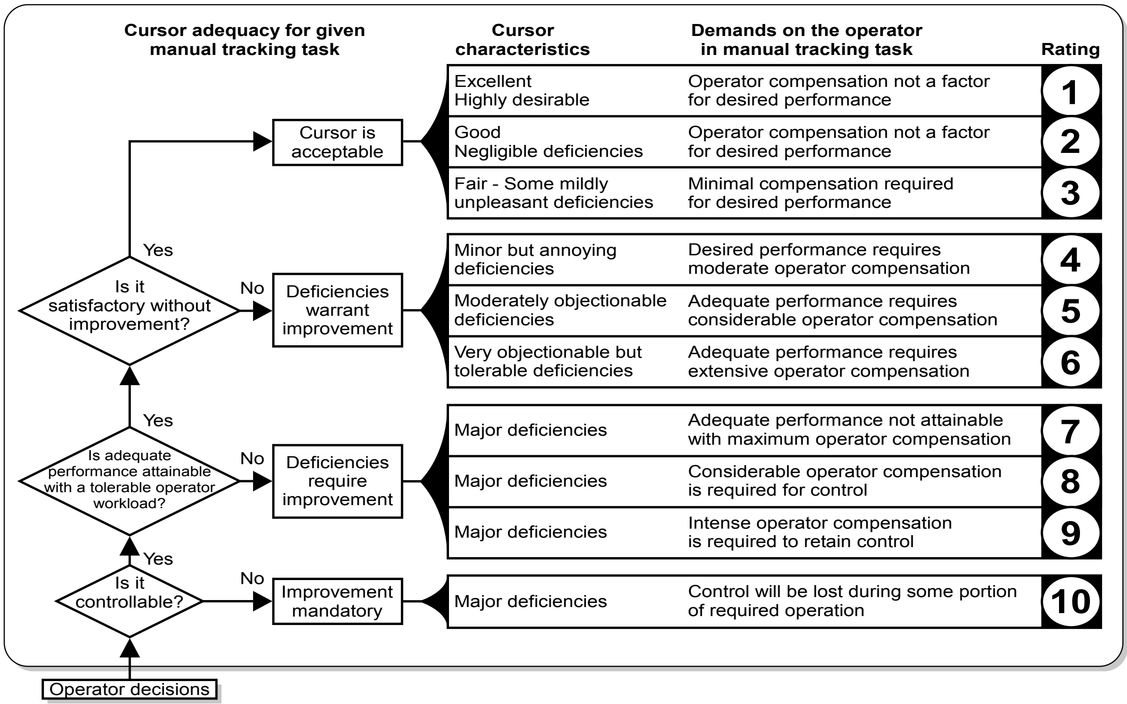

Figure 90: Modified Cooper-Harper rating scale for cursor handling qualities

describing the risks and rewards involved in the experiment. The experiment took around one hour, and participants were not paid for their participation.

5.3.2 Results

5.3.2.1 Tracking Performance

Tracking performance was quantified by root-mean-squared (RMS) tracking error during the 100-second test period. For the integrator and input-shaped controlled elements, strong linear relationships between mean tracking error and time delay were observed. The error as a function of time delay for the both controlled elements is shown in Figure 91. The line fit equations for the integrator and input-shaped flexible elements are:

$$e_{integrator}(\tau) = 0.844 + 1.130\tau \tag{42}$$

$$e_{input-shaped}(\tau) = 1.486 + 0.86\tau \tag{43}$$

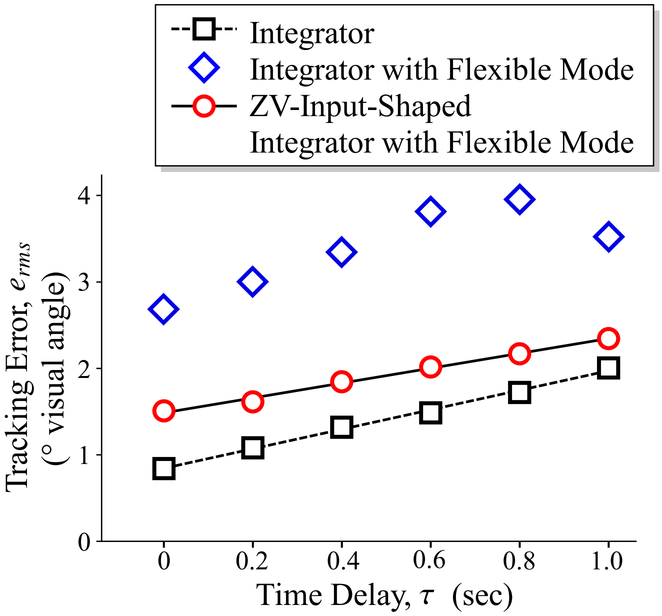

Figure 91: Mean tracking error and linear fits

with R^2 values of 0.996 and 0.994, respectively. The unshaped flexible element was not well-characterized by a line fit.

Figure 92 shows the tracking performance for all controlled elements. As expected, the simple integrator had the lowest error in all cases. For all time delay values, the unshaped flexible system showed the largest mean tracking error, and the addition of input shaping greatly reduced the error. Input shaping improved tracking performance with the flexible system enough to nearly match performance with the integrator.

Error for the integrator and input-shaped elements showed a consistent upward trend with increasing time delay. This degradation of tracking with increased time delay is consistent with previous investigations [30]. The unshaped flexible element trended upward, and then showed a slight decrease in error when the delay was increased from 0.8 to 1 second. It will be shown in Section 5.3.3.1 that the crossover frequency for the 1 second time delay decreased significantly. This decreased aggressiveness on the part of the human operator may have improved tracking performance by reducing excitation of the flexible mode. Decreasing the crossover frequency to

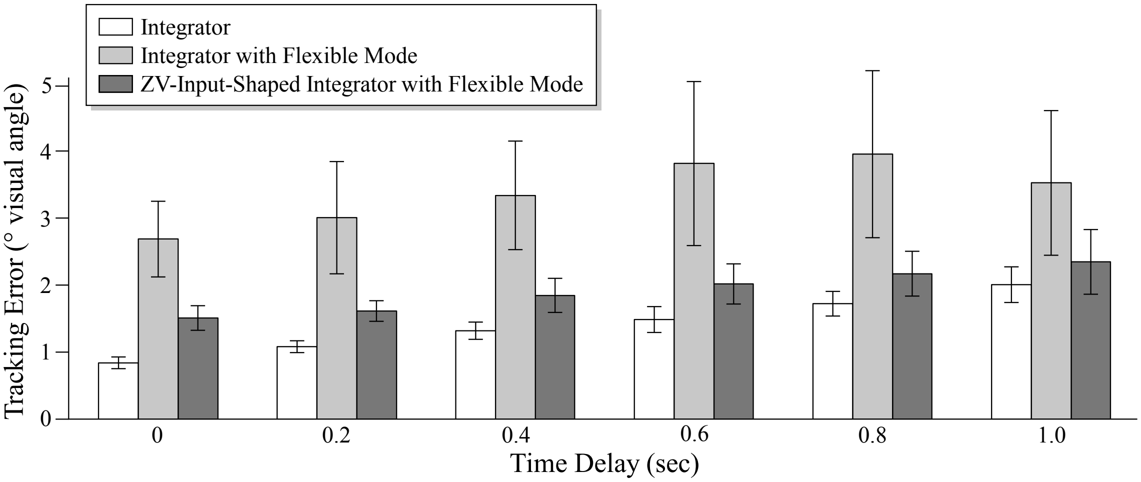

Figure 92: Tracking error for 18 subjects (mean ± SD)

improve tracking performance, especially with difficult controlled elements or forcing functions, is a well-known phenomenon called *crossover regression* [6].

Two tests were used to determine statistical significance. A two-way analysis of variance (ANOVA) tested for significant main effects and interaction effects between the two factors of Time Delay [0, 0.2, 0.4, 0.6, 0.8, 1.0 sec] × Controlled Element [integrator, integrator with flexible mode, input-shaped integrator with flexible mode], and a Tukey's honest significant difference (HSD) tested for significant differences between different conditions. Before running these statistical tests, the tracking error data were log-transformed to correct for heteroscedasticity [25].

Significant main effects of Time Delay ($F(5, 306) = 61.94$, $p < 0.0001$) and Controlled Element ($F(2, 306) = 597.59$, $p < 0.0001$) were found, along with a significant interaction effect ($F(10, 306) = 6.08$, $p < 0.0001$). Post-hoc comparisons using Tukey's HSD test found that within each time delay value, tracking error for the unshaped flexible element was significantly ($p < 0.001$) larger than error for the integrator and the input-shaped elements. There was a small difference between the mean tracking error for the input-shaped flexible element and the integrator element, but this difference was statistically significant ($p < 0.05$) for all time delay values except for the 1-second time delay, where they were not significantly different ($p = 0.65$).

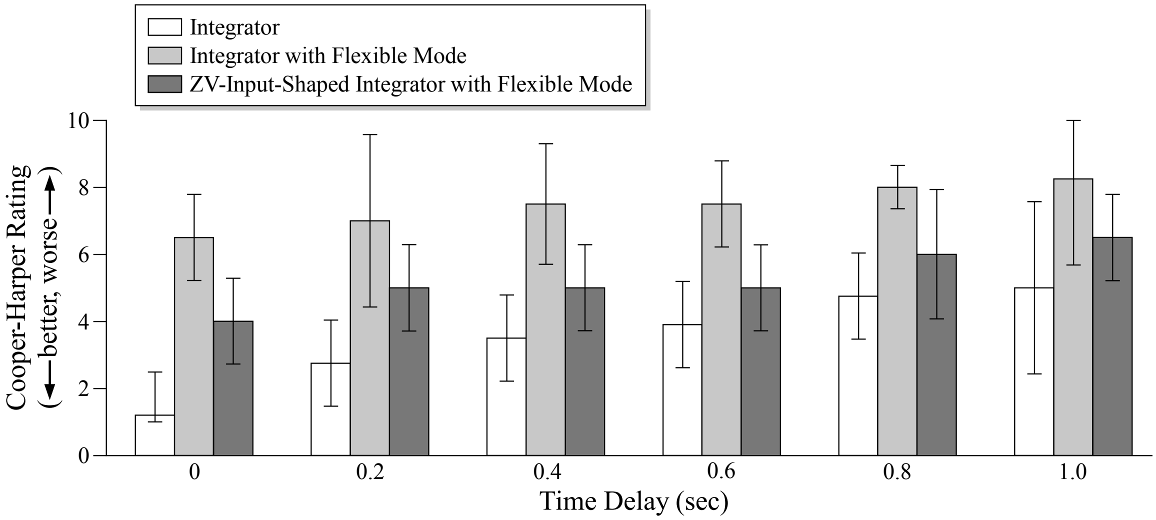

Figure 93: Cooper-Harper rating for 18 operators. (median with 95% CI)

5.3.2.2 Subjective Rating

Figure 93 shows the Cooper-Harper ratings for each controlled element. Note that by definition, the confidence interval cannot go below 1 or above 10 on the scale. The Cooper-Harper ratings are ordinal, but not interval or ratio [53] – for instance, a rating of 4 may not be twice as "bad" as a rating of 2, and the difference between ratings of 2 and 3 is not necessarily the same as the difference between 4 and 5. To account for this, medians were compared instead of means, and the Wilcoxon rank-sum test was used for pairwise comparisons instead of Tukey's HSD test [25].

The ratings showed trends similar to RMS error. For all time delay values, the integrator was significantly ($p < 0.05$) better than the other two controlled elements, and the input-shaped flexible element was significantly ($p < 0.05$) better than the unshaped flexible element. Ratings generally got worse as the time delay increased, which was expected from previous studies. The study in [30] showed that time delays require the human operator to generate an increased amount of phase lead, and requiring humans to generate phase lead tends to make them rate a system more poorly [56].

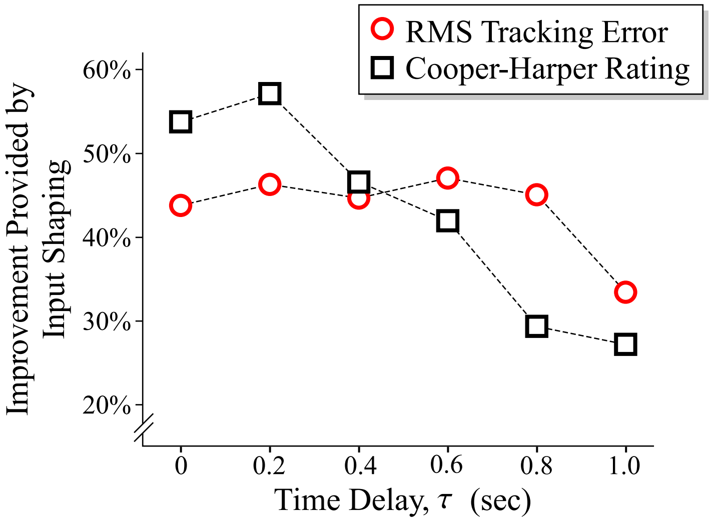

Figure 94: Improvement of adding input shaping to flexible element

5.3.3 Improvement with Input Shaping

Figures 92 and 93 can be used to investigate how the benefit of input shaping depended on the amount of time delay. Figure 94 displays the average improvement of the input-shaped element over the unshaped flexible element for all six time delay values. Note that the dotted lines connecting data points are added to improve readability, not to imply interpolation between points. The performance improvement is normalized by the performance of the unshaped flexible element. More precisely, the graph shows:

$$\% \text{ improvement} = 100 \times \left(\frac{x_{\text{flexible}} - x_{\text{input-shaped}}}{x_{\text{flexible}}} \right) \tag{44}$$

at a given time delay value, where x is either mean RMS tracking error or median Cooper-Harper rating.

The ZV input shaper improved tracking performance by between 30% and 60% in both the qualitative and quantitative performance measures. This benefit decreased as the time delay values increased.

5.3.3.1 Control Behavior

Operators used a variety of different strategies to control difficult (sluggish and/or oscillatory) controlled elements. Two strategies are illustrated in Figure 95. Some

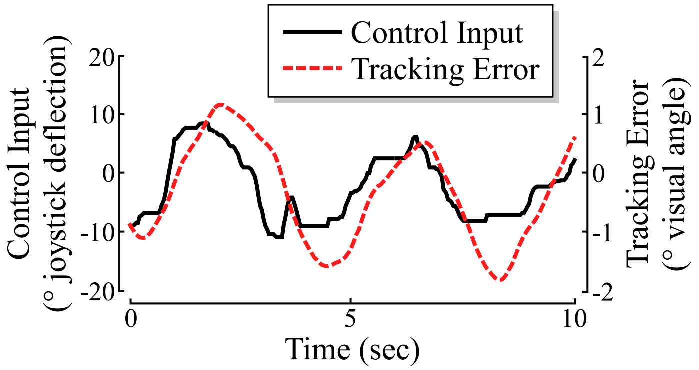

(a) Continuous Control

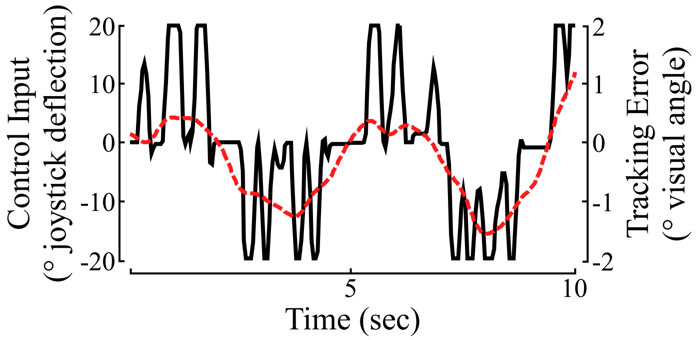

(b) Pulsive Control

Figure 95: Strategies for controlling difficult elements

operators used continuous control, shown in Figure 95(a). Other operators used a kind of on-off or pulsive control that has been discussed in [107] and [29], and is shown in Figure 95(b). These operators used the continuous-input device in a "bang-bang" manner. They quickly moved the joystick to its maximum angle, then returned the joystick to its neutral position. To increase the amount of control input, they either used more pulses, or increased the duration of the pulses. In [107], it was proposed that human operators use pulsive control in an attempt to ease the mental computation needed to integrate their own control inputs. It is easier to remember a number of consistently sized pulses than it is to mentally integrate a smooth function.

With difficult controlled elements, about one third of the operators preferred to use continuous inputs, one third preferred to use on-off inputs, and the other third used strategies that do not fit into either category. It should be emphasized that operators were not told about any special control strategies before the experiment.

Table 16 shows Crossover model parameters for the Time-Delay experiment. For controlling the driven base, increasing the time delay tended to decrease the open-loop gain, increase the effective time delay, decrease the phase margin, and decrease the Crossover model fit.

When operators controlled the flexible load, the addition of input shaping improved the mean phase margin for all but the 1-second time delay, and increased the Crossover model fit for all time delay values. As in previous experiments, adding input shaping to the flexible system made control of the flexible element behave more like the Crossover model.

When operators controlled the flexible load without input shaping, there was a large decrease in gain K between the 0.8 and 1-second time delay cases, which corresponded to an improvement in tracking performance. As noted in Section 5.3.2.1,

Table 16: Crossover model parameters for Time-Delay experiment [mean (SD)]

Element	Shaper	Delay	K (rad/s)	τ (sec)	ϕ_m (deg)	$\%_{fit}$
Base	None	0	1.47 (0.52)	0.26 (0.11)	69.12 (8.41)	87.73 (3.07)
Base	None	0.2	0.94 (0.33)	0.38 (0.16)	71.22 (6.75)	88.07 (4.70)
Base	None	0.4	0.91 (0.40)	0.57 (0.22)	59.97 (16.02)	84.59 (4.69)
Base	None	0.6	0.82 (0.24)	0.76 (0.28)	54.72 (14.23)	83.30 (5.64)
Base	None	0.8	0.63 (0.25)	0.91 (0.30)	56.98 (14.79)	78.16 (8.54)
Base	None	1.0	0.85 (0.24)	1.04 (0.17)	39.51 (15.04)	80.25 (7.13)
Load	None	0	0.43 (0.25)	0.92 (0.40)	45.93 (50.05)	66.51 (13.52)
Load	None	0.2	0.68 (0.40)	0.92 (0.27)	42.39 (37.86)	65.46 (12.26)
Load	None	0.4	0.72 (0.42)	1.00 (0.31)	38.08 (37.61)	60.60 (11.03)
Load	None	0.6	0.78 (0.39)	1.01 (0.28)	33.08 (36.28)	64.06 (13.08)
Load	None	0.8	0.76 (0.45)	0.93 (0.40)	24.14 (46.53)	63.91 (9.22)
Load	None	1.0	0.60 (0.49)	1.18 (0.50)	38.97 (42.37)	65.80 (12.07)
Load	ZV	0	0.62 (0.22)	1.00 (0.33)	56.06 (16.26)	87.87 (3.83)
Load	ZV	0.2	0.51 (0.18)	1.24 (0.43)	54.73 (12.90)	88.41 (3.30)
Load	ZV	0.4	0.53 (0.20)	1.32 (0.22)	49.27 (17.30)	85.25 (5.84)
Load	ZV	0.6	0.60 (0.14)	1.47 (0.23)	39.76 (11.84)	86.03 (3.09)
Load	ZV	0.8	0.56 (0.18)	1.81 (0.33)	34.06 (18.62)	86.40 (4.69)
Load	ZV	1.0	0.59 (0.19)	1.92 (0.46)	27.31 (18.39)	84.76 (5.30)

this is likely an example of crossover regression [6]. The operators were less aggressive with the extremely delayed system, which resulted in smaller overall tracking error because the load swing was not excited as strongly.

5.3.3.2 Correlations

The mean tracking errors from Figure 92 and median ratings from Figure 93 for each time delay value are plotted against each other in Figure 96. There was a strong relationship between the two variables, given by:

$$r_{CH} = 4.3043\, ln(e_{RMS}) + 2.3219, \tag{45}$$

where r_{CH} is Cooper-Harper rating and e_{RMS} is root-mean-squared tracking error. The dashed black curve in Figure 96 shows this function. The R^2 value for this curve is 0.971, the correlation coefficient between $ln(e_{RMS})$ and r_{CH} is 0.985, and the p-value is less than 0.0001, indicating a significant correlation.

Figure 97 compares log-transformed mean tracking error of the 18 trials to the Crossover model fit and phase margin for those trials. Both correlations are significant with $p < 0.0001$ and R^2 values of 0.67 for the model fit in Figure 97(a), and 0.68 for

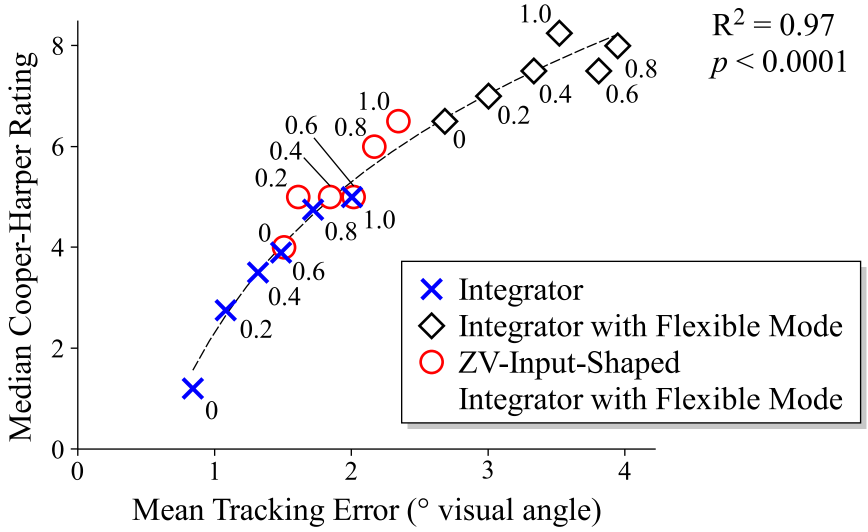

Figure 96: Comparison of quantitative performance to subjective rating (numbers give time delay for each point)

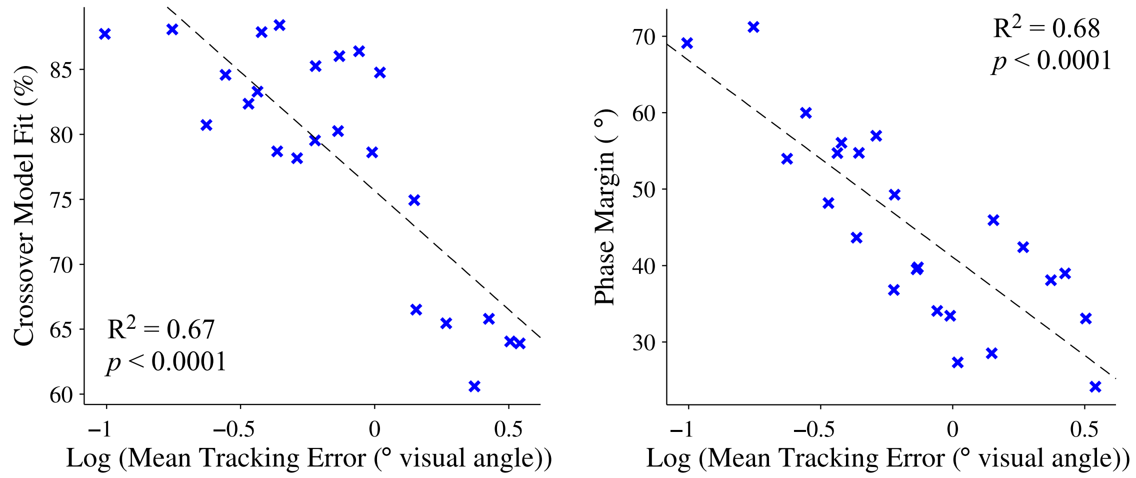

(a) Fit to Crossover model (b) Phase margin

Figure 97: Tracking error vs. Crossover model parameters

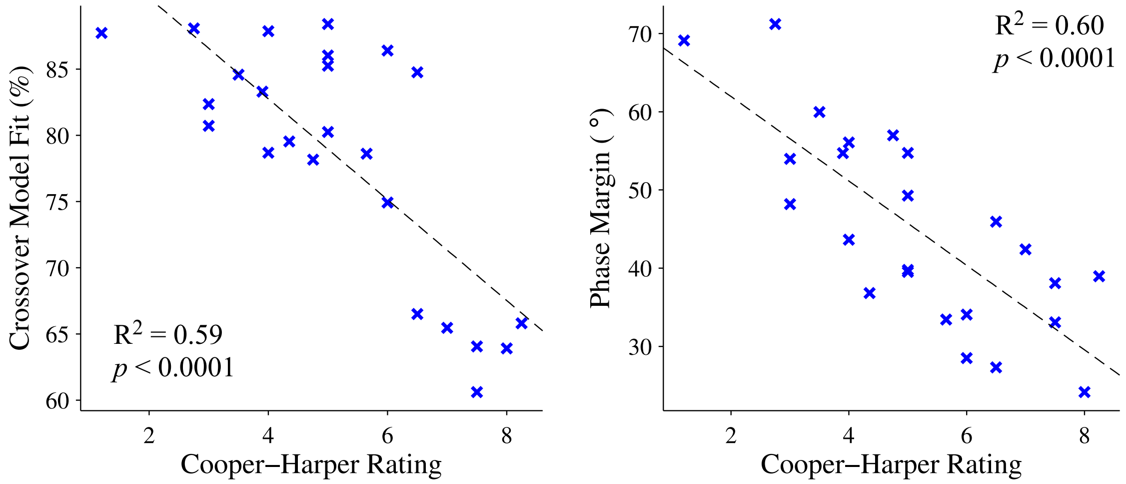

(a) Fit to Crossover model (b) Phase margin

Figure 98: Subjective rating vs. Crossover model parameters

the phase margin in Figure 97(b).

Figure 98 plots the median Cooper-Harper rating against the mean Crossover model fit and phase margin. The correlations are nearly identical to the tracking error correlations in Figure 97. Both correlations had a significant ($p < 0.0001$) probability of a non-zero correlation, and R^2 values of 0.59 and 0.60.

5.3.4 Discussion

The ZV input shaper was beneficial for a ground-fixed pursuit display. The benefit decreased somewhat as the time delay increased. However, for all time delay values, input shaping increased the magnitude and decreased the standard deviation of the phase margin, and greatly increased the system's fit to the crossover model. A better fit to the crossover model while controlling the flexible element should reduce mental workload. This expectation is confirmed by the significantly reduced Cooper-Harper ratings with input shaping.

It was found that the Crossover model fit and phase margin of the human-machine system was strongly correlated with (log-transformed) tracking error. The results support McRuer's findings that the resemblance of a human-machine system' control behavior to the Crossover model is highly connected to the system's tracking performance [57, 58, 53]. The results also support findings that phase margin is a relatively good predictor of tracking performance [6]. It is not surprising that the correlations with the Cooper-Harper rating were similar to the tracking error correlations because the tracking error and subjective rating were closely related by (45).

5.4 Conclusions

5.4.1 Touchscreen Input Devices

A manual tracking experiment was conducted to investigate the operator performance using three different interface designs on a portable touchscreen device, and comparing them to a physical joystick. The joystick was superior to the touchscreen interfaces as quantified by tracking error, but operators rated the preferability of two interface designs nearly the same as the joystick. For tracking performance, a touchscreen interface with large discrete buttons was second best, and an interface that used physical tilting of the device was third. The worst interface used finger position on the screen to determine the amplitude of the command. The author recommends that touchscreen interface designs for machine control should not require visual monitoring. Additionally, discrete (as opposed to continuous) input should be considered by the interface designer. Past studies have shown that humans often use continuous input devices in a discrete manner to control difficult elements [107, 29]. Tracking performance with the discrete buttons interface was only slightly worse than with the physical joystick.

5.4.2 Effects of Time Delay on Input-Shaping Effectiveness

A manual tracking experiment was used to investigate human operator performance of one-dimensional tracking tasks with flexibility and time-delayed systems. Results showed that operators were best at tracking with the integrator, and rated its dynamics as the most desirable. Some operators naturally used pulsive-type control with difficult elements, a phenomenon found in previous studies. For all tested time delay values, applying input shaping to the flexible controlled element decreased the average tracking error, improved the median Cooper-Harper rating, and increased the human-machine system's resemblance to the Crossover model. As in previous experiments, a better fit to the Crossover model was associated with better performance and subjective rating.

CHAPTER VI

HORIZONTAL REPOSITIONING MANEUVERS ON A MICRO-COAXIAL HELICOPTER

The previous chapters on manual control have been generic in nature – the results are applicable to, but not specific to, helicopter control. The next two chapters will focus on helicopters. This chapter describes an experimental testbed with a small coaxial helicopter and motion-capture-based state measurement. Dynamic models of the helicopter's lateral motion are constructed in Section 6.2, and simulations are used to investigate the effectiveness of input shaping for horizontal repositioning maneuvers in Section 6.3.

6.1 Experimental Setup

Any study of load-swing-reduction techniques requires a simulated and/or experimental helicopter and suspended load system. Figure 99 shows one such experimental system in the Georgia Institute of Technology's Indoor Flight Facility (IFF). The helicopter is an E-Flite Blade® CX3. The custom-made suspended load is designed to have a low aerodynamic profile in the vertical direction so that the influence of rotor downwash[1] on the payload swing is minimized. The distance from the cable attachment point to the suspended load's center of gravity is 1 m.

A motion-capture system calculates the position of the helicopter and load, and sends this information to a MATLAB program that uses feedback to automatically

---

[1] *Rotor downwash* is the downward wind created by the main rotor.

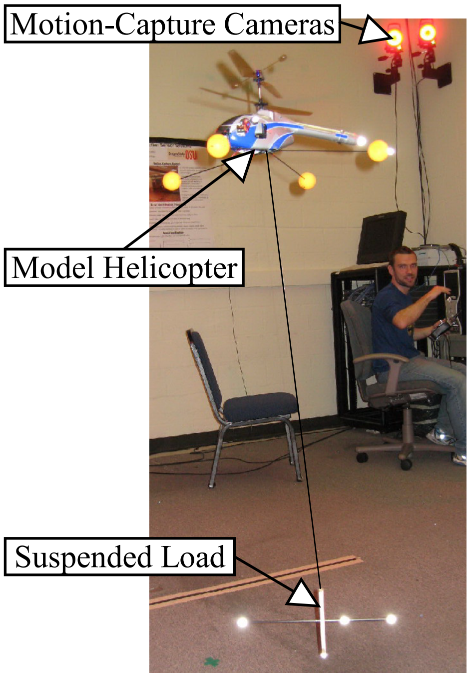

Figure 99: Micro coaxial helicopter and suspended load

control the position and orientation of the helicopter. For lateral repositioning maneuvers, roll commands are sent to the helicopter, and feedback is used to suppress motion in all of the helicopter's degrees of freedom except for the lateral motion and roll angle. Suspended load position is recorded but not used for control purposes

Figure 100 gives a block diagram representation of the equipment and signal flows. The 12 MX-3+ cameras connect to 2 Vicon[2] MX Ultranet HD units that stream camera data to the computer at 120 Hz. Vicon iQ version 2.5 software running on the computer processes the camera data. The resulting position and orientation measurements are exported to MATLAB using the Vicon Tarsus Realtime data streaming application. The spatial and orientation information sent to MATLAB is converted from the ZYX Tait-Bryan convention to Euler angles, and used in a feedback controller to automatically control the position and orientation of the helicopter. The control signals calculated by the feedback controller are sent to the helicopter through

---

[2] VICON Motion Systems Inc., Los Angeles, CA

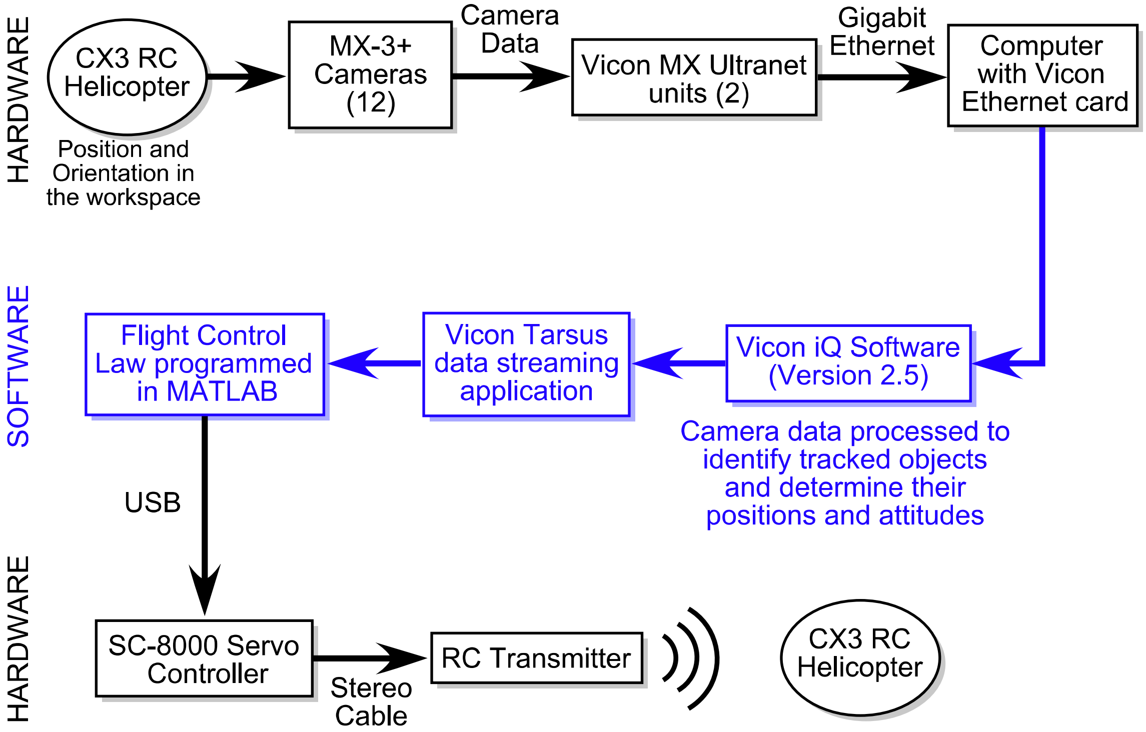

Figure 100: Motion capture and flight controller signal flow [1]

a Spektrum DX6i transmitter connected to the computer using a SC-8000 Servo Controller that performs a serial-to-Pulse-Position-Modulation (PPM) conversion.

6.2 Dynamic Models

Helicopter and suspended-load models vary widely in their levels of complexity. Some researchers have used system identification techniques to construct system models from recorded data [93, 63, 75]. Others have started from first principles, using different levels of detail. Several studies proposed models for systems in which multiple helicopters are attached to the same external load [10, 8]. One model considered only the translational motion of the helicopter and load [19]. This model was used to evaluate techniques for controlling the load swing [20].

When constructing a model for a given system, it is important to ensure that the model complexity is appropriate for the intended analysis [19]. In this case, the model will be used to predict the load swing that results from horizontal translations of the helicopter. Any factors which do not significantly affect the load motion during these translations are not included in the model. Several studies have found that simple models can be used to describe a model helicopter's translational motion [9]. This chapter will introduce two simple translational dynamic models based on experimental behavior of the helicopter system.

6.2.1 Simple Crane-Like Model

A simple dynamic model was based on experimental measurements of the helicopter's response to control inputs. A lateral step command was sent to the helicopter, and a first-order velocity response was observed. The response, shown in Figure 101, had a steady-state amplitude of 1.1 m/s, and a time constant of 0.70 s.

In a separate experiment, the helicopter was held in a stable hover, and the load was displaced. The resulting load swing is shown in Figure 102. The swing showed a lightly damped second-order response with a damping ratio of approximately $\zeta = 0.11$, and a damped natural frequency of approximately $\omega_d = 3.1$ rad/s.

These two responses were used to construct the overall system model shown in Figure 103. A lateral input $u(t)$ to the helicopter produces a first-order velocity response, which is integrated to find the helicopter position, $x(t)$. The second-order

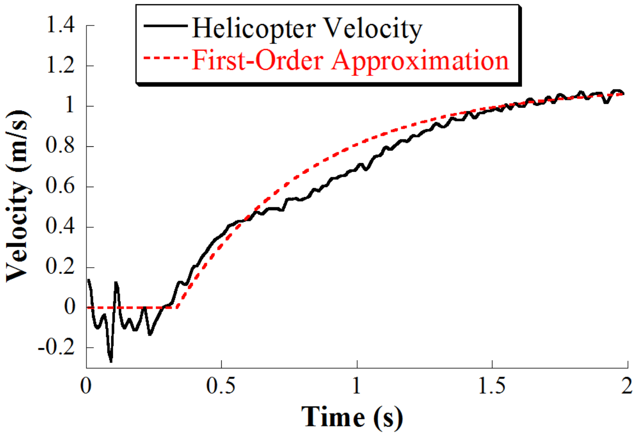

Figure 101: Velocity response to lateral step input, and first-order approximation ($K = 1.1$ m/s, $\tau = 0.70$ s)

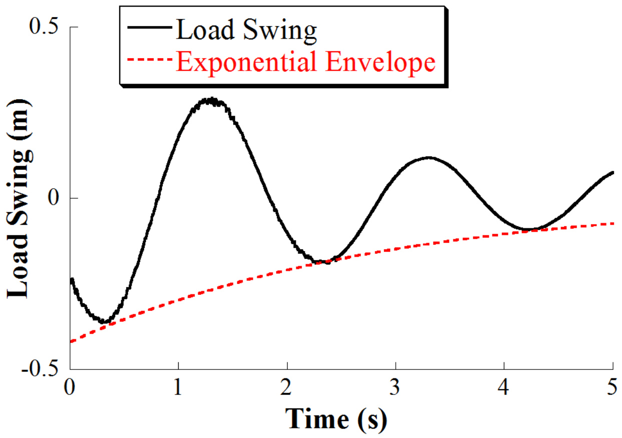

Figure 102: Load swing and exponential envelope ($\zeta = 0.11$)

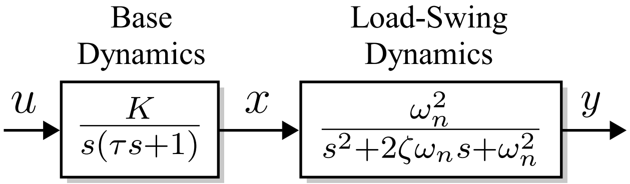

Figure 103: Simple Crane-Like dynamic model

load swing dynamics uses $x(t)$ as the input, and gives load position, $y(t)$, as the output. Substituting the experimentally determined values into the block diagram, the transfer functions relating input $u(s)$ to outputs $x(s)$ and $y(s)$ are

$$\frac{x(s)}{u(s)} = \frac{1.1}{s(0.70s+1)}, \tag{46}$$

and

$$\frac{y(s)}{u(s)} = \frac{1.1(9.61)}{s(0.70s+1)(s^2+0.682s+9.61)}. \tag{47}$$

This model closely resembles the model of a planar crane.

6.2.2 Backdriven Translation Model[3]

A more complicated model that incorporates the backdriving effect of the load on the helicopter is now formed. The Backdriven Translation model is shown in Figure 104. The suspension cable is assumed to be massless and to never go slack. Due to the

---

[3] This section is based on work by C.J. Adams.

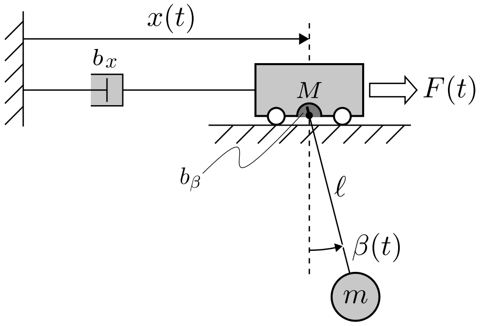

Figure 104: Backdriven translation dynamic model

low speeds attained by the model helicopter, the effects of aerodynamic drag are modeled as viscous damping terms on the helicopter position and cable angle. Rotor downwash effects are ignored. Because it is a lateral planar model, it is assumed that the helicopter maintains a constant heading and altitude, and the helicopter's attitude and position in the longitudinal direction remain constant.

The control input is a horizontal force on the helicopter, $F(t)$. System damping is added with a translational damper with coefficient b_x on the helicopter position, $x(t)$, and a rotational damper with coefficient b_β on the load swing angle, $\beta(t)$. The equations of motion for this model are [21]:

$$\ddot{x} = \frac{-(g\cos(\beta)+\ell\dot{\beta}^2)m\sin(\beta)}{M+m\sin^2(\beta)} + \frac{1}{M+m\sin^2(\beta)}F - \frac{b_x}{M}\dot{x}, \tag{48}$$

$$\ddot{\beta} = \frac{-(m+M)g\sin(\beta) - m\ell\dot{\beta}^2\sin(\beta)\cos(\beta)}{M\ell+m\ell\sin^2(\beta)} + \frac{\cos(\beta)}{M\ell+m\ell\sin^2(\beta)}F - \frac{b_\beta}{m}\dot{\beta}, \tag{49}$$

where the helicopter and payload masses are M and m, and the suspension cable length is ℓ. Note that the load position relative to the helicopter position can be expressed as $x_{load} = \ell\sin(\beta)$.

Several parameters of this model can be directly measured. The values of M, m, and ℓ were 242 g, 15 g, and 1.03 m, respectively. The other parameters, b_x and b_β, were estimated by comparing experimental data from the helicopter to simulated data using a range of parameter values. A lateral repositioning maneuver was performed to provide experimental data for model fitting.

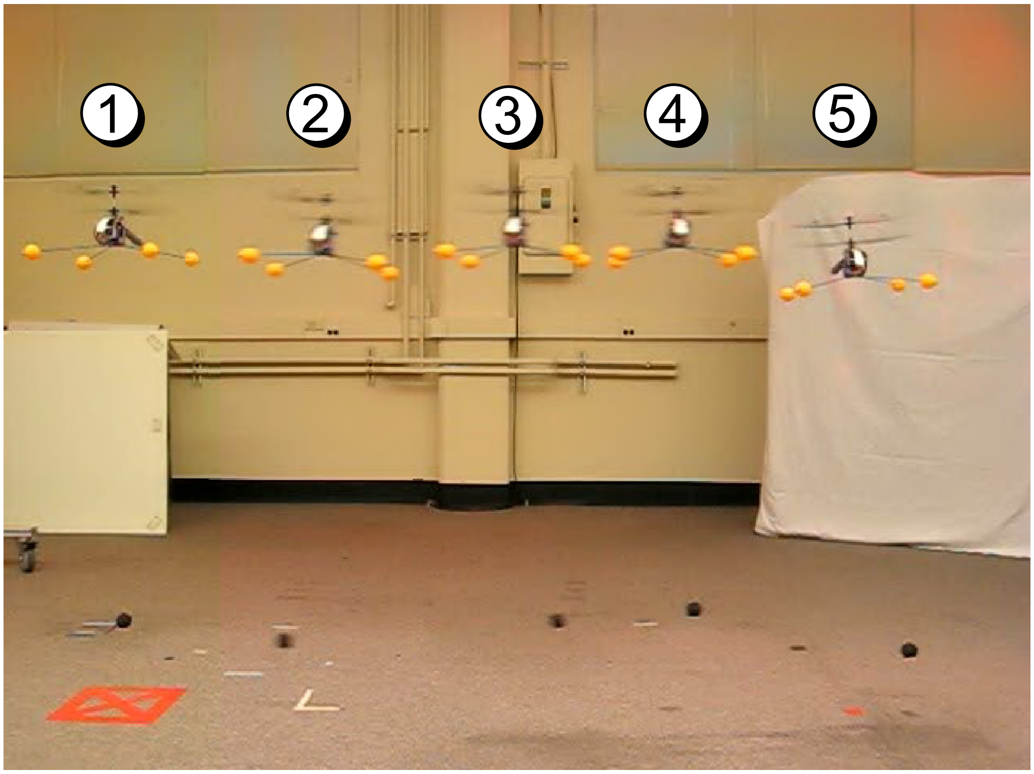

Figure 105: CX3 helicopter performing a lateral repositioning maneuver

The lateral move executed by the helicopter is illustrated by the photo composite shown in Figure 105. The helicopter begins in a stable hover at the left of the image (step 1), moves to the right approximately 7 feet (steps 2-4), and resumes hovering at the target location (step 5). The command sent to the helicopter to execute this lateral move was recorded for use in the simulation.

The values of b_x and b_β were tuned until a good fit to the experimental data was acquired. Experimental and simulated responses to the lateral pulse command are shown in Figure 106. The chosen values were $b_x = 0.008\ \frac{N \cdot s}{m}$ and $b_\beta = 0.009\ N \cdot m \cdot s$.

While the helicopter response is not as accurately predicted by the model as is the payload response, an accurate prediction of the payload response is more important for designing input shapers to suppress the payload swing. The natural frequency and damping ratio of the experimental payload swing were approximately 3.2 rad/s and 0.09, respectively, while the values predicted by linearizing the simulation model

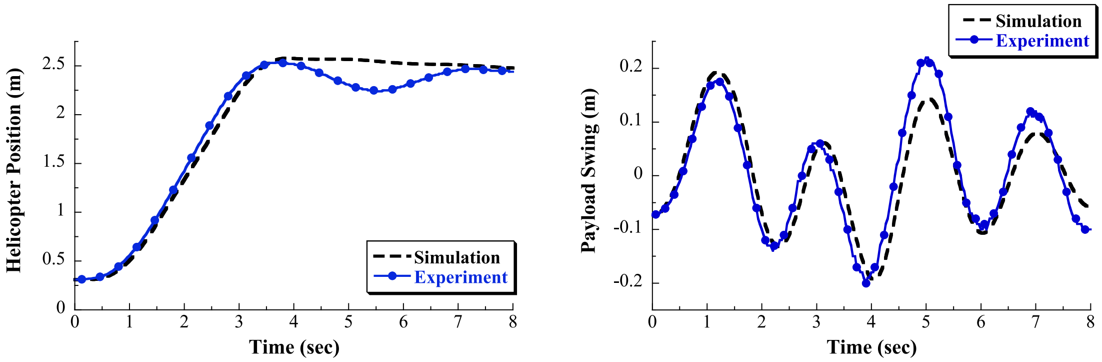

(a) Helicopter response (b) Load response

Figure 106: Experimental and simulated responses to lateral pulse command

are 3.15 rad/s and 0.1. This shows close agreement between the simulation and the experimental trial in terms of the two important input shaper design parameters.

A third way to estimate the swing mode parameters is to use the common approximation for the load swing frequency, $\omega_n = \sqrt{\frac{g}{\ell}(\frac{1}{1-LMR})}$ rad/s. This equation predicts a natural frequency of 3.18 rad/s for the helicopter, which is very close to the experimental and simulated estimates. A ZV input shaper was designed using this approximate swing frequency and zero damping ratio.

Figure 107 shows the results of unshaped and ZV-shaped lateral repositioning maneuvers. The lateral command began at 1.35 seconds. As shown in Figure 107(b), the ZV shaper significantly reduced the amount of payload swing caused by the helicopter motion. However, the swing was not completely eliminated because the input shaper did not specifically target the small amount of initial swing present when the command was initiated at 1.35 seconds. The ZV shaped helicopter response shown in Figure 107(a) is only slightly slower due to the time lag introduced by the shaper. Also, the helicopter arrives at the final hover position with much less overshoot than in the unshaped case.

This is a positive result for input shaping on the micro coaxial helicopter system. However, after extensive testing, it was found that the helicopter could not lift loads

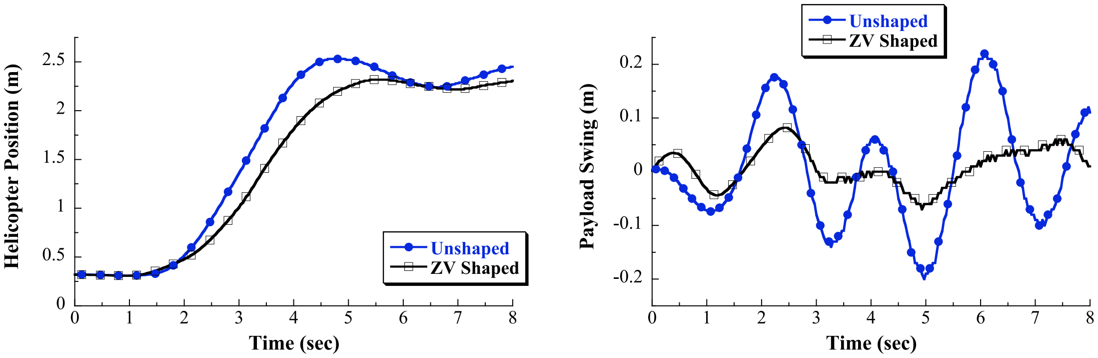

(a) Helicopter response

(b) Load response

Figure 107: Unshaped and ZV-shaped responses to lateral pulse command

heavy enough to make the backdriving effect significant. Therefore, the Simple Crane-Like model of the helicopter will be used for the remainder of this chapter.

6.3 Simulation Results

The Simple Crane-Like model from Section 6.2.1 was used to simulate lateral horizontal moves up to 12 m, with and without input shaping. Figure 108 shows the residual swing amplitude for each distance using different input shapers. Each input shaper greatly reduced the residual load swing to a very small fraction of the swing obtained for the unshaped case. The input-shaped curves are difficult to distinguish from each other because they are all grouped together just above the horizontal axis.

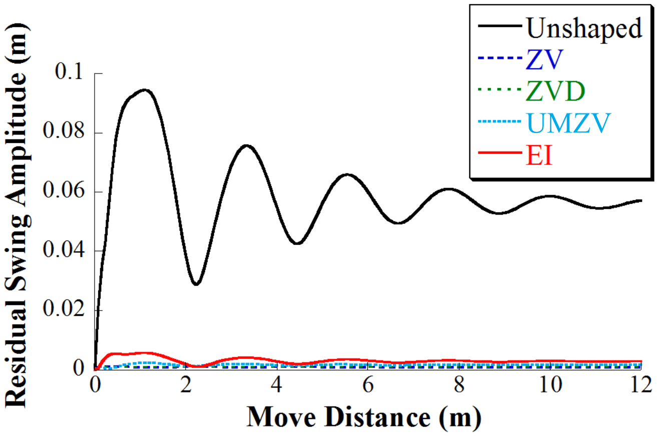

Figure 108: Residual swing amplitude as a function of move distance

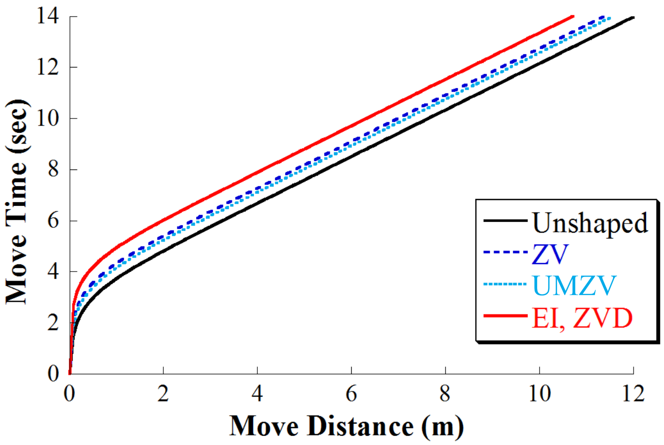

Figure 109: Move time as a function of move distance

As shown in Figure 109, this reduction in swing does not cause a significant increase in move time. For move distances farther than a few meters, the shaper delay is a small percentage of the total move time.

Note that in Figure 108, the residual swing amplitudes for the ZV, ZVD, and UMZV input shapers are nonzero, even though these shapers are designed to yield zero vibration when ω_n and ζ are known exactly. The swing is nonzero because in this simulation, residual swing is recorded when the helicopter enters a zone that is 1 cm from its final position. The zero-vibration input shapers would eliminate all swing if measurements were taken when the helicopter reached its final position. The EI shaper is designed to allow some vibration even when the system parameters are known exactly, so its nonzero residual swing was expected.

6.3.1 Robustness to Errors in Estimated Natural Frequency

For the simulated results in Figure 108, it was assumed that the load swing natural frequency and damping ratio were exactly known. In real situations, there is always some error in the estimated parameter values. Figure 110 demonstrates the effect of error in the estimated ω_n on residual load swing when using a ZV shaper. The top curve shows results for an error of +50%. That is, the estimated ω_n was 1.5 times its true value.

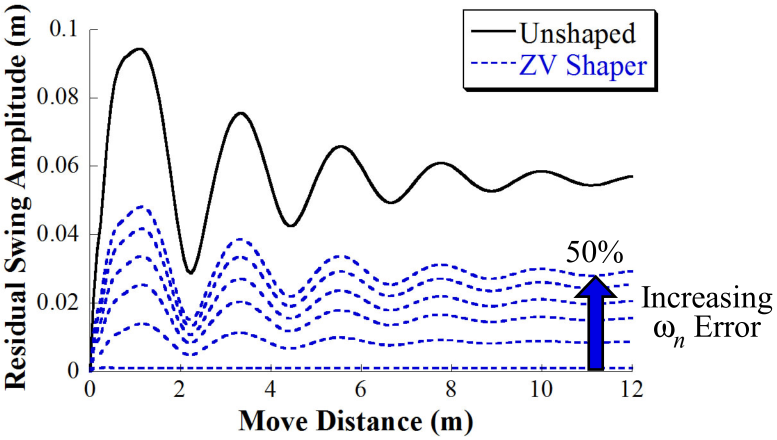

Figure 110: Residual swing amplitude of unshaped and ZV-shaped moves

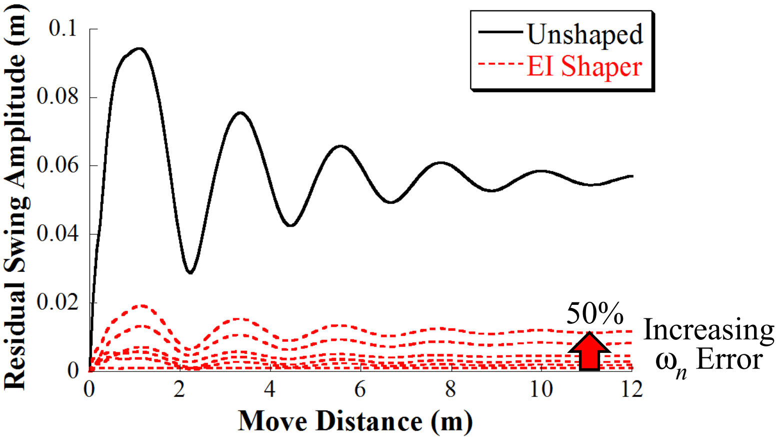

Figure 111: Residual swing amplitude of unshaped and EI-shaped moves

It is clear that a poor estimate of ω_n reduces the effectiveness of the ZV shaper for suppressing load swing. More robust shapers, such as the EI shaper, maintain effectiveness in the presence of modeling errors. Figure 111 shows that for the same errors in ω_n, the EI shaper keeps the swing amplitude at a much lower level than the ZV shaper. There is generally a tradeoff between shaper robustness and move time. Recall that the EI-shaped moves in Figure 109 took slightly longer than the ZV-shaped moves.

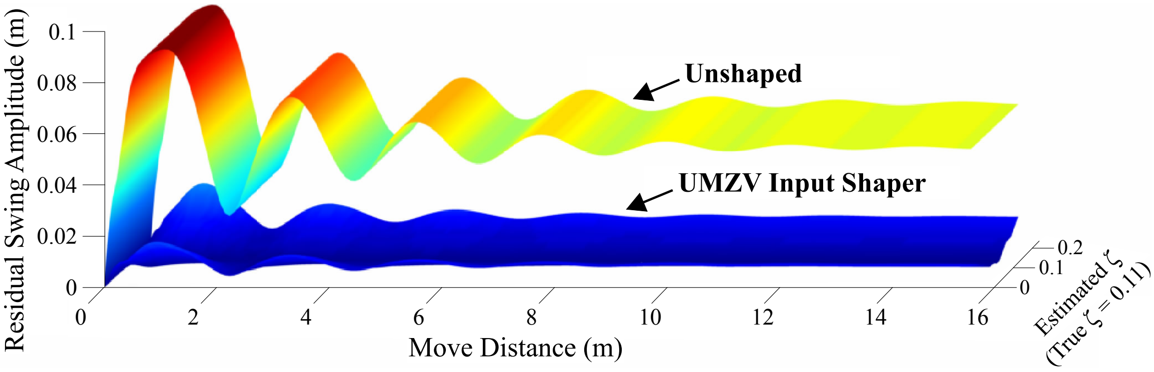

Figure 112: Residual load swing for move distances and modeled damping ratios

6.3.2 Robustness to Errors in Estimated Damping Ratio

There will also be errors in the estimated damping ratio in real-world situations. For all input shapers, it was found that the swing-reducing effectiveness was degraded much less by these errors than it was for errors in ω_n. Figure 112 shows the residual swing amplitude of UMZV-shaped moves as a function of move distance *and* estimated damping ratio. When the estimated damping ratio is equal to the true value, the residual swing amplitude is nearly zero. As the ζ error increases, the swing amplitude increases, but stays far below the amplitude for unshaped moves. Only the UMZV shaper results are shown because it is the least-robust shaper to errors in ζ. The results for other shapers are even more favorable.

6.4 Conclusions

A dynamic model was created to simulate the behavior of a model helicopter and suspended-load system in response to lateral control inputs. The model was used to simulate point-to-point motions with and without input shaping. The simulated trials with input shaping showed a large reduction in residual swing amplitude with only a minor increase in move time. The ZV shaper was not as effective as robust shapers when errors existed in the modeled frequency and damping ratio. Errors in the estimated natural frequency were more detrimental to input shaper performance than errors in damping ratio. Experiments showed that for a move distance of 2.5 m, a UMZV input shaper decreased residual load swing by about 70%.

The micro-coaxial helicopter was safe to fly indoors, but was relatively weak – it could not lift loads that were heavy enough to affect its translational motion. The next chapter employs a more powerful helicopter with a larger payload capacity. The helicopter is mechanically constrained to prevent crashes, thereby increasing safety and saving time that would be spent repairing the helicopter.

CHAPTER VII

HORIZONTAL REPOSITIONING MANEUVERS ON A SMALL-SCALE HELICOPTER WITH PLANAR CONSTRAINTS

This chapter describes a helicopter testbed that allows horizontal repositioning maneuvers, while constraining unnecessary degrees of freedom. Section 7.2 describes the experimental setup. In Section 7.3, a dynamic model of the helicopter is presented, and a grey-box modeling technique is used to estimate the unknown model parameters. Section 7.4 describes a human-pilot-like helicopter control scheme from the literature, and Section 7.5 shows how it can be dynamically scaled to match the fast dynamics of the testbed helicopter. Horizontal repositioning tasks are performed in simulation and on the experimental helicopter in Section 7.6.

7.1 Motivation

Helicopters have complex dynamics, especially when heavy suspended loads are attached. They have many degrees of freedom, and they often exhibit nonlinearity, cross coupling, and occasionally instability. These factors can make theoretical development of helicopter controls and dynamics difficult. For many of the same reasons, it is difficult to test free-flying helicopters experimentally. For any helicopter testbed, the designer must consider factors such as fuel or battery duration, safety in the event of degraded helicopter control, weight of equipment added to the helicopter, noise in the wireless communication, and environmental factors such as wind.

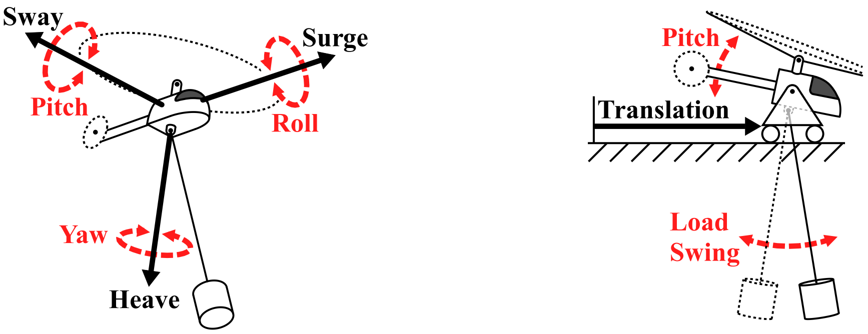

(a) Free-flying (b) Constrained

Figure 113: Helicopter degrees of freedom

As shown in Figure 113a, a free-flying helicopter may translate longitudinally (surge), laterally (sway), and vertically (heave). It may also rotate about the longitudinal axis (roll), the lateral axis (pitch), and the vertical axis (yaw). To reduce the cost, time, and difficulty of using free-flying helicopters, many researchers have built mechanisms to eliminate the degrees of freedom that are not required for the specific research question being investigated. For example, some testbeds allow pitch rotation and vertical motion, while constraining the helicopter to rotate about an elbow joint [35]. Some mechanisms allow all rotations while constraining only horizontal translations [49], or all translations [64], and others constrain all degrees of freedom except the pitch and yaw rotations [103]. Test stands have been constructed to allow some freedom in all directions within a limited envelope [67]. Other studies have attached a tether between the rotorcraft and the ground [74]. For these testbeds, the most important consideration is that the fundamental dynamics of the degrees-of-freedom *of interest* are unchanged, or at least minimally affected.

For basic investigations of the swing of suspended loads, the helicopter must be allowed to translate in a horizontal direction, and rotate in a vertical plane along this direction. Additional requirements of such a testbed include: the load must be able to swing freely under the helicopter; the helicopter must be high enough above the ground to avoid aerodynamic ground effects, and to allow a wide range of cable lengths; the helicopter must be able to travel relatively large horizontal distances to perform load-repositioning maneuvers. None of the helicopter constraint systems referenced above meet these requirements. The testbed shown in Figure 114 was constructed to fulfill these requirements. The testbed limits the helicopter's degrees of freedom to those shown in Figure 113b. Longitudinal translation and pitch rotation are allowed, and all other degrees of freedom are constrained. The suspended load swings in the vertical plane, which adds a third degree of freedom to the system.

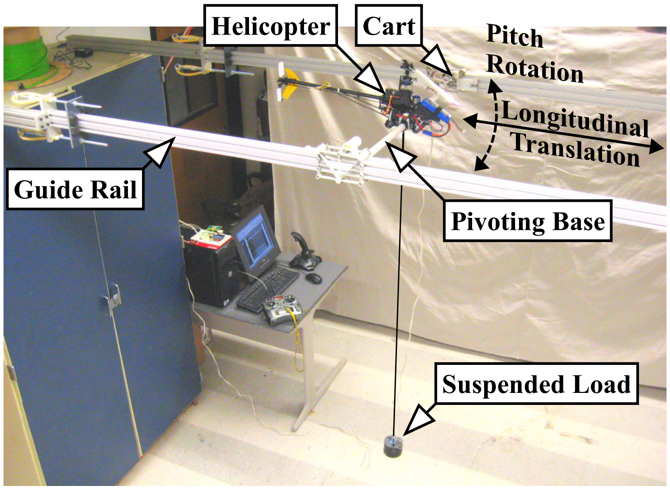

Figure 114: Planar Experimental Remote-Controlled Helicopter (PERCH) testbed

7.2 Experimental Setup[1]

The testbed consists of an electric E-Flite Blade 400 helicopter and a Spektrum DX6i transmitter. The helicopter is attached to a pivoting base suspended between two carts. The carts translate horizontally along two guide rails and allow the helicopter to pitch forward and backward. The extruded-aluminum guide rails allow a maximum horizontal travel of 72 inches, and keep the helicopter 84 inches (3-times the main rotor diameter of 28 inches) above the floor to reduce aerodynamic ground effect. There is also adequate space above the helicopter to prevent unusual aerodynamic conditions.

---

[1] Ryan Simpson assisted with troubleshooting, calibration, and data collection on this testbed.

A load with adjustable weight and cable length is suspended from the underside of the helicopter. The testbed uses a computer and microcontroller to read sensor inputs, perform control calculations, and generate commands. A radio transmitter sends these commands to the helicopter. A preliminary version of this testbed was presented in [1]. On that earlier version, states were measured with vision tracking instead of electromechanical sensors.

7.2.1 Mechanical Features

Figure 115 shows one of the two carts that slide along the guide rails on a set of roller bearings to constrain the translational motion. The pivoting base rotates around posts attached to the carts, thereby allowing pitch rotation. The axis of pitch rotation passes through the center of gravity of the helicopter and base to avoid extra rotational dynamic effects.

To prevent the helicopter from reaching extreme angles (which produce high velocities, and therefore dangerous experimental conditions), the angular hard stops shown in Figure 115 limit the helicopter pitch angle to ±45°. As another important safety feature, the helicopter is decelerated by bumpers when it reaches the end of the guide rails. One of the bumpers is shown in Figure 116. The carts collide with the sliding plates, and the motion is resisted by elastic tubing.

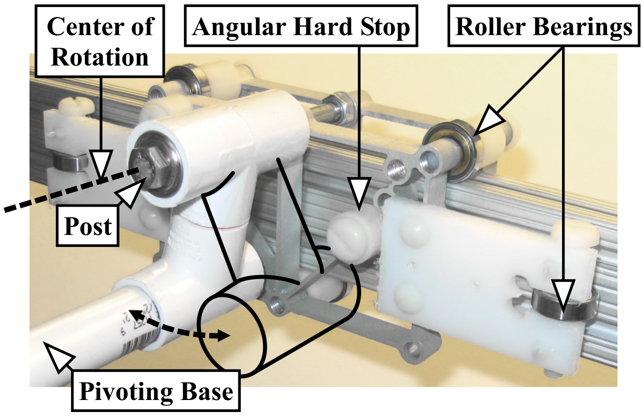

Figure 115: Sliding cart with angular hard stops

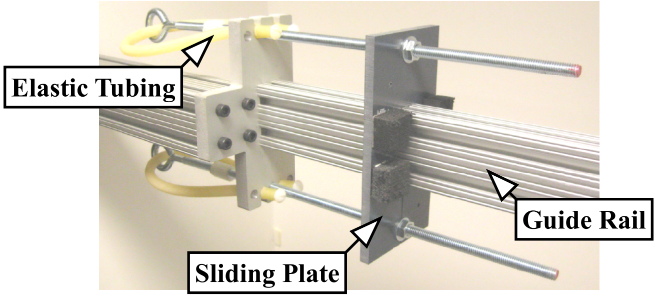

Figure 116: Bumper at end of guide rail

7.2.2 Sensors and Control

A schematic diagram of the testbed is given in Figure 117. The left side shows mechanical components, and the right side shows signals, software, and electronic components. A master control program reads both sensor values from a microcontroller and human input values from a joystick. It then makes control decisions and specifies command voltages through the microcontroller to the transmitter. The transmitter determines command inputs based on the voltage across potentiometers attached to the control sticks. Wires to these potentiometers are routed to the microcontroller outputs in order to send commands to the helicopter.

There are three main states that must be recorded: helicopter horizontal position, helicopter pitch angle, and suspended load cable angle. The position sensor shown in Figure 117 is an optical encoder. A string attached to the rolling cart encircles the

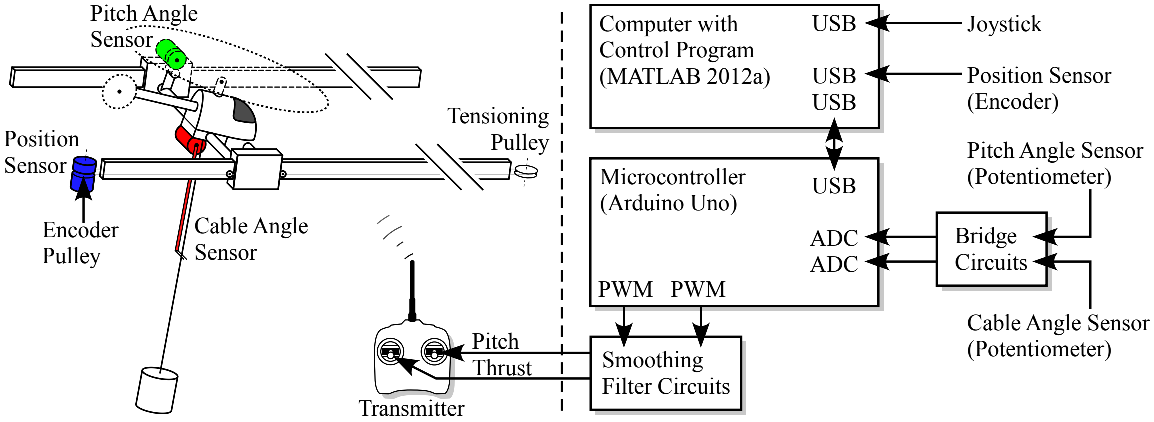

Figure 117: Sensors and signal flows of helicopter testbed

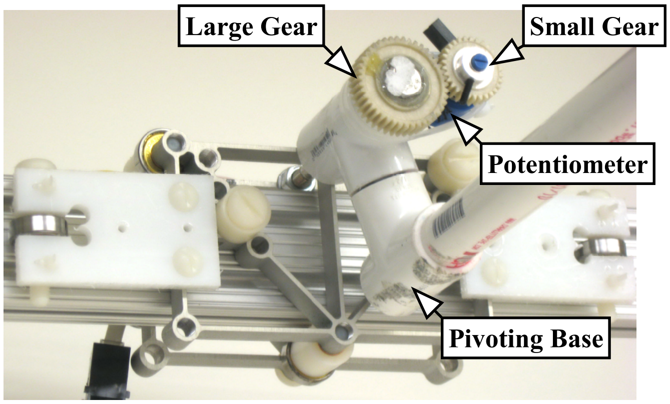

Figure 118: Pitch angle sensor

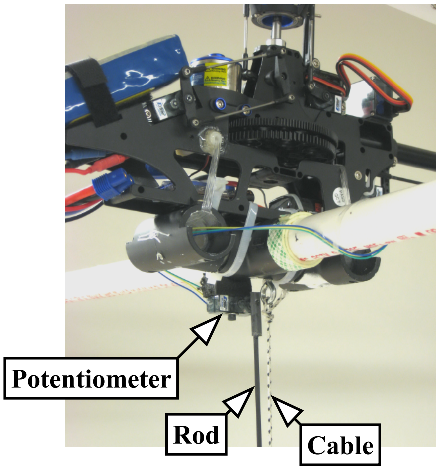

Figure 119: Cable angle sensor

encoder pulley and is kept in tension by a pulley on the opposite end of the rail.

Pitch angle is measured by a potentiometer attached to the pivoting base. Figure 118 shows where one end of the helicopter base is connected to a cart. The large gear is attached to the cart post and does not rotate. The smaller gear is attached to a potentiometer fixed to the pivoting base. This mechanism enables the potentiometer to measure the rotation of the base. A bridge circuit converts the resistance of the potentiometer into a voltage, which is measured by the microcontroller's analog-to-digital converter. This voltage is calibrated to indicate the pitch angle.

The cable angle sensor shown in Figure 119 works similarly to the pitch angle sensor. A light-weight rod which is mounted on a potentiometer shaft rotates with the suspension cable. A bridge circuit converts the resistance of this potentiometer into a voltage proportional to the cable angle. It is important to ensure that the axis of rotation of the potentiometer passes through the pivot point of the cable. Additionally, any rotational friction in the potentiometer shaft can greatly affect the measured cable angle and slightly changes the load-swing dynamics. This type of cable angle sensor is suitable for the testbed, but it tends to be difficult to implement on full-scale helicopters.

7.2.3 Trim & Calibration

Forces and torques from the guide rails should be minimized to ensure that the helicopter dynamics in the unconstrained directions are largely unchanged. To minimize these loads, the control efforts that result in a neutral, non-accelerating state should be found for the constrained degrees of freedom. This is called ‘trimming’ the aircraft.

7.2.3.1 Neutral Roll and Yaw Commands

The neutral roll and yaw commands can be found by manually ‘hovering’ the constrained helicopter and using the transmitter’s trim adjustment levers.

To find the neutral yaw command, an observer stands below the helicopter, and looks upward at the pivoting base and carts. If the helicopter is applying yaw torque, the pivoting base will be slightly rotated in the yaw axis, and one cart will be slightly in front of the other. The yaw trim is adjusted until the pivoting base is perpendicular to the rails, and the carts are even.

To find a neutral roll command, the helicopter is viewed from the front or the rear. While the helicopter is in a controlled hover, the roll trim is adjusted until the rotor disk (the circle formed by the spinning tips of the rotor blades) is perpendicular to the main rotor shaft, and parallel to the pivoting base. These tests should be performed both before and after calibrating the main rotor thrust. Trim may change slightly with different rotor speeds and collective blade pitch angles.

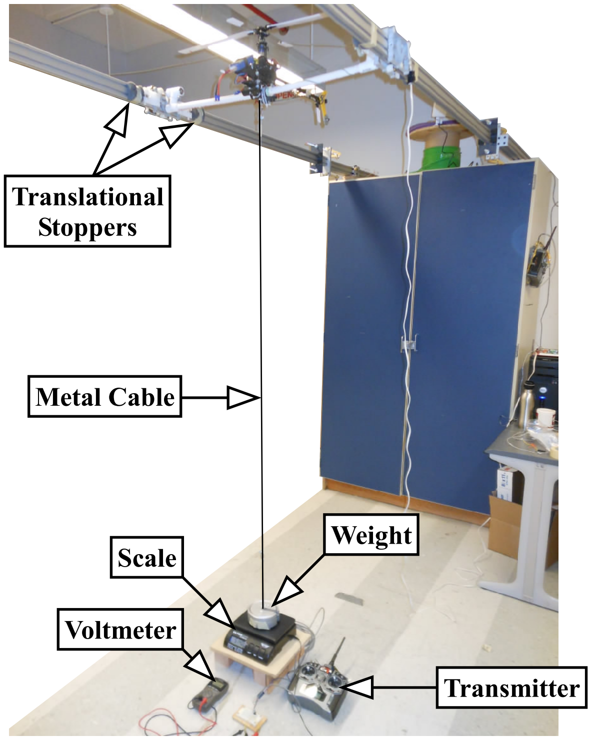

Figure 120: Setup for main rotor thrust calibration

7.2.3.2 Thrust Calibration

When the helicopter's main rotor is spinning, it should provide enough thrust force to lift the helicopter, base, and suspended load. Therefore, it is necessary to determine the transmitter thrust command that is required to lift a given amount of weight.

Figure 120 shows a setup for calibrating the main rotor thrust. The helicopter is held in place by translational stoppers on the rails, and rotational stoppers (not shown in Figure 120) on the carts. A weight is placed on a scale and attached to the helicopter with a metal cable. When the main rotor produces thrust, the weight supported by the helicopter increases and the weight on the scale decreases. A voltmeter measures the voltage across the transmitter's thrust-channel potentiometer, and the scale measures the resulting amount of thrust. Each voltage value is held until the thrust is steady for at least one second.

The resulting measurements of thrust voltage V_T and corresponding thrust force

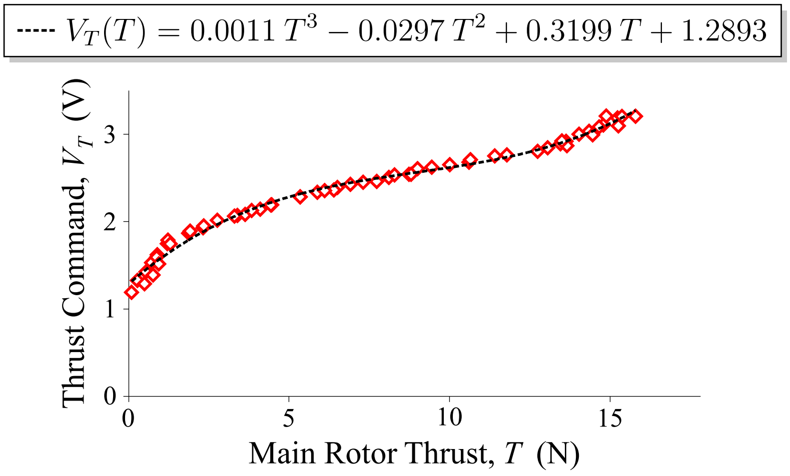

Figure 121: Command voltage versus rotor thrust force

T are shown in Figure 121. Note that below approximately 1.2 Volts, no positive thrust was produced. A dashed line shows a cubic curve fit to the data. To minimize vertical force on the guide rails, V_T should be calculated by setting T equal to the combined weight of the helicopter, pivoting base, and suspended load.

7.3 Dynamic Model

Now that the experimental setup has been described, the next section will derive its equations of motion using a Lagrangian approach.

7.3.1 Model Definition

Figure 122 shows a planar sketch of the helicopter pinned through its center of gravity, G to a horizontally sliding cart. The helicopter's horizontal location is $x(t)$, and its pitch angle is $\theta(t)$. The suspended load has swing angle $\beta(t)$ relative to vertical. A thrust force $T(t)$ is produced by the rotor disk, and the angle of the thrust vector relative to the helicopter body is $\alpha(t)$. This model is similar to previous planar models of externally loaded helicopters near hover [72, 19].

In the proposed model, the main rotor disk angle is *specified* by α – the rotor disk is not modeled as a separate rigid body. It is further assumed that the rotor disk angle α can change instantaneously. This assumption (called the *quasistatic rotor*

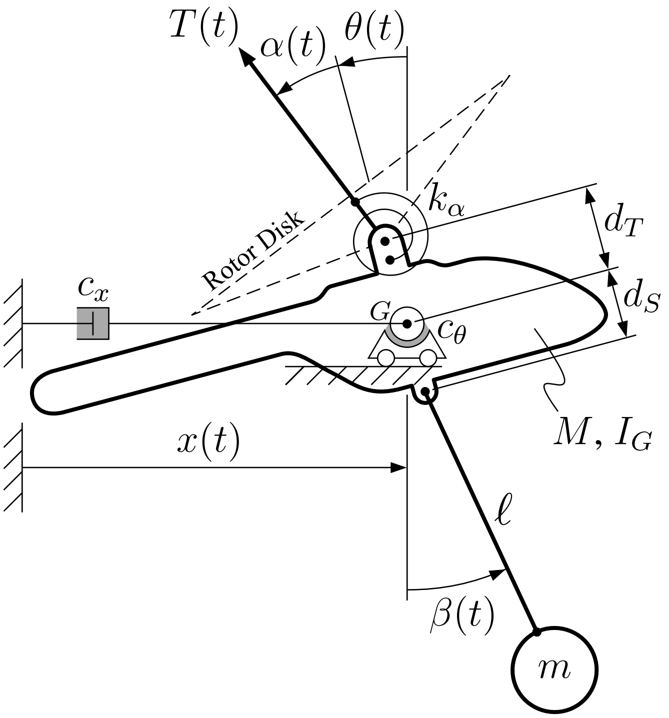

Figure 122: Dynamic model of helicopter and load

assumption [72]) is commonly used because for most helicopters, the main rotor's flapping response is fast relative to the helicopter's gross motion and the pilot's control inputs. To capture the effect of rotor stiffness, a torsional spring with stiffness k_α is attached from the helicopter to the rotor disk [72, 62]. When the rotor disk rotates relative to the helicopter, a torque is applied to the helicopter equal to $k_\alpha \alpha$.

The helicopter has mass M and rotational inertia I_G about point G, and the load has mass m. There are dampers with coefficients c_x and c_θ on the helicopter position $x(t)$ and helicopter pitch angle $\theta(t)$, respectively. A suspension cable of length ℓ connects the load to the helicopter. In helicopter-body-fixed coordinates, the load suspension point is a distance d_S below the helicopter's center of gravity, and the rotor thrust force is applied a distance d_T above the helicopter's center of gravity. It is assumed that the suspension cable is inextensible, the load has no rotational inertia (it is a point mass), and aerodynamic effects on the load are negligible.

This type of planar constraint matches some simplifying assumptions which are

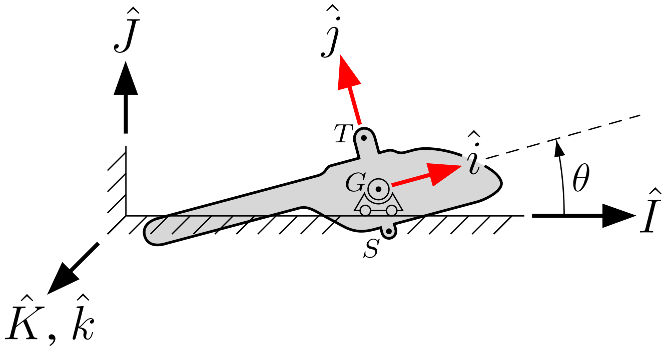

Figure 123: Coordinate frames

commonly made for helicopter dynamic models – it is often assumed that the helicopter has a heading-hold controller to prevent yaw rotation and a height-hold controller to prevent vertical translation [72]. Additionally, for helicopters near hover, lateral and longitudinal dynamics may experience some cross-coupling, but they are often treated separately for controller design and stability analysis [69].

The derivation will require two frames: an inertial frame with unit vectors $\hat{I}$ and $\hat{J}$, and a frame attached to the helicopter with unit vectors $\hat{\imath}$ and $\hat{\jmath}$. These frames are shown in Figure 123. The vector from the helicopter center of gravity, G, to the load suspension point, S, is defined as

$$\vec{r}_{S/G} = d_S(-\hat{\jmath}) \tag{50}$$

The vector between the helicopter center of gravity and the point where main rotor thrust is applied, T, is given by

$$\vec{r}_{T/G} = d_T\hat{\jmath} \tag{51}$$

7.3.2 Equations of Motion[2]

Lagrange's equations will now be used to derive the model's equations of motion. The generalized coordinates are x, θ, and β. Lagrange's equations are given by

$$\frac{d}{dt}\left(\frac{\partial T}{\partial \dot{q}_j}\right) - \frac{\partial T}{\partial q_j} + \frac{\partial V}{\partial q_j} = Q_j, \qquad j = 1, 2, \ldots, N \tag{52}$$

---

[2] C.J. Adams made significant contributions to this section.

where q_j are the generalized coordinates, T is the total kinetic energy of the system, V is the total potential energy of the system, Q_j are the generalized forces, and N is the total number of generalized coordinates (in this case, $N = 3$).

The total kinetic energy of the helicopter and suspended load is

$$T = \frac{1}{2}M\left(\vec{v}_G \cdot \vec{v}_G\right) + \frac{1}{2}I_G\dot{\theta}^2 + \frac{1}{2}m\left(\vec{v}_m \cdot \vec{v}_m\right), \tag{53}$$

where v_G is the velocity of the point G, and v_m is the velocity of the payload. The velocity of point G is given by

$$\vec{v}_G = \dot{x}\hat{I}, \tag{54}$$

and the velocity of the payload is

$$\vec{v}_m = \big(d_S\dot{\theta} + \dot{x}\cos\theta + \ell\dot{\beta}\cos(\beta - \theta)\big)\hat{\imath} + \big(-\dot{x}\sin\theta + \ell\dot{\beta}\sin(\beta - \theta)\big)\hat{\jmath}. \tag{55}$$

Substituting (54) and (55) into (53) and simplifying gives the following expression for the kinetic energy:

$$\begin{aligned} T =& \frac{1}{2}M\dot{x}^2 + \frac{1}{2}(I_G + md_S^2)\dot{\theta}^2 \\ &+ \frac{1}{2}m\left[\dot{x}^2 + (\ell\dot{\beta})^2 + 2\ell\dot{\beta}\dot{x}\cos\beta + 2d_S\dot{\theta}\dot{x}\cos\theta + 2\ell d_S\dot{\beta}\dot{\theta}\cos(\beta - \theta)\right]. \end{aligned} \tag{56}$$

The total potential energy of the helicopter and suspended load is

$$V = mg\left(-L\cos\beta + d_S\cos\theta\right), \tag{57}$$

where the potential energy datum is a horizontal line passing through point G. Equations (56) and (57) express the kinetic and potential energy of the system as functions of the generalized coordinates and velocities. These functions can be differentiated with respect to the generalized coordinates for use in Lagrange's equations.

The generalized forces were found using the method of virtual displacements. The generalized force for the helicopter position generalized coordinate x is

$$Q_x = -F\sin\left(\alpha + \theta\right) - c_x\dot{x} \tag{58}$$

The generalized force for the helicopter attitude generalized coordinate θ is

$$Q_\theta = F d_T \sin\alpha - c_\theta \dot{\theta} \tag{59}$$

The generalized force for the payload deflection angle generalized coordinate β is

$$Q_\beta = 0 \tag{60}$$

The partial derivatives of T and V with respect to the generalized coordinates and velocities are:

$$\begin{aligned}
\frac{\partial T}{\partial x} &= 0 && (61)\\
\frac{\partial T}{\partial \theta} &= -m d_S \big(\dot{x}\sin\theta - \ell\dot{\beta}\sin(\beta-\theta)\big)\dot{\theta} && (62)\\
\frac{\partial T}{\partial \beta} &= -m\ell \big(\dot{x}\sin\beta + d_S\dot{\theta}\sin(\beta-\theta)\big)\dot{\beta} && (63)
\end{aligned}$$

$$\begin{aligned}
\frac{\partial V}{\partial x} &= 0 && (64)\\
\frac{\partial V}{\partial \theta} &= -mgd_S\sin\theta && (65)\\
\frac{\partial V}{\partial \beta} &= -mg\ell\sin\beta && (66)
\end{aligned}$$

$$\begin{aligned}
\frac{\partial T}{\partial \dot{x}} &= (M+m)\dot{x} + m\ell\dot{\beta}\cos\beta + md_S\dot{\theta}\cos\theta && (67)\\
\frac{\partial T}{\partial \dot{\theta}} &= (I_G + md_s^2)\dot{\theta} + (md_S\cos\theta)\dot{x} + m\ell d_S\cos(\beta-\theta)\dot{\beta} && (68)\\
\frac{\partial T}{\partial \dot{\beta}} &= m\ell\big(\ell\dot{\beta} + \dot{x}\cos\beta + d_S\dot{\theta}\cos(\beta-\theta)\big) && (69)
\end{aligned}$$

The time derivatives of (67), (68), and (69) are:

$$\begin{aligned}
\frac{d}{dt}\left(\frac{\partial T}{\partial \dot{x}}\right) &= (M+m)\ddot{x} + (md_S\cos\theta)\ddot{\theta} + (m\ell\cos\beta)\ddot{\beta} \\
&\quad -(md_S\sin\theta)\dot{\theta}^2 - (m\ell\sin\beta)\dot{\beta}^2 \qquad (70) \\
\frac{d}{dt}\left(\frac{\partial T}{\partial \dot{\theta}}\right) &= (md_S)\ddot{x} + (I_G + md_s^2)\ddot{\theta} + \big(m\ell d_S\cos(\beta-\theta)\big)\ddot{\beta} \\
&\quad -m\ell d_S\sin(\beta-\theta)\dot{\beta}^2 + m\ell d_S\sin(\beta-\theta)\dot{\theta}\dot{\beta} - (md_S\sin\theta)\dot{x}\dot{\theta} \qquad (71) \\
\frac{d}{dt}\left(\frac{\partial T}{\partial \dot{\beta}}\right) &= (m\ell\cos\beta)\ddot{x} + m\ell d_S\cos(\beta-\theta)\ddot{\theta} + (m\ell^2)\ddot{\beta} \\
&\quad +m\ell d_S\sin(\beta-\theta)\dot{\theta}^2 - m\ell d_S\sin(\beta-\theta)\dot{\theta}\dot{\beta} - m\ell\sin\beta\dot{x}\dot{\beta} \qquad (72)
\end{aligned}$$

The generalized forces (58) through (60), differentiated terms (61) through (66), and (70) through (72) are substituted into Lagrange's equation (52). This yields the following equations of motion for x, θ, and β:

$$\begin{aligned}
&(M+m)\ddot{x} + (md_S\cos\theta)\ddot{\theta} + (m\ell\cos\beta)\ddot{\beta} + (md_S\sin\theta)\dot{\theta}^2 - (m\ell\sin\beta)\dot{\beta}^2 \\
&= -F\sin(\alpha+\theta) - c_x\dot{x}
\end{aligned} \qquad (73)$$

$$\begin{aligned}
&(md_S\cos\theta)\ddot{x} + (I_G + md_S^2)\ddot{\theta} + m\ell d_S\cos(\beta-\theta)\ddot{\beta} - m\ell d_S\sin(\beta-\theta)\dot{\beta}^2 \\
&- gmd_S\sin\theta = Fd_T\sin\alpha - c_\theta\dot{\theta}
\end{aligned} \qquad (74)$$

$$(m\cos\beta)\ddot{x} + md_S\cos(\beta-\theta)\ddot{\theta} + (m\ell)\ddot{\beta} + md_S\sin(\beta-\theta)\dot{\theta}^2 + mg\sin\beta = 0 \qquad (75)$$

These equations describe the dynamics of the helicopter translation, helicopter orientation, and the payload swing for this model. The correctness of the equations was verified using a commercial dynamic modeling software package [43], and the program given in Appendix B.3. After factoring m out of (75), the equations of motion are given by:

$$\left[\begin{array}{c|c|c} M+m & md_S\cos\theta & m\ell\cos\beta \\ \hline md_S\cos\theta & I_G+md_S^2 & m\ell d_S\cos(\beta-\theta) \\ \hline \cos\beta & d_S\cos(\beta-\theta) & \ell \end{array}\right]\left[\begin{array}{c} \ddot{x} \\ \ddot{\theta} \\ \ddot{\beta} \end{array}\right]=\left[\begin{array}{c} -\dot{x}c_x+m(d_S\sin\theta+\ell\sin\beta)\dot{\theta}^2 \\ -F\sin(\alpha+\theta) \\ \hline md_S\big(\ell\sin(\beta-\theta)\dot{\theta}^2-g\sin\theta\big) \\ +k_\alpha\alpha-c_\theta\dot{\theta}+(d_T\sin\alpha)T \\ \hline -d_S\sin(\beta-\theta)\dot{\theta}^2-g\sin\beta \end{array}\right] \tag{76}$$

7.3.3 Parameter Estimation

Several parameters of the helicopter-load system were directly measured. The helicopter mass is $M = 1.724\ kg$ (composed of $1.134\ kg$ for the helicopter itself and $0.590\ kg$ for the carts), the load mass is $m = 0.312\ kg$, and the suspension cable length is $\ell = 1.2\ m$. The distance from the center of gravity to the suspension point is $d_S = 8.0\ cm$, and the center of gravity to main rotor hub distance is $d_T = 13.0\ cm$. The center of gravity location was determined by physically balancing the helicopter and rotating base on a support point. That is, the rotating base was detached from the carts, the helicopter and base were rotated perpendicular to the ground, and a small support was placed under different parts of the helicopter. The center of gravity was the point at which the helicopter and base physically balanced

System-identification software was used to estimate the parameter values in (76) that could not be directly measured. The helicopter was flown along the guide rails while the helicopter and load states were recorded. A sinusoidal input that tested the helicopter over a range of input frequencies was generated. The helicopter velocity, pitch angle, and load swing angle were used for model fitting.

Figure 124 shows the experimental and simulated responses to a sinusoidal $\alpha(t)$ input with increasing frequency. The simulated helicopter velocity and pitch angle peaks have slightly lower magnitudes than the experimental data, but provide a fairly good fit. Simulated load swing is very similar to the experimentally recorded swing.

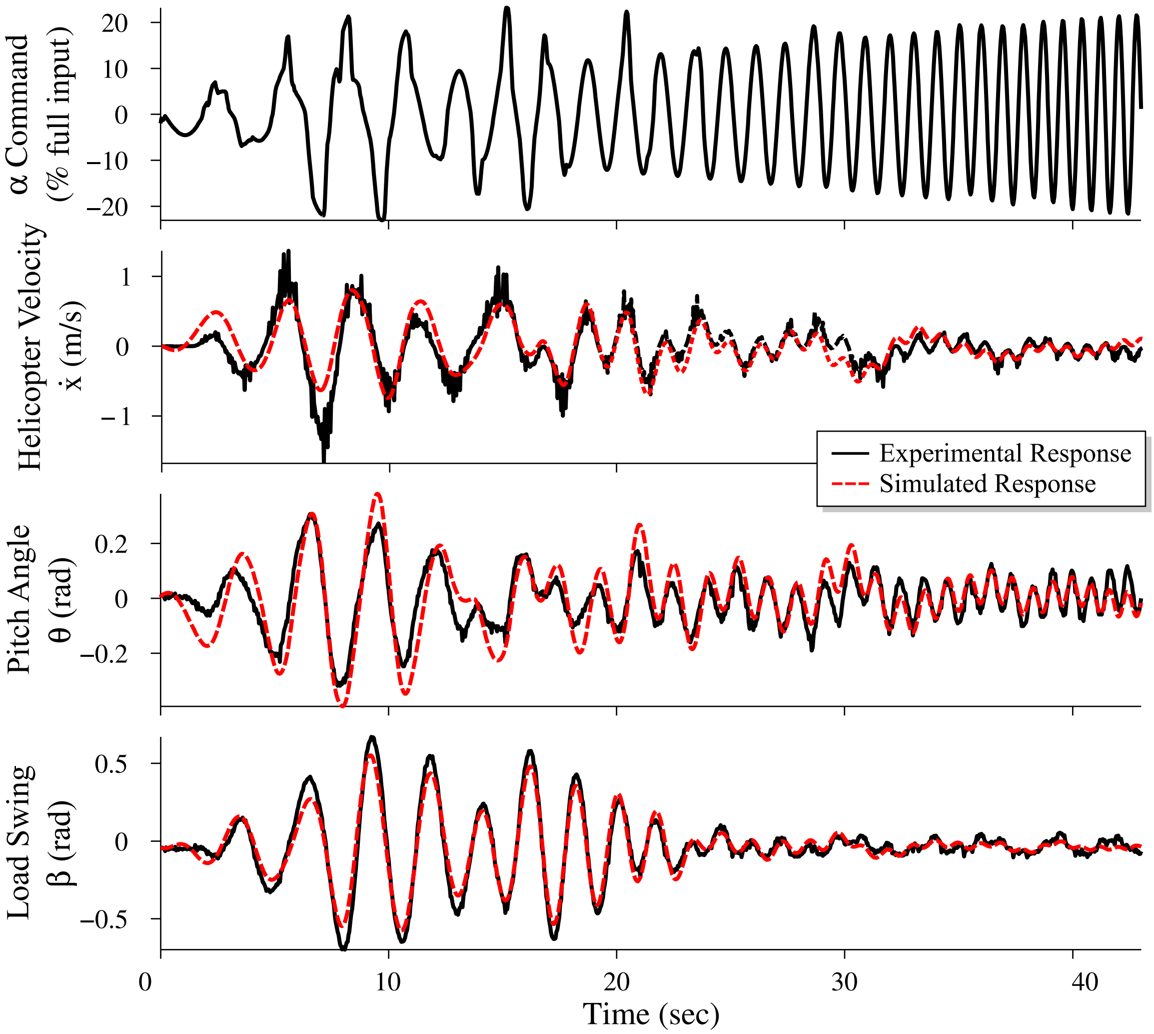

Figure 124: Time responses to α frequency sweep

In order to obtain the simulation results shown in Figure 124, the experimental data sets and (76) were used in a nonlinear grey-box model identification routine. The routine accepts information about which parameters are already known (these parameters are held constant, and are given a *fixed* constraint), and it varies those which are not. A range of acceptable values can be specified for non-fixed parameters. It produces a set of parameter values that result in responses which most-closely match the experimental data in a least sum-of-squared-errors sense. The constraints for each parameter, along with the final values, are shown in Table 17.

A suspended load mass of 0.312 kg is used for this paper. This load was heavy

Table 17: Dynamic model parameters

Parameter	Units	Constraint	Value
M	kg	Fixed	1.724
m	kg	Fixed	0.312
ℓ	m	Fixed	1.20
d_S	cm	Fixed	8.0
d_T	cm	Fixed	13.0
I_G	$kg \cdot m^2$	≥ 0	0.0857
c_x	$\frac{N \cdot s}{m}$	≥ 0	3.6035
c_θ	$\frac{N \cdot m \cdot s}{rad}$	≥ 0	0.1795
k_α	$\frac{N \cdot m}{rad}$	≥ 0	390.87

enough to affect the helicopter motion, but light enough to allow several minutes of flight time on one battery charge.

7.3.4 Dynamic Behavior

Figure 125 shows a pole-zero plot for the helicopter-load dynamic model. The effect of different poles can be identified by analyzing the eigenvector corresponding to each pole's eigenvalue [41, 1].

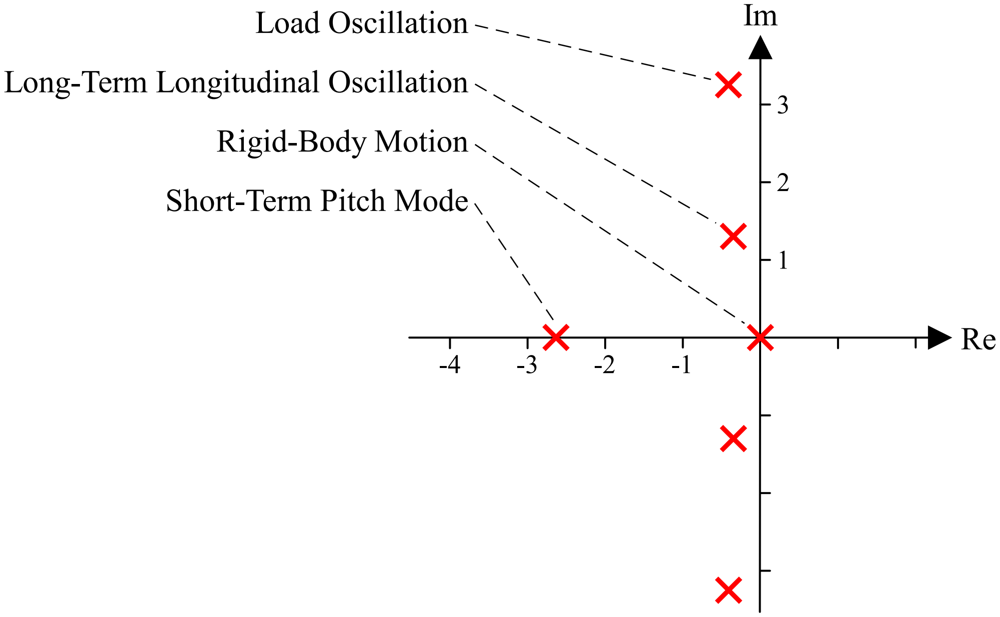

Figure 125: Poles of dynamic model linearized about hover

The pole at the origin is the helicopter's longitudinal *rigid-body motion*. Two modes strongly couple the helicopter pitch and longitudinal velocity – the *short-term pitch mode* represents the fast coupling effects, and the underdamped *long-term longitudinal oscillation* poles represent the slower coupling effects. The lightly damped *load oscillation* mode represents the suspended load swing. A planar helicopter model in [50] found a similar pair of lightly damped modes, and simply called them the *helicopter mode* and the *load mode*.

7.4 Control With a Virtual Pilot

Helicopter control is often broken into two main feedback loops: the *inner loop* drives the helicopter to a desired angle (or *attitude*), and the *outer loop* drives the helicopter to a desired position by specifying the desired angle that is given to the inner loop controller [40]. Several control schemes that use this inner/outer loop organization have been used to approximate the control behavior of human pilots. One such model is the *Simplified Pursuit* model, which was developed as "... a unified, albeit simplified, pilot modelling approach that requires a minimum set of application rules and that is applicable to the study of realistic piloting tasks [32]."

The Simplified Pursuit model is shown in Figure 126 [32]. It contains four gains

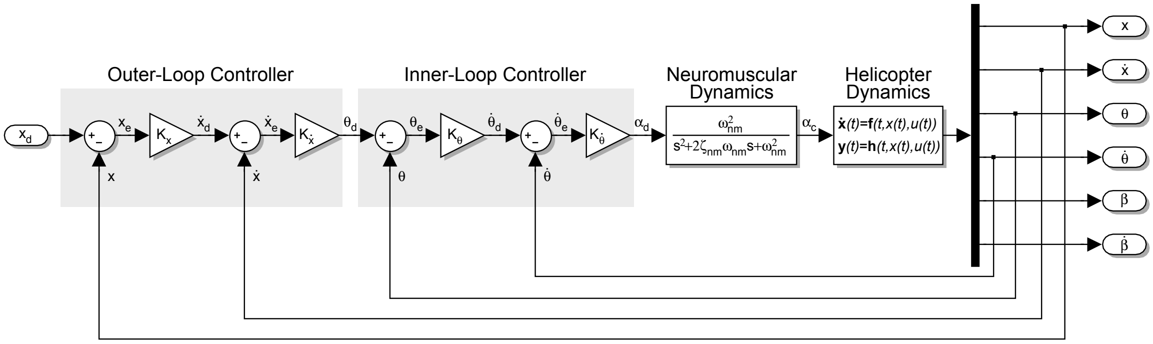

Figure 126: Model helicopter controlled by virtual pilot

and a second-order filter which represents the pilot's neuromuscular dynamics. Desired position x_d is compared to the current position x, and the difference x_e is multiplied by gain K_x to specify the desired velocity $\dot{x}_d$. This is compared to the current velocity $\dot{x}$, and the difference $\dot{x}_e$ is used to specify the desired pitch angle θ_d. After two more comparisons, a desired disk-angle command α_d is determined. This is sent through the neuromuscular filter to create the α_c command issued to the helicopter.

The neuromuscular parameters ω_{nm} and ζ_{nm} have been determined experimentally [27]. The gains K_x, $K_{\dot{x}}$, K_θ, and $K_{\dot{\theta}}$ are tuned by closing one loop at a time and using humanly attainable values for the performance of each loop, as quantified by responses in the frequency domain.

To tune $K_{\dot{\theta}}$, the frequency response of $\frac{\dot{\theta}(j\omega)}{\dot{\theta}_d(j\omega)}$ is computed, and the gain is increased until the pilot's neuromuscular mode creates a magnitude peak that is 5 dB above the low-frequency baseline magnitude. K_θ is tuned to yield a crossover frequency of 1 $\frac{rad}{sec}$ in the $\frac{\theta(j\omega)}{\theta_e(j\omega)}$ frequency response. $K_{\dot{x}}$ is tuned to yield a crossover frequency of 1 $\frac{rad}{sec}$ in $\frac{\dot{x}(j\omega)}{\dot{x}_e(j\omega)}$, and K_x is tuned for a crossover frequency of 1/3 $\frac{rad}{sec}$ in $\frac{x(j\omega)}{x_e(j\omega)}$. For additional details about the tuning method, see [32]. To reflect the reduced aggressiveness of helicopter pilots when carrying suspended loads, these crossover-frequency values are less aggressive than the ones prescribed in [32].

7.5 Dynamic Scaling

The goal of this research is to draw conclusions applicable to full-scale helicopters with human pilots. The model helicopter has much faster dynamics than full-scale helicopters, and unaugmented human pilot dynamics would be comparatively much slower [13, 22]. Therefore, the pilot needs to be "faster" to match the fast dynamics of the model helicopter. This is accomplished by using the pilot model from the previous section, but with dynamically scaled parameter values.

Table 18: Dynamically scaled human pilot parameters

Parameter	Full-Scale (Robinson R22)	Simulation (E-Flite Blade 400)
$D_{Main\ Rotor}$	$7.67\ m$	$0.71\ m$
ω_{nm}	$10\ \frac{rad}{s}$	$32.87\ \frac{rad}{s}$
ζ_{nm}	0.707	0.707
$\omega_{crossover}^{\theta\ loop}$	$1\ \frac{rad}{s}$	$3.29\ \frac{rad}{s}$
$\omega_{crossover}^{\dot{x}\ loop}$	$1\ \frac{rad}{s}$	$3.29\ \frac{rad}{s}$
$\omega_{crossover}^{x\ loop}$	$0.33\ \frac{rad}{s}$	$1.10\ \frac{rad}{s}$

Dynamic scaling has been used to compare frequency, time, velocity, and geometric parameters between helicopters of different sizes [62, 63]. While the small-scale helicopters in those studies were larger than the helicopter in this testbed (main-rotor diameters of 1.54 m vs. 0.71 m), it is expected that the same techniques should apply reasonably well to the current helicopter.

First, the ratio of helicopter sizes is computed, often using main rotor diameter as the characteristic length: $N = \frac{D_{full}}{D_{model}}$. This scaling factor N can be used to adjust other parameters using the following Froude scaling relationships [62]:

$$L_{model} = \left(\frac{1}{N}\right) L_{full} \tag{77}$$

$$\omega_{model} = \left(\sqrt{N}\right) \omega_{full} \tag{78}$$

$$v_{model} = \left(\frac{1}{\sqrt{N}}\right) v_{full} \tag{79}$$

$$\tau_{model} = \left(\frac{1}{\sqrt{N}}\right) \tau_{full} \tag{80}$$

where L, ω, v, and τ are length, frequency, velocity, and time. Using these dynamic scaling factors, parameters of the virtual pilot and Depart/Abort task were modified to the values shown in Table 18. The full-scale helicopter chosen for comparison was the Robinson R22, a light utility helicopter.

Feedback controller gains were tuned using the helicopter dynamic model in (76) and the modified pilot parameters given in Table 18. Figure 127 shows frequency

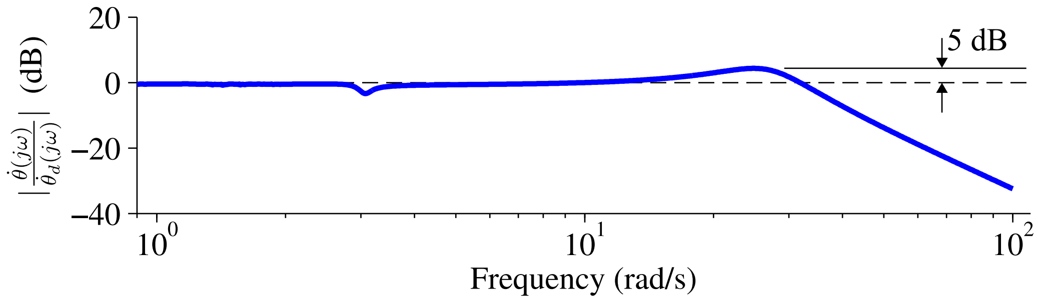

(a) Tuning $K_{\dot{\theta}}$

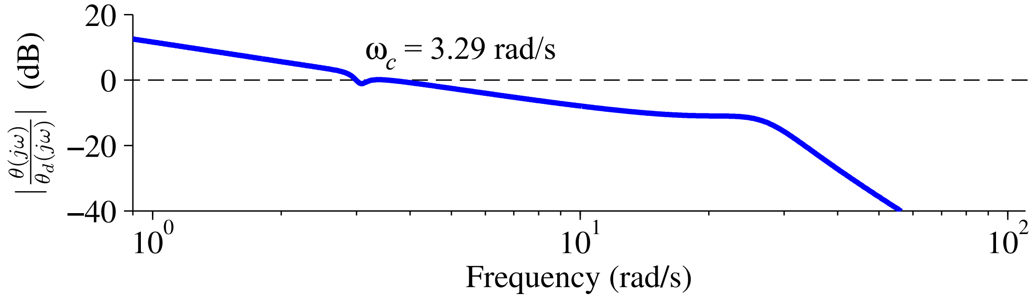

(b) Tuning K_θ

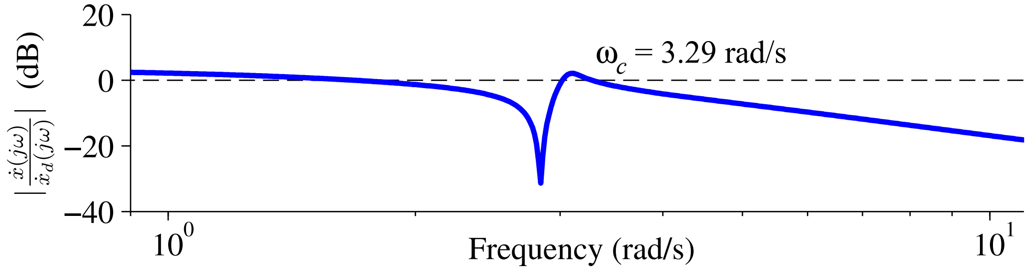

(c) Tuning $K_{\dot{x}}$

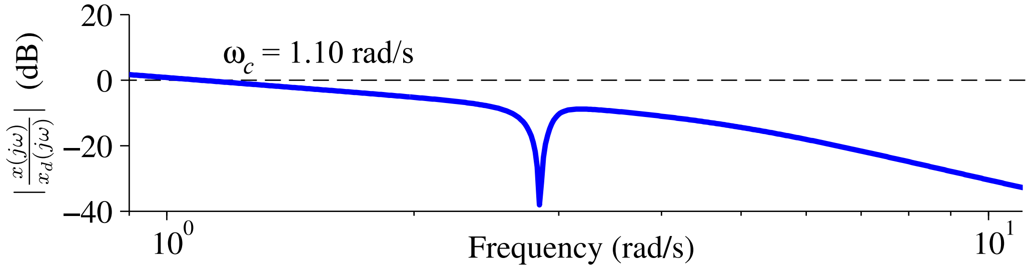

(d) Tuning K_x

Figure 127: Gain tuning for Simplified Pursuit model with 0.155 load-mass ratio

response magnitude curves for each of the feedback loops to be tuned. The tuning rules described in the previous section yielded gain values of $K_{\dot{\theta}} = 3.181$, $K_\theta = 5.334$, $K_{\dot{x}} = -0.716$, and $K_x = 2.468$. Note that $K_{\dot{x}}$ has a negative value because of the variable definitions in Figure 122. A positive velocity is produced by rotating the helicopter forward (nose-down), which is defined as a negative pitch rotation. If any of the dynamic parameter values in Tables 17 or 127 are modified, the tuning procedure must be repeated.

The ratio of main rotor diameters yields a scaling factor of $N = 10.80$. This scaling factor will be used to modify the prescribed distances and time durations used for a common helicopter evaluation task, described in the next section.

7.6 Input Shaping on Different Response Types

Human pilots use a control stick (the “cyclic” stick) to control a helicopter’s horizontal motion. Most modern helicopters are equipped with automatic feedback controllers which can improve stability and performance. These feedback controllers can also be used to change the *type* of helicopter response to the pilot’s commands. For example, an Attitude Command response type means that the pilot’s stick input specifies a desired angle for the helicopter, and the automatic feedback controller drives the helicopter to this angle. Other response types can allow the pilot’s stick input to specify a desired horizontal velocity, angular rate, position, etc.

This thesis will focus on the four response types shown in Figure 128. The pilot’s input δ is converted into one of four commanded states that the helicopter automatically pursues: α_c, $\dot{\theta}_c$, θ_c, or $\dot{x}_c$. These are called Unaugmented, Angular Rate,

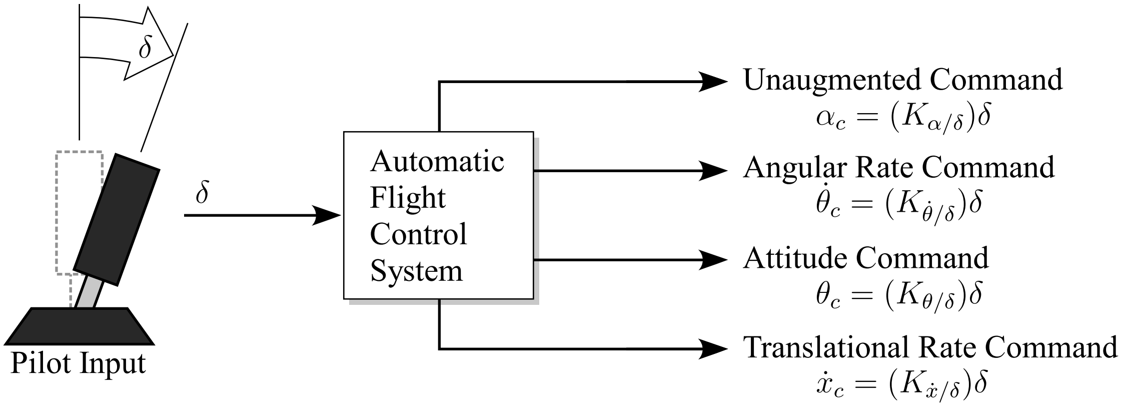

Figure 128: Different helicopter responses to pilot input

Attitude, and Translational Rate Commands, respectively. A Position Command response type also exists, but it will not be addressed in this thesis. The Position Command is less common than the response types listed in Figure 128, and it has not been the focus of ADS-33E, or of the major reports on suspended-load handling qualities [65, 33].

The gains $K_{\alpha/\delta}$ through $K_{\dot{x}/\delta}$ in Figure 128 are scaling factors between the stick-input magnitude and the commanded-state magnitude (for example, $K_{\dot{x}/\delta}$ could be $2\ \frac{m}{s}\frac{1}{^\circ\ \text{stick angle}}$ for a Translational Rate Command). The three augmented response types are extensively discussed in ADS-33E.

To simulate different response types, this section will apply the pilot's neuromuscular filter to the desired command. Input shaping is then applied to the filtered command. The flight-control-system gains "downstream" of the pilot input are not changed from their original values because the human-like controller is a well-tuned control system with good performance in the frequency range of manual control, and it is assumed that an automatic feedback controller would be tuned to behave similarly.

In the following sections, Depart/Abort maneuvers will be simulated with input shaping applied to the chosen response types, and performance metrics will be used to compare the effectiveness in each case. The Depart/Abort maneuver is illustrated in Figure 129. The helicopter begins in a stable hover, moves forward a prescribed distance x_{travel}, and resumes hovering over a target position. For full-scale helicopters,

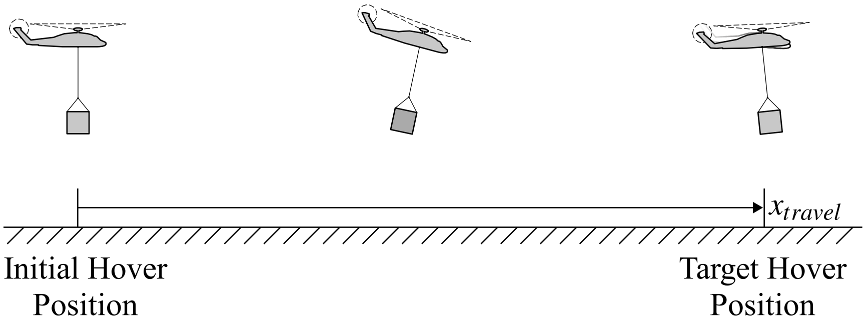

Figure 129: Depart/Abort maneuver

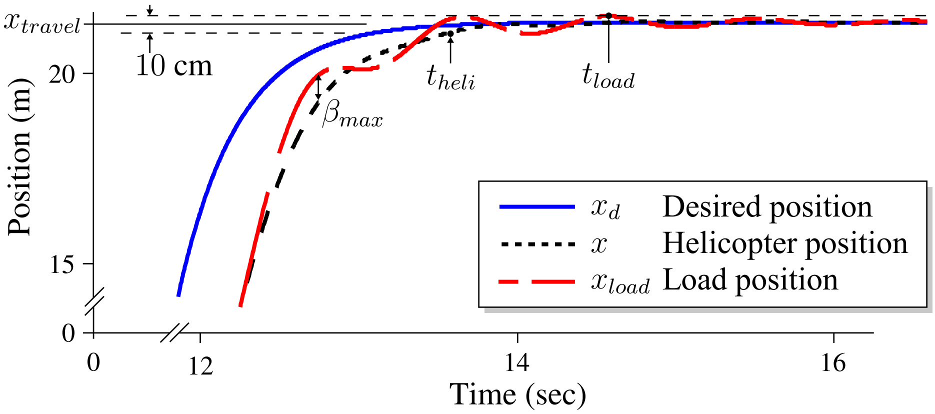

Figure 130: Performance metrics for horizontal repositioning maneuvers

the move distance is $x_{travel} = 243.84\ m$, and should be completed in 35 sec for adequate performance with a suspended load [4].

Using the dynamic scaling from Table 18, the model helicopter should complete a 22.58 m maneuver in 10.65 sec for adequate performance. A trajectory for $x_d(t)$ (desired position) was specified and the virtual pilot and flight control system attempted to follow the trajectory. The trajectory was a ramp with slope $\frac{22.58\ m}{10.65\ sec} = 2.12\ m/s$, filtered through a first-order low-pass filter with time constant 0.91 sec.

The performance metrics illustrated in Figure 130 are computed for each Depart/Abort maneuver. Figure 130 shows the very end of the maneuver where the helicopter and load decelerate to a hover over the target position. The time at which the helicopter and load stay within ±5 cm of the final position are defined as t_{heli} and t_{load}, respectively. The maximum swing angle at any point in the maneuver is defined as β_{max}.

When a suspended load must be deposited in a specific location, the pilot may compare the load's current position to its desired position, and make control decisions based on this difference. In other words, the pilot may use load position instead of helicopter position in the outer-most control loop. To mimic this load-positioning situation, a modification to the Simplified Pursuit model is defined in Figure 131. For helicopter positioning in Figure 131(a), desired position is compared to the helicopter

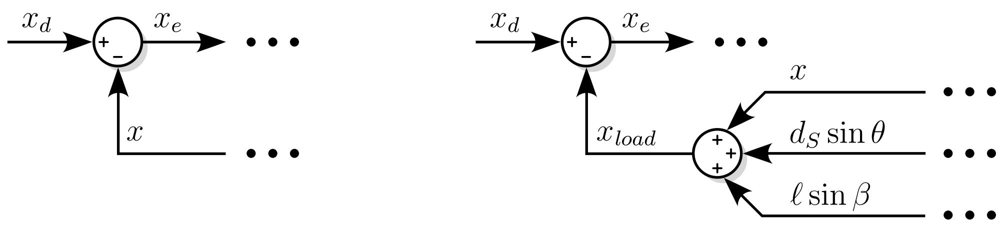

(a) Helicopter positioning (b) Load positioning

Figure 131: Outer-loop position control

position x, and the position error x_e is used to specify a desired velocity. For load positioning in Figure 131(b), desired position is instead compared to the load position to form x_e. Load position is given by

$$x_{load} = x + d_S \sin\theta + \ell \sin\beta. \tag{81}$$

To determine load-swing mode frequencies and damping ratios for different response types, the response of each system to pilot stick input was linearized about hover. The load-swing pole was then identified on a pole-zero plot (as shown in Figure 125). The resulting swing modes are shown in Table 19.

For comparison, the common approximation for the load swing frequency is:

$$\omega_L = \sqrt{\frac{g}{\ell}\left(\frac{1}{1-LMR}\right)} = \sqrt{\frac{9.81}{1.2}\left(\frac{1}{1-0.155}\right)} = 3.11\ rad/s \tag{82}$$

This gives an estimate that is within 8% of the true swing frequencies for any of the response types. Input shapers can easily be designed to accommodate this error. However, for the following sections, input shapers will be designed with the accurate frequencies and damping ratios in Table 19.

Table 19: Load-swing modes for different response types

	Response Type			
	Unaugmented	Angular Rate	Attitude	Translational Rate
ω_n (rad/s)	3.28	3.02	3.01	2.87
ζ	0.13	0.05	0.04	0.06

Table 20: Input shapers applied to different response types

Input Shaper	$V_{partial}$ (%)	Impulse Amplitudes					Impulse Times (sec)				
None	N/A	[1]					[0]				
ZV	0	[0.56	0.44]				[0	1.05]			
	25	[0.70	0.30]				[0	1.05]			
SNA(0.5)	0	[0.81	-0.500	0.69]			[0	0.43	0.82]		
	25	[0.87	-0.35	0.48]			[0	0.43	0.82]		
UMZV	0	[1	-1	1]			[0	0.40	0.70]		
	25	[1	-0.70	0.70]			[0	0.40	0.70]		
ZVD	0	[0.32	0.49	0.19]			[0	1.05	2.10]		
	25	[0.60	0.29	0.11]			[0	1.05	2.10]		
RM$_3$	0	[0.85	0.38	-0.23]			[0	1.12	2.01]		
	25	[0.91	0.23	-0.14]			[0	1.12	2.01]		
RM$_4$	0	[0.92	0.18	-0.25	0.15]		[0	1.09	2.16	3.05]	
	25	[0.96	0.08	-0.12	0.07]		[0	1.09	2.16	3.05]	
RM$_4$D	0	[0.72	0.46	-0.33	0.15]		[0	1.04	2.11	4.21]	
	25	[0.91	0.14	-0.10	0.05]		[0	1.04	2.11	4.21]	
RM$_5$	0	[0.96	0.10	-0.12	0.17	-0.10]	[0	1.09	2.13	3.20	4.10]
	25	[0.99	0.03	-0.04	0.06	-0.03]	[0	1.09	2.13	3.20	4.10]
RM$_5$D	0	[0.72	0.51	-0.31	-0.05	0.14]	[0	1.08	2.07	3.41	4.13]
	25	[0.91	0.16	-0.10	-0.02	0.04]	[0	1.08	2.07	3.41	4.13]

7.6.1 Input Shapers

Each response type in Figure 128 was tested with a variety of full and partial input shapers shown in Table 20. The input shapers in are designed for a natural frequency of 3.0 rad/s, and a damping ratio of 0.08. The input shapers used for each response type will be similar to those in Table 20, but with slight changes due to the differing swing frequency and damping ratio for each response type.

Table 20 lists the impulse amplitudes of each input shaper, and the respective time locations of the impulses. The conventional and new input shapers are separated by dashed lines. Partial versions of the input shapers in Table 20 allow 25% residual vibration at the modeled frequency. The first impulse amplitude of these partial input shapers gets larger and the other impulse amplitudes shrink. The impulse times are unchanged. Allowing increasingly large amounts of vibration for any of the input shapers makes the first impulse amplitude approach 1, and makes later impulses amplitudes approach zero, rendering their time locations unimportant. A more thorough description of partial input shaping was given in Section 4.2.

Reports on helicopter pilot-induced oscillation have concluded that both flexibility and time delays are undesirable [59, 66]. With input shaping, we are essentially introducing small, strategic time delays to suppress highly detrimental flexibility. Partial input shaping allows a compromise that suppresses only some of the vibration while introducing smaller time delay effects than the original input shaper.

The next sections present results from simulated Depart/Abort maneuvers using each of the response types in Figure 128. Input shapers from Table 20 are applied to pilot commands. The pilot-like controller is not retuned after input shaping is added to the control system. This means that any positive results of input shaping in the following sections are achieved without requiring pilot adjustment or retraining.

7.6.2 Unaugmented Command

Figure 132 shows the control system for an Unaugmented Command response type. The pilot's stick input commands a rotor disk angle, α_c. Input shaping is applied to create the shaped command, α_c^*. Table 21 shows the performance metrics for Depart/Abort maneuvers with this control system.

The simulation duration was set to 120 seconds. If t_{heli} or t_{load} is equal to 120, it

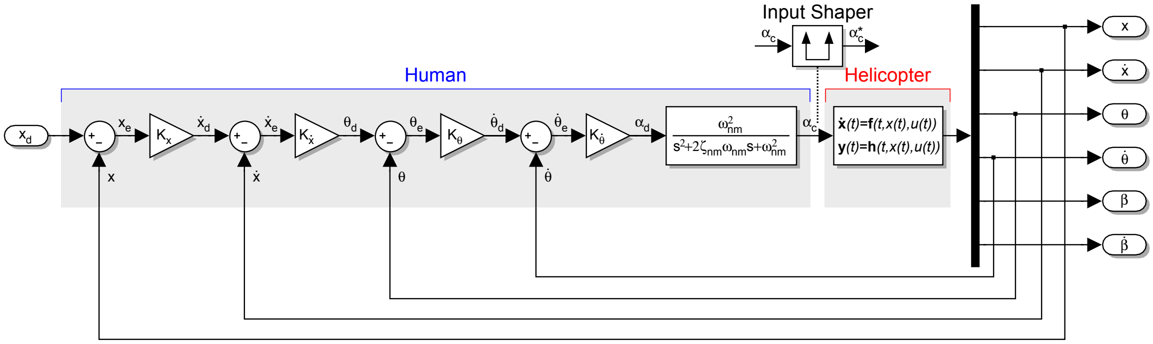

Figure 132: Control system for Unaugmented Command

Table 21: Depart/Abort maneuvers for Unaugmented Command

Input Shaper	$V_{partial}$ (%)	Helicopter Positioning			Load Positioning		
		t_{heli}	t_{load}	β_{max}	t_{heli}	t_{load}	β_{max}
None		13.52	14.89	13.46	120	120	134.45
ZV	0	28.82	28.87	9.44	120	120	1216.68
	25	19.41	19.41	11.24	120	120	141.31
SNA(0.5)	0		N/A			N/A	
	25		N/A			N/A	
UMZV	0		N/A			N/A	
	25		N/A			N/A	
ZVD	0		N/A			N/A	
	25		N/A		120	120	140.54
RM_3	0	13.59	16.88	13.14	120	120	138.76
	25	13.57	15.75	13.06	120	120	137.02
RM_4	0	13.58	16.75	13.06	120	120	137.12
	25	13.57	15.68	13.03	120	120	135.15
RM_4D	0	13.66	20.04	13.29	120	120	1236.71
	10	13.57	15.73	13.07	120	120	136.86
RM_5	0	13.58	15.69	13.03	120	120	135.22
	10	13.58	15.67	13.02	120	120	134.96
RM_5D	0	13.64	21.04	13.31	120	120	871.10
	10	13.57	16.84	13.12	120	120	139.02

means that a steady hover was not attained. In some cases, the helicopter and load reached a stable limit cycle, and in other cases, the system was unstable. Unstable cases are most easily identified by extremely large maximum swing angles (for example, $\beta_{max} = 134.45°$ for the unshaped case). For systems that reached a steady state, the swing angle is usually less than 30°. In other unstable cases, the simulation was unable to finish because the program ran out of memory. These cases are labeled N/A in Table 21.

None of the input shapers improved the load or helicopter settling times. In fact, only the ZV and RM input shapers maintained a stable helicopter-positioning system. These shapers slightly reduced the peak swing angle, but the load required longer to settle. For load positioning, all cases were unstable, including the unshaped case.

7.6.3 Angular Rate Command

Figure 133 shows the helicopter control system with an Angular Rate Command response type. The human gives a pitch rate command, $\dot{\theta}_c$, and the helicopter's automatic flight control system attempts to make the helicopter attain this pitch rate. Input shaping is applied to $\dot{\theta}_c$ to create the shaped command $\dot{\theta}_c^*$. Simulation results are shown in Table 22.

For helicopter positioning, the 5-impulse RM shaper appeared to yield the best performance, but it was not improved from the unshaped case for the chosen performance metrics. Once again, allowing $V_{partial} = 25\%$ was beneficial to performance for all input shapers.

Load positioning did not converge under any input-shaping condition (including no input shaping). This means that the helicopter pilot would need to modify his or her control strategy if using only the load as the outer-loop reference position. Retuning gains in the pilot model with input shaping included in the control system may be able to improve performance with the input-shaped cases. However, the next sections will show that other response types do perform well with input shaping without any pilot adjustment.

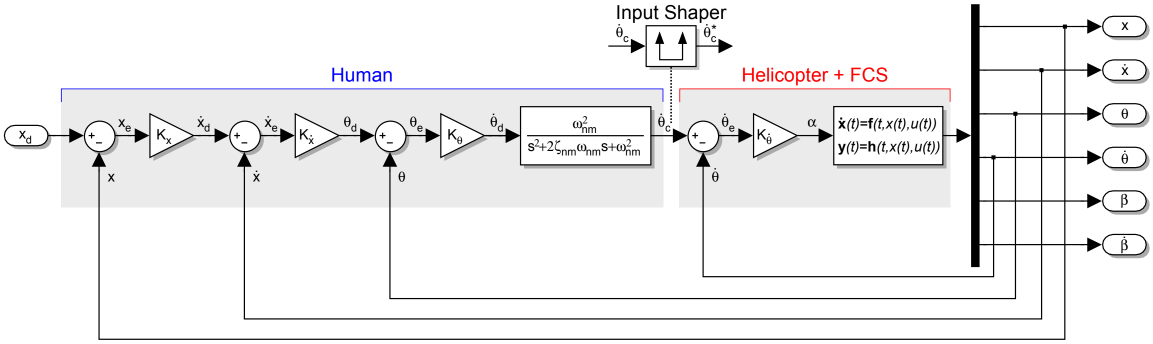

Figure 133: Control system for Angular Rate Command

Table 22: Depart/Abort maneuvers for Angular Rate Command

Input Shaper	$V_{partial}$ (%)	Helicopter Positioning t_{heli}	t_{load}	β_{max}	Load Positioning t_{heli}	t_{load}	β_{max}
None		13.55	15.77	13.47	120	120	136.44
ZV	0	30.55	119.16	15.94	120	120	1213.78
	25	15.09	19.56	14.15	120	120	509.55
SNA(0.5)	0	120	120	73.54	120	120	85.39
	25	17.96	29.99	15.09	120	120	92.09
UMZV	0	120	120	67.44	120	120	97.02
	25	15.49	24.58	14.46	120	120	95.7
ZVD	0	120	120	1613.98	120	120	6978.06
	25	120	120	20.04	120	120	77.99
RM_3	0	120	120	2994.06	120	120	1200.41
	25	14.98	33.45	15.9	120	120	877.74
RM_4	0	120	120	65.05	120	120	4428.65
	25	13.45	23.09	14.11	120	120	1236.31
RM_4D	0	120	120	3370.96	120	120	156.02
	25	29.32	71.08	17.77	120	120	107.09
RM_5	0	14.17	53.41	13.6	120	120	5140.96
	25	13.62	19.32	13.54	120	120	151.36
RM_5D	0	120	120	1558.46	120	120	134.98
	25	25.49	58.23	17.38	120	120	103.02

7.6.4 Attitude Command

Figure 134 shows the helicopter control system with an Attitude Command response type. The human gives a pitch angle command, θ_c, and the helicopter's automatic flight control system attempts to force the helicopter to this pitch angle. Input shaping is applied to θ_c to create the input-shaped command, θ_c^*. Simulation results are shown in Table 23.

For helicopter positioning, both the SNA and UMZV input shapers with $V_{partial} =$ 25% reduced the peak load swing and load settling time relative to the unshaped case. The RM_4 input shaper with $V_{partial} = 25\%$ also performed well. For all input shapers, allowing $V_{partial} = 25\%$ reduced the helicopter and load settling times.

For load positioning, only the ZVD input shaper with $V_{partial} = 25\%$ case converged to the target position. While it took over 30 seconds for the helicopter and

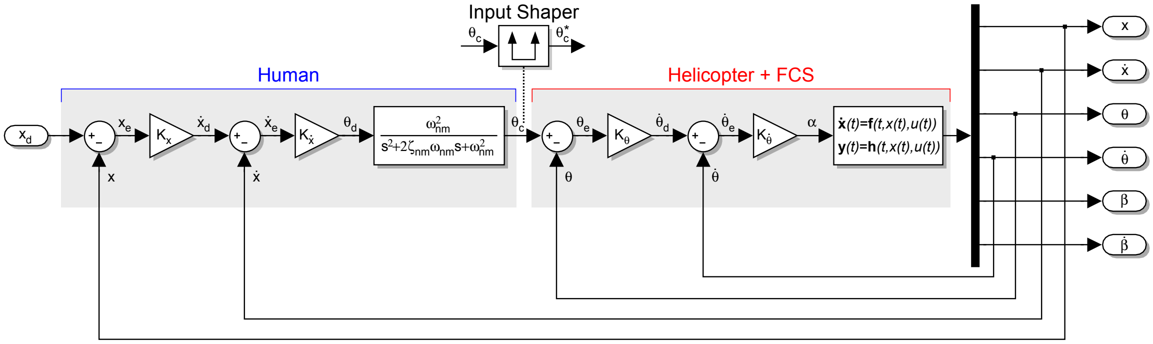

Figure 134: Control system for Attitude Command

load to settle over the target, the maximum swing of $\beta_{max} = 12.17°$ was very small, indicating that the load swing was under control. Note that the unshaped case was again unstable.

The addition of the partial-ZVD input shaper allowed the pilot to use the load

Table 23: Depart/Abort maneuvers for Attitude Command

Input Shaper	$V_{partial}$ (%)	Helicopter Positioning t_{heli}	t_{load}	β_{max}	Load Positioning t_{heli}	t_{load}	β_{max}
None		13.52	15.76	13.72	120	120	1319.42
ZV	0	24.74	28.29	13.11	120	120	38.74
	25	15.09	17.01	12.9	120	120	18.49
SNA(0.5)	0	17.29	18.97	12.04	120	120	30.58
	25	13.94	13.76	12.36	120	120	16.18
UMZV	0	15.4	18.45	11.46	120	120	15.47
	25	13.89	13.68	12.06	120	120	14.09
ZVD	0	120	120	34.53	120	120	64.52
	25	20.81	22.9	11.11	33.75	37.86	12.17
RM_3	0	20.39	29.21	12.69	120	120	58.97
	25	15.69	18.64	13.4	120	120	66.45
RM_4	0	18.2	29.11	13.35	120	120	82.94
	25	13.3	17.98	13.96	120	120	92.18
RM_4D	0	120	120	53	120	120	99.06
	25	21.93	29.76	13.12	120	120	56.47
RM_5	0	15.53	28.17	15.11	120	120	98
	25	15.25	17.65	14.47	120	120	155.97
RM_5D	0	120	120	51.34	120	120	100.48
	25	20.6	26.8	13.43	120	120	55.78

as a position reference instead of the helicopter. This important result will be further discussed in Section 7.6.7. Input shaping was more beneficial on the Attitude Command response type than on the Angular Rate Command.

7.6.5 Translational Rate Command

Figure 135 shows the helicopter control system with a Translational Rate Command response type. The human gives a longitudinal velocity command, $\dot{x}_c$, and the helicopter's automatic flight control system drives the helicopter to this velocity. Input shaping is applied to $\dot{x}_c$ to yield the input-shaped command $\dot{x}_c^*$. Simulation results are shown in Table 24.

The first thing to notice about Table 24 is that the helicopter positioning was stable for all of the tested input shapers. The SNA, UMZV, and RM$_4$ input shapers with $V_{partial} = 25\%$ were able to reduce the settling times and load swing relative to the unshaped case. Among the input shapers with $V_{partial} = 0$, the RM$_3$ shaper had the fastest helicopter settling time, the RM$_4$ shaper had the lowest load settling time, and the UMZV shaper had the smallest maximum swing angle. Partial input shaping again improved the helicopter and load settling times for all input shapers.

Load positioning was unstable without input shaping, and was stabilized by all conventional input shapers except for the ZV shaper. The SNA and UMZV input

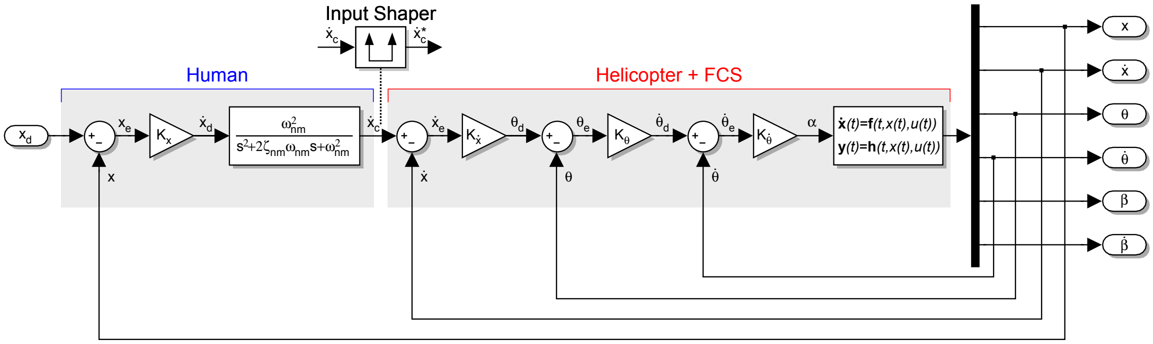

Figure 135: Control system for Translational Rate Command response type

Table 24: Depart/Abort maneuvers for Translational Rate Command

Input Shaper	$V_{partial}$ (%)	Helicopter Positioning			Load Positioning		
		t_{heli}	t_{load}	β_{max}	t_{heli}	t_{load}	β_{max}
None		13.52	14.89	13.46	120	120	134.9
ZV	0	28.82	28.87	9.44	120	120	57.26
	25	19.41	19.41	11.24	120	120	115.53
SNA(0.5)	0	15.41	15.42	9.03	14.52	14.46	10.39
	25	12.64	14.91	10.18	13.53	18.81	11.7
UMZV	0	15.14	15.22	8.82	14.25	14.12	10.27
	25	11.91	14.77	10.02	13.43	22.34	11.62
ZVD	0	35.55	35.76	10.4	46.18	46.4	12.77
	25	19.14	19.1	9.01	18.33	18.67	9.84
RM_3	0	14.36	17.3	12.25	50.49	69.36	15.14
	25	14.27	14.14	12.63	120	120	15.17
RM_4	0	15.09	14.98	12.85	120	120	55.71
	25	13.35	14.39	13.08	120	120	78.32
RM_4D	0	28.55	32.33	12.66	120	120	44.31
	25	16.11	16.05	12.39	17.24	120	15.41
RM_5	0	16.15	16.03	12.95	120	120	75.2
	25	15.42	15.43	13.3	120	120	108.19
RM_5D	0	26.94	29.02	11.86	120	120	41.71
	25	15.9	16.97	12.29	16.93	120	15.51

shapers yielded performance that was comparable to helicopter positioning. Interestingly, the ZVD shaper performed poorly in its original form, but performed well when $V_{partial}$ was increased to 25%. The RM shapers performed poorly for load positioning.

Input shaping was most beneficial for the Translational Rate Command. The remaining sections will focus mainly on this response type.

7.6.6 Experimental Validation

Depart/Abort maneuvers were performed on the experimental helicopter with input shaping applied to a Translational Rate Command response type. Due to the testbed's limited travel, move distances of 1.5 *m* and move times of 3 *sec* were used. The same controller gains were used for the experimental control system, except for $K_{\dot{\theta}}$, which was reduced by a factor of 3. Noise from differentiating the θ signal caused unsteadiness and stability problems when the original gain was used. Figure 136 shows experimental trials for helicopter positioning.

The two robust input shapers that performed poorly in simulation (ZVD and RM_4D) also performed poorly in this experiment, in that the helicopter overshot the target location and ran into the bumpers at the end of the guide rails. All other input shapers stayed well within the limits of the workspace. Most of the input shapers reduced the amplitude of residual load swing at the final position. The partial RM_4 and RM_5 shapers created a helicopter response much like the unshaped response, but the load responses were damped out more quickly. The SNA and UMZV shapers changed the helicopter response somewhat, but eliminated the load swing very quickly.

For load positioning, only the SNA and UMZV input shapers were able to perform the maneuver without hitting the end bumpers. Two trials with the SNA input shaper are shown in Figure 137(a), and two trials with the UMZV shaper are shown in Figure 137(b). Multiple trials are shown to demonstrate the system's repeatability. The SNA and UMZV responses are similar. The helicopter initially overshoots the target position, but then settles to a steady-state position that is close to the desired position. The steady-state error is not eliminated because the load is used for the position reference instead of the helicopter, and the load position oscillates near the desired position. Unlike in simulation, the experimental load swing does not vanish over time, and reaches a low-amplitude steady-state oscillation.

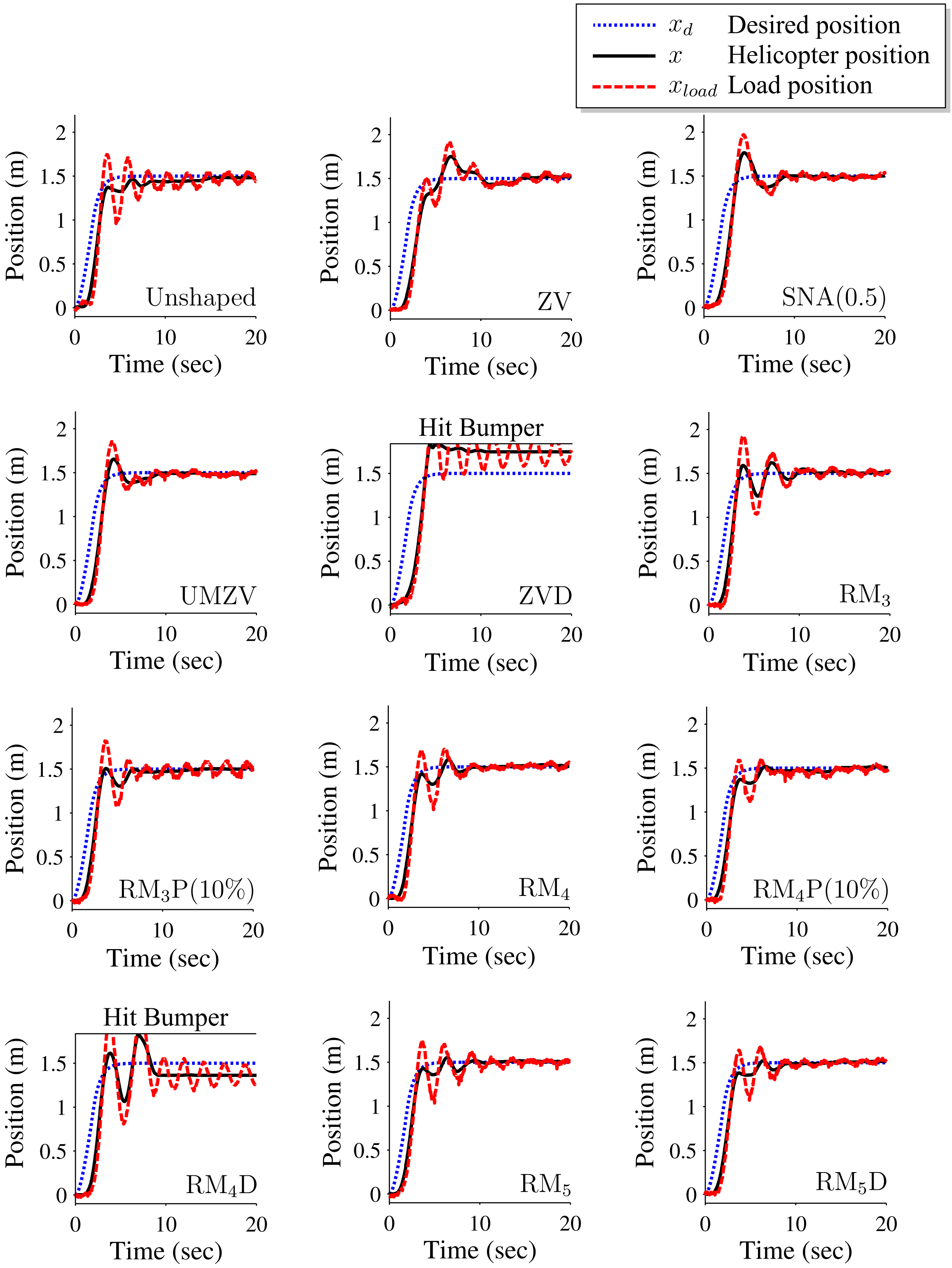

Figure 136: Experimental Depart/Abort maneuvers with input-shaped Translational Rate Command and helicopter-positioning outer loop

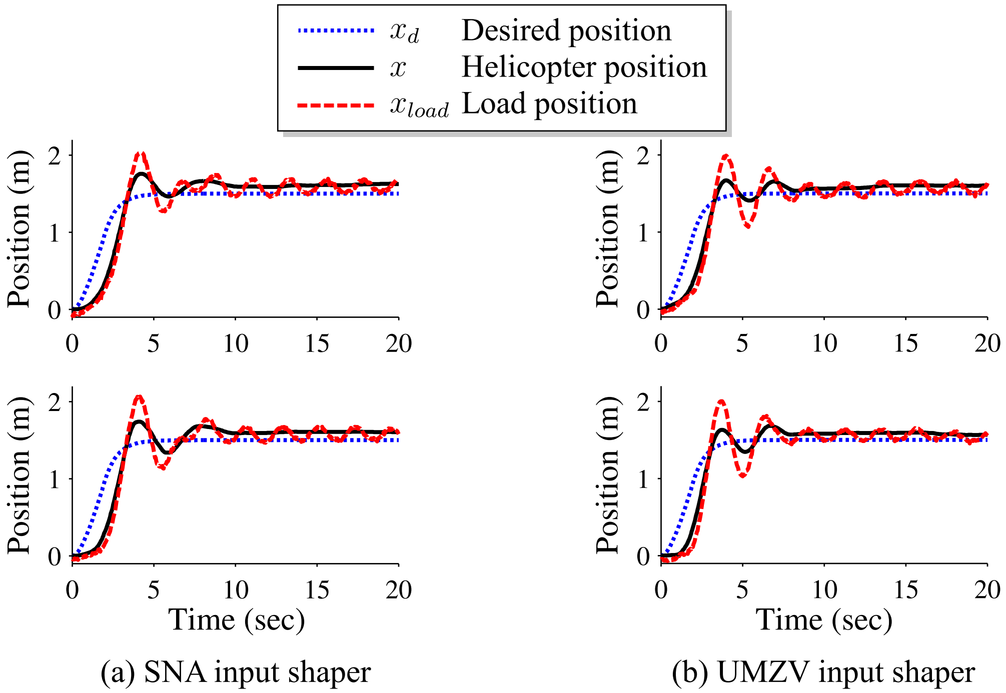

(a) SNA input shaper

(b) UMZV input shaper

Figure 137: Experimental Depart/Abort maneuvers with input-shaped Translational Rate Command and load-positioning outer loop

7.6.7 Discussion

From these analyses, it appears that input shaping is best applied to either Attitude Command or Translational Rate Command response types. This is a positive result for input shaping because these are common response types on heavy lift helicopters. The less augmented response types (Unaugmented and Angular Rate) were not even investigated in several of the major studies of suspended load handling qualities [65, 33]. These studies assumed at least an Attitude Command response type.

One reason why input shaping may be most beneficial when applied to the outer control loops is that the outer-loop translational dynamics are much slower (approximately 3-times slower [31]) than inner-loop rotational dynamics. In other words, the helicopter's pitch rotation is on a faster time scale than its horizontal movement. Because the input shaper applied to each loop was approximately the same, the same time delays would be smaller relative to the slower outer-loop dynamics.

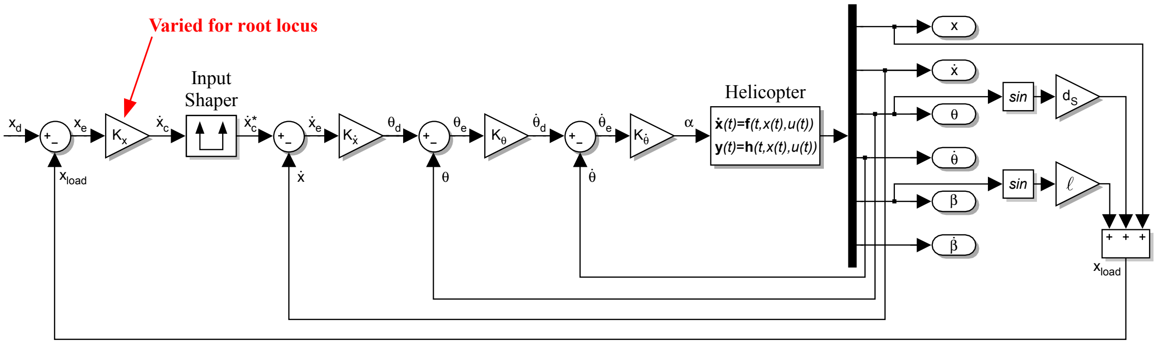

Figure 138: Block diagram for load-positioning root loci

4-impulse RM input shaper seemed to be outstanding for helicopter positioning. The SNA, UMZV, and robust input shapers with a large $V_{partial}$ worked well for load positioning, and fairly well for helicopter positioning.

With a Translational Rate Command response type, input shapers (especially SNA and UMZV) were able to stabilize the load-positioning system without modifying any controller gains. Root locus diagrams will be used to investigate this result. Figure 138 shows the system used for the root locus plots in Figures 139 and 140. The input to this system is the pilot's velocity command, $\dot{x}_c$, and the output is the load position, x_{load}. The root locus tracks the location of the system poles when load position is fed-back, and gain K_x is applied to the error. The gain K_x is varied to form the root locus.

A root locus of the unshaped case is shown in Figure 139. The load oscillation mode quickly goes unstable. When the UMZV input shaper is added, the root locus in Figure 140 results. Zeros are placed on top of the load-oscillation poles and prevents them from moving into the right-half plane. On root locus diagrams, input shapers inside a feedback loop add an infinite number of open-loop zeros and an infinite number of open-loop poles at $-\infty \pm j\omega$ [34]. The two zeros closest to the real axis are used to suppress the unwanted vibration.

Without input shaping, the system becomes unstable with an outer-loop gain of $K_x = 0.707$. The UMZV input shaper increases this allowable gain to $K_x = 3.675$.

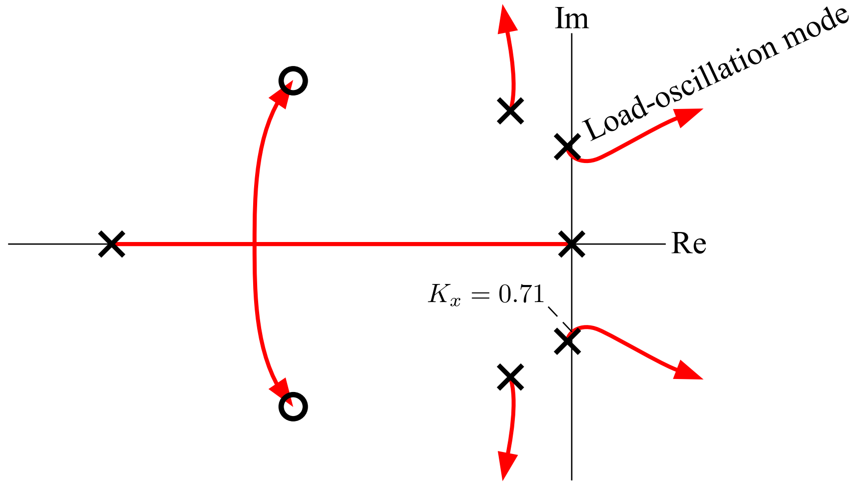

Figure 139: Load positioning with Translational Rate Command

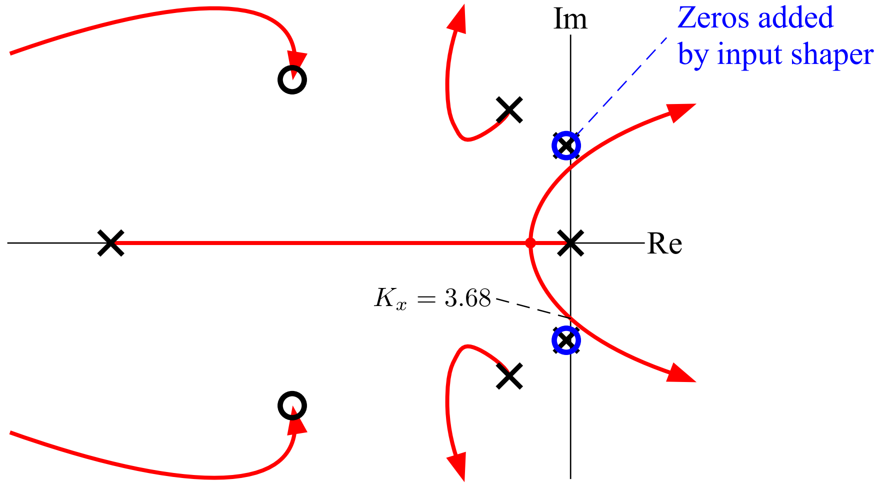

Figure 140: Load positioning with UMZV-shaped Translational Rate Command

The Simplified-Pursuit tuning rules resulted in a value of $K_x = 2.468$. As predicted from the root loci, this gain would drive the unshaped system unstable, but not the UMZV-shaped system.

7.6.8 Collocated and Non-Collocated Control

The preceding results showed that load positioning with a Translational Rate Command was originally unstable, and could be stabilized by applying an input shaper. This same result was found in [34] when a trajectory-following experiment was performed with a damped mass-spring-mass system. The problem was framed as a collocated control vs. non-collocated control problem – positioning the larger mass (equivalent to the helicopter) by controlling the larger mass is collocated control, whereas positioning the smaller mass (equivalent to the suspended load) by controlling the larger mass is non-collocated. As noted in [34], researchers have begun adding time delays to stabilize non-collocated control systems [48, 44, 97]. Input shapers are a set of strategic time delays that target vibration at a chosen frequency.

Manual tracking results from Chapters 3 and 4 support the findings that input shaping can improve the stability of non-collocated control systems. Many of the manual tracking experiments used essentially a damped mass-spring-mass as the controlled system, and found that input shaping improved the stability of non-collocated control (controlling the load by moving the base), as quantified by phase margin. Figure 141 compares the backdriven-translation model to a mass-spring-mass system

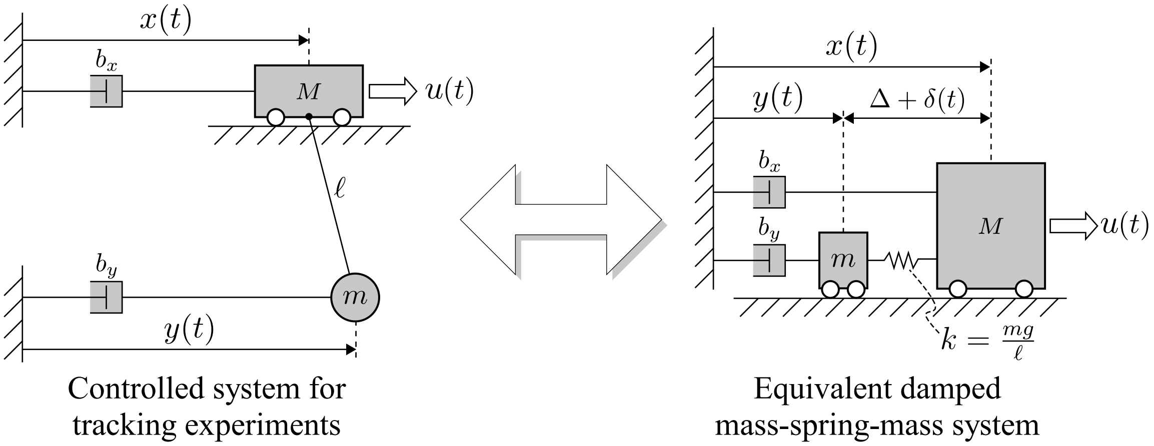

Figure 141: Backdriven-translation system from tracking experiments and equivalent mass-spring-mass model from [34]

similar to the one studied in [34]. The main difference between the two is that a spring with stiffness $k = \frac{mg}{\ell}$ replaces the suspension cable.

7.6.9 Root Loci for Helicopter Positioning

Input shapers did not appear to be helpful for the Unaugmented and Angular Rate Command response types in this particular experiment. This result can be explored using root locus diagrams.

The system shown in Figure 142 is used to generate the root loci. The input to this system is the pilot's desired velocity, $\dot{x}_c$, and the output is the helicopter position, x. The root locus tracks the location of the system poles when load position is fed-back, and gain K_x is applied to the error. The gain K_x is varied to form the root locus. The K_x value represents the pilot's aggressiveness in converting a position error into a command. For the horizontal-repositioning maneuvers in this section, this gain was set to $K_x = 2.468$.

For input shaping different response types, one of the input shapers in Figure 142 is applied to the appropriate command. UMZV input shapers will be used for the present analysis.

A root locus for position control of the unshaped helicopter is shown in Figure 143. The rectangle shows a closeup view of the pole and zero near the imaginary axis. There are two oscillatory modes near the imaginary axis – the helicopter mode and

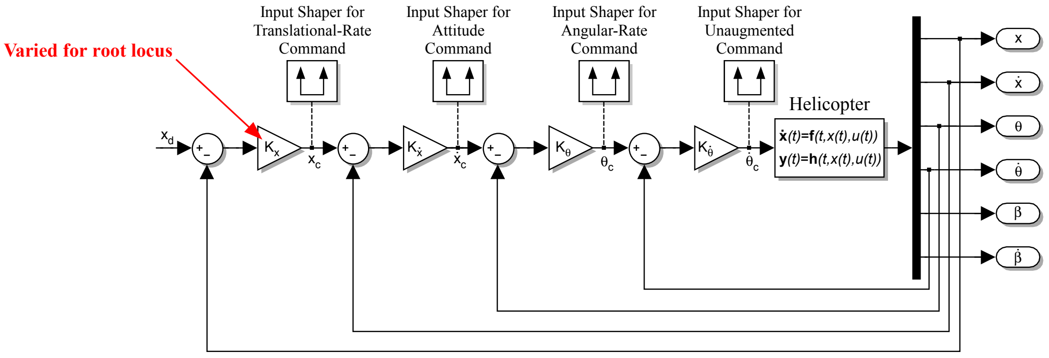

Figure 142: Block diagram for helicopter-positioning root loci

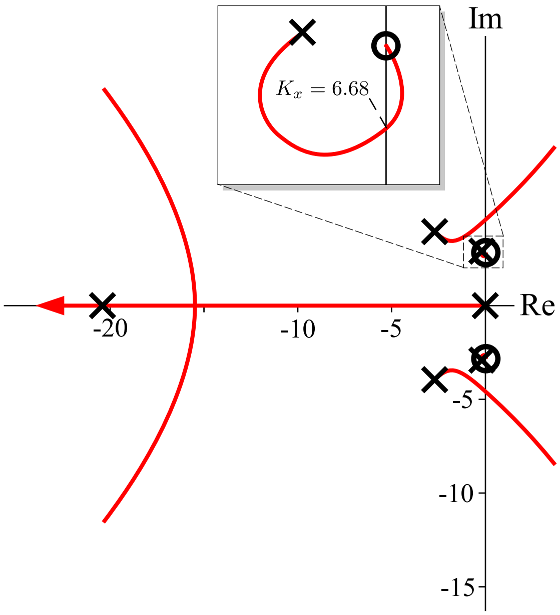

Figure 143: Unshaped helicopter positioning

the load mode discussed in Section 7.3.4. The load mode crosses into the right-half plane at a gain value of $K_x = 6.68$, and the helicopter mode crosses over at $K_x = 8.14$. This system is stable for the controller gain of $K_x = 2.468$, but the load mode is very lightly damped and problematic. The goal of applying input shaping is to place zeros over the load-mode poles while maintaining desirable system dynamics.

When a UMZV input shaper is applied to the Unagumented command, the root locus in Figure 144 results. A pair of zeros, colored in blue, are indeed placed over the load-swing mode poles. However, additional poles and zeros also appear, and one of the new poles is unstable for any value of K_x. This pole is near $j\omega = -15$. The eigenvector corresponding to this pole has a large component in the helicopter's angular rate, indicating that the helicopter's pitch rotation is most affected by this instability.

A UMZV input shaper applied to the Angular Rate Command produces the root locus in Figure 145. Once again, zeros are placed over the load-swing mode poles. The load mode is no longer problematic, but the helicopter's long term oscillatory

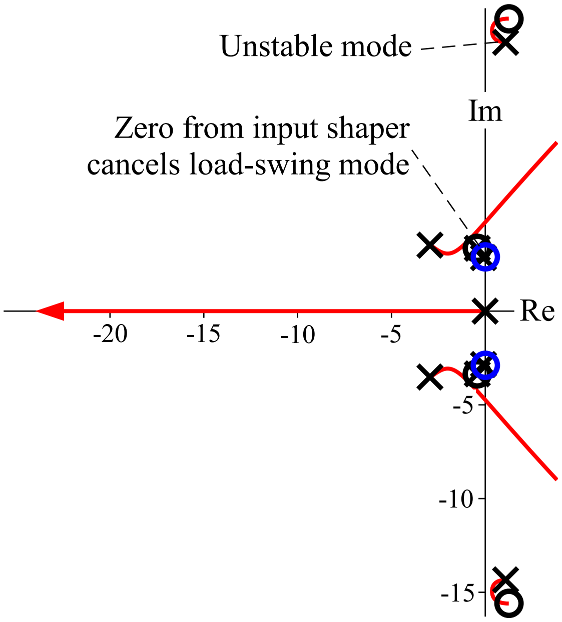

Figure 144: Helicopter positioning with UMZV-shaped Unaugmented Command

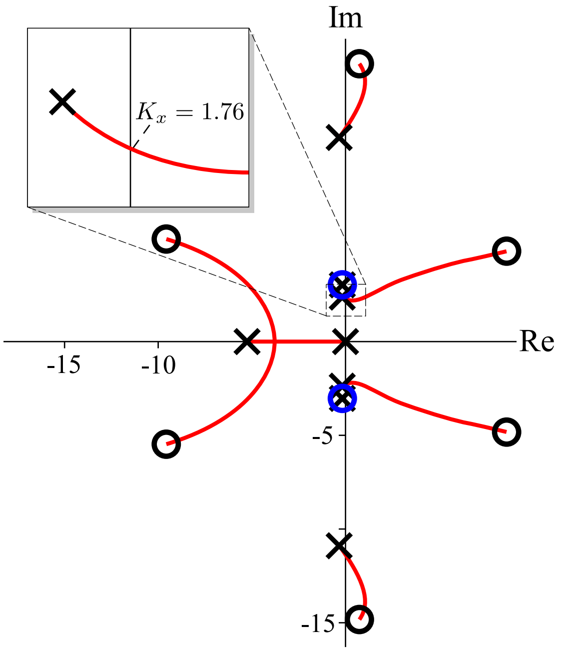

Figure 145: Helicopter positioning with UMZV-shaped Angular Rate Command

mode shifts closer to the imaginary axis, and a gain value of $K_x = 1.76$ makes this mode unstable. The Simplified-Pursuit controller gain of $K_x = 2.468$ would be too large, as confirmed from the results in Table 22.

Applying a UMZV input shaper to the Attitude Command produces the root

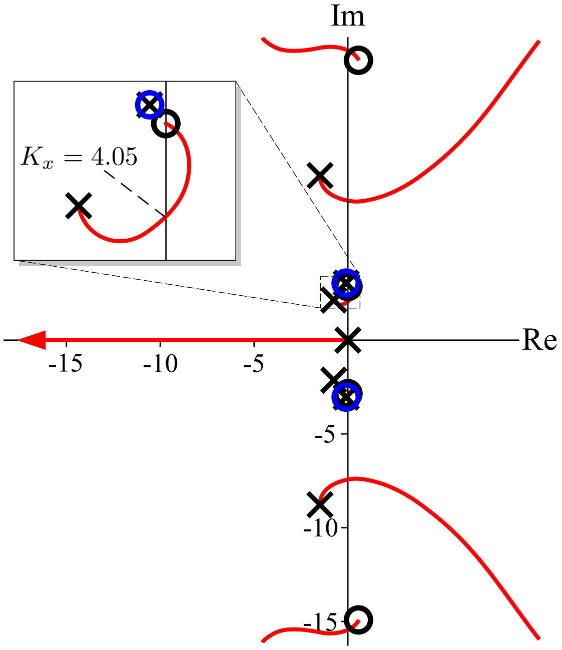

Figure 146: Helicopter positioning with UMZV-shaped Attitude Command

locus in Figure 146. The load-swing mode poles are neutralized by the zeros of the UMZV input shaper. The helicopter's long-term oscillatory mode is again the first to go unstable, but in this case, the gain value can be up to $K_x = 4.05$ before instability results. The Simplified-Pursuit controller gain of $K_x = 2.468$ is well below this threshold.

A UMZV input shaper applied to the Angular Rate Command produces the root locus in Figure 147. The UMZV shaper places poles over the load-swing mode, and the helicopter oscillatory mode is stable for much larger gain values than it was for the Attitude Command response type. The short-term pitch mode and helicopter rigid-body mode combine, and break away from the real axis to form an underdamped pair of poles. These poles cross into the right-half plane at a gain value of $K_x = 7.08$. This appears to be the most stable of the examined implementations of input shaping, and the results in Table 24 showed that it also had the best performance for horizontal repositioning maneuvers.

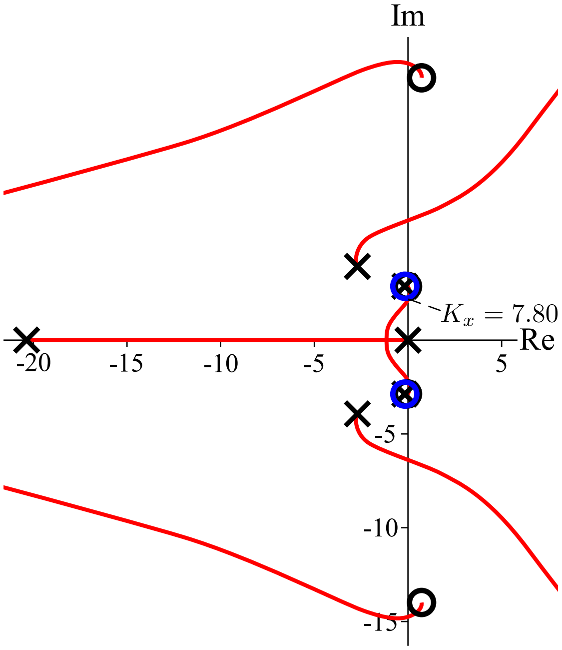

Figure 147: Helicopter positioning with UMZV-shaped Translational Rate Command

7.7 Conclusions

An experimental testbed was constructed to investigate the dynamics and control of a helicopter carrying a suspended load. A dynamic model of the planar helicopter was presented and its parameter values were estimated with a grey-box system identification program. The resulting dynamic model captured the most important dynamics of the system and gave an adequate fit to the experimental data for the purposes of controller design and testing. The simulation model was controlled by a human-like feedback controller from the literature, and was scaled to the fast dynamics of the model helicopter relative to a full-scale helicopter. The feedback controller was modified to simulate different helicopter responses to pilot input. Horizontal repositioning maneuvers were simulated with input shaping applied to different response types.

It was shown that input shaping is effective when applied to a Translational Rate Command response type, and to a lesser extent, an Attitude Command response type. The addition of input shaping to the Translational Rate Command allowed the load position to be used as a position reference instead of the helicopter position. Without input shaping, using the load position as a position reference resulted in an unstable system. This is another example where input shaping greatly improved the position control of a flexible element, as was found in the manual tracking experiments of previous chapters.

The horizontal repositioning maneuvers were performed without adjusting any gains after adding input shaping to the control system. It is likely that better performance could have been attained with all input shaping cases if the controller gains were retuned for each shaper. Indeed, it would be expected for real human pilots to adjust their “gains” in mid flight to accommodate an input shaper because humans are highly adaptable controllers and can reorganize and retune their control behavior to fit a given system. However, this analysis showed that input shaping could improve performance of certain response types even without pilot adjustment.

CHAPTER VIII

OPTIMIZING INPUT SHAPER PARAMETERS USING HUMAN-CONTROLLED-SYSTEM PERFORMANCE

Partial input shaping is a technique that increases the size of the first impulse of any input shaper relative to later impulses. This technique gives all input shapers a continuous degree of freedom. In Section 7.6, it was found that one value along this continuum improved performance relative to either extreme (unshaped and fully shaped). Section 8.1 studies the whole spectrum of possible input shapers using the same horizontal repositioning maneuver from Chapter 7. SNA input shapers have a second degree of freedom – amplitude of the negative impulse. Section 8.2 presents a manual tracking experiment that searches for the negative amplitude of an SNA shaper that yields the best tracking performance.

8.1 Partial Input Shaping Study using Horizontal Repositioning

In Section 7.6, it was found that applying partial input shaping with an allowable vibration of $V_{partial} = 25\%$ enabled the helicopter and load to settle over the target position faster than original input shapers. It is likely that a value of $V_{partial}$ other than 25% would enable even better performance. Recall that to form a partial input shaper, an amount α is added to the first impulse, and the shaper is rescaled to maintain a sum of 1. The α value determines the first-impulse weighting.

This section studies the whole spectrum between a standard input shaper and no input shaper. The α value will be varied between 0 (fully shaped, allowing no residual vibration) and 10 (practically unshaped, allowing 100% vibration). Simulated Depart/Abort maneuvers will be performed using either the helicopter position or the load position as the outer-loop reference.

A Translational Rate Command response type will be used for all analyses in this section. The performance metric will be settling time, t_{sett}. This is defined as the larger of the helicopter and load setting times:

$$t_{sett} = \max(t_{heli}, t_{load}). \tag{83}$$

Settling time indicates the time required for both the load and the helicopter positions to stabilize over the target position.

8.1.1 Helicopter Positioning

Figure 148 shows how various input shapers behave when α is varied between 0 and 10. Recall from Section 4.2 that the amount α is added to the first impulse of the input shaper, and then all amplitudes are rescaled to maintain a sum of 1. The curves in Figure 148 have a stepped appearance because the load settling time depends on

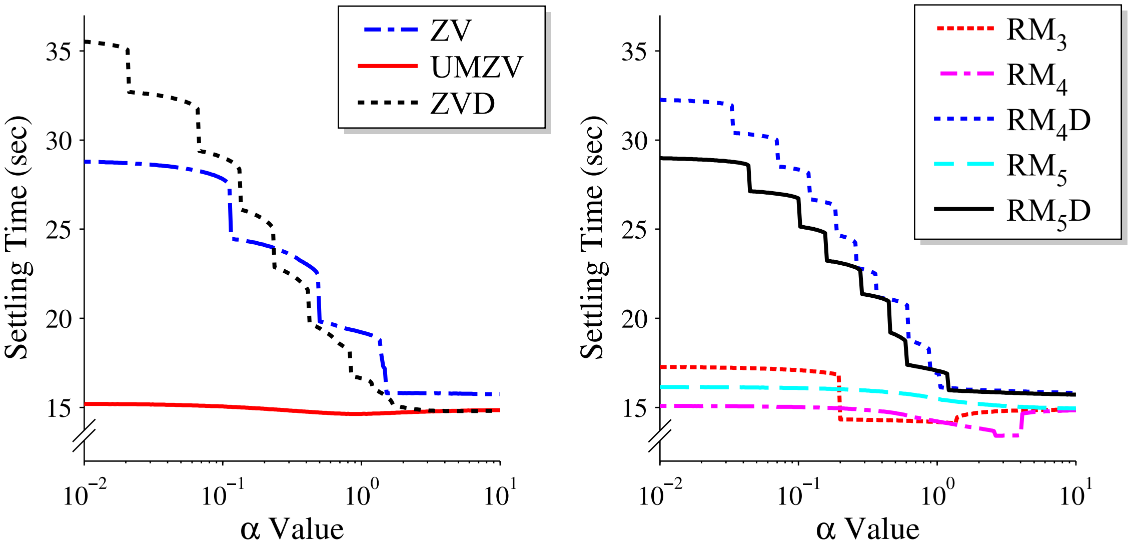

(a) Conventional input shapers (b) Reduced-modification input shapers

Figure 148: Settling time vs. α for helicopter positioning

how fast the helicopter reaches the target position, as well as the phase of the swing angle when the helicopter arrives. These two factors make t_{load} vary cyclically.

The ZV and ZVD input shapers in Figure 148(a) have relatively long settling times, and the times decrease as α is increased. The UMZV shaper produces a fast settling time for any value of α, and appears to reach a minimum at around $\alpha = 1$.

Results for the RM shapers are shown in Figure 148(b). The robust 4- and 5-impulse shapers behave much like the ZVD shaper. They have a large settling time until the α value is increased to around 1. From that point on, the input shapers converge toward the same value because they all approach the unshaped case. The RM_3 and RM_4 shapers have regions where the settling time is very small.

Because the SNA input shaper has two degrees of freedom when α, the amount added to the first impulse, is included, a settling-time surface is shown in Figure 149 instead of a curve. This surface can be used to pinpoint the ideal values of both b and α. The height of the surface in Figure 149 gives the settling time, the front-left axis shows a range of α values, and the front-right axis shows a range of b values. Note that the upper-left edge of the plot is essentially unshaped, the front corner is a UMZV shaper, and the right corner is a ZV shaper.

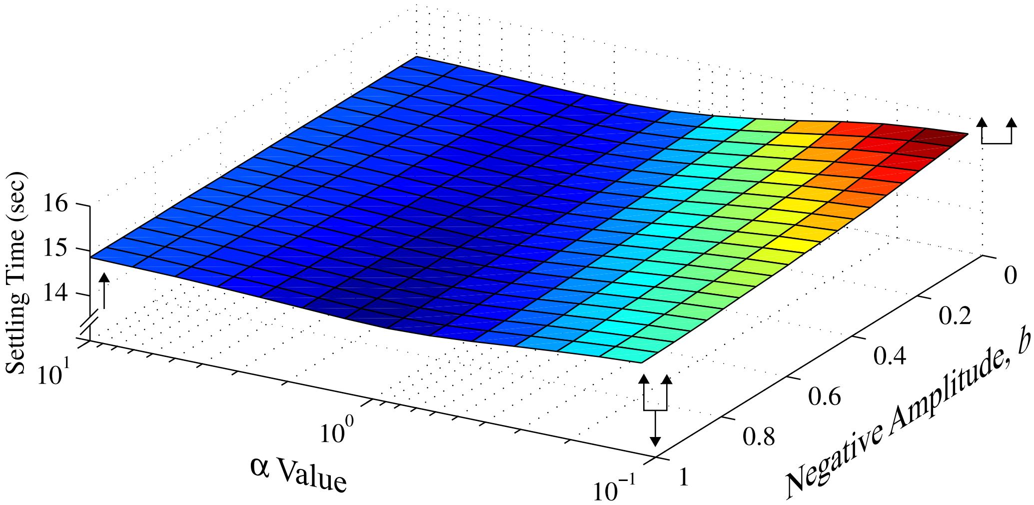

Figure 149: Settling time for helicopter control with SNA input shaper

The surface reaches a minimum when $b = 1$ and $\alpha = 0.89$. The settling time for this case is $t_{sett} = 14.64\ sec$. The input shaper that produces this minimum is:

$$\begin{bmatrix} A_i \\ t_i \end{bmatrix}_{SNA_{heli}} = \begin{bmatrix} 1 & -0.529 & 0.529 \\ 0 & 0.404 & 0.732 \end{bmatrix}. \tag{84}$$

Approximately 43.9% vibration is allowed by this input shaper, which is much higher than the 25% tested in the previous chapter.

8.1.2 Load Positioning

Settling-time curves for positioning the load are given in Figure 150. Not all input shapers are shown because only some of the input shapers produced a system that was stable and converged to the target location. The settling time with all input shapers increases out of the plot window when α is increased to around 1. This is the point at which the input shapers become too much like the unshaped command, and the ability of the system to converge to the target position is lost.

The UMZV input shaper produced a quickly settling system for α values below 0.3. An unexpected result was that the ZVD input shaper has a region of very fast settling time around $\alpha = 0.7$. This partial-ZVD input shaper is given by:

$$\begin{bmatrix} A_i \\ t_i \end{bmatrix}_{ZVD(\alpha=0.7)} = \begin{bmatrix} 0.588 & 0.291 & 0.121 \\ 0 & 1.097 & 2.193 \end{bmatrix}. \tag{85}$$

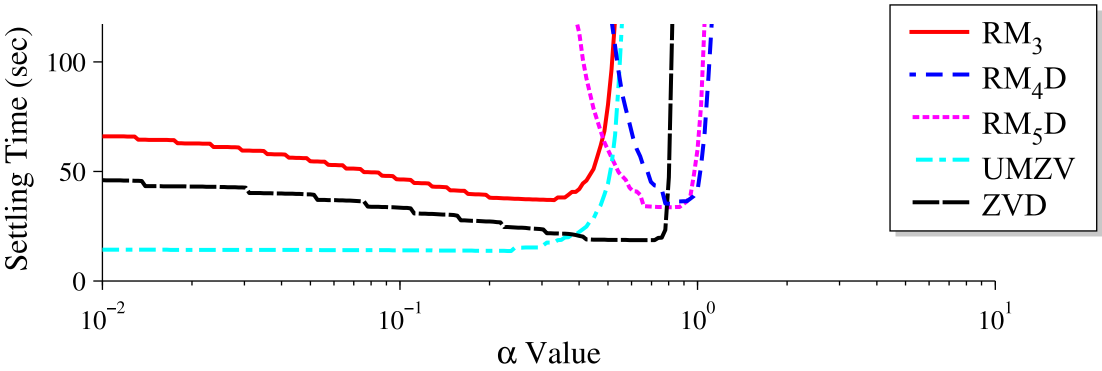

Figure 150: Settling time vs. α for load positioning

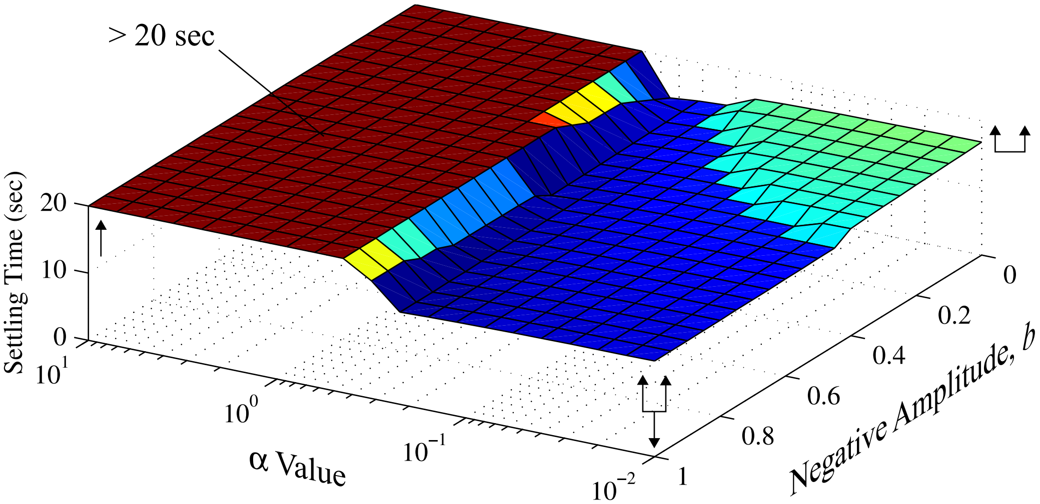

Figure 151: Settling time for load control with SNA input shaper

This input shaper allows 28% residual vibration at the modeled frequency. When α was increased to around 0.8, the system performance dropped steeply.

The SNA input shaper α-b surface for controlling the load position is given in Figure 151. As the α value increases toward the upper left of the plot, the settling time suddenly increases to over 120 seconds for any value of b. Again, when α is large, the input shaped command becomes too much like the unshaped command, and the load-positioning system becomes unstable. The surface reached a minimum where $b = 1$, $\alpha = 0.22$, and $t_{sett} = 13.70\ sec$. The input shaper that produced this minimum was:

$$\begin{bmatrix} A_i \\ t_i \end{bmatrix}_{SNA_{load}} = \begin{bmatrix} 1 & -0.820 & 0.820 \\ 0 & 0.404 & 0.732 \end{bmatrix}, \tag{86}$$

Residual vibration of approximately 16.3% was allowed by this input shaper. It makes intuitive sense that the input shaper in (86), which is best for load control, allowed less vibration than the input shaper in (84), which is best for helicopter control. Manual tracking experiments, and now simulated horizontal repositioning maneuvers, have demonstrated that an unshaped command tends to be better for controlling the driven base, and an input-shaped command tends to be better for controlling the flexible element.

8.1.3 Discussion

For the analyses in this section, input shapers yielded the best performance when at least some vibration was allowed ($\alpha > 0$). Partial input shaping proved to be a useful technique for this task.

The RM input shapers were good for helicopter positioning in Figure 148, but very poor for load positioning as shown in Figure 150. Recall, the Shaper-Validation experiment in Chapter 4 indicated that the RM shapers were poor at reducing load swing when the operators were not concentrating on the load.

The UMZV and SNA input shaper have consistently shown the best performance for controlling the load position, and fairly good performance for controlling the helicopter position while keeping the load swing to a minimum. With this in mind, the following recommendations can be made for researchers seeking to add input shaping to a human-piloted helicopter control system:

- Input shaping will likely be most effective when applied to Attitude or Translational Rate commands.
- If a continuous input device (such as a dial) for adjusting the input shaper is available to the pilot, then a UMZV input shaper with dial-controlled partial input shaping should be implemented. If the pilot must apply input shaping with a discrete on/off switch, then an SNA input shaper may be the best option.

8.2 Tracking Study # 6: Golden-Search Experiment

In many cases, the machine dynamics in a human-machine system can be well-characterized by a transfer function. Human control behavior, on the other hand, is more difficult to quantify. The human reorganizes and refines his or her control behavior depending on the machine configuration, the task, and the operating conditions. Therefore, the human is difficult to model with a transfer function.

Manually controlled machines may include additional control systems, such as feedback controllers, feedforward controllers, and command shapers. These elements attempt to improve stability and performance of the human-machine system. It is often difficult to choose the optimal values for these control system parameters with a human "in the loop." Adaptability of the human operator is a double-edged sword: the human may be able to attain comparable performance with a wide variety of parameter values (sometimes at the expense of high mental workload), but unfortunately this same variability makes it difficult to calculate the best control parameter values analytically.

Instead of trying to quantitatively model the human operator, this section proposes that the combined human-machine system can be tested experimentally to find the best value for a control parameter. An experimental task can be used to assess performance of the system for a given control parameter value, and an optimization routine can be used to strategically choose new parameter values to test based on previous values.

This overall construct is not new. Previous studies have used humans as participants in optimization loops. One notable example is a technique called Interactive Evolutionary Computation (IEC) [91]. This technique uses a human to assign a numerical rating to the system being optimized, and an evolutionary algorithm (such as a genetic algorithm) is used to generate new variations of the system. This technique has been used to design and evaluate sounds, animations, and artwork, where specifying an explicit cost function would be nearly impossible due to the large number of variables involved.

In contrast, this section investigates one-dimensional optimization. As shown in Figure 152, the independent variable is a parameter value in the control system, and the dependent variable is a quantitative measure of performance. The goal is to "optimize" performance of the human-machine system with respect to one of the

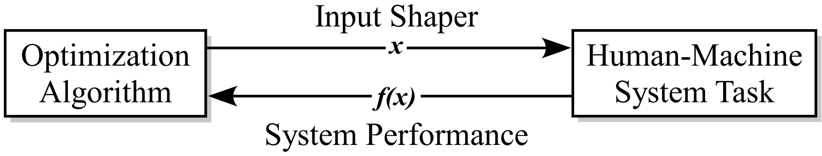

Figure 152: Optimization using a human-machine performance

control parameters.

The rest of this section focuses on a specific application of the concept. The human-machine system is a simulated overhead crane with continuous motor control and a joystick input device. The controller parameter being optimized is the negative impulse in a specified-negative-amplitude (SNA) input shaper [81] that is used to reduce oscillation of the crane payload. A manual tracking task with a sum-of-sines reference signal is used to test performance of the human-machine system. A golden-section search is used to optimize the input-shaper parameter value.

The design task is to choose the b value in the range of $-1 \leq b \leq 0$ that yields the best performance for the manually controlled crane. It is likely that the best value will vary from operator to operator.

8.2.1 Optimization Method

One strategy for choosing test values of b is to use evenly spaced points over the whole parameter range. However, this strategy does not use any knowledge of previous results, so many parameter values that could be ruled out by past trends might needlessly be tested. Extra trials may overwork the human operator being tested. Studies have shown that operator fatigue is an important factor which can affect experimental outcomes [104]. Instead, an optimization algorithm could be used to choose b values in a systematic way, thereby reducing the required number of trials.

There are many kinds of one-dimensional optimization algorithms that could be used to choose b values. The one that will be used in this study is the golden-section search [15] illustrated in Figure 153. This search is only guaranteed to converge to

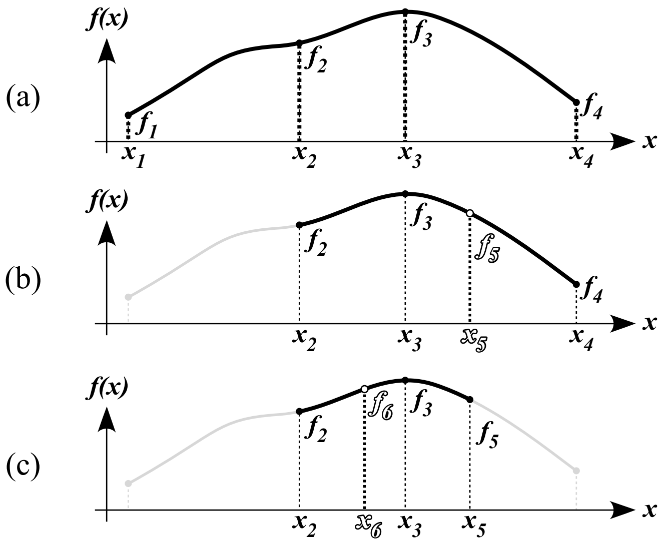

Figure 153: Golden-section search method

the maximum value if the function is unimodal, meaning that the function has only one global maximum in the region of interest, and no other local maxima. If the experimentally determined function has many peaks, or has so much experimental variability that the shape of the function is difficult to determine, then it may be advisable to try a different optimization method or change the experimental approach.

The golden-section search method is illustrated in Figure 153. In Figure 153(a), four initial points are tested, including the low (x_1) and high (x_4) parameter endpoints. Two internal points (x_2 and x_3) are also tested. Their locations are determined by using the *golden ratio*, which gives the technique its name. Points x_2 and x_3 are chosen such that $\frac{x_3-x_1}{x_2-x_1} = 1.618$ and $\frac{x_4-x_2}{x_4-x_3} = 1.618$.

In Figure 153(a), f_3 is larger than f_2. This means that the maximum value for $f(x)$ cannot be to the left of x_2, so the search region is reduced to the interval between x_2 and x_4, as shown in Figure 153(b). The next test point is chosen such that the ratios of distances between points in the new bracket is the same as the ratios in the old bracket. This allows previously tested points to be used in the new bracket. The same process is followed for each step of the search algorithm; intervals that cannot contain the maximum value are removed from the search.

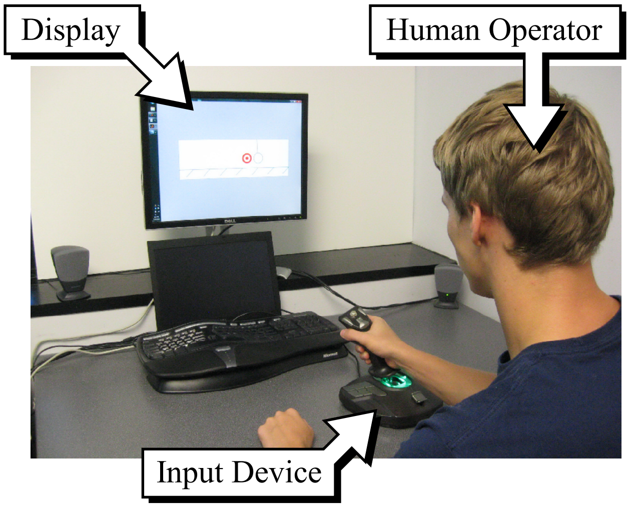

Figure 154: Experimental setup for Golden-Search experiment

8.2.2 Participants & Procedure

The experimental setup is shown in Figure 154. Four novice human operators were tested for this study. Each human operator was shown a pursuit display, and used a *Thrustmaster T16000* spring-centered joystick to control the cursor. The operator controlled a simulated crane shown in Figure 155. During tracking tasks, only the area inside the lower rectangle in Figure 155 was displayed to the human operator. Unlike in previous tracking studies, the suspension cable was visible to the operator. The rectangle spanned approximately 10° of the operator's visual field. Table 25 shows the sum-of-sines forcing function used to drive the target position.

For the crane dynamics, the model given in Figure 156 was used with the following

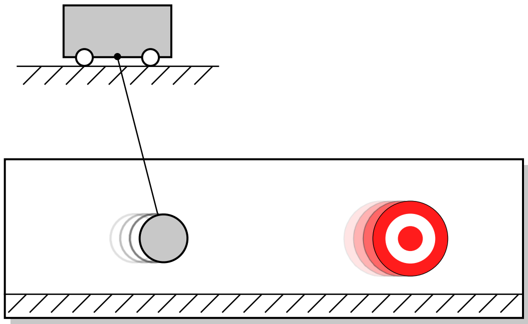

Figure 155: Ground-fixed display for Golden-Search experiment

Table 25: Forcing function for Golden-Search experiment

Wave Number, i	Frequency, ω_i (rad/s)	Amplitude, B_i (° visual angle)
1	3.456	0.200
2	2.073	0.272
3	1.194	0.349
4	0.691	0.426
5	0.314	0.536
6	0.188	0.607
7	0.031	8.583

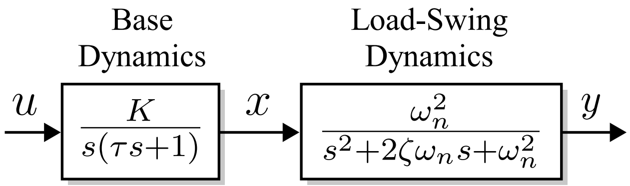

Figure 156: Dynamic model of crane

parameter values: $\omega_n = 1.269$ rad/sec, $\tau = 0.5$ sec, and $\zeta = 0$. These values simulate an overhead crane with a 20-foot load-suspension cable. The value of gain K was chosen to allow the crane's maximum velocity to match the maximum velocity of the reference input using reasonable joystick deflections.

After each tracking task, performance was quantified by the inverse of the root-mean-squared (RMS) tracking error:

$$P = \frac{1}{e_{RMS}} = \frac{1}{\sqrt{\frac{1}{T}\int_0^T e^2(t)dt}}, \tag{87}$$

where T is the duration of the tracking task, and $e(t)$ is the error between the target and payload. Low overall error results in high performance values.

In preliminary manual tracking tests, it was found that the RMS error usually converged to a steady value within 75 seconds. Thus, a trial duration of 75 sec was chosen. It was also found that testing the same b value multiple times yielded slightly different performance values. To reduce the effect of this experimental noise,

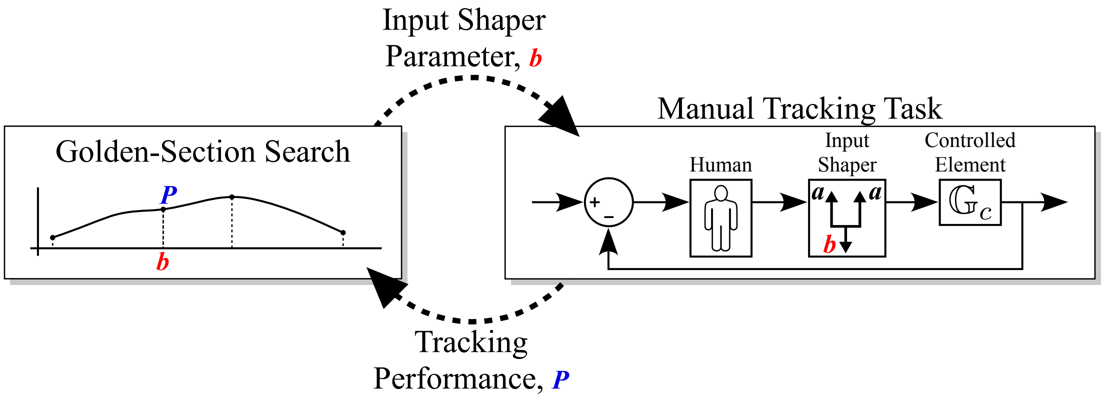

Figure 157: Optimization procedure

performance was characterized by the average of 2 consecutive trials with the same b value. Two practice trials were performed before the real experiment. Including the practice trials, a total of 18 trials were performed by each human operator. Each experiment lasted approximately 40 minutes.

Figure 157 shows an overview of the optimization procedure. The golden-section search picks new values for b. The tracking task described above is used to assign a performance value to the chosen b value. The optimization loop can be stopped either when a certain number of b values have been tested, or when the performance improvement for successive b values is lower than a specified threshold value.

8.2.3 Results

Figure 158 shows the experimental results. The markers show the average of the two trials at each value of b. Lines between markers are added to improve readability. As expected, different operators showed different levels of performance, and the optimization converged to different amplitudes of b.

Operators 1 and 2 performed similarly, and converged to a relatively low amplitude of b. This means that they performed best with an input shaper that resembles the 2-impulse ZV shaper. Operator 3 converged to approximately $|b| = 0.6$, and Operator 4 converged to $|b| = 0.9$.

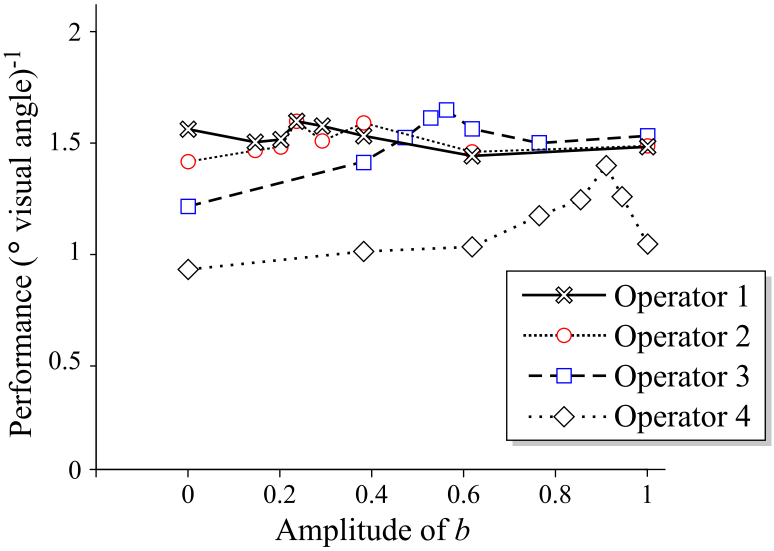

Figure 158: Tracking error results of Golden-Search experiment

For each operator, there were regions with low overall performance (for example, $0 \le |b| \le 0.4$ for Operator 4). The golden-section search quickly stopped testing points in these regions, and focused on the regions of high performance.

8.2.4 Discussion

An important assumption in this operator experiment was that operator performance was unimodal. From Figure 158, the performance curves appear roughly unimodal. However, this could be due partly to learning effects: later trials tend to have higher performance because operator skill improves. In other words, the later trials may have had better performance partly because they converged to a better value of b, and partly because the operator was getting better at the task.

The size of this effect was not measured. The effect could have been reduced by including more practice trials, and only starting real trials after performance had reached a constant level. It is also possible that this learning effect was partially offset by operator fatigue, which decreases performance, and becomes more problematic for later trials.

It would also be interesting to perform a parameter sweep method, where evenly spaced points along the parameter range are tested, and to compare results to the optimization method presented in this section. Another follow-up experiment could optimize other input-shaper parameters, such as the $V_{partial}$ for a partial input shaper.

8.3 Conclusions

Settling time during a simulated Depart/Abort maneuver with a Translation Rate Command response type was plotted as a function of α, the amount added to the first impulse of an input shaper to form a partial shaper. When the virtual pilot focused on positioning the helicopter, robust input shapers produced long settling times for small values of α. The RM input shapers yielded good performance, as did the SNA and UMZV input shapers. When the virtual pilot attempted to position the load, the UMZV input shaper yielded the shortest settling time. Two-dimensional surfaces showed the settling time produced by different forms of an SNA shaper, and the forms that produced the minimum settling time for helicopter positioning and load positioning were identified. The best input shaper for helicopter positioning allowed more residual vibration than the best shaper for load positioning.

An operator experiment searched for the best negative impulse amplitude in an input shaper used to control a simulated crane. An optimization routine was used to reduce the required number of trials. Experimental results showed that the method focused on an optimal range for the parameter value, and this range varied between operators. Future work could examine the effects of operator learning and operator fatigue on experimental results. It would also be interesting to perform a parametric-sweep method (where evenly spaced points along the parameter range are tested in random order), and compare results to the optimization-based method.

CHAPTER IX

CLOSING

This chapter summarizes the methods, findings, and contributions of this thesis, and proposes directions for future research.

9.1 Dissertation Summary & Contributions

This thesis has worked toward understanding and improving the control performance of human-machine systems with flexibility, with a focus on human-piloted helicopters carrying suspended loads. The investigation was conducted with two complementary approaches: human-in-the-loop tracking tasks, and horizontal maneuvers on small-scale helicopter testbeds. Both of these approaches were used to investigate how input shaping affected control over the flexible element (suspended load) and the driven base (helicopter).

Using human operator studies, it was first confirmed that a relatively low-frequency flexible mode is more detrimental to tracking performance than a high-frequency flexible mode. It was then shown that when humans control the position of a flexible element, conventional input shapers greatly improve tracking performance, subjective difficulty, and resemblance of the human-machine system's control behavior to McRuer's important *Crossover model.* When operators control a driven base (to which the flexible element is attached), input shaping tends to degrade tracking performance and increase subjective difficulty. However, vibration of the flexible element attached to the base is reduced, especially by SNA and UMZV input shapers.

To allow more flexibility in addressing this tradeoff between control of the flexible and driven elements, a method for adjusting the vibration-limiting aggressiveness of any input shaper was presented. These "partial" input shapers do not eliminate all vibration, but modify the original command less than full input shapers. In addition, a new class of input shapers was specifically designed to reduce modification of the original command. These *reduced modification* (RM) input shapers are only useful on systems that are not driven near their performance limits, as they briefly require over 100% of the original commanded effort.

An operator study showed that the RM input shapers improve control of the driven base compared to traditional input shapers, but do not improve control of the flexible element as much. The best input shapers for controlling the flexible element were the SNA and UMZV shapers. They produced large improvements in the human-machine system's tracking performance, subjective difficulty, phase margin, and fit to the Crossover model. For all tracking experiments, a strong correlation was found between log-transformed tracking error and median subjective rating. There were also significant correlations between tracking performance (both qualitative and quantitative) and control behavior (parameters from the Crossover model fit). Results in this thesis support the usefulness of the Crossover model as a descriptor of the human-machine system's behavior and a predictor of its tracking performance.

Two operator studies were used to investigate manual tracking with communication delays and nontraditional input devices. It was found that the benefit of input shaping for controlling a flexible element was somewhat decreased as the time delay was increased, but the tracking performance was still improved up to the maximum tested delay of 1 second. A separate operator study compared a traditional joystick to 3 different touchscreen interfaces. Performance was best with the joystick, but a touchscreen interface with two buttons and discrete on/off commands was a reasonable alternative. The use of discrete input should be considered by designers of remotely operated human-controlled systems.

Next, initial investigations of horizontal maneuvers with and without input shaping were conducted on a free-flying micro coaxial helicopter. Simple translational dynamic models of the helicopter were formed, and they were used to show that input shaping reduces load settling time after a lateral repositioning maneuver. It was also found that input shapers are more sensitive to modeling error in the modeled oscillatory frequency than in the damping ratio.

Second, a novel testbed was designed to constrain the helicopter and load to move in a vertical plane. A dynamic model was formed, and position control was achieved with a multi-loop feedback controller that mimics a human pilot. Several implementations of input shaping were tested. It was found that input shaping yields the greatest performance improvements when applied to Attitude Command and Translational Rate Command response types. These are common response types which have been the focus of several reports on externally loaded helicopters.

For horizontal repositioning maneuvers with a Translation Rate Command response type, the SNA and UMZV input shapers produced the largest performance improvements. Helicopter settling time, load settling time, and peak load swing were all reduced from the unshaped case. Furthermore, partially shaped versions of the SNA and UMZV input shapers resulted in even greater improvements, demonstrating the potential usefulness of partial input shaping on flexible systems controlled by humans, or human-like feedback controllers.

When the same controller was used to position the load instead of the helicopter, the system was unstable without input shaping. Several of the conventional input shapers were able to stabilize the system, and the UMZV and SNA input shapers yielded performance that almost equaled the helicopter-positioning performance. This improvement was accomplished without modifying any gains in the pilot-like feedback controller, indicating that human pilots would not need to adjust their control behavior in order to benefit.

In summary, the following contributions were made:

- A thorough study of conventional input shapers for manual control of systems with a lightly damped flexible mode (Chapters 3, 4, and 5)
- The finding that when humans control a low-frequency, lightly damped flexible element, the addition of input shaping allows the system to be well-characterized by the Crossover model (Chapters 3, 4, and 5).
- Novel input shapers designed to maximize human-controlled-system performance while controlling a driven base (Chapters 4 and 8).
- A method for continuously varying the vibration-limiting aggressiveness of any input shaper between unshaped and fully shaped (Chapter 4).
- A testbed and simulation model for studying the near-hover dynamics of a helicopter with a suspended load (Chapter 7).
- A study of the effectiveness of different implementations of input shaping for horizontal repositioning maneuvers (Chapter 7), including the result that conventional input shapers stabilize a system that uses load position as the outer-loop reference instead of helicopter position.

9.2 Future Work

The research presented in this thesis can be extended in many different directions. While this work only considered single modes, many real-world systems include two or more flexible modes. Operator studies on overhead cranes have shown that these systems tend to be more difficult for humans to control than systems with a single mode [46]. Input shaping has the potential to greatly improve manual tracking when multiple oscillatory modes are present.

Initial results with partial input shapers (presented in Chapters 4, 7 and 8) were encouraging. Future work could investigate alternative algorithms to convert a standard input shaper into a partial input shaper. Additionally, operator tests on cranes and other types of human-controlled machines could further tests how partial input shapers perform relative to standard shapers.

Manual tracking studies in this thesis used only novice operators. The main goal was to assess the inherent difficulty of a given tracking situation for a generic, *non-specialized* human controller. Future tracking studies with input shaping could be conducted with expert human controllers, such as professional helicopter pilots or crane operators, to quantify the differences in performance from novice operators, and to ensure that the same beneficial effects of input shaping found with novice operators also occur with skilled operators.

Different control systems and a larger variety of load weights and cable lengths could be tested on the planar small-scale helicopter testbed. Previous studies have found that a helicopter's roll dynamics are more negatively affected by a heavy suspended load than its pitch dynamics [33]. This is because the helicopter's angular moment of inertia is generally much smaller about the roll axis. To study the roll dynamics, the planar helicopter testbed could be redesigned to move laterally instead of longitudinally.

This thesis investigated several implementations of input shaping on just one type of multi-loop feedback controller; countless other control schemes exist for helicopter systems. The effectiveness of input-shaping implementations on other control systems should be explored. Additionally, future work could investigate the combination of input shaping and load-state feedback control [36]. This combination has already been applied to overhead cranes and has yielded gains in positioning accuracy and swing reduction [90]. By leveraging the advantages of both approaches, a control system that outperforms either approach alone can be produced.

APPENDIX A

LOAD-MASS RATIO PARAMETER STUDY

A.1 Helicopter-Load Dynamics

A load mass ratio of 0.155 was used for results in the body of the thesis. This was the heaviest load that could reasonably be carried by the experimental helicopter system. On full-scale helicopters, heavier loads resulting in load-mass ratios of 0.25 and 0.33 are often encountered. A load-mass ratio of 0.5 is considered extremely high.

This appendix contains many of the same analyses presented in Chapters 7 and 8, but with different load weights. Table 26 gives controller gains that were attained using the Simplified Pursuit tuning methods presented in Section 7.4. Note that the change in gain from one load mass ratio to another is not always predictable. The most consistent trend appears to be a decrease in the $K_{\dot{\theta}}$ gain. This gain decreases as the load weight is increased.

Table 27 gives the frequency and damping ratio of the load swing mode for a variety of load mass ratios and response types. Parameters in the first 5 rows were computed by linearizing the helicopter and control system about hover and identifying the load swing mode on a pole-zero plot.

As the load weight increases, the swing frequency and damping generally increase.

Table 26: Controller gains for different load weights

	Load-Mass Ratio				
	0	0.155	0.25	0.33	0.5
$K_{\dot{\theta}}$	1.6712	1.6528	1.6282	1.5909	1.3318
K_{θ}	3.5649	4.0039	5.0185	5.0608	4.5964
$K_{\dot{x}}$	0.7893	0.3945	0.2553	0.2667	0.4094
K_{x}	1.5068	1.8051	2.0957	1.9369	1.4835

Table 27: Load swing mode for different response types (ω_n; ζ)

	Load-Mass Ratio				
	0	0.155	0.25	0.33	0.5
α response	2.86; 0.00	3.28; 0.13	3.82; 0.17	4.35; 0.18	5.70; 0.16
$\dot{\theta}$ response	2.86; 0.00	3.02; 0.05	3.17; 0.10	3.35; 0.13	4.00; 0.24
θ response	2.86; 0.00	3.01; 0.04	3.14; 0.07	3.27; 0.10	3.64; 0.17
$\dot{x}$ response	2.86; 0.00	2.87; 0.06	2.95; 0.11	2.93; 0.15	2.69; 0.17
x response	2.86; 0.00	2.79; 0.09	2.84; 0.20	2.62; 0.24	2.44; 0.15
Predicted	2.86; N/A	3.11; N/A	3.30; N/A	3.49; N/A	4.04; N/A

This is most true for the bare-airframe response to α input, shown in the top row of Table 27. The predicted swing mode frequency was obtained using the formula:

$$\omega_L = \sqrt{\frac{g}{\ell}\left(\frac{1}{1 - LMR}\right)} \tag{88}$$

where g is gravitational acceleration, and ℓ is the suspension cable length. The damping ratio is not addressed by this approximation, which is why the value of the damping ratio in the bottom row of Table 27 is not applicable (N/A). From flight tests, it has been found that the damping during low-speed flight ranges from around 0.1 to 0.3 [65].

The predicted load swing frequency is generally similar to the frequencies with Angular Rate Command ($\dot{\theta}$) and Attitude Command (θ) response types. The swing frequency with a Translational Rate Command ($\dot{x}$) response type is lower than the predicted frequency, except in the unloaded case (LMR = 0).

Figure 159 gives the helicopter's horizontal velocity response ($\dot{x}$) to control inputs (δ) when an Attitude Command response type is implemented. Frequency responses for load mass ratios of 0, 0.155, 0.25, 0.33, and 0.5 are shown. The unloaded helicopter has fairly smooth magnitude and phase curves. The addition of a suspended load creates a notch in the magnitude curve, which results in two crossover frequencies. The phase curve is distorted near the same frequency as the notch in the magnitude curve. These features become more pronounced as the load weight increases.

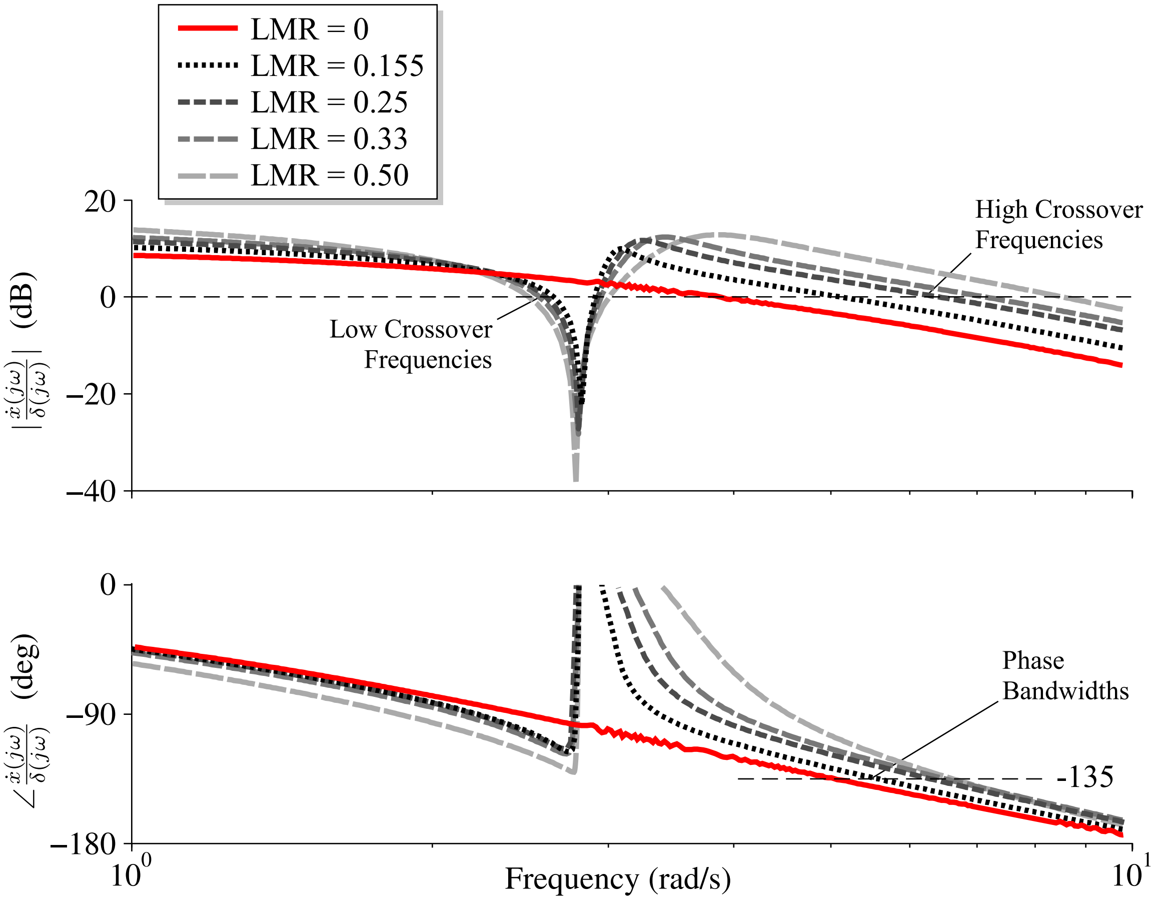

Figure 159: Translational rate bandwidth with Attitude Command response type

Figure 159 closely resembles the Figure E-2 in [33], which displays the same frequency response for a Boeing Chinook helicopter with a variety of load weights. The main difference between the plots is that the load effects happen at a higher frequency on the small-scale helicopter in the testbed. It is on a faster time scale than the full-scale helicopter.

A.2 SNA Surfaces for Depart/Abort Maneuvers

The Depart/Abort maneuvers described in Section 7.6 were performed with the same input shapers, response type, and move distance, but with several heavier loads. The surface plots in Figure 160 show the setting time yielded by different α and b values of an SNA input shaper, for a helicopter-positioning task. In each plot, there is a groove, or valley, in the surface that yields the smallest settling times. As the load weight increases, the valley shifts to the right, which corresponds to a smaller α value, and toward a greater amount of input shaping. As the load gets heavier, its effect on the helicopter gets stronger, and swing gets more problematic. Therefore, suppressing the load swing becomes more beneficial.

For helicopter positioning, the following input shapers yielded the smallest settling times for the 0.25, 0.33, and 0.50 load-mass ratios, respectively:

$$\begin{bmatrix} A_i \\ t_i \end{bmatrix}_{LMR=0.25} = \begin{bmatrix} 0.8934 & -0.1549 & 0.2616 \\ 0 & 0.4690 & 0.8902 \end{bmatrix} \tag{89}$$

$$\begin{bmatrix} A_i \\ t_i \end{bmatrix}_{LMR=0.33} = \begin{bmatrix} 0.8753 & -0.1586 & 0.2833 \\ 0 & 0.4944 & 0.9195 \end{bmatrix} \tag{90}$$

$$\begin{bmatrix} A_i \\ t_i \end{bmatrix}_{LMR=0.50} = \begin{bmatrix} 0.8132 & -0.1899 & 0.3768 \\ 0 & 0.5589 & 1.028 \end{bmatrix} \tag{91}$$

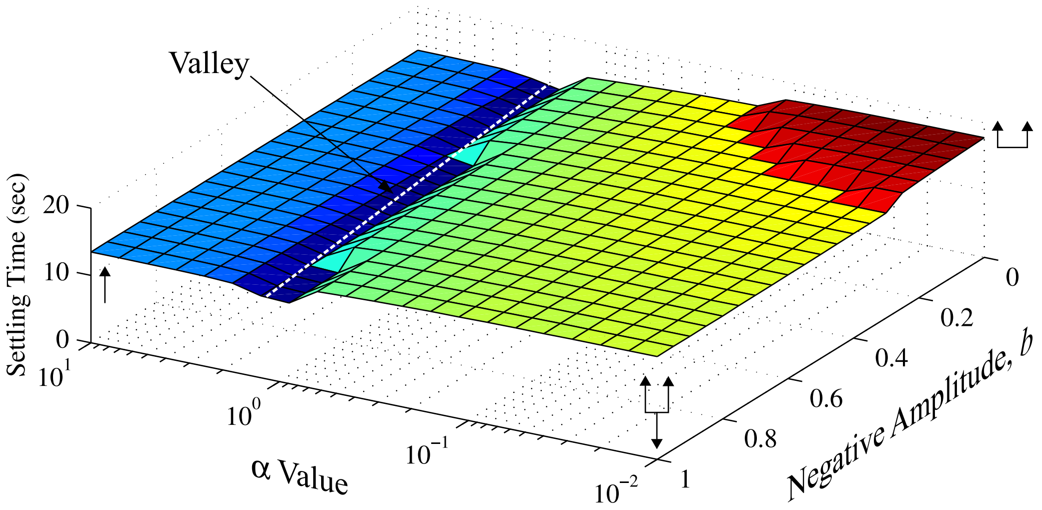

(a) 0.25 load mass ratio

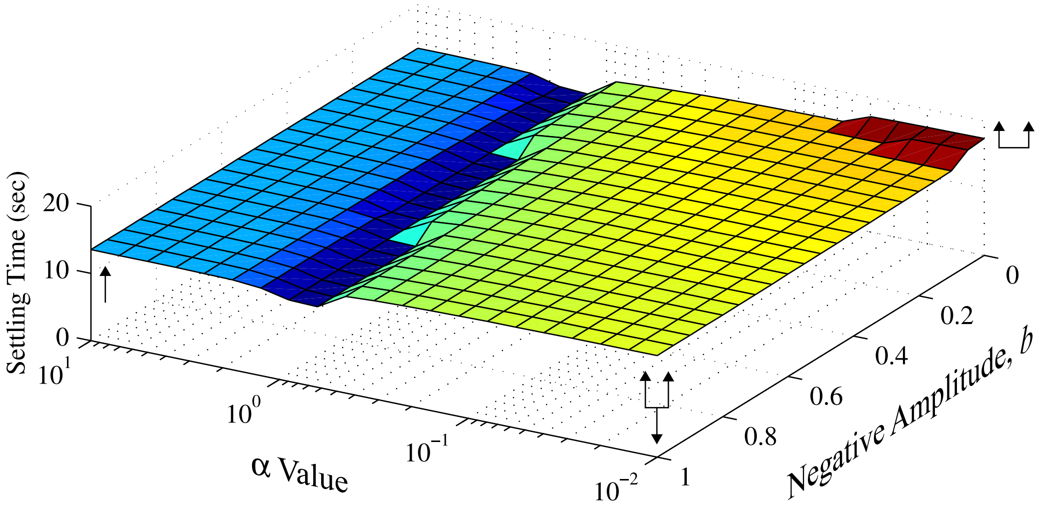

(b) 0.33 load mass ratio

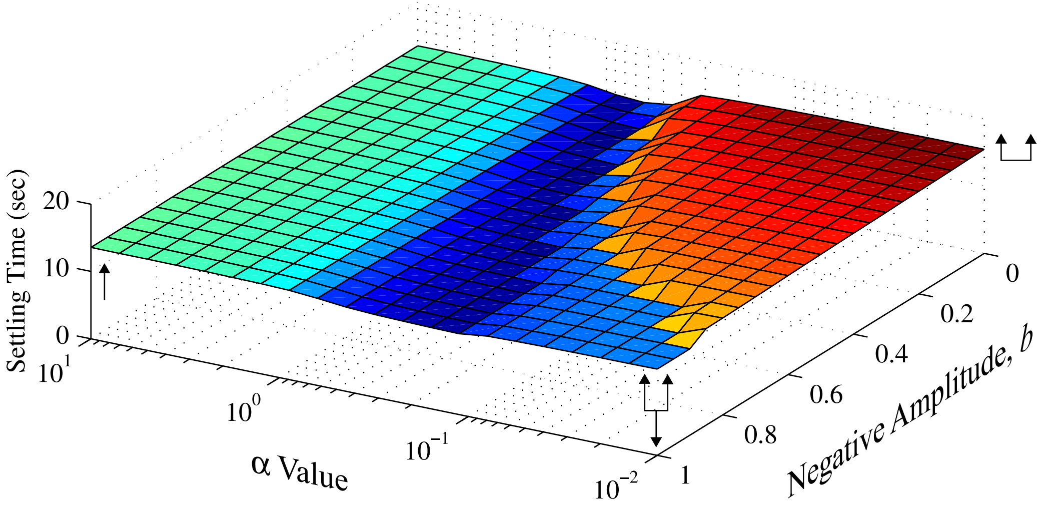

(c) 0.50 load mass ratio

Figure 160: Settling time vs. α for helicopter positioning with different load weights

Surface plots for load positioning are shown in Figure 161. In the upper left of each plot, there is a region of settling times over 20 seconds. As the load-mass ratio increases from 0.25 in Figure 161(a) to 0.5 in Figure 161(c), this region shifts rightward. The other prominent feature is a plateau of higher settling times in the right corner of Figure 161(a) and 161(b), where the input shaper resembles a ZV shaper. This plateau disappears in Figure 161(c).

The smallest settling times for load positioning were yielded by the following three input shapers:

$$\begin{bmatrix} A_i \\ t_i \end{bmatrix}_{LMR=0.25} = \begin{bmatrix} 1.0000 & -0.6567 & 0.6567 \\ 0 & 0.4174 & 0.7240 \end{bmatrix} \tag{92}$$

$$\begin{bmatrix} A_i \\ t_i \end{bmatrix}_{LMR=0.33} = \begin{bmatrix} 1.0000 & -0.6567 & 0.6567 \\ 0 & 0.4488 & 0.7337 \end{bmatrix} \tag{93}$$

$$\begin{bmatrix} A_i \\ t_i \end{bmatrix}_{LMR=0.50} = \begin{bmatrix} 0.9098 & -0.3799 & 0.4701 \\ 0 & 0.4956 & 0.9215 \end{bmatrix} \tag{94}$$

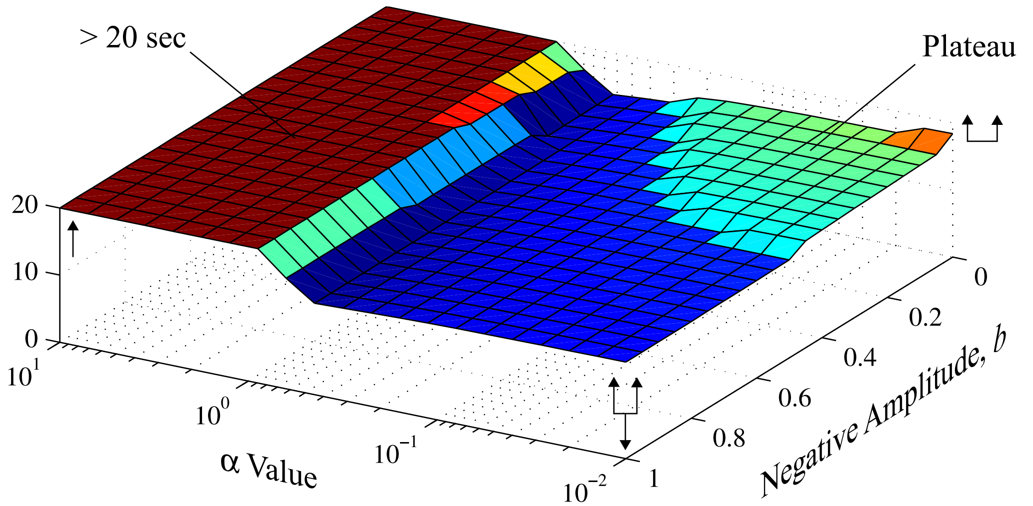

(a) 0.25 load mass ratio

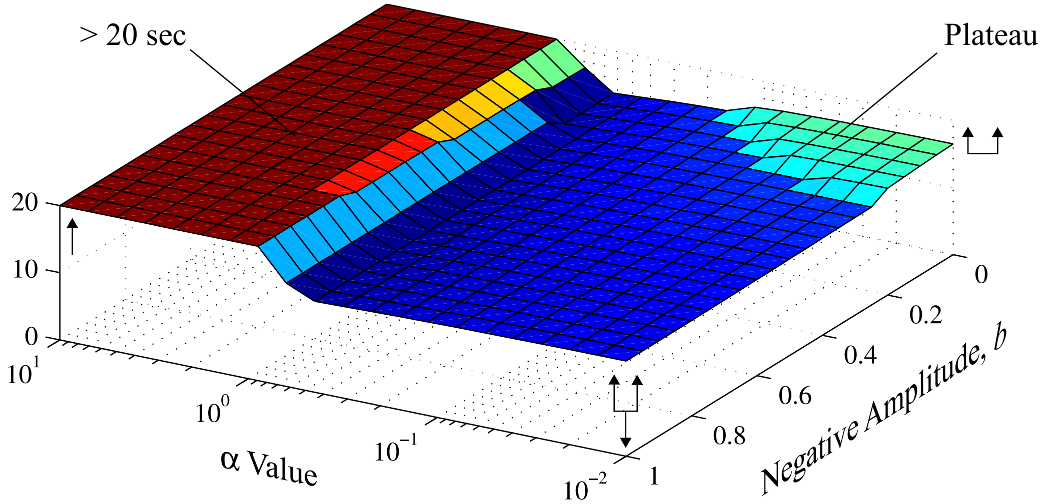

(b) 0.33 load mass ratio

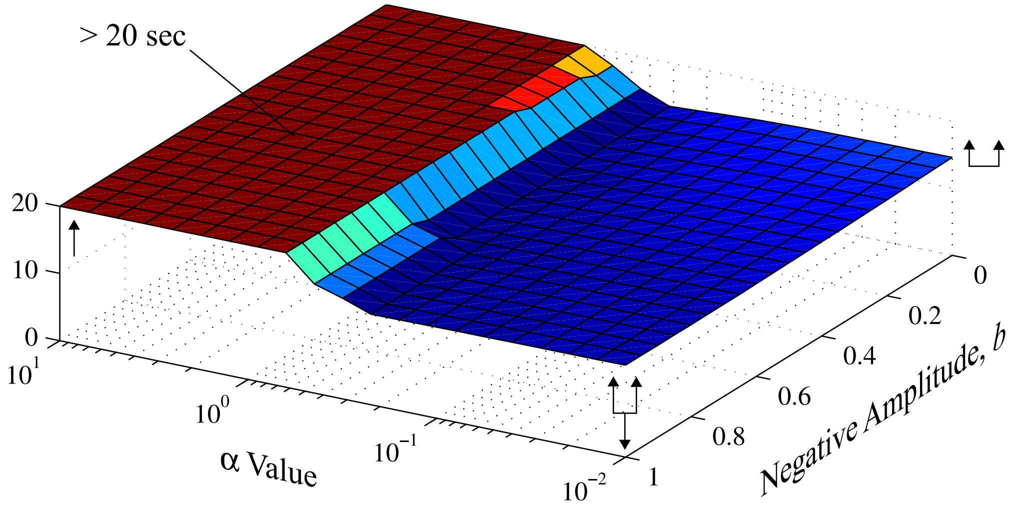

(c) 0.50 load mass ratio

Figure 161: Settling time vs. α for load positioning with different load weights

APPENDIX B

COMPUTER PROGRAMS

B.1 MATLAB Program for Generating a Sum-of-Sines Forcing Function

```
function [phiVec, sineMat, cosMat, targetVec] = ...
    MakeForcingFunction(ampVec, freqVec, timeVec, velBounds, accelBounds)
%==========================================================================%
% INPUTS:
%     ampVec      = amplitude of each sine wave
%     freqVec     = frequency (in rad/sec) of each sine wave
%     timeVec     = vector of time instants (frames) for forcing function
%     velBounds   = lower and upper bounds on target velocity
%     accelBounds = lower and upper bounds on target acceleration
% OUTPUTS:
%     phiVec    = vector of phase values for each sine wave
%     sineMat   = matrix of sine waves at instants in timeVec
%     cosMat    = matrix of cosine waves at instants in timeVec
%     targetVec = target trajectory at instants in timeVec
%==========================================================================%
% Re-seed random number generator
    rng shuffle

% Find number of sine waves and time frames
    numSines = length(freqVec);
    numTimes = length(timeVec);
    dt = timeVec(2)-timeVec(1);     % Time per frame

% Initialize numbers and arrays
    sineMat = zeros(numSines, numTimes);
    cosMat = zeros(numSines, numTimes);
    velAverage = 0;
    accelAverage = 0;

% Keep generating target trajectories until one is within bounds
    while (velAverage > velBounds(2)) || ...
          (velAverage < velBounds(1)) || ...
          (accelAverage > accelBounds(2)) || ...
          (accelAverage < accelBounds(1))

    % Generate random phase values
```

```
        phiVec = 2*pi*rand(numSines,1);

    % Calculate sine and cosine time histories
        for i = 1:numSines
            sineMat(i,:) = ampVec(i)*sin(freqVec(i)*timeVec + phiVec(i));
            cosMat(i,:) = ampVec(i)*cos(freqVec(i)*timeVec + phiVec(i));
        end

    % Find target trajectory, average velocity and acceleration
        targetVec = sum(sineMat, 1);

        targetVel  = (targetVec(2:end) - targetVec(1:end-1))/dt;
        targetAccel  = (targetVel(2:end) - targetVel(1:end-1))/dt;

        velAverage = mean(abs(targetVel));
        accelAverage = mean(abs(targetAccel));
    end
end
```

B.2 MATLAB Program for Calculating Input-Shaper Characteristics

```
function [charOut] = InputShaperCharacteristic(inputShaper, charName)
%=====================================================================%
% INPUTS:
%     inputShaper = row vector of impulse amplitudes, then times
%     charName = code name of characteristic
% OUTPUTS:
%     charOut  = value of chosen characteristic for input shaper
% DEMO FUNCTION CALL:
%     [mychar] = InputShaperCharacteristic([0.5, 0.5, 0, 1.5], 'inte2')
%=====================================================================%
% Unpack shaper amplitudes and times
    n = round(length(inputShaper)/2); % number of shaper impulses
    A = inputShaper(1:n);             % shaper impulse amplitudes
    t = inputShaper(n+1:2*n);         % shaper impulse times
    E = 1-cumsum(A);                  % impulse differences from step

% Calculate characteristic value
    if strcmp(costName, 'tn')
        costOut = t(n);
    elseif strcmp(costName, 'maxAbsE')
        costOut = max(abs(E));
    elseif strcmp(costName, 'sumA')
        costOut = sum(A);
    elseif strcmp(costName, 'sumE')
        costOut = sum(E);
```

```
    elseif strcmp(costName, 'sumAbsE')
        costOut = sum(abs(E));
    elseif strcmp(costName, 'sumA2')
        costOut = sum(A.^2);
    elseif strcmp(costName, 'sumAbsA')
        costOut = sum(abs(A));
    elseif strcmp(costName, 'sumAt')
        costOut = sum(A.*t);
    elseif strcmp(costName, 'sumAbsAt')
        costOut = sum(abs(A).*t);
    elseif strcmp(costName, 'sumA2t')
        costOut = sum(A.^2.*t);
    elseif strcmp(costName, 'sumEt')
        costOut = sum(E.*t);
    elseif strcmp(costName, 'sumE2t')
        costOut = sum(E.^2.*t);
    elseif strcmp(costName, 'sumEt2')
        costOut = sum(E.*t.^2);
    elseif strcmp(costName, 'sumAt2')
        costOut = sum(A.*t.^2);
    elseif strcmp(costName, 'sumAbsAt2')
        costOut = sum(abs(A).*t.^2);
    elseif strcmp(costName, 'sumA2t2')
        costOut = sum(A.^2.*t.^2);
    elseif strcmp(costName, 'sumAt_sumA')
        costOut = sum(A.*t)/sum(A);
    elseif strcmp(costName, 'sumAbsAt_sumAbsA')
        costOut = sum(abs(A).*t)/sum(abs(A));
    elseif strcmp(costName, 'sumAbsEt')
        costOut = sum(abs(E).*t);
    elseif strcmp(costName, 'sumE2')
        costOut = sum(E.^2);
    elseif strcmp(costName, 'sumA2')
        costOut = sum(A.^2);
    elseif strcmp(costName, 'sumAbsEt2')
        costOut = sum(abs(E).*t.^2);
    elseif strcmp(costName, 'sumE2t2')
        costOut = sum(E.^2.*t.^2);

% Characteristic requires integration
    elseif strcmp(costName, 'intAbse') || strcmp(costName, 'inte') ...
|| strcmp(costName, 'intet') || strcmp(costName, 'inte2') ...
|| strcmp(costName, 'intAbset') || strcmp(costName, 'inte2t') ...
|| strcmp(costName, 'intAbset2') || strcmp(costName, 'intet2') ...
|| strcmp(costName, 'inte2t2')
        costOut = 0;
        for u = 1:n-1
```

```
            timeFrame = t(u+1)-t(u);
            if strcmp(costName, 'intAbse')
                costOut = costOut + timeFrame*abs(E(u));
            elseif strcmp(costName, 'inte')
                costOut = costOut + timeFrame*E(u);
            elseif strcmp(costName, 'intet')
                costOut = costOut + 0.5*E(u)*(t(u+1)^2 - t(u)^2);
            elseif strcmp(costName, 'inte2')
                costOut = costOut + timeFrame*E(u)^2;
            elseif strcmp(costName, 'intAbset')
                costOut = costOut + 0.5*abs(E(u))*(t(u+1)^2 - t(u)^2);
            elseif strcmp(costName, 'inte2t')
                costOut = costOut + 0.5*E(u)^2*(t(u+1)^2 - t(u)^2);
            elseif strcmp(costName, 'intAbset2')
                costOut = costOut + (1/3)*abs(E(u))*(t(u+1)^3 - t(u)^3);
            elseif strcmp(costName, 'intet2')
                costOut = costOut + (1/3)*E(u)*(t(u+1)^3 - t(u)^3);
            elseif strcmp(costName, 'inte2t2')
                costOut = costOut + (1/3)*E(u)^2*(t(u+1)^3 - t(u)^3);
            end
        end
    else
        error('Not an expected characteristic name!');
    end
end
```

B.3 Motion Genesis Program for Generating Equations of Motion for Planar Testbed

```
% SYSTEM: Planar Experimental Remote-Controlled Helicopter (PERCH)
% DESCRIPTION: cart with body pinned through its CG, no horizontal
% (relative to body frame) offsets of thrust point or suspension point,
% and specified rotor disc angle 'alpha' and thrust magnitude 'thrust'.
% Damping on linear helicopter motion and angular helicopter motion.
% Rotational spring between alpha disk angle and helicopter
% theta angle to represent torque on hub from rotor stiffness. Offsets
% thetaOff and betaOff are included to account for differences between
% assumed and actual neutral angles while helicopter is in a stable
% hover (helicopter theta may not be at zero degrees when trimmed).

%--------------------------------------------------------------------
% FRAMES AND PARTICLES
%--------------------------------------------------------------------
    NewtonianFrame N        % Newtonian reference frame (ground)
    RigidBody      H        % Helicopter body
    RigidFrame     T        % Thrust frame
    RigidFrame     S        % Load swing frame
```

```
    Point          R(H)     % Thrust force application point
    Point          A(H)     % Load suspension point
    Particle       P        % Suspended load as a massive particle

%--------------------------------------------------------------------
% VARIABLES AND CONSTANTS
%--------------------------------------------------------------------
    Variable x’’      % Distance from No to Ho/Hcm
    Variable theta’’  % Angle of helicopter body (+ angle nose-up)
    Variable beta’’   % Inertial swing angle (+ swing noseward)
    Specified alpha   % Main rotor disk angle
                      % with quasi-steady rotor assumption
                      % (+ angle tailward) relative to helicopter
    Specified thrust  % Thrust force
    constant thetaOff % Offset for neutral helicopter angle
    constant betaOff  % Offset for neutral swing angle
    Constant g        % Gravity
    Constant L        % Suspension cable length
    Constant cx       % Linear damping on body H
    Constant ctheta   % Rotational damping on body H
    Constant kalpha   % Torsion spring between main rotor and helicopter
    Constant yR       % Thrust application point in H-body coordinates
    Constant yA       % Load suspension point in H-body coordinates
    P.SetMass( mP )   % Load mass
    H.SetMass( mH )   % Helicopter mass
    H.SetInertia( Hcm, 0, 0, IH )   % Helicopter inertia

%--------------------------------------------------------------------
% KINEMATICS
%--------------------------------------------------------------------
    SetGeneralizedSpeed( x’ )
    SetGeneralizedSpeed( beta’ )
    SetGeneralizedSpeed( theta’ )

    H.RotateZ( N, theta + thetaOff )
    T.RotateZ( H, alpha )
    S.RotateZ( N, beta + betaOff )

    Ho.Translate( No, x*Nx> )
    Hcm.Translate( Ho, 0> )
    R.Translate( Ho, yR*Hy> )
    A.Translate( Ho, yA*Hy> )   % Note: yA should be a negative number!
    P.Translate( A, -L*Sy> )
```

```
%---------------------------------------------------------------------
% FORCES
%---------------------------------------------------------------------
    System.AddForceGravity( -g*Ny> )
    R.AddForce( thrust*Ty> )

    H.AddTorque( -ctheta*theta'*Nz> )
    H.AddTorque( kalpha*alpha*Nz> )

    Ho.AddForce( -cx*x'*Nx> )

%---------------------------------------------------------------------
% EQUATIONS OF MOTION
%---------------------------------------------------------------------
    KaneEquations = System.GetDynamicsKane()

%---------------------------------------------------------------------
% SIMPLIFY AND SOLVE
%---------------------------------------------------------------------
    FactorLinear( KaneEquations, x'', beta'', theta'' )
    Save PERCH.all
```

REFERENCES

[1] Adams, C., "Modeling and control of helicopters carrying suspended loads," Master's thesis, Georgia Institute of Technology, Mechanical Engineering, Atlanta, GA, USA, 2012.

[2] Adams, J. L., "An investigation of the effects of the time lag due to long transmission distance upon remote control: Phase I - tracking experiments." NASA Technical Note D-1211, Dec. 1961.

[3] Allen, R. W. and Jex, H. R., "A simple Fourier analysis technique for measuring the dynamic response of manual control systems," *IEEE Transactions on Systems, Man, and Cybernetics*, vol. SMC-2, pp. 638–643, Nov. 1972.

[4] Anon., "Handling qualities requirements for military rotorcraft, ADS-33E-PRF," tech. rep., U.S. Army Aviation and Missile Command, Redstone Arsenal, AL, Mar. 2000.

[5] Banerjee, A. K., "Dynamics and control of the WISP shuttle-antennae system," *Journal of the Astronautical Sciences*, vol. 41, no. 1, pp. 73–90, 1993.

[6] Beerens, G. C., Damveld, H. J., Mulder, M., van Paassen, M. M., and van der Vaart, J. C., "Investigation into crossover regression in compensatory manual tracking tasks," *AIAA Journal of Guidance, Control, and Dynamics*, vol. 32, pp. 1429–1445, Sep.-Oct. 2009.

[7] Bekey, G. A., Burnham, G. O., and Seo, J., "Control theoretic models of human drivers in car following," *Human Factors*, vol. 19, pp. 399–413, Aug. 1977.

[8] Bernard, M. and Kondak, K., "Generic slung load transportation system using small size helicopters," in *IEEE Int. Conf. Rob. Autom.*, (Kobe, Japan), pp. 3258–3264, May 2009.

[9] Bernard, M., Kondak, K., and Hommel, G., "Load transportation system based on autonomous small size helicopters," *Aeronautical Journal*, vol. 114, pp. 191–198, 2010.

[10] Bisgaard, M., Bendtsen, J., and La Cour-Harbo, A., "Modelling of generic slung load system," in *AIAA Model. Simul. Technol. Conf.*, (Keystone, CO), Aug. 2006.

[11] Bisgaard, M., La Cour-Harbo, A., and Bendtsen, J., "Adaptive control system for autonomous helicopter slung load operations," *Control Engineering Practice*, vol. 18, pp. 800–811, Jul. 2010. Special Issue on Aerial Robotics.

[12] Blackburn, D., Singhose, W., Kitchen, J., Patrangenaru, V., Lawrence, J., Kamoi, T., and Taura, A., "Command shaping for nonlinear crane dynamics," *Journal of Vibration and Control*, vol. 16, pp. 477–501, Apr. 2010.

[13] Bortoff, S. A., "The University of Toronto RC helicopter: a test bed for nonlinear control," in *IEEE Int. Conf. Control App.*, vol. 1, (Kohala Coast, HI), pp. 333–338, Aug. 1999.

[14] Brown, E. M., *The Helicopter In Civil Operations*, ch. 6, pp. 56–71. Van Nostrand Reinhold Co., 1981.

[15] Chapra, S. C. and Canale, R. P., *Numerical Methods for Engineers*, ch. 13, pp. 342–349. McGraw-Hill, Inc., 3 ed., 1998.

[16] Cooper, G. E. and Harper Jr., R. P., "The use of pilot rating in the evaluation of aircraft handling qualities," Tech. Rep. AGARD Report 567, Cornell Aeronautical Laboratory, Moffett Field, CA, Apr. 1969.

[17] Damveld, H. J., Beerens, G. C., van Paassen, M. M., and Mulder, M., "Design of forcing functions for the identification of human control behavior," *AIAA Journal of Guidance, Control, and Dynamics*, vol. 33, pp. 1064–1081, Jul.-Aug. 2010.

[18] Drapeau, V. and Wang, D., "Verification of a closed-loop shaped-input controller for a five-bar-linkage manipulator," in *IEEE International Conference on Robotics and Automation*, (Atlanta, GA), pp. 216–221, May 1993.

[19] Dukes, T. A., "Maneuvering heavy sling loads near hover part I: Damping the pendulous motion," *Journal of the American Helicopter Society*, vol. 18, no. 2, pp. 2–11, 1973.

[20] Dukes, T. A., "Maneuvering heavy sling loads near hover part II: Some elementary maneuvers," *Journal of the American Helicopter Society*, vol. 18, no. 3, pp. 17–22, 1973.

[21] Fantoni, I. and Lozano, R., *Non-linear Control for Underactuated Mechanical Systems*. Springer Verlag, 2001.

[22] Gavrilets, V., Mettler, B., and Feron, E., "Human-inspired control logic for automated maneuvering of miniature helicopter," *Journal of Guidance, Control, and Dynamics*, vol. 27, pp. 752–759, Sep.-Oct. 2004.

[23] Gawron, V. J., *Human Performance, Workload, and Situational Awareness Measures Handbook*, ch. 3.3.2.5, pp. 167–170. Taylor & Francis, 2 ed., 2008.

[24] Gerisch, H., Staude, G., Wolf, W., and Bauch, G., "A three-component model of the control error in manual tracking of continuous random signals," *Human Factors*, May 2013. Available online.

[25] Gotelli, N. J. and Ellison, A. M., *A Primer of Ecological Statistics*, ch. 9, pp. 259–262. Sunderland, MA: Sinauer Associates, Inc., 2004.

[26] Grosser, K. and Singhose, W., "Command generation for reducing perceived lag in flexible telerobotic arms," *JSME International Journal, Series C*, vol. 43, no. 3, pp. 755–761, 2000.

[27] Hess, R. A., "Unified theory for aircraft handling qualities and adverse aircraft-pilot coupling," *AIAA Journal of Guidance, Control, and Dynamics*, vol. 20, pp. 1141–1148, Nov. 1997.

[28] Hess, R. A. and Modjtahedzadeh, A., "A control theoretic model of driver steering behavior," *IEEE Control Systems Magazine*, vol. 10, pp. 3–8, Aug. 1990.

[29] Hess, R. A., "A rationale for human operator pulsive control behavior," *Journal of Guidance and Control*, vol. 2, pp. 221–227, May-Jun. 1979.

[30] Hess, R. A., "Effects of time delays on systems subject to manual control," *AIAA Journal of Guidance, Control, and Dynamics*, vol. 7, pp. 416–421, Jul.-Aug. 1984.

[31] Hess, R. A., *Feedback Control Models – Manual Control and Tracking*, ch. 38, pp. 1249–1294. Hoboken, NJ: John Wiley & Sons, Inc., 3 ed., 2006.

[32] Hess, R. A., "Simplified approach for modelling pilot pursuit control behaviour in multi-loop flight control tasks," *Proceedings of the IMechE, Part G: Journal of Aerospace Engineering*, vol. 220, pp. 85–102, 2006.

[33] Hoh, R. H., Heffley, R. K., and Mitchell, D. G., "Development of handling qualities criteria for rotorcraft with externally slung loads," Tech. Rep. NASA CR-213488, Ames Research Center, Moffett Field, CA, Oct. 2006.

[34] Huey, J. R., *The Intelligent Combination of Input Shaping and PID Feedback Control.* PhD thesis, Georgia Institute of Technology, Mechanical Engineering, Atlanta, GA, Jul. 2006.

[35] Ishitobi, M., Nishi, M., and Nakasaki, K., "Nonlinear adaptive model following control for a 3-DOF tandem-rotor model helicopter," *Control Engineering Practice*, vol. 18, pp. 936–943, Aug. 2010.

[36] Ivler, C. M., *Design and Flight Test of a Cable Angle Feedback Control System for Improving Helicopter Slung Load Operations at Low Speed.* PhD thesis, Stanford University, Aeronautics and Astronautics, Stanford, CA, Oct. 2012.

[37] Ivler, C. M., Powell, J. D., Tischler, M. B., Fletcher, J. W., and Ott, M. C., "Design and flight test of a cable angle/rate feedback flight control system for the RASCAL JUH-60 helicopter," in *American Helicopter Soc. Forum*, (Fort-Worth, TX), May 2012.

[38] Jagacinski, R. J., "A qualitative look at feedback control theory as a style of describing behavior," *Human Factors*, vol. 19, pp. 331–347, Aug. 1977.

[39] Jagacinski, R. J. and Flach, J. M., *Control Theory for Humans: Quantitative Approaches to Modeling Performance.* New York, NY: CRC Press, 2003.

[40] Johnson, E. N. and Pritchett, A. R., "Generic pilot and flight control model for use in simulation studies," in *AIAA Model. Sim. Tech. Conf.*, (Monterey, CA), Aug. 2002.

[41] Johnson, W., *Helicopter Theory*, ch. 15, p. 802. New York: Dover Publications, Inc., 1994.

[42] Jones, S. and Ulsoy, A. G., "An approach to control input shaping with application to coordinate measuring machines," *Journal of Dynamic Systems, Measurement, and Control*, vol. 121, pp. 242–247, Jun. 1999.

[43] Kane, T. R. and Mitiguy, P., "MotionGenesis – kane 5.2." http://www.motiongenesis.com/, 2011.

[44] Kang, M. and Yang, B., "Discrete time noncollocated control of flexible mechanical systems using time delay," *Journal of Dynamic*, vol. 116, pp. 216–222, 1994.

[45] Khalid, A., Huey, J., Singhose, W., Lawrence, J., and Frakes, D., "Human operator performance testing using an input-shaped bridge crane," *Journal of Dynamic Systems, Measurement, and Control*, vol. 128, pp. 835–841, Dec. 2006.

[46] Kim, D. and Singhose, W., "Performance studies of human operators driving double-pendulum bridge cranes," *Control Engineering Practice*, vol. 18, pp. 567–576, Jun. 2010.

[47] Kleinman, D. L. and Perkins, T. R., "Modeling human performance in a time-varying anti-aircraft tracking loop," *IEEE Transactions on Automatic Control*, vol. AC-19, pp. 297–306, Aug. 1974.

[48] Kumar, R., "Effects of time delays on the stability of collocated and noncollocated point control of discrete dynamic structural systems," *Applied Math*, vol. 70, pp. 215–232, 1995.

[49] Leonard, F., Martini, A., and Abba, G., "Robust nonlinear controls of model-scale helicopters under lateral and vertical wind gusts," *IEEE Transactions on Control Systems Technology*, vol. 20, pp. 154–163, Jan. 2012.

[50] Lucassen, L. R. and Sterk, F. J., "Dynamic stability analysis of a hovering helicopter with a sling load," *Journal of the American Helicopter Society*, vol. 10, no. 2, pp. 6–12, 1965.

[51] Magee, D. P. and Book, W. J., "Filtering micro-manipulator wrist commands to prevent flexible base motion," in *American Control Conference*, (Seattle, WA), pp. 924–928, Jun. 1995.

[52] Mansur, M., Tischler, M., Bielefield, M., Bacon, J., Cheung, K., Berrios, M., and Rothman, K., "Full flight envelope inner-loop control law development for the unmanned K-MAX," in *American Helicopter Soc. Forum*, (Virginia Beach, VA), May 2011.

[53] McRuer, D. and Weir, D. H., "Theory of manual vehicular control," *IEEE Transactions on Man-Machine Systems*, vol. 10, no. 4, pp. 257–291, 1969.

[54] McRuer, D. T., "Human dynamics in man-machine systems," *Automatica*, vol. 16, pp. 237–253, May 1980.

[55] McRuer, D. T., Graham, D., Krendel, E. S., and Reisener, W., J., "Human pilot dynamics in compensatory systems," Tech. Rep. AFFDL-TR-65-15, Air Force Flight Dynamics Laboratory, Wright-Patterson AFB, OH, 1965.

[56] McRuer, D. T. and Jex, H. R., "A review of quasi-linear pilot models," *IEEE Transactions on Human Factors in Electronics*, vol. HFE-8, pp. 231–249, Sep. 1967.

[57] McRuer, D. T. and Krendel, E. S., "Dynamic response of human operators," Tech. Rep. WADC-TR-56-524, Oct. 1957.

[58] McRuer, D. T. and Krendel, E. S., "The man-machine system concept," *Proceedings of the IRE*, vol. 50, pp. 1117–1123, May 1962.

[59] McRuer, D. T., "Pilot induced oscillations and human dynamic behavior," Tech. Rep. NASA CR-4683, Jul. 1995.

[60] McRuer, D. T., Graham, D., and Krendel, E. S., "Manual control of single-loop systems: Part I," *Journal of the Franklin Institute*, vol. 283, pp. 1–29, Jan. 1967.

[61] McRuer, D. T., Weir, D. H., Jex, H. R., Magdaleno, R. E., and Allen, R. W., "Measurement of driver-vehicle multiloop response properties with a single disturbance input," *IEEE Transactions on Systems, Man, and Cybernetics*, vol. SMC-5, no. 5, pp. 490–497, 1975.

[62] Mettler, B., Dever, C., and Feron, E., "Scaling effects and dynamic characteristics of miniature rotorcraft," *Journal of Guidance, Control, and Dynamics*, vol. 27, pp. 466–478, May-Jun. 2004.

[63] Mettler, B., Tischler, M. B., and Kanade, T., "System identification of small-size unmanned helicopter dynamics," in *American Helicopter Soc. Forum*, (Montreal, Quebec, Canada), May 1999.

[64] Morris, J. C., van Nieuwstadt, M., and Bendotti, P., "Identification and control of a model helicopter in hover," in *American Control Conf.*, vol. 2, pp. 1238–1242, Jul. 1994.

[65] Nicoll, T. K. and Mitchell, D. G., "ADS-33 handling qualities specification development for externally loaded cargo/utility helicopter," in *AIAA Atmos. Flight Mech. Conf.*, 2009.

[66] on the Effects of Aircraft-Pilot Coupling on Flight Safety, U. N. R. C. C., *Aviation Safety and Pilot Control: Understanding and Preventing Unfavorable Pilot-Vehicle Interactions.* National Academies Press, 1997.

[67] Ortega, C. E., Ma, O., and Ruble, K., "Gravity-balanced test stand for testing micro air vehicles," in *AIAA Atmospheric Flight Mechanics Conference*, (Chicago, IL), Aug. 2009.

[68] Ottander, J. A. and Johnson, E. N., "Precision slung cargo delivery onto a moving platform," in *AIAA Model. Simul. Technol. Conf.*, (Toronto, Ontario, Canada), pp. 1–15, Aug. 2010.

[69] Padfield, G. D., *Helicopter Flight Dynamics: The Theory and Application of Flying Qualities and Simulation Modeling.* AIAA Educational Series, Washington, DC: American Institute of Aeronautics and Astronautics, Inc., 1996.

[70] Potter, J. J. and Singhose, W. E., "Improving manual tracking of systems with oscillatory dynamics," *IEEE Transactions on Human-Machine Systems*, vol. 43, pp. 46–52, Jan. 2013.

[71] Poulton, R. C., *Tracking Skills and Manual Control.* New York, NY: Academic Press, 1974.

[72] Prouty, R. W., *Helicopter Performance, Stability, and Control.* Malabar, FL: Krieger Publishing Company, Inc., 1990.

[73] Ricard, G. L., "Manual control with delays: A bibliography," *ACM SIGGRAPH Computer Graphics*, vol. 28, pp. 149–154, May 1994.

[74] Rye, D. C., "Longitudinal stability of a hovering, tethered rotorcraft," *Journal of Guidance*, vol. 8, pp. 743–752, Nov.-Dec. 1985.

[75] Shim, H. D., Kim, H. J., and Sastry, S., "Control system design for rotorcraft-based unmanned aerial vehicles using time-domain system identification," in *IEEE Int. Conf. Control Appl.*, (Anchorage, AK), pp. 808–813, Sep. 2000.

[76] Singer, N. C., *Residual Vibration Reduction in Computer Controlled Machines.* PhD thesis, Massachusetts Institute of Technology, Feb. 1989.

[77] Singer, N. C. and Seering, W. P., "Preshaping command inputs to reduce system vibration," *Journal of Dynamic Systems, Measurement, and Control*, vol. 112, pp. 76–82, Mar. 1990.

[78] Singhose, W., Derezinski, S., and Singer, N., "Extra-insensitive input shapers for controlling flexible spacecraft," *AIAA Journal of Guidance, Control, and Dynamics*, vol. 9, no. 2, pp. 385–391, 1996.

[79] Singhose, W., Kim, D., and Kenison, M., "Input shaping control of double-pendulum bridge crane oscillations," *Journal of Dynamic Systems, Measurement, and Control*, vol. 130, p. 034504, May 2008.

[80] Singhose, W., Seering, W., and Singer, N., "Residual vibration reduction using vector diagrams to generate shaped inputs," *Journal of Mechanical Design*, vol. 116, pp. 654–659, Jun. 1994.

[81] Singhose, W., Biediger, E. O., Chen, Y., and Mills, B., "Reference command shaping using specified-negative-amplitude input shapers for vibration reduction," *Journal of Dynamic Systems, Measurement, and Control*, vol. 126, pp. 210–214, Mar. 2004.

[82] Singhose, W., Bohlke, K., and Seering, W., "Fuel-efficient pulse command profiles for flexible spacecraft," *AIAA Journal of Guidance, Control, and Dynamics*, vol. 19, no. 4, pp. 954–960, 1996.

[83] Singhose, W. and Seering, W., *Command Generation for Dynamic Systems.* Lulu Press, Inc., 2009.

[84] Singhose, W., Seering, W., and Singer, N., "Input shaping for vibration reduction with specified insensitivity to modeling errors," in *Japan-USA Symposium on Flexible Automation*, vol. 1, (Boston, MA), 1996.

[85] Singhose, W., Singer, N., and Seering, W., "Improving repeatability of coordinate measuring machines with shaped command signals," *Precision Engineering*, vol. 18, pp. 138–146, Apr. 1996.

[86] Smith, J. H., Allen, G. M., and Vensel, D., "Design, fabrication, and flight test of the active arm external load stabilization system for cargo handling helicopters," tech. rep., Boeing Vertol Co., Sep. 1973.

[87] Smith, O. J. M., *Feedback Control Systems.* New York, NY: McGraw-Hill Book Co., Inc., 1958.

[88] Smith, O. J. M., "Posicast control of damped oscillatory systems," *Proceedings of the IRE*, vol. 45, pp. 1249–1255, Sep. 1957.

[89] Sorensen, K., *Operational Performance Enhancement of Human Operated Flexible Systems.* PhD thesis, Georgia Institute of Technology, Mechanical Engineering, Atlanta, GA, Aug. 2008.

[90] Sorensen, K. L., Singhose, W., and Dickerson, S., "A controller enabling precise positioning and sway reduction in bridge and gantry cranes," *Control Engineering Practice*, vol. 15, pp. 825–837, Jul. 2007. Special Issue on Award Winning Applications, 2005 IFAC World Congress.

[91] Takagi, H., "Interactive evolutionary computation: fusion of the capabilities of EC optimization and human evaluation," *Proceedings of the IEEE*, vol. 89, pp. 1275–1296, Sep. 2001.

[92] Thompson, P. M., Klyde, D. H., and Brenner, M. J., "Wavelet-based time-varying human operator models," in *AIAA Atmospheric Flight Mechanics Conference*, (Montreal, Canada), Aug. 2001.

[93] Tischler, M. B., "System identification requirements for high-bandwidth rotorcraft flight control system design," in *American Control Conf.*, (Boston, MA), pp. 2494–2502, Jun. 1991.

[94] Todosiev, E. P., Rose, R. E., and Summers, L. G., "Human performance in single and two-axis tracking systems," *IEEE Transactions on Human Factors in Electronics*, vol. HFE-8, pp. 125–129, Jun. 1967.

[95] Tustin, A., "The nature of the operator's response in manual control, and its implications for controller design," *Journal of the Institution of Electrical Engineers*, vol. 94, pp. 190–206, May 1947.

[96] Tuttle, T. and Seering, W., "Experimental verification of vibration reduction in flexible spacecraft using input shaping," *AIAA Journal of Guidance, Control, and Dynamics*, vol. 20, pp. 658–664, Jul. 1997.

[97] Udwadia, F. E., "Noncollocated control of distributed-parameter nondispersive systems with tip inertias using time delays," *Applied Mathematics and Computation*, pp. 47–75, 1992.

[98] UK Civil Aviation Authority Safety Regulation Group, The Stationery Office, *Helicopter External Load Operations*, CAP 426 ed., Apr. 2006.

[99] Vaughan, J., *Dynamics and Control of Mobile Cranes.* PhD thesis, Georgia Institute of Technology, Mechanical Engineering, Atlanta, GA, Jul. 2008.

[100] Vaughan, J., Jurek, P., and Singhose, W., "Reducing overshoot in human-operated flexible systems," *Journal of Dynamic Systems, Measurement, and Control*, vol. 133, no. 1, p. 011010, 2011.

[101] Vaughan, J., Yano, A., and Singhose, W., "Comparison of robust input shapers," *Journal of Sound and Vibration*, vol. 315, pp. 797–815, Sep. 2008.

[102] Vaughan, J., Yano, A., and Singhose, W., "Robust negative input shapers for vibration suppression," *Journal of Dynamic Systems, Measurement, and Control*, vol. 131, p. 031014, May 2009.

[103] Velagic, J. and Osmic, N., "Identification and control of 2DOF nonlinear helicopter model using intelligent methods," in *IEEE Int. Conf. Syst. Man Cybern.*, pp. 2267–2275, Oct. 2010.

[104] Wang, S., Wang, X., and Takagi, H., "User fatigue reduction by an absolute rating data-trained predictor in IEC," in *IEEE Congr. Evol. Comput.*, (Vancouver, British Columbia, Canada), pp. 2195–2200, Jul. 2006.

[105] Wickens, C. D., Gordon, S. E., and Liu, Y., *An Introduction to Human Factors Engineering*, ch. 10, pp. 386–432. New York, NY: Addison-Wesley Longman, Inc., 1998.

[106] Wie, B., Sinha, R., Sunkel, J., and Cox, K., "Robust fuel- and time-optimal control of uncertain flexible space structures," in *AIAA Guidance, Navigation, and Control Conference*, (Monterey, CA), pp. 939–948, Aug. 1993.

[107] Young, L. R. and Meiry, J. L., "Bang-bang aspects of manual control in high-order systems," *IEEE Transactions on Automatic Control*, vol. 10, pp. 336–341, Jul. 1965.